



**TESE DE DOUTORADO EM CIÊNCIAS  
MECÂNICAS**

**STRESS GRADIENTS IN FRETTING FATIGUE**

**MR JOHAN BELLECAVE**

**UNIVERSIDADE DE BRASÍLIA**

**FACULDADE DE TECNOLOGIA**

**DEPARTAMENTO DE ENGENHARIA MECÂNICA**

**UNIVERSIDADE DE BRASÍLIA**

**FACULDADE DE TECNOLOGIA**

**DEPARTAMENTO DE ENGENHARIA MECÂNICA**

**TESE DE DOUTORADO EM CIÊNCIAS MECÂNICAS**

**STRESS GRADIENTS IN FRETTING FATIGUE**

**JOHAN BELLECAVE**

**ORIENTADORS: J. ALEXANDER ARAÚJO**

**SYLVIE POMMIER**

**PUBLICAÇÃO: ENM.TD – 029/2015**

**BRASÍLIA/DF: SETEMBRO – 2015**

**UNIVERSIDADE DE BRASÍLIA**

**FACULDADE DE TECNOLOGIA**

**DEPARTAMENTO DE ENGENHARIA MECÂNICA**

**TESE DE DOUTORADO EM CIÊNCIAS MECÂNICAS**

# STRESS GRADIENTS IN FRETTING FATIGUE

JOHAN BELLECAVE

TESE DE DOUTORADO SUBMETIDA AO DEPARTAMENTO DE ENGENHARIA MECÂNICA DA FACULDADE DE TECNOLOGIA DA UNIVERSIDADE DE BRASÍLIA COMO PARTE DOS REQUISITOS NECESSÁRIOS PARA A OBTENÇÃO DO GRAU DE DOUTOR.

BANCA EXAMINADORA:

---

Prof. Sylvie POMMIER. (LMT – ENS Cachan) – Orientadora

---

Prof. J. Alexander ARAÚJO. (ENM – FT – UnB) – Orientador

---

Prof. Edgar Nobuo MAMIYA. (ENM – FT – UnB) – Examinador Interno

---

Prof. Yves NADOT. (P' PRIME – ENSMA) – Examinador Externo

---

Prof. Marco A. MEGGIOLARO. (PUC – Rio) – Examinador Externo

BRASÍLIA/DF, 09 DE SETEMBRO DE 2015.

## FICHA CATALOGRÁFICA

BELLECAVE, JOHAN	
STRESS GRADIENTS IN FRETTING FATIGUE	
xxvii, 170p., 210 x 297 mm (ENM/FT/UnB, Doutor, Ciências Mecânicas, 2015)	
Tese de Doutorado – Universidade de Brasília, Faculdade de Tecnologia.	
Departamento de Engenharia Mecânica.	
1. Fretting fatigue	2. Multiaxial
3. Gradient	4. Short crack arrest
5. T-stress	
I. ENM/FT/UnB	II. Título (série)

## REFERÊNCIA BIBLIOGRÁFICA

BELLECAVE, J. (2015). Stress gradient in fretting fatigue. Tese de doutorado, Publicação ENM.TD – 029/2015, Departamento de Engenharia Mecânica, Universidade de Brasília, DF, 170p.

## CESSÃO DE DIREITOS

**AUTOR:** Johan BELLECAVE

**TÍTULO:** Stress gradient in fretting fatigue.

**GRAU:** Doutor

**ANO:** 2015

É concedida à Universidade de Brasília permissão para reproduzir cópias desta tese de doutorado e para emprestar ou vender tais cópias somente para propósitos acadêmicos e científicos. O autor reserva outros direitos de publicação e nenhuma parte dessa tese de doutorado pode ser reproduzida sem autorização por escrito do autor.

---

Johan BELLECAVE

[jbellecave@gmail.com](mailto:jbellecave@gmail.com)

**THESIS  
OF L'ÉCOLE NORMALE SUPÉRIEURE DE CACHAN  
AND UNIVERSIDADE DE BRASÍLIA**

Presented by  
Mr Johan Bellecave

to obtain the degree of  
**DOCTEUR DE L'ÉCOLE NORMALE SUPÉRIEURE DE CACHAN  
DOUTOR EM CIÊNCIAS MECÂNICAS DA UNIVERSIDADE DE BRASÍLIA**

Area: **SOLID MECHANICS**

Name of the thesis:

**STRESS GRADIENTS IN FRETTING FATIGUE**

Thesis presented at Universidade de Brasília the 9th September 2015 with the examination committee:

Sylvie POMMIER	Professor	ENS Cachan	Supervisor
J. Alexander ARAÚJO	Professor	ENM, UNB, Brasília	Supervisor
Yves NADOT	Professor	ENSMA, P' PRIME	Reviewer
Marco A. MEGGIOLARO	Professor	PUC-Rio	Reviewer
Edgar N. MAMIYA	Professor	ENM, UNB, Brasília	Examiner

LMT  
ENS Cachan, CNRS, Université Paris Saclay  
61, avenue du Président Wilson  
94235 CACHAN CEDEX France

Departamento de Engenharia Mecânica  
FT - UnB  
Asa Norte - Brasília / DF  
C.E.P: 70910-900 Brasil

## Abstract

This thesis is part of an international research program (IRG Cognac) initiated by the engine manufacturer SNECMA (SAFRAN group) involving ENS Cachan, UnB, ENSMA, CNRS, Snecma, Turbomeca et Messier Bugatti Dowty. The thesis focuses on the effect of a stress gradient in fretting fatigue.

Fretting-fatigue refers to the damage process localized at the frontier of the contact between two contacting bodies subjected to fatigue loadings. The prediction of this phenomenon is of major importance in determining, for instance, the lifetime of fan's disc. In the vicinity of the contact front, the stress field inherited from the contact loads is maximal at the surface and displays a strong gradient from the surface.

It was shown in this thesis, for a TA64V alloy, that local approaches, based on local stresses at the most critical point, are not appropriate to predict fretting fatigue lives. As a matter of fact, short cracks initiated at the most critical point may stop if the stress decay from the surface is strong enough or may continue their growth, up to the failure of the component, if the stress gradient from the surface is not strong enough. A second difficulty is the multiaxial and non-proportional nature of the loading conditions. Fatigue-fretting stems from the combination of loads that have neither the same spatial distribution nor the same time-dependency. In fretting-fatigue tests, three loading components are considered, the fatigue loading of the component (cyclic), the normal part (assumed to be constant) and the in-plane part (cyclic) of the loads between the two contacting components. To quantify the effect of the stress gradient, tests were carried out on a fatigue testing contact bench developed at the University of Brasilia, with experimental conditions ensuring different stress gradient while keeping the maximal stress the same. Damage mechanisms were studied using post-mortem analysis and optical microscopy on the contact elements tested.

The prediction of the fretting fatigue life was done using different approaches. The first one is based on the Critical Distance Method and a fatigue criterion. The second is based on a K-based short crack arrest method. Finally, a new criterion was proposed. This method considers a generalized von Mises yield criterion for the crack tip region and accounts for the T-stresses in the asymptotic LEFM development.

### **Remerciements - Agradecimentos - Acknowledgements**

Avant tout autre chose, je souhaiterais remercier Jean Mériaux, Sylvie Pommier et Alex Araújo qui ont suivi et dirigé ma thèse. Merci pour leur confiance, leur patience et leur ténacité. Au delà de leurs compétences scientifiques reconnues. Je remercie l'ANRT et SNECMA (Groupe SAFRAN) pour le cofinancement de ma thèse. Et je remercie également Fabienne Fong pour son soutien et son aide.

Me arriscarei no português para agradecer as pessoas que marcaram a minha estadia no Brasil. Obrigado a Jordana Peixoto, Julia Ayla, Patricia Vitorino, Elissa Massote, Guillaume Tessier, Wallison Martins e todos os outros. Graças a eles a minha experiência no Brasil foi uma verdadeira alegria. Tais encontros tiveram uma enorme influência na minha aprendizagem do português e me fizeram descobrir os melhores aspectos da rica cultura brasileira. Agradeço igualmente aos meus colegas de laboratório, particularmente Miguel Garcia que muito me ajudou com meus testes. Agradeço aos professores Fabio Castro, Edgar Nobuo Mamiya, Jorge Luiz de Almeida Ferreira e todos os outros professores do ENM por terem me ajudado diversas vezes. Obrigado ainda ao National Council of Technological and Scientific Development - CNPq (contrato 304648/2010-8) pelo apoio e suporte.

# Contents

<b>Contents</b>	<b>i</b>
<b>1 Introduction.</b>	<b>1</b>
1.1 Context of the study. . . . .	1
1.2 The contact problem. . . . .	3
1.3 Stress gradient and scale effect. . . . .	5
1.4 Thesis scope. . . . .	6
<b>2 Literature Review.</b>	<b>9</b>
2.1 Fretting . . . . .	9
2.1.1 Introduction. . . . .	9
2.1.2 Tribological behaviour of contact. . . . .	9
2.1.3 Subsurface stress field. . . . .	16
2.1.4 Numerical modelling of fretting fatigue. . . . .	24
2.2 Titanium Ti-6Al-4V . . . . .	31
2.2.1 Macrozones of the Ti-6Al-4V alloy . . . . .	34
2.2.2 Microstructure and material properties observed in literature . . . . .	35
2.3 Fatigue of materials. . . . .	38
2.3.1 Basic concepts. . . . .	38
2.3.2 Uniaxial tests and influence of the loading ratio. . . . .	41
2.3.3 Criteria based on stress invariants . . . . .	43
2.3.4 Critical plane approach . . . . .	44
2.3.5 Gradient effect - Local vs Non local approach . . . . .	48
2.3.6 Scale effect - Probabilistic approach . . . . .	49
2.4 Fracture mechanics. . . . .	50
2.4.1 Introduction. . . . .	50
2.4.2 Fracture modes . . . . .	51
2.4.3 Asymptotic solution . . . . .	51
2.4.4 J-integral . . . . .	54
2.4.5 Method of distribution of dislocations. . . . .	55
2.4.6 Paris Law . . . . .	56
2.4.7 The Kitagawa–Takahashi (K–T) diagram . . . . .	56
2.4.8 Crack closure or effect of the loading ratio. . . . .	58
2.4.9 Gradient effect - Critical distance. . . . .	60
2.4.10 T-stress. . . . .	61

2.5	Summary of the literature review. . . . .	63
<b>3</b>	<b>Test design and experimental protocol</b>	<b>65</b>
3.1	Introduction . . . . .	65
3.2	Apparatus configuration and preliminary test . . . . .	65
3.2.1	Pads and Specimen . . . . .	65
3.2.2	Experimental set-up used for cylinder-plane fretting fatigue research . . . . .	68
3.2.3	Digital Image Correlation applied to fretting fatigue . . . . .	71
3.2.4	Experimental set-up for spherical-plane fretting bi-axial fatigue research . . . . .	73
3.2.5	Coefficient of friction . . . . .	75
3.3	Finite element modelling of fretting fatigue tests . . . . .	79
3.3.1	Basic 2D model . . . . .	79
3.3.2	Comparison with 3D model . . . . .	82
3.3.3	Crack modeling . . . . .	84
<b>4</b>	<b>Experimental results</b>	<b>89</b>
4.1	Results of cylinder/plane fretting fatigue test . . . . .	89
4.1.1	First set of tests . . . . .	89
4.1.2	Comparison among different gradients . . . . .	92
4.2	Results of spherical/plane fretting fatigue test . . . . .	103
4.2.1	Objective . . . . .	103
4.2.2	Experimental test realized . . . . .	104
4.3	Conclusion of the experimental tests. . . . .	106
<b>5</b>	<b>Prediction of fretting fatigue life</b>	<b>109</b>
5.1	Introduction . . . . .	109
5.1.1	Material properties and coefficient of friction of Ti-6Al-4V alloy. . . . .	109
5.1.2	On the use of the analytical formulation of the contact problem. . . . .	110
5.1.3	Location of the critical site for crack initiation. . . . .	110
5.2	Multiaxial stress fatigue model. . . . .	114
5.2.1	Fretting map and comparison with experimental results. . . . .	114
5.2.2	Discussion on the model. . . . .	116
5.2.3	Proposition of criterion parameter. . . . .	118
5.3	Short crack arrest approach. . . . .	120
5.3.1	Introduction. . . . .	120
5.3.2	Comparison with experimental results. . . . .	121
5.3.3	Effect of the loading ratio. . . . .	123
5.3.4	Conclusion. . . . .	124
5.4	A new methodology - Using the T-stress . . . . .	125
5.4.1	Assumptions . . . . .	125
5.4.2	Expression of the criterion. . . . .	125
5.4.3	Identification of the parameters . . . . .	126
5.4.4	Representation of the criterion. . . . .	127
5.4.5	Application to fretting . . . . .	129

---

<b>6</b>	<b>Conclusions, recommendations and future work</b>	<b>139</b>
6.1	Overview. . . . .	139
6.2	Methodology used in this study. . . . .	139
6.2.1	Experimental set-up . . . . .	139
6.2.2	Analytical and numerical modeling of the problem. . . . .	140
6.2.3	Prediction of fretting fatigue lifetime . . . . .	140
6.3	Main conclusions . . . . .	141
6.3.1	Fretting fatigue experiments . . . . .	141
6.3.2	Prediction of the fretting fatigue lifetime . . . . .	141
6.4	The scale effect. . . . .	142
6.5	Notch analogy. . . . .	143

# Nomenclature

$\Delta K_0$	Long crack stress intensity threshold
$\Delta K_{th}$	Threshold of the stress-intensity range
$\mu$	Coefficient of friction
$\mu_m$	Average coefficient of friction
$\mu_s$	Coefficient of friction at the slip zones
$\mu_t$	Coefficient of friction at the transition partial/gross slip
$\nu$	Poisson's ratio
$\sigma_a$	Stress amplitude
$\sigma_m$	Mean stress
$\sigma_u$	Ultimate stress
$\sigma_y$	Yield strength
$\sigma_{-1, \sigma_{0.1}}$	Fatigue limit ( $\sigma_{max}$ ) in traction for $R_\sigma = -1$ and $R_\sigma = 0.1$
$\sigma_n$	Normal stress
$\tau_a$	Shear stress amplitude
$A$	Composite compliance
$a$	Contact semi-width
$B$	Bulk load
$b$	Crack size
$b_0$	Intrinsic crack length (El Haddad parameter)
$b_x$	Burgers vector
$c$	Half size of the central stick region
$E$	Modulus of rigidity

---

$e$	Stick zone offset.
$F$	Airy function
$G$	Shearing mode
$g(x)$	Relative tangential displacement
$h(x)$	Normal displacement distribution
$I_{max}$	Hydrostatic stress max
$I_{moy}$	Mean hydrostatic stress
$J_a$	Second invariant amplitude
$K_{III}$	Stress intensity factor in mode III
$K_{II}$	Stress intensity factor in mode II
$K_I$	Stress intensity factor in mode I
$l_{LM}$	Critical distance, line method
$l_{PM}$	Critical distance, point method
$p(x)$	Pressure distribution
$p_0$	Peak pressure
$Q$	Tangential load
$q(x)$	Shear traction distribution
$R$	Pad radius
$R_a, R_q$	Roughness parameters
$R_c$	Load ratio
$S$	Stress deviator tensor
$T_{ra}$	Generalised shear stress amplitude
$U$	Distortional energy per unit of length of the crack front
$W$	Strain energy density
$\epsilon_a$	Tensile strain amplitude
$\gamma_a$	Shear strain amplitude

# Chapter 1

## Introduction.

### 1.1 Context of the study.

Most commercial engines developed by *Snecma (Safran Group)* operate on the principle of the turbojet using an architecture ‘dual stream’ and ‘body double’.

In a turbofan, the majority of the thrust is provided by a large fan at the front of the engine. Air that passes through the fan is split into two streams. One flow continues through the turbine section of the engine. The rest is bypassed around the turbine, it goes through a duct that surrounds the core to the back of the jet engine. The ratio of secondary airflow to primary airflow is known as the bypass ratio. Mixing of the cold secondary flow with the hot exhaust gasses at the rear of the engine is the greatest source of noise at cruise conditions.

While the duct section provides a great part of the force that propels the airplane forward, it is in the core section that the processes of compression, combustion and expansion occur. These three processes are respectively split amongst the compressor, combustor and turbine (FIG.1.1).

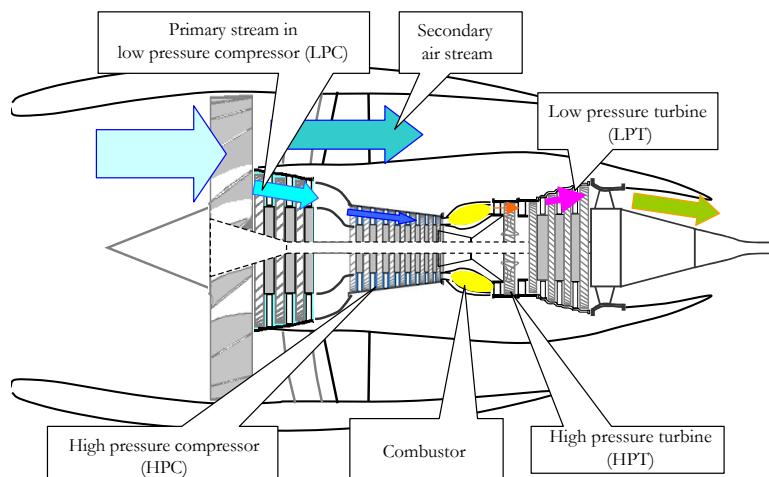


Figure 1.1: Illustration of a dual stream and body double turbojet engine, adapted from (Thevenin 2004).

Dovetail roots are used to fix the blades on the disks for the fan assembly and in the low pressure stages of rotating compressors. This configuration makes the changing of a damaged blade possible

without necessarily changing an entire bloc.



Figure 1.2: Photography of a) blade b) fan c) disk.

The blade-disk attachment experiences two sources of fretting damage (FIG.1.3). The first is associated with the variations of the rotational speed. As the disc spins up the hoop stress will increase causing an expansion of the disc and its fixing slots. Under the action of the centrifugal force, the blade will then move slightly upwards giving rise to a relative motion between the contacting surfaces.

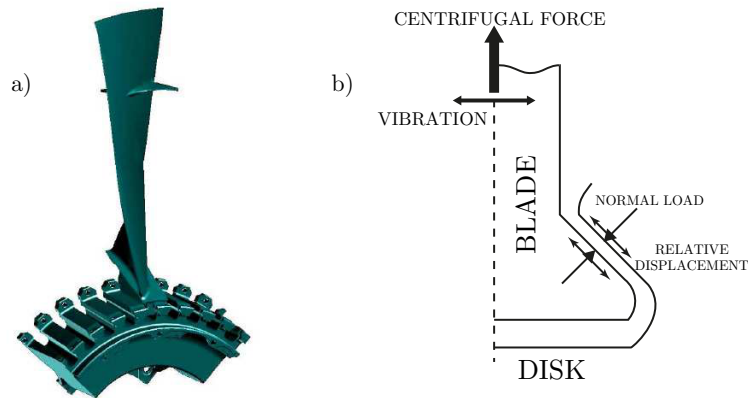


Figure 1.3: Schematic diagram of the dovetail fixing and load configuration.

The second source of fretting damage in this configuration comes from high-frequency vibrational loads caused by aerodynamic forces. The interaction between air and blade will generate bending moments at the root of the fixing leading to small relative displacements at the interface.

However, estimation in terms of pressure, displacement and frequency is extremely complex since measurements on board are nearly impossible. A basic flight cycle, and relative displacement between the blades and the disc may be simplified into three distinct phases illustrated in FIG.1.4.

The casing of the engine is designed in order to contain the possible failure of a blade. The failure of a blade generally provokes the destruction of the engine but is not critical for the structure of the airplane. For example, in 2007, a Southwest Airlines' Boeing 737-300 experienced an initial blade failure provoking damages in all the fan blades and a large penetration hole was noted on the right-hand side of the fan cowl (FIG.1.5A), but no breaches on any of the engine cases or signs of fire damage were noted.

However, failure of the disk can lead to much more critical accidents. For example, in 1996, a McDonnell Douglas MD-88 operated by Delta Air Lines suffered from an uncontained failure of the fan

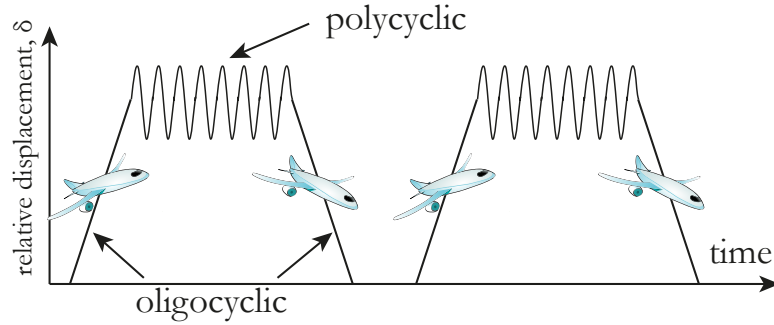


Figure 1.4: Illustration of relative displacement during the plane life (adapted from (Mary 2009)).

disk (FIG.1.5B ). Debris entered the passenger cabin, causing the death of two passengers. More recently, in 2006, an American Airlines B767-223(ER), equipped with General Electric CF6-80A engines experienced an uncontained failure of a high pressure turbine disk during a high-power ground run. The engine caught fire and the plane sustained significant damage on the left wing, fuselage, and tail section. FIG.1.5C shows one of the disk piece lodged into the second engine cowling.

Because of high-frequency aerodynamic vibrations of the blades, small relative movements occur at the dovetail between the fan blades and the disc. This fretting process, added to the fatigue load generated by the centrifugal force, has been associated with a number of critical engine failure. The following work will participate to the recent efforts devoted to better understand this phenomenon of fretting fatigue.

## 1.2 The contact problem.

Elementary properties of the contact problem were discovered in the 15th century by Amontons (Blau 2013). He formulated the empirical laws of friction:

- The force of friction is directly proportional to the applied load.
- The force of friction is independent of the apparent area of contact.
- Kinetic friction is independent of the sliding velocity (later confirmed by Charles-Augustin de Coulomb).

When two solid objects are not moving relative to each other, the friction is named static friction. The famous approximate model describing the force of static friction was named after Charles-Augustin de Coulomb, and can be written as:

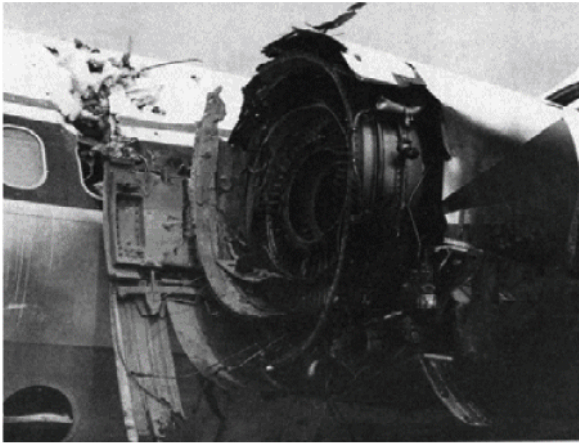
$$Q \leq \mu P \quad (1.1)$$

where  $Q$  is the force of friction, parallel to the surface, exerted by each surface on the other,  $\mu$  is the coefficient of friction, which is here assumed to be an empirical property of the contacting materials, and  $P$  is the normal force perpendicular to the surface.

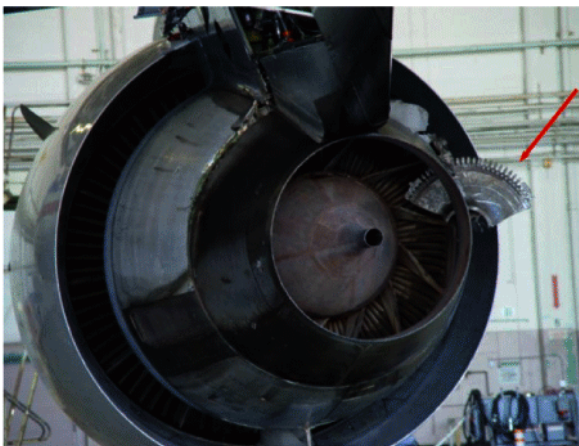
When the tangential force applied between the bodies is superior to  $\mu P$ , the contact passes in what is called the gross slip regime. In this regime, the resisting force of friction is constant and sometimes called traction. The traction is often different than  $\mu P$ , and a kinetic friction  $\mu_k$  is defined as the ratio between the traction and the normal force.



A



B



C



Figure 1.5: Photography of A. a fan blade failure in 2007 in Dallas (Herald 2009), B. a dramatic uncontained failure of the fan disk, which caused the death of two passengers (Wikipedia 2015) and C. an uncontained failure of a high-pressure turbine disk.

In contact geometries encountered in mechanical systems, a contact pressure generally drops at the sides of the contact. FIG.1.6 illustrates the distribution in a contact between a pad with rounded edges and a flat surface. On both sides of the contact, the drop in the pressure distribution allows a local slip of the surfaces in contact. This is called the partial slip regime.

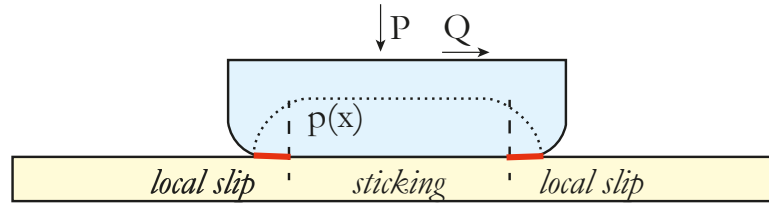


Figure 1.6: Illustration of a partial slip fretting contact.

A local stress concentration may be observed in the neighboring of the slipping zone of the contact. This concentration may lead to crack initiation as illustrated in FIG.1.7. This stress concentration depends on the load applied on the bodies in contact, but also on the geometry of the trailing edges. The sharper the edge is, the more localized the slip zone and the stress concentration are.

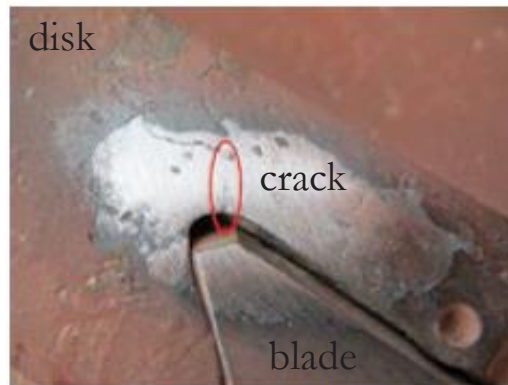


Figure 1.7: Dovetail cracks in wheels of a gas turbine compressor rotor (CCJ 2015).

The friction between two bodies in contact is very complex. Even if the bodies are not sliding one against the other, local slipping may occur on the edges of the contact. This localized kinetic friction generates stress concentration. The general aim of this study is to analyze the effect of this stress concentration on the cracking process.

### 1.3 Stress gradient and scale effect.

Stress generated by fretting fatigue is very localized and concentrated. This stress gradient is usually much higher than those associated with typical design features of components, only a very sharp notch can present such steep decrease. In addition to the gradient, it has been shown that the size of the contact, or in other words, the scale of the problem, also has an impact on the failure behavior.

The size effect on fatigue limit has been studied by several authors. Pogoretskii (1966) conducted rotating bending fatigue tests on steel specimens of various lengths and radiuses (FIG.1.8). It showed

a significant decrease in the endurance limit with increasing size specimens. In bending, this effect can not be dissociated from the stress gradient effect because the more thin the specimen is, the stronger the stress gradient (or stress decrease) is.

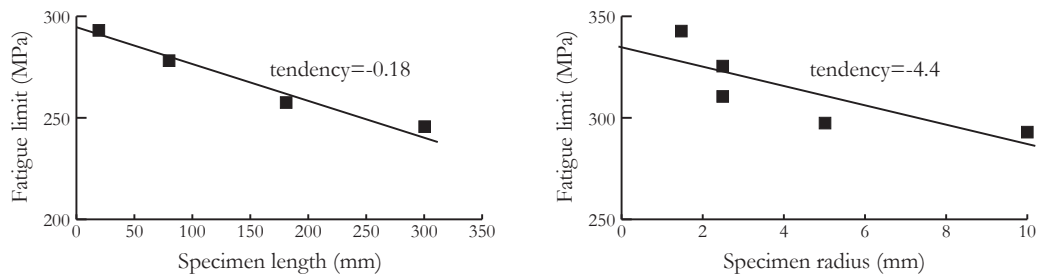


Figure 1.8: Scale and gradient effect, bending test results from Pogoretskii (1966).

Based on data from the literature, Papadopoulos and Panoskaltsis (1996) concluded that the gradient effect is more significant than the scale effect in the case of cylindrical specimens under bending. Indeed, considering a constant radius, if the specimen length varies, the gradient remains the same and, therefore, the size effect only plays a role. However, at a constant length, and for a variable radius, the two effects act together. FIG.1.8 shows that the fatigue limit varies much faster with the radius than with the length of the specimen, which supports the conclusion of Papadopoulos, provided that the size effect is the same in the two cases studied.

The scale effect can be explained from a statistical point of view. Assuming that in a given volume of material there are a number of ideal sites for the initiation of fatigue cracks, the bigger this volume is, the higher the risk of crack nucleation is. Taking the argument further, the gradient effect can be explained by a disguised scale effect. In bending for example, when the stress gradient is high enough, the center is subjected to little stress, unlike its surface. Then, the modification of the sample radius not only changes the general volume but also the representative loaded volume. The analysis of Papadopoulos would then require additional analyzes to be fully validated.

When the stress gradients are very strong, another behavior may also be observed. Until now, it was implicitly assumed that an initiated fatigue crack necessarily leads to failure. However, in the situation of a strong gradient, an initiated crack can stop growing when the state of stress crossed becomes so small that the fracture will not continue at the tip. This phenomenon called ‘crack arrest’ will be further discussed in the SEC.2.4.9.

The design of the dovetail roots used to fix the blades on the disks has to consider both the gradient and the scale effect. For example, because of the scale effect, the size of the surface in contact will influence the risk of fretting crack. Moreover, the geometry of the trailing edges of the contact will generate different stress concentration. A sharp geometry of the blade edge will localize the slipping edge of the contact and will create a strong stress gradient, while with a smoother trailing edge the slipping zones will be larger and the stress gradient very smooth.

## 1.4 Thesis scope.

The general aim of this research is to investigate the role of the stress gradient on the fretting fatigue phenomenon. Two goals were defined:

- design and execution considering fretting configurations that are nominally equivalent but present different stress gradients;
- proposition of a model to estimate fretting fatigue strength that is capable to handle the stress gradient, the multiaxial stresses under the contact, but that still can be applied considering only laboratory data from plain fatigue tests.

For this purpose, this thesis is organized as follows:

**Chapter 2** presents a literature review on relevant works, discussing the state of the art in the fields according to the scope of this thesis. It consists of contact mechanics, fatigue of material and fracture mechanics.

**Chapter 3** introduces the experimental and numerical tools necessary for the study of fretting fatigue.

**Chapter 4** presents the experimental results of fretting fatigue tests with different stress gradients. The fretted and fractured surfaces of the failed specimens are analyzed in order to define fretting fatigue failure characteristics.

**Chapter 5** investigates two criteria and their abilities to account for the gradient effect in the failure prediction. A new criterion and methodology are also proposed.

**Chapter 6** outlines the conclusions from this dissertation and makes recommendations for future work.



## Chapter 2

# Literature Review.

### 2.1 Fretting

#### 2.1.1 Introduction.

Eden et al. (1911) were the first to report the observation of oxide debris formation between the steel grids and the specimen in a plain fatigue test. In the years since then, there must have been many researchers who have suffered unintended fretting fatigue failures in this configuration. Tomlinson (1927) investigated the process and confirmed that damage could be caused by very small amplitudes of movements, where relative movement, which he termed ‘slip’, had to occur. After that, the term ‘fretting fatigue’ came into common use to describe situations where micro slip between contacting surfaces appears to give rise to a reduction in fatigue life when compared to a plain component (Nowell et al. 2006a). Indeed, Warlow-Davies (1941) carried tensile fatigue test on steel specimens which were beforehand subjected to fretting damage and showed strength reduction varying between 13% and 17% compared with the fatigue tests of unfretted specimens. Later other experiments reported that the conjoint action of fretting and fatigue may produce strength reduction factors varying from 2 up to 10 compared to plain fatigue (McDowell 1952).

This section will first introduce basic concepts of fretting fatigue and set-ups used to study the phenomenon in laboratories. The presentation will focus on limited conditions of ‘partial slip’ in the atmospheric environment, that is to say, the description of the phenomenon of friction or corrosion will be very limited. After detailing the assumptions and general analytic formulations of the problem, several works from the last 30 years will be summarized.

#### 2.1.2 Tribological behaviour of contact.

Tribology is defined as the study of relative motion, dealing with the design of the contact and the concepts of friction, wear, and lubrication of interacting surfaces.

The contact geometries encountered in mechanical systems are often complex. In order to model most of these contacts, three cases of reference are generally defined according to the number of dimensions studied:

- Convex fretting pads loaded against a plane specimen. Formalized by Hertz analysis (Hertz 1881), this configuration presents a contact pressure falling continuously to zero at the edges of the contact. This means that, if the contact loads are not very severe (within the elastic limit) the contact pressure is free from singularities and a complete elastic analytical solution can be

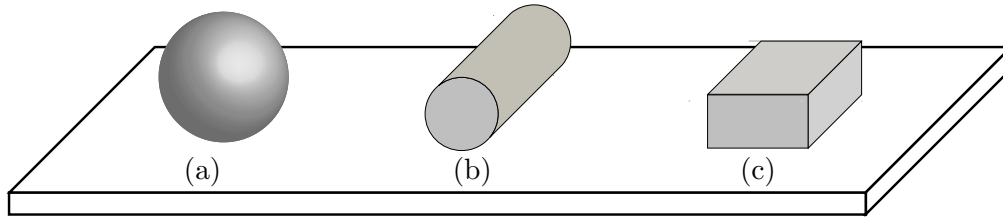


Figure 2.1: Type of simplified contact problem: (a) sphere/plane (b) cylinder/plane (c) plane/plane.

obtained for the subsurface stress/strain fields (Johnson 1985). Convex fretting pads can be either cylindrical or spherical.

- Spherical fretting pads loaded against a plane specimen. Because of the point contact, this contact geometry does not require alignment, then it has the advantage of being simpler to implement experimentally. However, analysis of cracking is relatively complex because it involves a three-dimensional description of the contact, which is very costly in time calculation. Blanpain et al. (1995) and Mohrbacher et al. (1995) distinguished three modes of fretting, illustrated in FIG.2.2.

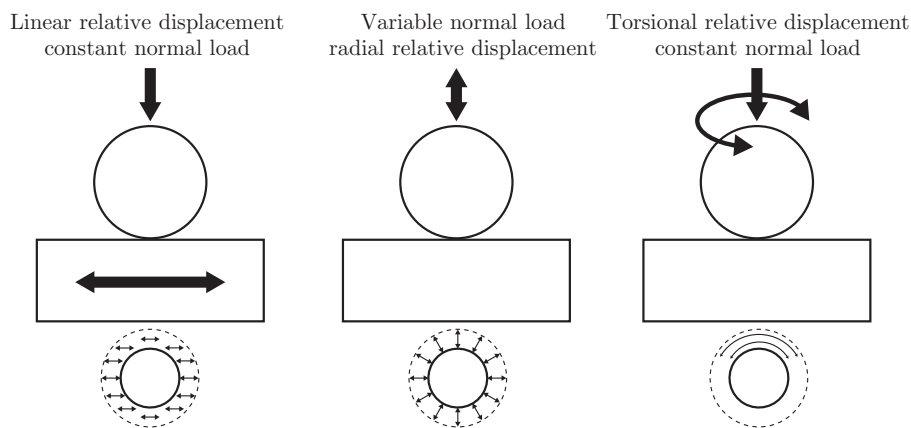


Figure 2.2: Schematic representation of the three basic fretting modes in sphere/plane problem (corrected from (Blanpain et al. 1995)).

- Cylindrical fretting pads loaded against a plane specimen: Cylindrical fretting pads have the advantage of allowing a straightforward two-dimensional elastic analysis of the contact problem. Further, they are much simpler to manufacture than spherical pads. On the other hand, they are more difficult to align and suffer from edge effects.
- Flat pads loaded against a plane specimen. This configuration has been widely used by other researchers (Lindley 1997; Nakazawa et al. 1992; Sato 1992). Nevertheless, there are difficulties to determine the pressure distribution and shear tractions for this kind of geometry. Another drawback of this configuration is its sensitiveness to the alignment issue. Moreover, the geometry is hypersensitive to manufacturing errors, and the entrapment of scarf between pad and specimen is also likely to change the contact pressure distribution markedly. (Edwards et al. 1977; Hills and Nowell 1992)

Contact geometry involved in a dovetail attachment is complex to model. In order to understand the effect of the stress gradient in the cracking process, a simplified contact geometry will be considered. We will focus the study on the contact of cylindrical fretting pads loaded against a plane specimen. The cylinder/plane configuration will be briefly considered and a new test design will be proposed.

### 2.1.2.i Experimental set-ups used for cylinder-plane fretting fatigue research.

Through a short literature review, it appears that many fretting fatigue experimental set-ups are used in the different laboratories. All of them have common features in order to control the fretting fatigue variables, such as the normal load, the tangential load or the bulk load. But the variety of configurations often makes it difficult to compare one another. Among those differences are the differing materials, the loadings (loads and displacements controlled), the contact geometry, surface integrity parameters such as finish, the environment and so on. However, ASTM recently proposed a standard guide for fretting fatigue testing (E2789-10 2011).

The choice of the fretting fatigue set-up depends on the context of the work and the scale of the test specimen. Full-scale test rigs are directly related to practical applications, for instance, the dovetail connection, bolted or riveted lap connection, splined coupling, leaf spring.

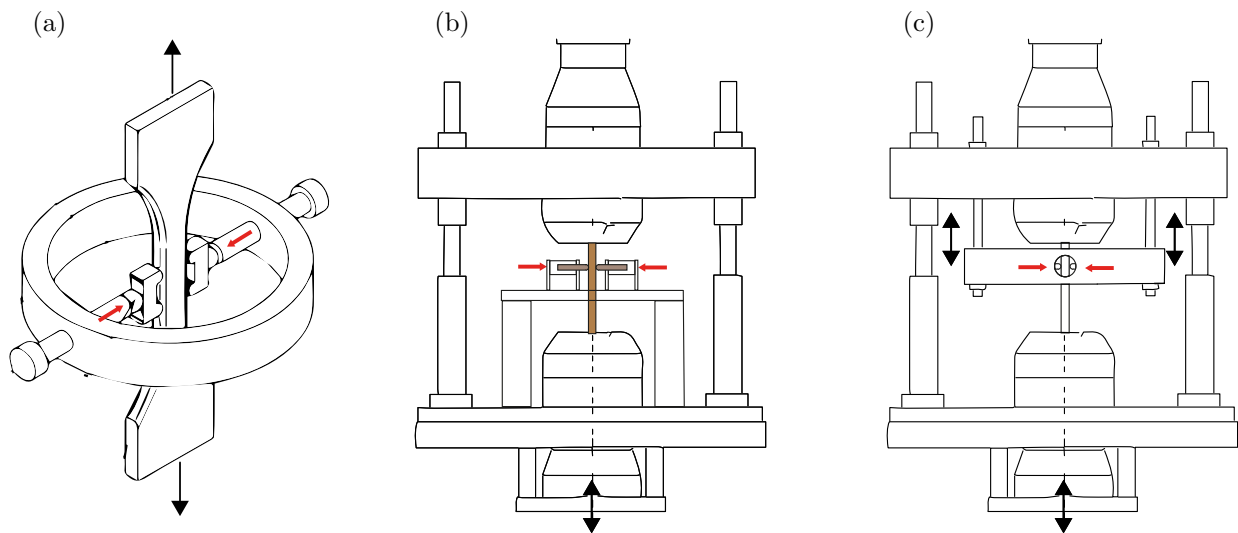


Figure 2.3: Scheme of fretting set-ups: (a) bridge-type test rig (b) single actuator rig, using a fretting apparatus (c) bi-actuators rig.

The fretting set-ups can be sorted according to their capability to apply a fretting slip amplitude:

- When the fretting slip does not have an influence or does not need to be controlled, the tests can be done using a bridge-type test rig. In this set-up, the fretting fatigue test is commonly carried out on a dynamic Servo hydraulic machines. The pressure required to produce fretting is transmitted via a calibrated proving ring (FIG.2.3(a)). Each pad has two contacting surfaces through which the fretting load is exerted on the fatigue specimen. More description and variation can be found in (Majzoubi et al. 2010; Sabsabi et al. 2011).

- The second type test rig was first developed by Nowell (1988). In this configuration, two fretting pads are pushed against the specimen by a constant contact force, and the fatigue specimen is subjected to cyclic axial stress (FIG.2.3(b)). The tension at either end of the fatigue specimen is unequal due to the tangential forces induced by attached spring to the fretting pads.
- A modification of the second type set-up involves the use of a second servo-hydraulic actuator attached to the fretting fixture, which then applies tangential force or relative slip to the pad through the fretting fixture. This modified test setup provides a better method to control the relative slip independently from other loadings (i.e., bulk stress on the specimen and normal contact load on the pad). However, when no load or displacement is applied through the second actuator, a tangential force on the pad is developed through the compliance of fretting fixture.

The variety of fretting fatigue test configurations makes sometimes difficult to compare a set of tests from one study to another. In this work, we will produce experimental results using the configuration (b) of FIG.2.3.

### 2.1.2.ii Fretting mechanism.

Fretting is a complex tribological problem, which depends on different parameters influencing the response of connected surfaces. Dobromirski (1992) counted fifty different variables, and classified them into two sets of primary and secondary variables, which have direct and indirect effects on fretting fatigue behaviour. The primary set of variables includes the coefficient of friction,  $\mu$ , magnitude of slip,  $\delta$ , and contact pressure acting at the fretting interface while the environmental conditions, the microstructure, the surface roughness and others, are gathered in the secondary set of variables.

In 1968, Nishioka and Hirakawa made a significant work on the effect of various factors on the fretting fatigue strength, such as contact pressure, relative slip amplitude, environmental conditions and materials (Nishioka and Hirakawa 1969a,b,c; Nishioka et al. 1968).

Vingsbo and Söderberg (1988) defined fretting damage as “the damage inflicted to tribosurfaces due to oscillatory displacements at low amplitude”, but underlined that there is no general definition for “low amplitude”. In this context, different regimes of fretting can be defined regarding the relative displacement measured (FIG.2.4):

- Stick regime; Very limited surface damage by oxidation and wear. No fatigue crack formation observed up to one million cycles. Low fretting damage.
- Mixed stick-slip regime; Wear and oxidation effects are small. Nishioka et al. (1968) showed that the amount of relative slip affected the fretting fatigue strength. However, they showed a very little effect of the frequency of the relative slip amplitude.
- Gross slip regime; Severe surface damage by wear, assisted by oxidation. Crack formation limited. Fretting wear.

During a flight cycle, the strong centrifugal force is generally too strong to allow a total sliding of the blade inside the groove of the disc. The present study will then focus on the mixed stick-slip regime.

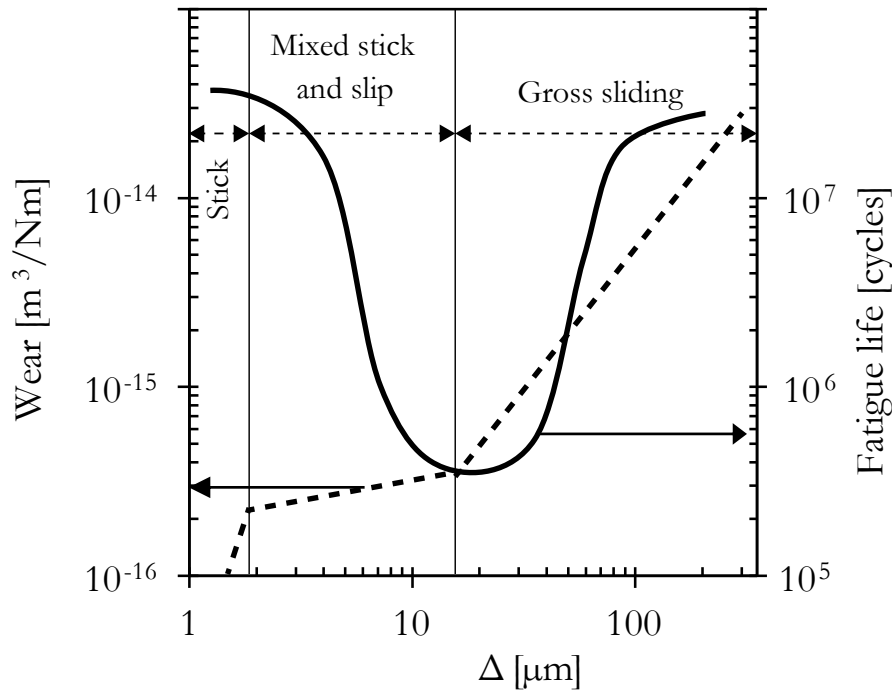


Figure 2.4: Variation in fretting fatigue life and fretting wear rate with experimentally measured global displacement amplitude (modified from (Vingsbo and Söderberg 1988)).

### 2.1.2.iii Friction.

Frictional resistance to the relative motion of two solid objects is usually proportional to the force that presses the surfaces together, as well as the roughness of the surfaces. The frictional force is also presumed to be proportional to the coefficient of friction. However, the amount of force required to move an object starting from rest is usually greater than the force required to keep it moving at constant velocity once it is started. In general, three coefficients of friction are defined:

- the coefficient of static friction,  $\mu_m$ , which can be measured either before a fretting fatigue test or after carrying out the fretting test for a certain number of cycles (Jin and Mall 2004).
- the coefficient of kinetic friction,  $\mu_k$ , is defined as the friction during gross sliding. Endo and Goto (1978) shows that the kinematic coefficient of friction is constant for all cycles considered and is almost independent of contact pressure and contact geometry.
- the coefficient of dynamic friction, which is equal to the kinetic coefficient of friction in gross sliding but smaller in partial sliding. Endo et al. showed that the coefficient of friction changes by increasing the number of cycles and also depends on the contact load.

FIG.2.5 shows results obtained by McColl et al. (2004) with high strength alloy steel. As confirmed by other authors (Bramhall 1973; Endo et al. 1969; Milestone and Janeczko 1971; Wright and O'Connor 1972), an increase in the coefficient of friction during the first few cycles of the experiments was observed. This figure also makes clear that  $\mu$  is reduced with an increase in normal load.

Other authors have studied the effect of other parameters on the coefficient of friction (Jin and Mall 2002; Lee and Mall 2004b). They found that an increase in slip amplitude results in an increase

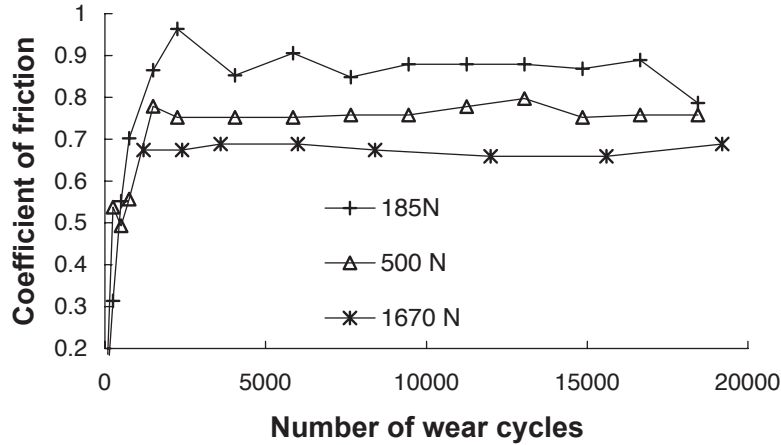


Figure 2.5: Coefficient of friction vs. number of fretting wear cycles (McColl et al. 2004).

of the coefficient of friction, while an increase in contact pressure, cyclic frequency, and temperature decreases the coefficient of friction. For Ti-6Al-4V alloy, Jin and Mall (2002) showed that the coefficient of friction increased linearly from 0.33 to 1.0 with slip amplitude until  $\delta = 50 - 60\mu\text{m}$  and after that it remain constant.

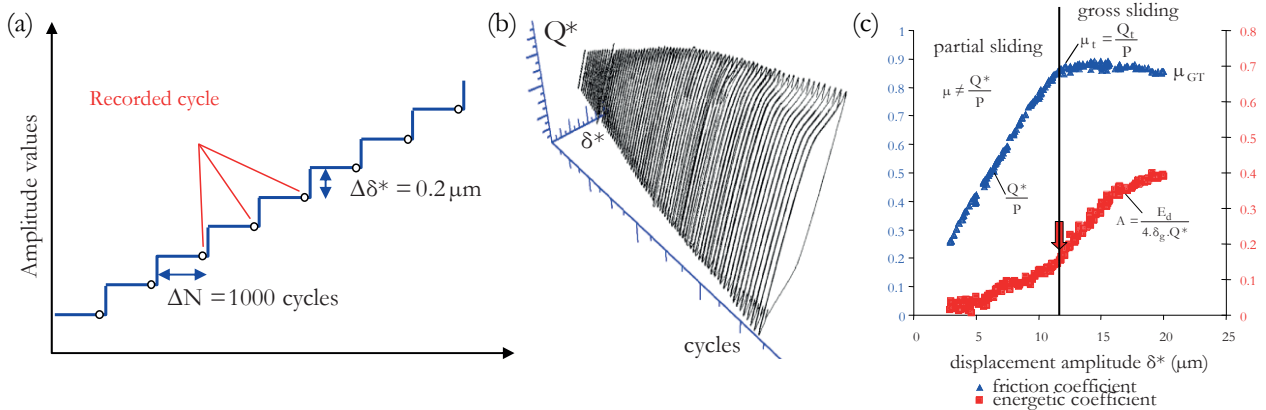


Figure 2.6: Illustration of the methodology to define the friction coefficient (Kubiak 2006) (a) incremental method (b) fretting loop (c) transition between partial and gross slip condition.

This complexity of the coefficient of friction leads to discussions when it comes to model the fretting. In most studies, under partial slip condition, the coefficient of friction is often assumed to be constant along the contact surface. Fouvry et al. (2004) tried to define the transition from partial to gross slip condition using an energy discontinuity analysis. For this purpose, they used incremental displacement method introduced by Voisin et al. (1995). This method consists in a successive increase of displacement amplitude from very small in partial slip regime to large displacement in gross sliding condition (FIG.2.6a).

When representing the hysteresis of the slip amplitude against the tangential force, the dissipated energy appears as the surface of the loop. This dissipated energy tends to increase when passing from partial slip regime to gross sliding (FIG.2.6c). The coefficient of friction corresponding to the

transition between the two regimes is considered as being the coefficient of friction to use in the model. Hills et al. (1988) have tried to relate the measured mean coefficient of friction,  $\mu_m$  to the true coefficient of friction in the slip zones. They assumed that the coefficient of friction in the slip zone was a function of fretting cycles and reached to a value  $\mu_n$  after  $n$  cycles. They divided the contact zone into three portions and derived an analytical equation relating the stick and slip zone coefficients of friction with the average  $\mu_m$ . The coefficient of friction in the sticking zone was considered to be constant during fretting at the initial value of  $\mu_0$ . The ratio of  $Q/F$  provides the average coefficient of friction, which corresponds to the static one as introduced above. Once  $\mu_m$  is measured,  $\mu_n$  can be calculated according to the procedure described in SEC.3.2.5.

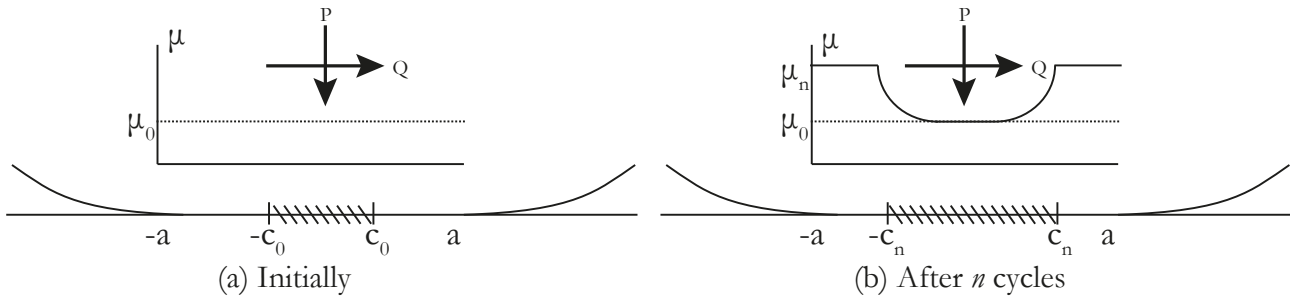


Figure 2.7: Model of variation of the coefficient of friction across contact (Nowell 1988).

Because of the partial slip regime, the definition of the coefficient of friction is complex. The different models used in this work do not consider different coefficient of friction for the sticking and slipping zone of the contact. We will assume here that the coefficient of friction of the slipping zone after stabilization is the most relevant to consider. Two methods will be used to estimate this coefficient.

#### 2.1.2.iv Oxidation.

The role of oxidation on the fretting process has been largely investigated. Wright (1952) observed first that the formation of oxides accelerates the development of fretting damage. Later Waterhouse and Allery (1965) compared fretting test in the air and in inert gas where corrosion is very limited. There were not enough differences of the fatigue strength in the two environments to establish a relation between the rate of occurrence of fretting corrosion and the reduction of fatigue strength (Collins and Marco 1964; Fenner and Field 1958).

#### 2.1.2.v Wear.

Wear is the gradual removal of material obtained at contacting surfaces in relative motion. Wear is usually associated with the full sliding regime, and often neglected in partial sliding regime (FIG.2.8). Many different wear mechanisms have been identified. A first classification of mechanisms is based on their relative importance in engineering practice. According to this, the following types of wear are often encountered:

- Adhesive Wear (plus Fretting Wear). Encountered in 23-45 % of cases.
- Abrasive Wear (plus Erosive Wear). Encountered in 36-58 % of cases.
- Surface Fatigue Wear. Encountered in 14-15 % of cases.

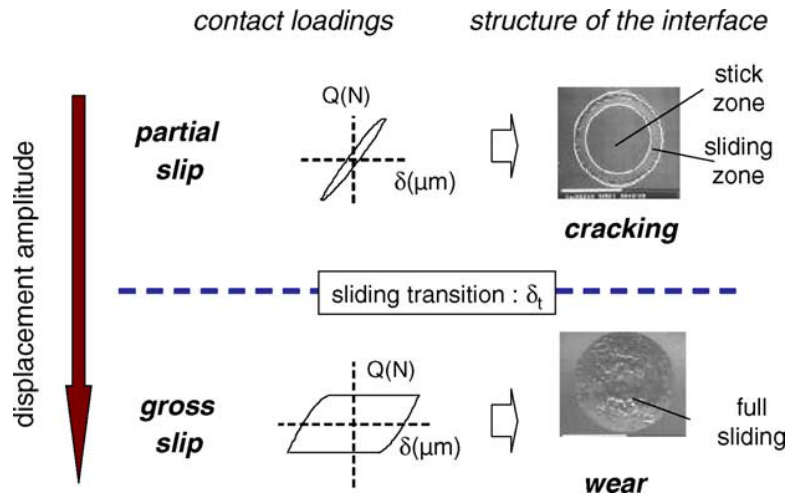


Figure 2.8: Illustration of the fretting damage versus the imposed sliding condition (Kubiak et al. 2005).

- Corrosive Wear. Encountered in 4-5 % of cases.

Wear is a complicated phenomenon which generates mechanism such as:

- modification of surfaces by removing material at the interface,
- creation of a third active body at the interface difficult to model,
- flow of debris inside and outside the contact,
- warming,
- ...

According to (Meng and Ludema, 1995), about 180 wear laws have been proposed. Archard's model (Archard, 1953) is the most commonly used to quantify wear. It considers that the wear volume is linked to the product of normal force and sliding velocity.

Wear coefficient quantification is conventionally performed by evaluating the worn volume as a function of normal load. The loss of material can be known by measuring the loss of mass, loss of dimensions, the evolution of Vickers microhardness imprints, or directly by surface profilometry. The present study is limited to the mixed regime where the wear phenomenon is generally not considered. On the specific topic of wear, we highly recommend the bibliography detailed by Salles (2010).

This study will be limited to the analysis of the fretting-fatigue at room conditions and in the partial slip regime. We will assume that the phenomena of oxidation and wear do not play significant roles here.

### 2.1.3 Subsurface stress field.

In this section, the analytic solution of the particular cylinder/plane fretting fatigue problem in partial regime will be detailed.

#### 2.1.3.i Surface traction.

The first step towards a solution for the subsurface stress field is to solve the contact problem itself, i.e., to find the magnitude and distribution of the surface tractions. Using the pressure distribution,

$p(x)$ , to normal displacement,  $h(x)$ , and shear traction,  $q(x)$ , to relative tangential displacement,  $g(x)$ , the problem may be solved using well-known integral equations, whose derivation is well described by Hills and Nowell (1993) and Johnson (1985). The integral equations for two elastically similar bodies are:

$$\frac{1}{A} \frac{\partial h}{\partial x} = \frac{1}{\pi} \int_{-a}^a \frac{p(\xi) d\xi}{x - \xi} \quad (2.1)$$

$$\frac{1}{A} \frac{\partial g}{\partial x} = \frac{1}{\pi} \int_{-a}^a \frac{q(\xi) d\xi}{x - \xi} \quad (2.2)$$

where  $A$  is the composite compliance defined as:

$$A = 2 \left( \frac{\kappa + 1}{4\mu} \right) \quad (2.3)$$

being  $\kappa = 3 - 4\nu$  in plane strain,  $\nu$  is the Poisson's ratio and  $E$  is the modulus of rigidity.

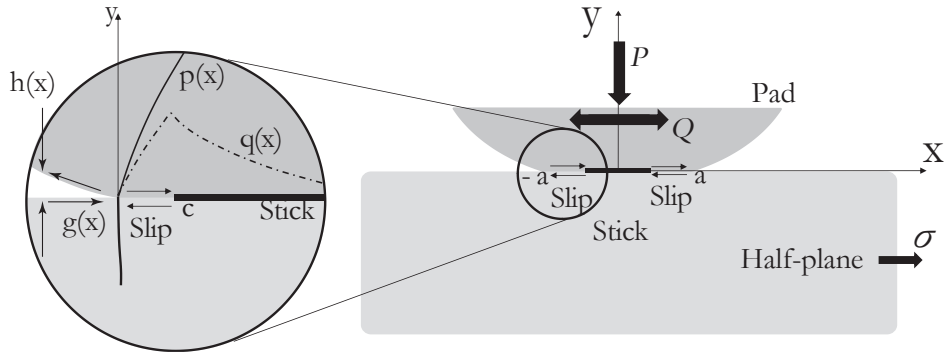


Figure 2.9: Schematic figure of the fretting fatigue related contact problem.

In the general case of our study, the pad radius,  $R$ , the normal load,  $P$ , and specimen thickness were defined so that each solid could be considered as an elastic half-space and the solution for the pressure distribution was Hertzian. The results of Hertz (1881) predict that due to a static normal force, an elliptical pressure distribution will develop:

$$p(x) = p_0 \sqrt{1 - \left( \frac{x}{a} \right)^2} \quad (2.4)$$

where  $p_0$  is the peak pressure

$$p_0 = \frac{2P}{\pi a} \quad (2.5)$$

and  $a$  is the contact semi-width

$$a = \sqrt{\frac{4PR}{\pi E^*}} \quad (2.6)$$

where

$$R = \left( \frac{1}{R_1} + \frac{1}{R_2} \right)^{-1} \quad (2.7)$$

and

$$E^* = \left( \frac{1 - \nu_1^2}{E_1} + \frac{1 - \nu_2^2}{E_2} \right)^{-1} \quad (2.8)$$

where the subscripts 1 and 2 stand for body 1 (for instance, the fretting pad) and body 2 (tensile specimen).

The tangential load on the other hand will give rise to shear traction,  $q(x)$ , as described firstly by Cattaneo (1938) and independently by Mindlin (1949). Since in fretting fatigue tests, the applied shear load is usually smaller than the threshold for full sliding, a partial slip regime develops where slip takes place within two symmetrical regions  $c \leq |x| < a$  which surround a central stick region  $|x| < c$ . Therefore it seems convenient to model the shear traction as a perturbation of the full sliding solution:

$$q(x) = \mu p_0 \sqrt{1 - \left(\frac{x}{a}\right)^2} + q'(x) \quad (2.9)$$

where the perturbation  $q'(x)$  is zero in the slip zones ( $c \leq |x| < a$ ). In the stick region the shape of  $q'(x)$  can be found by (i) recognizing there is no variation in the relative displacement between corresponding points ( $g(x)$ ) in this region, and (ii) solving the integral equation given by EQ.(2.2) (Hills and Nowell 1993). Therefore,

$$q'(x)/\mu p_0 = \begin{cases} 0 & \text{if } c \leq |x| < a \\ \frac{c}{a} \sqrt{1 - \left(\frac{x}{c}\right)^2} & \text{if } |x| < c \end{cases} \quad (2.10)$$

The size of the stick zone,  $c$ , is revealed by considering tangential equilibrium.

$$\frac{c}{a} = \sqrt{1 - \left(\frac{Q}{\mu P}\right)} \quad (2.11)$$

The plot in FIG.2.10 depicts an example of normalized distribution of pressure and shear traction. The central stick zone where the shear traction is reduced due to the perturbation in the full solution is immediately apparent.

To evaluate the traction and consequently the stresses and/or strains at any other instant of the fretting cylindrical it is necessary to examine what happens at the reversal of the load.

The well known Amonton's law gives the relation between the shear traction and the tangential load within the slip zone:

$$|q(x)| = -\mu p(x) \quad (2.12)$$

and the direction of the shear traction opposes the relative motion of the surfaces, yielding

$$\text{sgn}(q(x)) = -\text{sgn}\left(\frac{\partial g}{\partial t}\right) \quad (2.13)$$

In the central region where there is no relative displacement between corresponding particles the shear traction must be less than the limiting frictional value, thus:

$$|q(x)| < -\mu p(x) \quad (2.14)$$

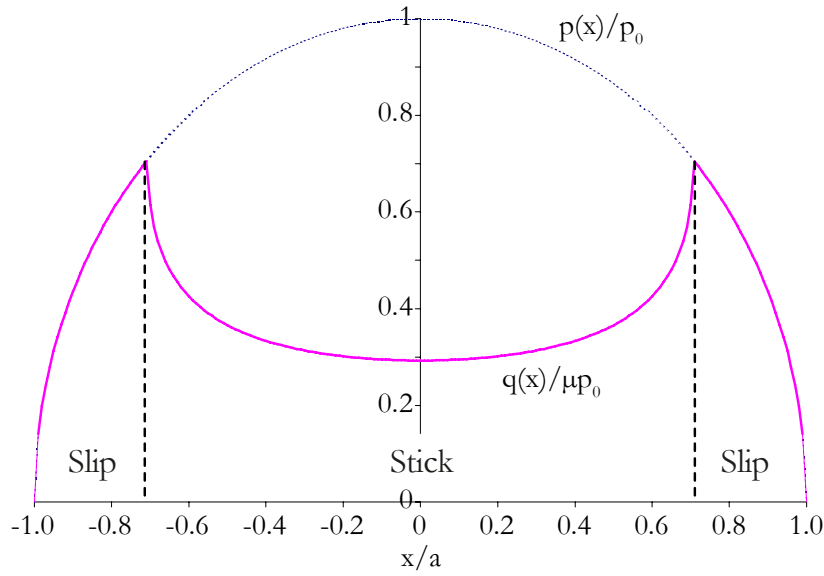


Figure 2.10: Pressure distribution and shear traction profile for a typical loading,  $Q/\mu P = 0.5$ ,  $\sigma_B/\mu p_0 = 0.0$ .

Returning to the determination of the shear traction, FIG.2.11 depicts the variation of the tangential load with time. When the load increases monotonically from 0 to  $Q_{max}$ , EQ.2.9 and EQ.2.10 describe the shear traction. Now consider that the load has been infinitesimally reduced from its maximum value to point B. This will cause a change of sign in the rate of change of the tangential displacement  $\partial g/\partial t$ , hence EQ.2.13 will be violated and stick is expected in everywhere within the contact. Further reducing the fretting load to point C will cause reverse slip at the contact edges. In these new slip zones ( $d < |x| \leq a$ ) the shear traction will have changed from  $\mu p(x)$  to  $-\mu p(x)$ . The corrective traction necessary to prevent slip is then:

$$q''(x) = +2\mu f p_0 \frac{d}{a} \sqrt{1 - \left(\frac{x}{d}\right)^2} \quad (2.15)$$

The net shear traction can finally be written as follows:

$$q(x)/\mu p_0 = \begin{cases} -\sqrt{1 - \left(\frac{x}{a}\right)^2} & \text{if } d < |x| \leq a \\ -\sqrt{1 - \left(\frac{x}{a}\right)^2} + 2\frac{d}{a}\sqrt{1 - \left(\frac{x}{d}\right)^2} & \text{if } c < |x| \leq d \\ -\sqrt{1 - \left(\frac{x}{a}\right)^2} + 2\frac{d}{a}\sqrt{1 - \left(\frac{x}{d}\right)^2} - \frac{c}{a}\sqrt{1 - \left(\frac{x}{c}\right)^2} & \text{if } |x| \leq c \end{cases} \quad (2.16)$$

As with the case of monotonic loading the size of the new stick zone at the reversal of load is obtained from the overall equilibrium, yielding:

$$\frac{d}{a} = \sqrt{1 - \left(\frac{Q_{max} - Q}{2\mu P}\right)} \quad (2.17)$$

FIG.2.12 depicts the variation of shear tractions at different values of  $Q$  corresponding to points A, C, D, E and F of the fully reversed fretting cycle (FIG.2.11).

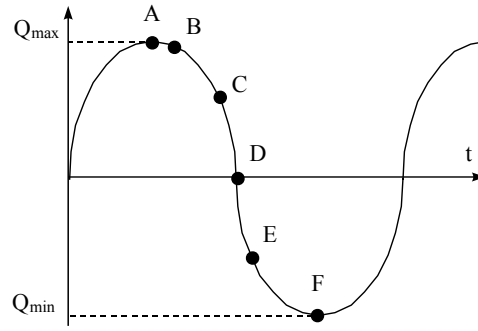


Figure 2.11: Variation of shear load  $Q$  with time  $t$ .

### 2.1.3.ii Effect of the bulk load on the shear traction distribution.

When the bulk tension is added to the fretting, a small modification on the classical Mindlin solution for the shear traction is required. The specimen bulk load causes a strain in the specimen that is not present in the pads. This mismatch in strain will cause an additional term in the tangential matching EQ.2.2 and the resultant shear tractions will differ from those arising in the absence of a bulk stress. Recognizing that the partial derivative of the relative tangential displacement is no longer zero in the stick zones and writing the left hand side of EQ.2.2 in form of stress yields:

$$-\frac{\sigma_B}{4\pi} = \frac{1}{\pi} \int_{-a}^a \frac{q(\xi)d\xi}{x-\xi} \quad (2.18)$$

The effect of the bulk tension is the offset of the stick zone, which was in central position in the absence of such bulk tension. That is, the domain of the perturbation in the full solution now becomes  $|x-e| < c$  rather than the former symmetrical  $|x| < c$ , where  $e$  is the offset of the center of the stick zone from the center of the contact. Application of appropriate boundary conditions in and outside the stick region together with the integration of EQ.2.2 defines the value of  $e$ :

$$e = \frac{\sigma_B a}{4\mu p_0} \quad (2.19)$$

Thus, the perturbation term for the shear traction becomes:

$$q'(x) = \mu p_0 \frac{c}{a} \sqrt{1 - \left(\frac{x-e}{c}\right)^2} \quad |x-e| < c \quad (2.20)$$

FIG.2.13 illustrates the superposition of the surface tractions in fretting and fretting fatigue. The solution developed above is satisfactory for moderate values of the bulk tension. If larger values of tension are applied one edge of the sticking zone will approach the edge of the contact. The current solution is therefore only valid if  $e+c \leq a$ .

### 2.1.3.iii Stress field.

Once the surface traction has been determined it is possible to evaluate stress in the specimen by superposing the effects of normal pressure, shear traction, and specimen load using Muskhelishvili's

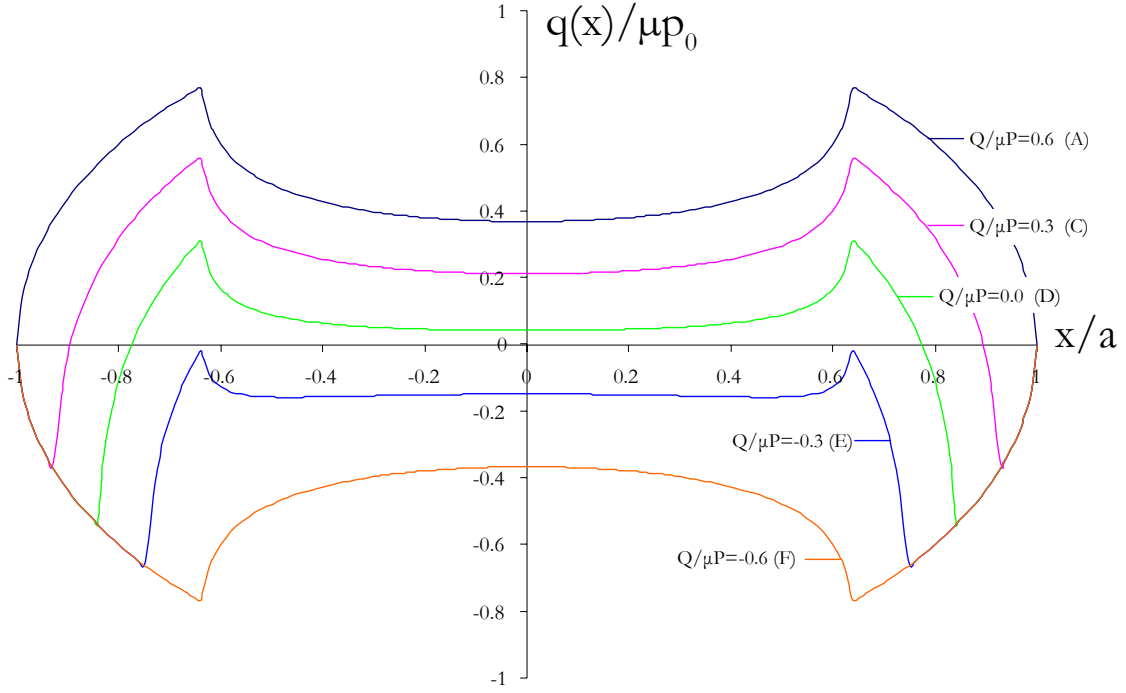


Figure 2.12: Variation of shear traction at different instants of the fully reversed fretting cycle.  $Q/\mu P$  varies from  $+0.6$  to  $-0.6$ .

potential theory (Muskhelishvili 1953). For most of the stress components, it is possible to use a half-plane assumption in the calculation of stresses due to the contact.

Evaluation of the  $xx$  component of stress due to the normal load can be obtained by superposition of the results for the elliptical tractions, although the shifted origins of the perturbation terms,  $q'(x)$  and  $q''(x)$ , will have to be taken in account. It is particularly worthy of note that four different combinations of superposition will be necessary to express the stress field at maximum and minimum load and during unloading and reloading. For instance, the normalized  $xx$  component of stress at each of these stages will be:

- At maximum load:

$$\frac{\sigma_{xx}(x, y)}{p_0} = \left( \frac{\sigma_{xx}^n \left( \frac{x}{a}, \frac{y}{a} \right)}{p_0} \right) + \mu \left( \frac{\sigma_{xx}^t \left( \frac{x}{a}, \frac{y}{a} \right)}{\mu p_0} \right) - \mu \frac{c}{a} \left( \frac{\sigma_{xx}^t \left( \frac{x-c}{c}, \frac{y}{c} \right)}{\mu p_0} \right) + \sigma_B \quad (2.21)$$

- During unloading:

$$\frac{\sigma_{xx}(x, y)}{p_0} = \left( \frac{\sigma_{xx}^n \left( \frac{x}{a}, \frac{y}{a} \right)}{p_0} \right) - \mu \left( \frac{\sigma_{xx}^t \left( \frac{x}{a}, \frac{y}{a} \right)}{\mu p_0} \right) + 2\mu \frac{d}{a} \left( \frac{\sigma_{xx}^t \left( \frac{x-d}{d}, \frac{y}{d} \right)}{\mu p_0} \right) - \mu \frac{c}{a} \left( \frac{\sigma_{xx}^t \left( \frac{x-c}{c}, \frac{y}{c} \right)}{\mu p_0} \right) + \sigma_B \quad (2.22)$$

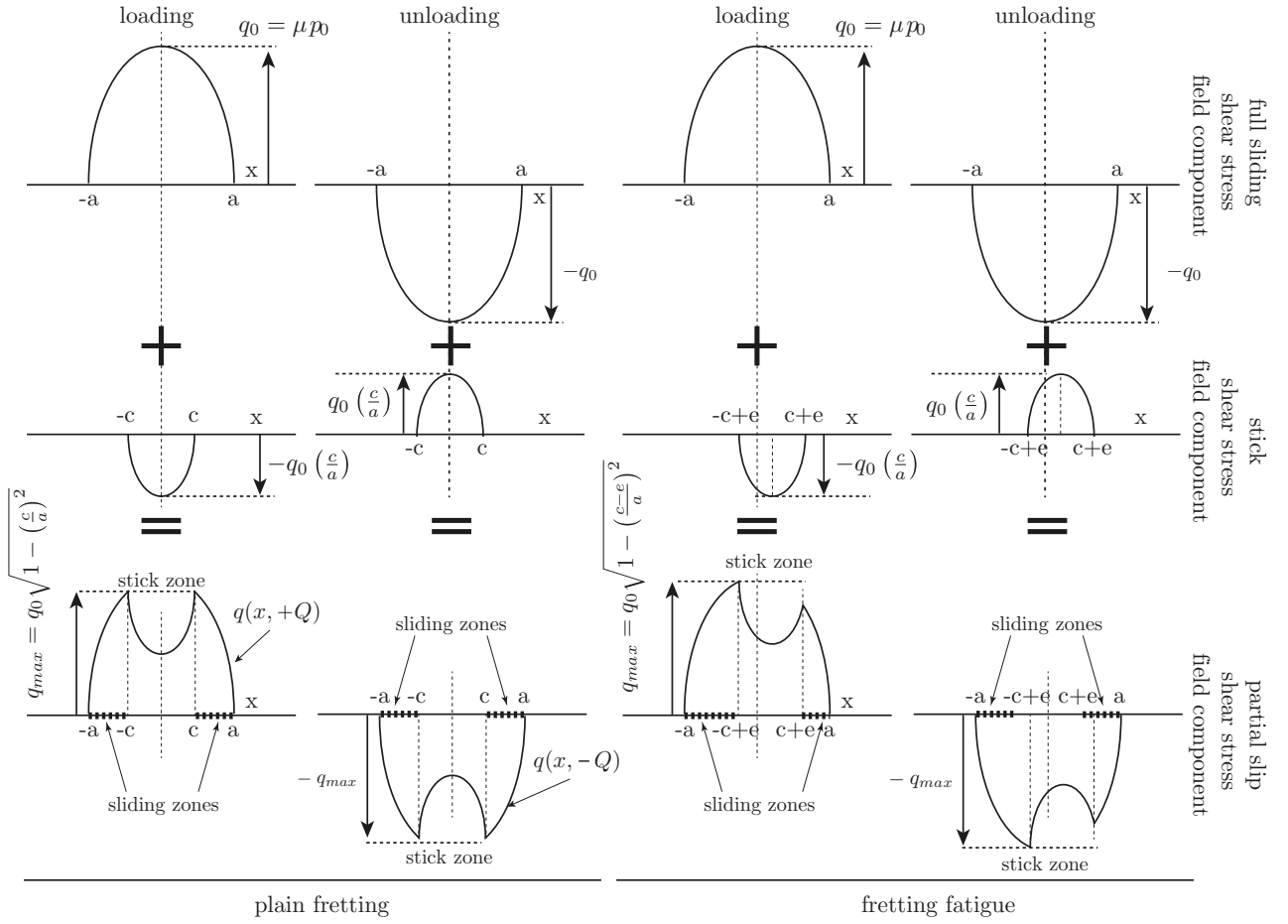


Figure 2.13: Illustration of Mindlin's surface shear distributions generated in partial slip cylinder/plane contact under plain fretting and fretting fatigue loading conditions.

- At minimum load:

$$\frac{\sigma_{xx}(x, y)}{p_0} = \left( \frac{\sigma_{xx}^n \left( \frac{x}{a}, \frac{y}{a} \right)}{p_0} \right) - \mu \left( \frac{\sigma_{xx}^t \left( \frac{x}{a}, \frac{y}{a} \right)}{\mu p_0} \right) + \mu \frac{c}{a} \left( \frac{\sigma_{xx}^t \left( \frac{x-e}{c}, \frac{y}{c} \right)}{\mu p_0} \right) + \sigma_B \quad (2.23)$$

- During reloading:

$$\frac{\sigma_{xx}(x, y)}{p_0} = \left( \frac{\sigma_{xx}^n \left( \frac{x}{a}, \frac{y}{a} \right)}{p_0} \right) + \mu \left( \frac{\sigma_{xx}^t \left( \frac{x}{a}, \frac{y}{a} \right)}{\mu p_0} \right) - 2\mu \frac{d}{a} \left( \frac{\sigma_{xx}^t \left( \frac{x-e'}{d}, \frac{y}{d} \right)}{\mu p_0} \right) + \mu \frac{c}{a} \left( \frac{\sigma_{xx}^t \left( \frac{x-e}{c}, \frac{y}{c} \right)}{\mu p_0} \right) + \sigma_B \quad (2.24)$$

where  $c$  is the stick zone half width,  $e$  is the offset of the center of the stick zone from the center of the contact,  $\sigma_{xx}^n$ ,  $\sigma_{xx}^t$ ,  $\sigma_B$ , are the  $xx$  components of the stress due to the normal, tangential and bulk loads respectively and  $\sigma_{xx}^c$  is the stress correction for the finite thickness effect. Similar formulations can be derived for the  $yy$  and  $xy$  components of stress at these same loading stages, being the  $zz$  component

obtained from the other two direct stresses (plane strain condition). The functions in brackets may be evaluated using Muskhelishvili's potentials (Hills and Nowell 1993; Muskhelishvili 1953).

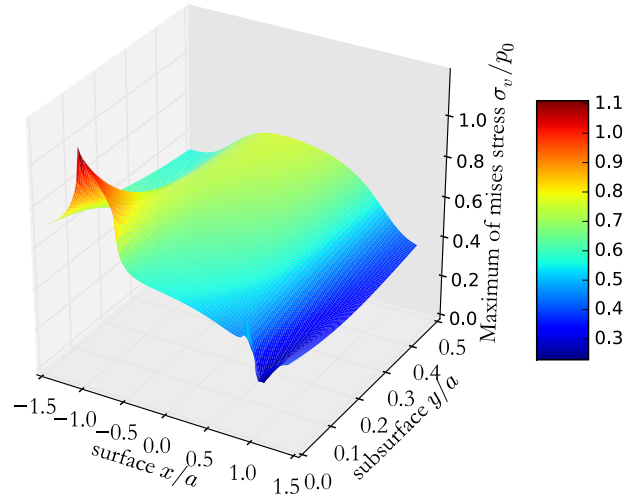


Figure 2.14: Subsurface distribution of the Von Mises equivalent stress computed for a flat/rounded fretting fatigue problem ( $R = 20\text{mm}$ ,  $Q/\mu P = 0.45$  and  $\sigma_B/\mu p_0 = 0.3$ ).

FIG.2.14 shows the Von Mises equivalent stress for an example of a flat/rounded fretting fatigue problem. A stress concentration clearly appears at the trailing edge of the contact  $x = -a$ , and the distribution is also characterized by very sharp gradients.

The Mindlin's 2D elastic analytical formulation of the surface tractions and the use of Muskhelishvili's potential to obtain stress below the contact assumes that:

- stress field are in plane strain condition;
- the bodies are infinite half-plane;
- the condition  $e + c < a$  is respected (no reverse slip);
- the fretting coefficient is constant on all the contact surface.

In order to be able to use this formulation to predict stress field of an experimental test, these assumptions respectively require:

- the pad and specimen are large enough in the direction  $z$ ;
- the thickness or distance between two pad in opposition is larger than  $10a$ ;
- the bulk load is not too high;
- the fretting coefficient of the stick and slip zone is are not very different and the cycles are stabilized.

This 2D analytical formulation of the contact problem was coded using in a Python script. It allows a rapid computation of the stress field at the surface and below the contact.

## 2.1.4 Numerical modelling of fretting fatigue.

### 2.1.4.i Introduction.

Early applications of finite element analysis (FEA) in fretting contact problems dates back to mid 1980s by Ruiz et al. (1984) and Stover et al. (1985). Numerical modelling techniques such as the FEA technique for analysing fretting fatigue behaviour have become very popular and widely used during the last decades. Hojjati Talemi (2014) counted more than 380 publications incorporating FEA in fretting and fretting fatigue research areas, with a clear tendency to the generalization of this approach (FIG.2.15).

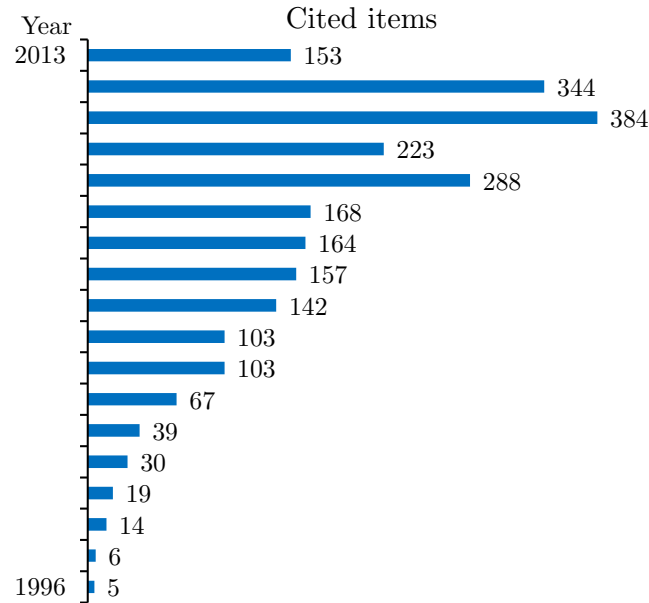


Figure 2.15: Cited FEA based ISI papers in field of fretting and fretting fatigue since 1996 until 2013 (up to june). (Hojjati Talemi 2014).

The FEA method provides the opportunity to quantify quantities such as non-linearity of contact problems along with non-proportionality and multiaxial stress states and deformation patterns due to applied external loads and different boundary conditions. One of the advantages of the FEA method is that it provides information, which cannot be obtained through experimental testing or analytical solutions.

Despite enormous FEA investigations of this problem, there are no standards or guidelines for FEA modelling of fretting and fretting fatigue phenomena. It is, however, possible to sort those FE models according to the level of simplification of the contact problem or depending on the loading and behavior they focus on. In order to model industrial problems such as riveted lap joints, dovetail joints, bearing shafts, steel wire connections, or others, some authors are using finite elements to model the whole geometry of the problem. Most of those studies require 3D modelling and an enormous number of elements. The load and boundary conditions applied on the different parts correspond to the conditions measured on the industrial problem. Because those studies required huge computing power, a lot of research focuses on simplified contact geometry and loading conditions which represent the local state of the contact. Those works usually assume that the local contact can be represented by a 2D plane strain model, or 2D axisymmetric in the case bearing shafts or shrink fitted joints. In the following,

some of those works are reviewed.

#### 2.1.4.ii Fretting wear.

Many research works using FEA to study the fretting wear focus on the cylinder-plane contact and use simplified plain strain 2D finite element model. In all cases, meshes are refined at the contact area, where stress discontinuity is the most severe. In this refined zone, structured quadrangular elements are often preferred, while, on the rest of the geometry, they can either be hexahedral or tetrahedral as illustrated in FIG.2.16.

McCull et al. (2004) have used the FEA method to simulate both fretting wear and the evolution of fretting variables with a number of wear cycles in a cylinder-on-flat fretting configuration for application to aero engine transmission components. In their model, they have simulated wear incrementally and the total simulation duration has been minimized via mesh and increment size optimization. Predicted wear profiles were also compared with profilometer measurements of fretting test scars.

Hyde et al. (2005) have suggested a methodology for the experimental simulation of fretting conditions in complex shaft couplings, using a simple representative specimen/test rig. The geometry and loading conditions of the representative specimen were designed using an iterative method, to model the stress and slip amplitude at contact interface, as predicted by detailed 3D FEA of the coupling.

Ding et al. (2007) presented the FEA model of the third body as a thin layer of elements with differing material properties which formed the top row of elements on the lower body. The third body properties were calibrated by matching the models behavior with experimentally recorded fretting loops. The contact geometry was incrementally updated to take into account the material removal calculated as a function of local contact pressure and local slip.

Fouvry et al. (2007) have performed a FEA investigation in order to formalize the fretting wear response of adhesive wear and non-adhesive wear interfaces and predict interface durability under fretting wear. They have shown that the wear depth kinetics can be predicted by considering the accumulated energy density. Mary and Fouvry (2007) have optimized the same FEA model by suggesting a criterion of the maximum wear depth per computation step.

Basseville et al. (2011) suggested models to improve surface and volume modelling, by taking into account the heterogeneity of stress fields due to the irregular interface. Zhang et al. (2011) have implemented FEA based energy wear simulation into the fretting contact problem. They have combined the method with a critical plane multiaxial fatigue prediction method for crack nucleation using the Smith-Watson-Topper (SWT) fatigue parameter and a nonlinear kinematic hardening model for cyclic plasticity.

Leonard et al. (2011) have proposed a new approach for modelling the fretting wear problem with and without coating, using the combined Finite Discrete Element Model (FDEM) in which multiple finite element bodies interact as distinct bodies. They have validated the FDEM by comparing the pressure and frictional shear stress results to the continuum mechanics solution for a Hertzian fretting contact.

#### 2.1.4.iii Fretting fatigue.

As said before, several experimental set-ups can be used to carry a fretting fatigue test (SEC.2.1.2.i). Bridge type tests typically involve two bridge-shaped fretting pads pushing against the gage section of fatigue specimen (FIG.2.3a).

Sato (1992) calculated the contact stress pressure distribution by using a boundary element method. The effect of different pad shapes on contact pressure distribution was investigated. Neu et al. (2000) used the FEA approach and multiaxial fatigue criteria based on the critical plane approach to estimate

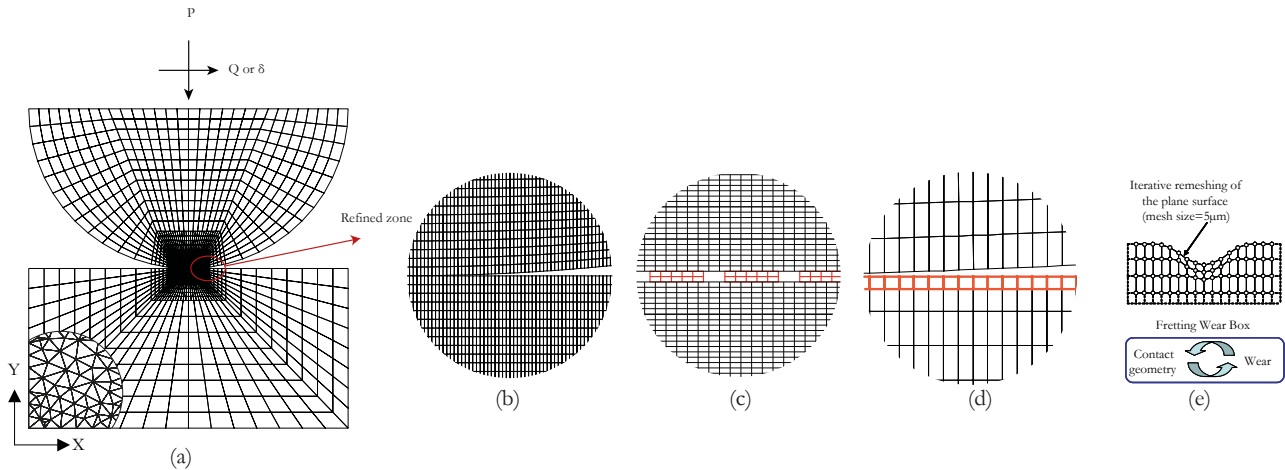


Figure 2.16: (a) 2D Mesh usually used for FEA of the wear of cylinder-plate contact model (b) structured refined zone under the contact (McColl et al. 2004) (c) third body modelled in the contact area by several rectangular particles (Basseville et al. 2011) (d) close-up view on a debris layer (Ding et al. 2007) (e) iterative methodology introduced to compute the local wear damage (Fouvry et al. 2007).

the local state stress at and near contact interface in order to predict the fretting fatigue crack nucleation lifetime.

Jayaprakash et al. (2010) and Mutoh and Xu (2003) proposed a new FEA approach based on a singular stress field near the contact edge and on fracture mechanics to predict fretting fatigue crack propagation lifetime. Modelling bridge type contact using FE allowed them to distinguish three regions along the contact interface (sticking, slipping, and gapping), and they underlined the influence of the pad stiffness on the stress distribution near the contact edge.

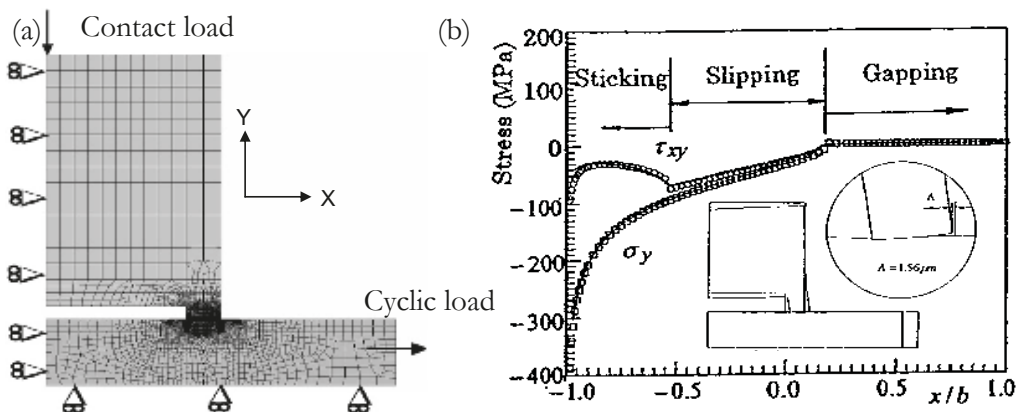


Figure 2.17: (a) 2D Mesh of the bridge type fretting fatigue (Jayaprakash et al. 2010) (b) Stress distribution on the interface under tension and definition of the sticking, slipping, and gapping regions (Mutoh and Xu 2003).

In other works, single clamp contact are used (FIG.2.3b-c). In contrast to the bridge type fretting fatigue test, there is a single fretting contact at each side of fatigue specimen.

Giannakopoulos and Suresh (1998) used a 3D finite element model to analyse spherical-plane fretting fatigue problems, and capture the evolution of the surface and sub-surface fields for different levels of partial slip, interfacial friction and externally imposed mean stress values.

Farris et al. (2000) combined FEA modelling and experimental observations, which led to thermography/FEM approach to understanding the influence of fretting on fatigue failure of riveted aircraft structures.

Tsai and Mall (2000) investigated the effect of plastic deformation under different fretting fatigue parameters, using elasto-plastic FEA of fretting stresses in a pre-stressed strip in contact with a cylindrical pad. Iyer and Mall (2001) used this model to analyse the effects of contact pressure and stress amplitude on the fretting fatigue lifetime. And by comparison with experimental results, they showed that local stress range computed from FEA may be sufficient to predict fretting fatigue life.

Using a full three-dimensional finite element model and a submodelling technique, Kim and Mall (2005) have investigated the effects of finite contact width using cylinder-on-flat and flat with rounded edge-on flat configurations.

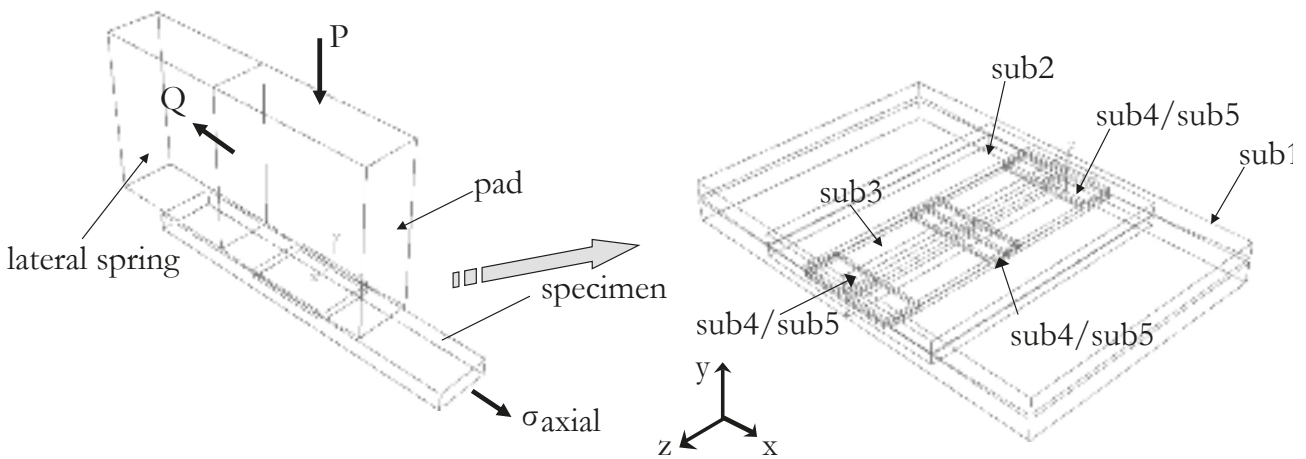


Figure 2.18: Details of submodels (Kim et al. 2011).

Submodelling is used to obtain an accurate stress and displacement state in the contact region while limiting computing time. It consists of running a global model analysis and saving the results in the vicinity of the submodel boundary; defining the total set of driven nodes in the submodel; defining the time variation of the driven variables in the submodel analysis by listing the actual nodes and degrees of freedom to be driven in each step; and running the submodel analysis using the driven variables to obtain the solution (ibid.). Sabelkin and Mall (2005) included the compliance of fretting texture and allowed the application of bending moment on the pad by adding a set of springs on the top of the fretting pad.

Bernardo et al. (2006) used a 2D finite element based methodology able to predict the pad size effect on the specimen life. The suggested model provides a direct evaluation of the fatigue strength at nodal points along with the stress/strain distribution results, and they showed that for fretting fatigue problems the stress state should be extracted using a process zone approach rather than in a single point. They have also revealed that selecting an appropriate mesh size ( $h_e * l_e$  in FIG.2.19) at contact interface allows to estimate the critical contact size effect successfully.

Madge et al. (2007) developed a FEA integrated wear modelling with fretting fatigue analysis to allow the prediction of the effects of material removal, due to fretting wear. Wang et al. (2007) simulate a

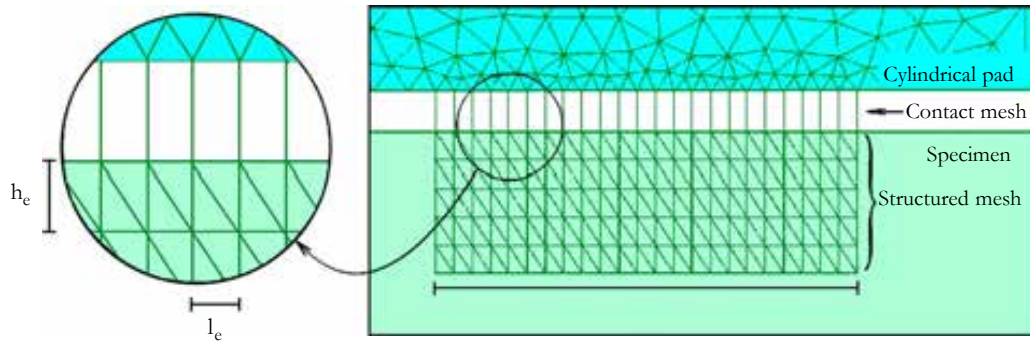


Figure 2.19: Bernardo et al. (2006) finite element mesh.

non-uniform friction distribution in the contact zone of their finite element model. They show that an equivalent constant coefficient of friction can be defined, and show little difference between the stress state in the contact region computed with this equivalent coefficient or with varying coefficient of friction.

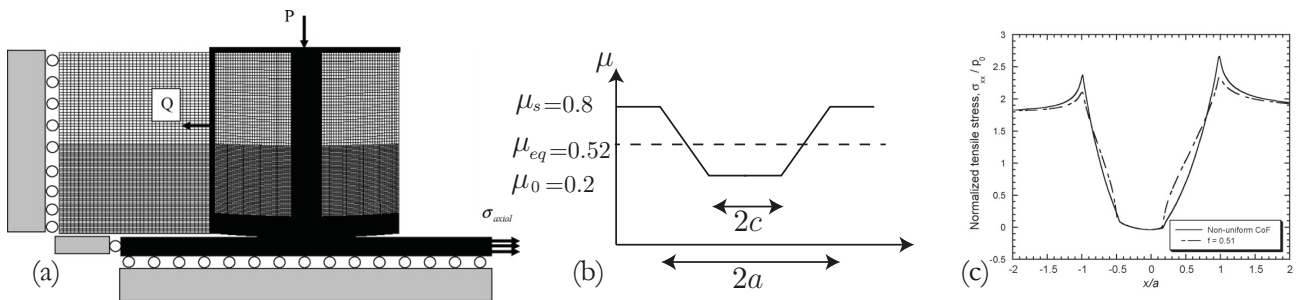


Figure 2.20: (a) Wang et al. (2007) finite element mesh (b) Friction distribution and equivalent constant friction coefficient (c) Comparison of normal stresses obtained from varying coefficient of friction and constant one.

Nesládek et al. (2012) have used the Digital Image Correlation (DIC) technique to calibrate the friction coefficient used in their finite element model.

#### 2.1.4.iv FEA of dovetail-attachment joints.

In other researches, 2D or 3D finite element analyses were applied to more complex contact geometry, closer to the industrial problem. Amongst all the applications mentioned in the introduction, we will present in the following some work on the dovetail-attachment joints (FIG.2.21a).

Boddington et al. (1985) presented a technique for the 2D numerical analysis of dovetail joints which is capable of modelling relative motion at the interface of the assembly (FIG.2.21b). The method is shown to give results in good agreement with experimental data and provide a basis for the analysis of interface motion in contacting assemblies.

Several works examine the effect of the critical geometrical features, such as flank length, flank angle, fillet radii and skew angle upon the resulting stress field:

- Papanikos et al. (1998) used a 3D nonlinear finite element analysis of the dovetail region (FIG.2.21c). The FE model has been validated using three-dimensional photoelastic stress freez-

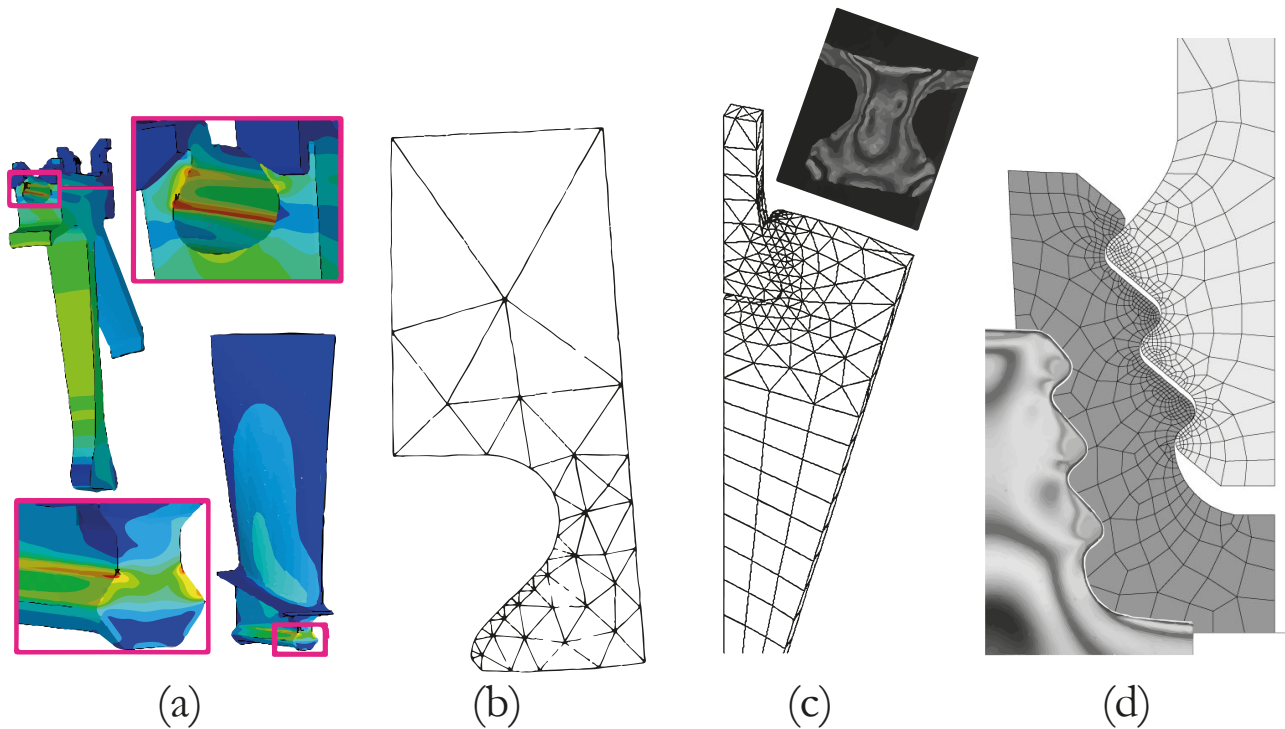


Figure 2.21: (a) Dovetail-attachment joints (Rao et al. 2008) (b) Boddington et al. (1985) 3D mesh for the analysis of dovetail blade fixing in rotating disk (c) 3D converged mesh (Papanikos et al. 1998) and photoelastic analysis (d) fir-tree 2D FEA and photoelastic analysis (Meguid et al. 2000).

ing results.

- Meguid et al. (2000) also used FEA and photoelastic stress freezing results to examine the effect of different critical geometrical features upon the stress field in the fir-tree region of a disc (FIG.2.21d).
- Sinclair et al. (2002) proposed a 2D submodeling procedure which allows really fine mesh in the critical region while computational effort are limited.
- Song et al. (2002) used a combination of intelligent computer-aided design system (ICAD) and FEA in order to optimize the design of a turbine blade fir-tree root.
- Arrieta et al. (2004) have modelled a two-dimensional finite element contact and paid a special attention to material models and surface interaction (friction coefficient and contact conditions) in order to balance computational effort with result accuracy.

Finite element analysis presents several advantages compared to the analytical formulation. It allows:

- the modelling of the contact problem in 3D;
- the modification of the contact geometry by element removal if wear occurs;
- the use of different coefficient of friction along the contact surface, or the incremental variation of the COF with the number of cycles;
- the analysis of elasto-plastic problems;
- the modelling of complex industrial contact geometries.

However, because of the stress gradients present in the fretting problem, FEA requires very small elements in the surrounding of the stress concentrations. Resolution of models with so many elements costs a huge amount of computing time which often limit the analysis to simplify academic problems.

## 2.2 Titanium Ti-6Al-4V

### 2.2.0.i Generality on titanium alloys

Pure titanium can exist under two crystallographic phases. At low temperature, the  $\alpha$ -field has a hexagonal closed packed structure (HCP). Above the temperature  $T_\beta = 882^\circ\text{C}$ , the structure becomes  $\beta$ -field with body-centered cubic (BCC). The melting point of pure titanium is  $1668^\circ\text{C}$ .

For a mechanical application, alloys with element addition or substitution are preferred to stabilize the structure in precise field  $\alpha$ ,  $\beta$  or  $\alpha + \beta$ . Elements such as aluminum, oxygen, nitrogen, carbon, gallium, germanium, lanthanum, and cerium stabilize the alpha phase to higher temperature and are thus referred to as  $\alpha$ -stabilizers.  $\beta$ -stabilizers, which raise the transition temperature between the field  $\beta$  and  $\alpha + \beta$ , are subdivided into two groups: beta-eutectoid (e.g., tungsten, chromium, iron, hydrogen) and beta-isomorphous (e.g. vanadium, niobium, tantalum, molybdenum, and rhenium). These last elements, when added in sufficient concentrations, can stabilize the beta phase at room temperature.

The  $\alpha$ -alloys display a good resistance to creep whereas  $\beta$ -alloys display a good ductility at low temperature. The  $\alpha + \beta$ -alloys present a good forging capability and thermal treatments allow to obtain excellent mechanical property. Thermo-mechanical treatments can change the morphologies of the phases, and can lead to different microstructure, even for the same alloy.

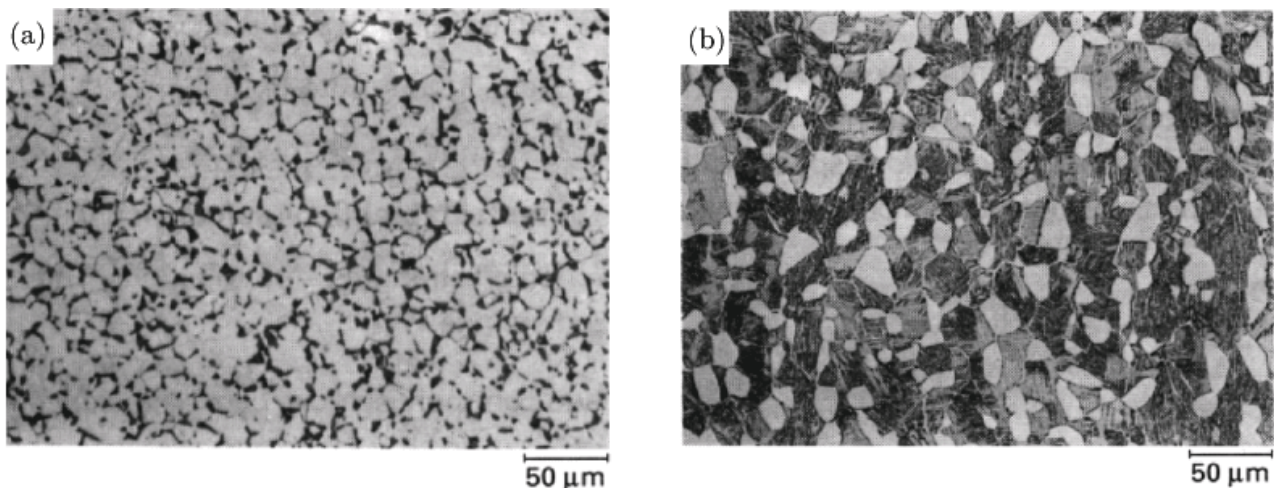


Figure 2.22: a) Ti-6Al-4V equiaxed:  $\alpha_s$  platelets in a  $\beta$ -matrix aged a) Ti-6Al-4V bimodal: equiaxed  $\alpha_p$  grains and lamellar grains in same proportion.

Titanium and titanium alloys are classified into 34 grades which refer to standard specifications ASTM B861 (2014). Grade 5, also known as Ti6Al4V, TA6V, Ti-6Al-4V or Ti 6-4, is the most commonly used Ti-alloy. It accounts for 50% of total titanium usage the world over. The composition of the alloy used by Snecma in the fan and disc is given in the TAB.2.1.

The aluminum, which generally accounts for 6% of the mass, is a  $\alpha$ -stabiliser. Aluminium increase mechanical strength and creep resistance, however, its percentage is limited to 7% to avoid the formation of  $\alpha_2$  phase which increase the brittleness. Vanadium (4%) plays the roles of  $\beta$ -stabiliser. It increase the ductility but decreases the oxidation resistance. The addition of these alloying elements modifies the phase diagram.

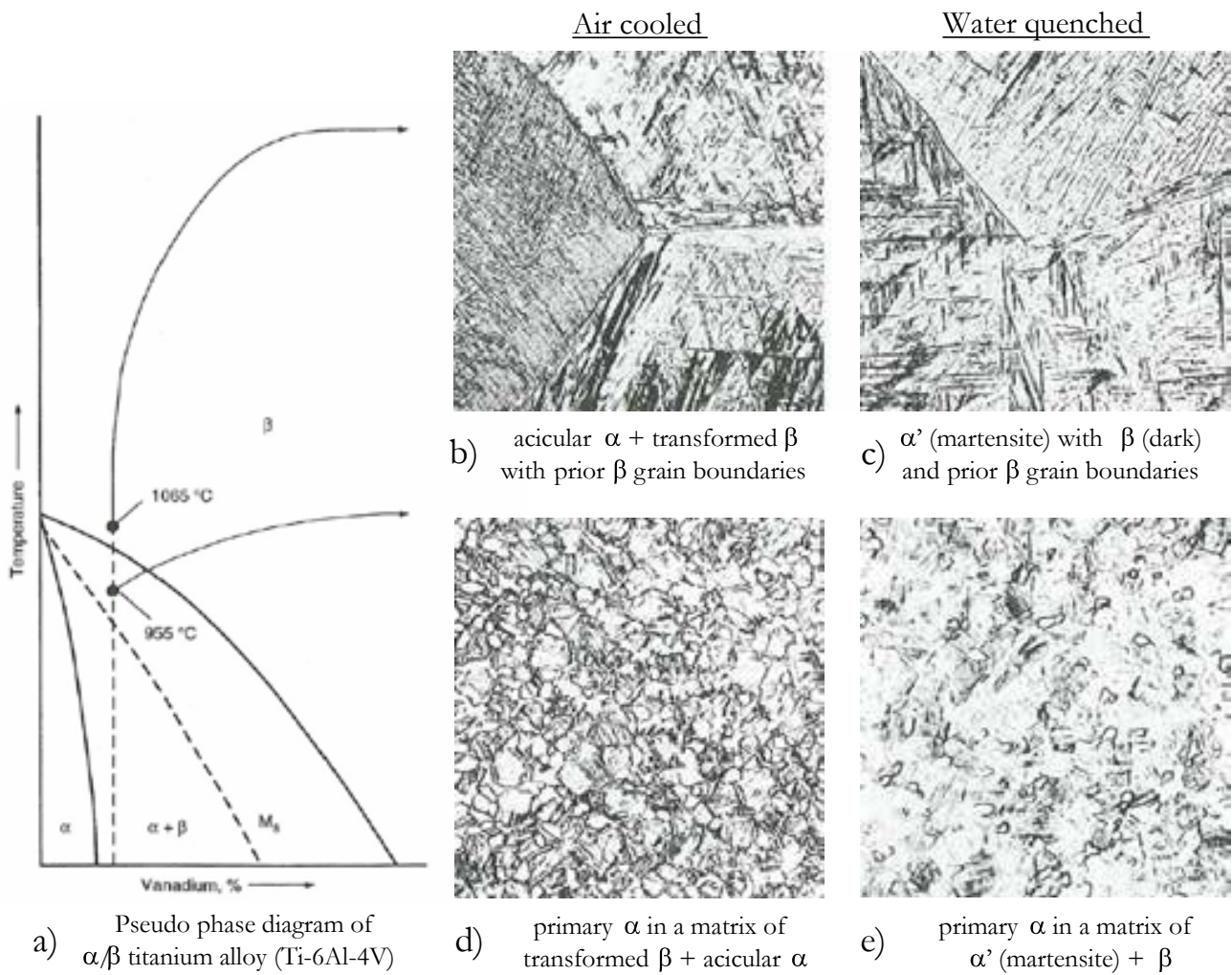


Figure 2.23: The microstructure of Ti-6Al-4V for different cooling processes. (Corinne 2008) adapted from (Donachie 2000).

Elements	Al %		V %		O (ppm)		H (ppm)	
	min	max	min	max	min	max	min	max
Specified	5.5	6.75	3.5	4.5	-	2000	-	100
Mesured								

Table 2.1: Principal elements of Ti-6Al-4V alloys - SNECMA fan disc and blade.

Consequently, the equilibrium microstructure of the alloy at room temperature consists mainly of the  $\alpha$  phase with some retained  $\beta$  phase. In the case of the Ti-6Al-4V, the  $\beta$ -transition (or  $\beta$ -transus) is increased to approximately  $T_\beta = 1000^\circ\text{C}$ . Different varieties of phase morphologies may form depending on the temperature history of the alloy. FIG.2.23 shows two different microstructures that can be formed depending on the cooling rate and the forging temperature.

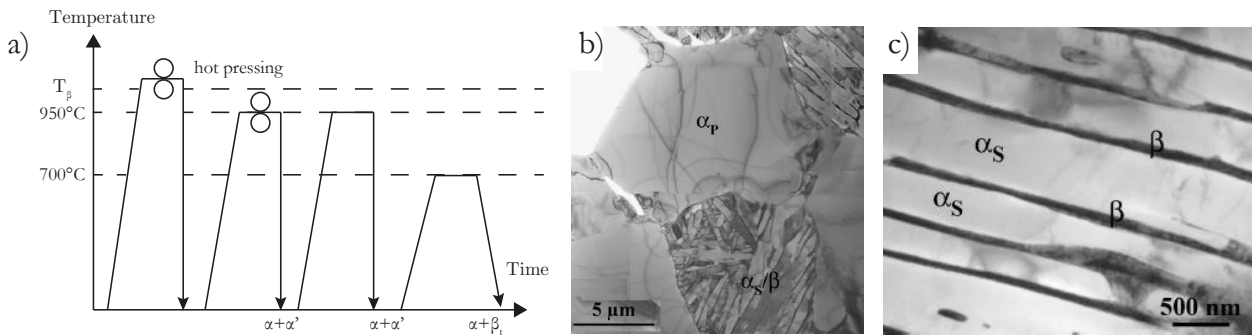


Figure 2.24: a) Thermo-mechanical treatment applied to the Ti-6Al-4V b) grain  $\alpha_p$  and  $\alpha + \beta$  lamellar grains c) detail of the lamellar grains constituted of secondary  $\alpha_s$  platelets in a  $\beta$ -matrix (Castany 2007).

The thermo-mechanical treatment applied to the Ti-6Al-4V alloy used in this study leads to a bimodal microstructure  $\alpha + \beta$ . The manufacturing process starts with a melting of the purified titanium with the stabilizer. For the disc and the blade of the fan, Ferré (2013) explains that the material goes through a first vacuum induction melting followed by three vacuum arc remelting. Those processes avoid oxide formation and ensure the homogeneity of the material without impurity.

The first stage of this treatment is usually a forge of the raw alloy in the domain  $\beta$ , in order to reduce  $\beta$  grain size. Next, a hot isostatic pressing is applied in the  $\alpha + \beta$  domain before the quenching. In the process used by Snecma, this forging is operated at  $940^\circ\text{C}$  (ibid.), but other forging temperatures are mentioned in other references (Le Biavant et al. 2002).

Follow another treatment where appear grain in the phase  $\alpha_p$  and a quenching where the phase  $\beta$  transform on metastable  $\alpha'$ . Finally an annealing around  $700^\circ\text{C}$  will transform the phase  $\alpha'$  in  $\alpha + \beta$  lamellar grains constituted of secondary  $\alpha_s$  platelets in a  $\beta$ -matrix.

### 2.2.1 Macrozones of the Ti-6Al-4V alloy

Le Biavant (2000) observed the presence of millimetric ghost structure in the Ti-6Al-4V alloy. Those macrozones, also named microtextures by other authors (Bantounas et al. 2010), can be observed with a chemical reaction or with simple mechanical tests (FIG.2.25). In these macrozones, the  $\alpha_p$  phase has a preferred orientation and neighbouring macros zones may display very different major  $\alpha_p$  grain orientation. The ex- $\beta$ -grains, from the first forging, is responsible for this macro structure. Indeed, despite the second forging in the  $\alpha + \beta$ , the  $\alpha_p$  grains and  $\alpha_s$  colonies inherited from a prior  $\beta$  tend to keep the same orientation or a Bürgers variant.

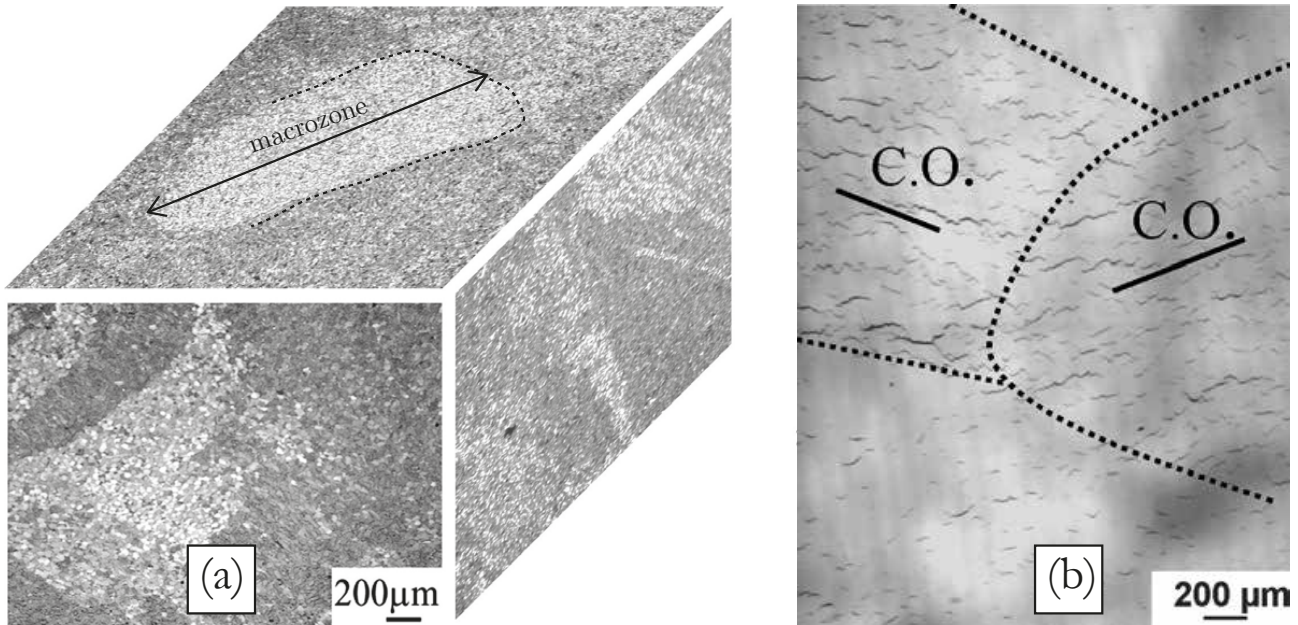


Figure 2.25: (a) Morphology of the macrozones after hydrofluoric acid attack (b) crack orientation observed by X ray after fatigue bending test (Le Biavant 2000).

Le Biavant et al. (2002) showed a high heterogeneity of crack initiation between different macrozones (FIG.2.25(b)). Indeed, in macrozones with orientation maximizing the shear stress on slip system, a high number of tiny cracks nucleate and coalescence is favored by the similar orientation of  $\alpha_p$  grain. For uniaxial tests, it results in a heterogeneity of the crack density at the scale of the macrozones and apparition of paralleled cracks inside each macrozone.

### 2.2.2 Microstructure and material properties observed in literature

In most cases, the Ti-6Al-4V alloy used in the industry has a bimodal microstructure consisting of equiaxed  $\alpha_p$  and transformed  $\beta$ -grains. However, depending on the parameters (e.g. temperature, time, cooling rate) of the thermomechanical treatment or heat treatment, the microstructure and mechanical properties can vary in a wide range (Oberwinkler et al. 2010; Stoschka et al. 2009; Wu et al. 2013). Indeed, the fatigue strength highly depends on the microstructural parameters such as the  $\alpha_p$  content and size in the bimodal microstructure.

TAB.2.3 summarizes information about microstructure parameters and high cyclic fatigue (HCF) strength found in the literature from 1984 to present. All fatigue tests were performed at room temperature in air under axial loading conditions with a sine wave on unnotched specimens. Note that fatigue limits are not defined as the stress amplitude,  $\sigma_a$ , but as the maximum stress,  $\sigma_{max} = \sigma_m + \sigma_a$ , leading to infinite life. FIG.2.26 summarizes in a graph the maximum strength in a tensile test of those literature data against the life limit considered. Despite the resemblance, note that this figure is not S-N curve. Each point corresponds of the fatigue limit after different test campaigns. Studies results show a dispersion contained in  $\pm 20\%$  the average fatigue strength. Basic uniaxial tests were not part of this work, and basic fatigue properties had to be taken from the literature. Hence, careful appreciation of some prediction results presented in this thesis will be necessary.

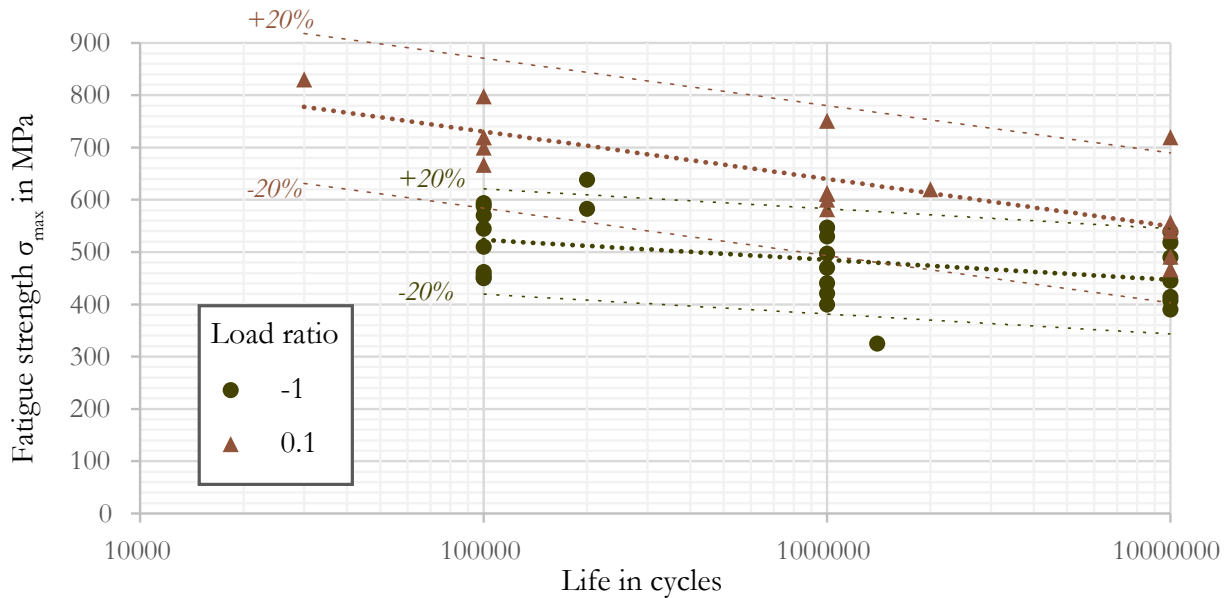


Figure 2.26: Fatigue strength of *Ti – 6Al – 4V* from TAB.2.2, for  $R_\sigma = 0.1$  and  $R_\sigma = -1$ .

More homogeneity is found in the literature for the static material properties of the Ti-6Al-4V. TAB.2.2 gives the Young Modulus  $E$ , the Vickers hardness  $HV_{0.3}$ , the Poisson coefficient  $\nu$  and the yield strength taken from (Le Biavant 2000).

Material	$E$ (GPa)	$HV_{0.3}$	$\nu$	$\sigma_u$ (MPa)	$R_{p0.2}$ (MPa)
Ti-6Al-4V	119.4	360	0.286	1000	850

Table 2.2: Basic material properties of the Ti-6Al-4V.

Reference	Ratio of $\alpha_p$ -grain in %	Average size of $\alpha_p$ -grain in $\mu m$	Frequency in Hz	Stress ratio	HCF fatigue limit $\sigma_{max}$ (MPa)		
					$10^5$	$10^6$	$10^7$
(Nalla et al. 2002)	64	20	25	0.1	700	600	540
				0.5	850	780	640
(Zuo et al. 2008a)	55	10	20kHz	-1		546	518
(Nagai et al. 1993)		4	20	0.01	800	720	640
		4			800	720	690
		2.8			800	740	720
				-1	588	547	539
(Peters et al. 1984)	6	80	-1	710	675	675	
(Bellows 1999)	60	13	60	-1	450	400	390
				0.1	667	611	556
				0.5	860	800	640
				0.8	950	920	900
(Hines and Lutjering 1999)	35	7.5	90	-1	545	470	445
(Ivanova et al. 2002)	60.5	8	30	0.1			467
	24.8	8.5			830 ( $3 \cdot 10^4$ )	620 ( $2 \cdot 10^6$ )	550
(Nalla et al. 2003)	64	20	5	-1	450		
(Zuo et al. 2008b)	55	10	25	-1	570	530	
(Ivanova et al. 1999)	60.5	8	30	-1	462	441	414
	24.8	8.5			455	421	407
	28.7	5.5			510	497	490
	60.5	8		0.1	720	582	491
	24.8	8.5			720	613	551
	28.7	5.5			798	751	720
(Lanning et al. 2005)				-1		482	
				0.1		591	
(Araújo et al. 2007)	65	5		0		596 ( $1.4 \cdot 10^6$ )	
				-1		325 ( $1.4 \cdot 10^6$ )	
(Ferré 2013; Meriaux 2010)	60	30		-1	593.97		
(Delahay 2004)				-1	638 ( $2 \cdot 10^5$ )	583 ( $2 \cdot 10^6$ )	
(Moshier et al. 2001)	60	20					
(Le Biavant et al. 2002)	50	15					
(Lee and Mall 2004a)	60	10					
(Bantounas et al. 2010)	80	15					

Table 2.3: Literature review of bimodal microstructure parameters and HCF data of Ti-6Al-4V alloys.

The variation of the fatigue properties of the Ti-6Al-4V alloy observed in the literature is explained by the variability of the microstructure resulting from the thermo-mechanical treatments. Moreover, test conditions and surface preparations of the samples also affect the fatigue limits. In this work, we will use an average of the values found in the literature. For a life of  $10^6$  cycles the fatigue limits adopted will be:

$$\sigma_{-1} = 480MPa \qquad \sigma_{0.1} = 640MPa \qquad (2.25)$$

But we will keep in mind that variations until  $\pm 20\%$  may be found in other studies.

## 2.3 Fatigue of materials.

Fatigue includes all the physical mechanisms responsible for the degradation of a mechanical part. We are particularly interested in fatigue induced by repetitive load application. It has been estimated that fatigue contributes to approximately 90% of all mechanical service failures (Campbel 2008). Three basic factors are necessary to cause fatigue: (a) a maximum tensile stress of sufficiently high value, (b) a large enough variation or fluctuation in the applied stress, and (c) a sufficiently large number of cycles of the applied stress.

### 2.3.1 Basic concepts.

Fatigue depends on many factors:

- material properties and microstructure,
- load frequency,
- load amplitude,
- the load loading ratio, i.e. the relation between the minimum and maximum applied,
- stress concentrations,
- stress multiaxiality,
- the scale of the structural component,
- environment,
- temperature.

Depending on the number of loading cycles seen by the structure, concepts of Low Cycle Fatigue (LCF) and High Cycle Fatigue (HCF) are defined. In LCF, the structure suffers high loads, its life is relatively short and significant plastic straining takes place. Note that some ductile steels can suffer cyclic plasticity and endure millions of cycles. However for most alloys, life is usually in this case function of applied stress or strain, and stress ratio is a parameter.

On another hand, HCF gathers problems that require more than  $10^4$  cycles to failure where stress is low and deformation is primarily elastic. In HCF, the concepts of infinite life and fatigue limit stress are often defined for a given number of cycles, usually  $10^6$  or  $10^7$ , after which it is assumed that the material will never break regardless of the number of cycles applied. Note that for some materials the fatigue limit stress may continue to decrease at cycle counts up to and beyond  $10^{10}$  cycles (Bathias 1999).

At the dovetail, components experience a combination of LCF and HCF, or Combined Cyclic Fatigue (CCF). The blades of turbine engine suffer an interaction of high cycle fatigue, due to vibration phenomena, and low cycle fatigue, due to ground-air-ground major engine cycling. In this study, we will, however, focus on the HCF regime, using the same fatigue and fretting load frequency.

In most cases, determining a fatigue limit strength assumes the absence of crack initiation. Indeed, even if the material survives infinite life, many microcracks may have initiated without propagating to failure. Miller (1987) explains this phenomenon by the existence of successive microstructural barriers that a short crack must cross to propagate. Thus, for short cracks, the non-propagation stress threshold is not a constant but varies with the crossing of microstructural barriers, and the fatigue stress limit can be defined as the stress level needed to overcome the last microstructural barrier (C in FIG.2.27).

Finally, Miller defined three categories of short cracks:

- Microstructurally short cracks: The size of the crack is comparable to the characteristic scale of the microstructure, some grain sizes, for example;
- mechanically short cracks: The size of the crack is comparable to the dimension of its plastic zone;
- physically short cracks: The size of the crack is greater than the grain size and the size of the plastic zone but does not exceed one millimeter.

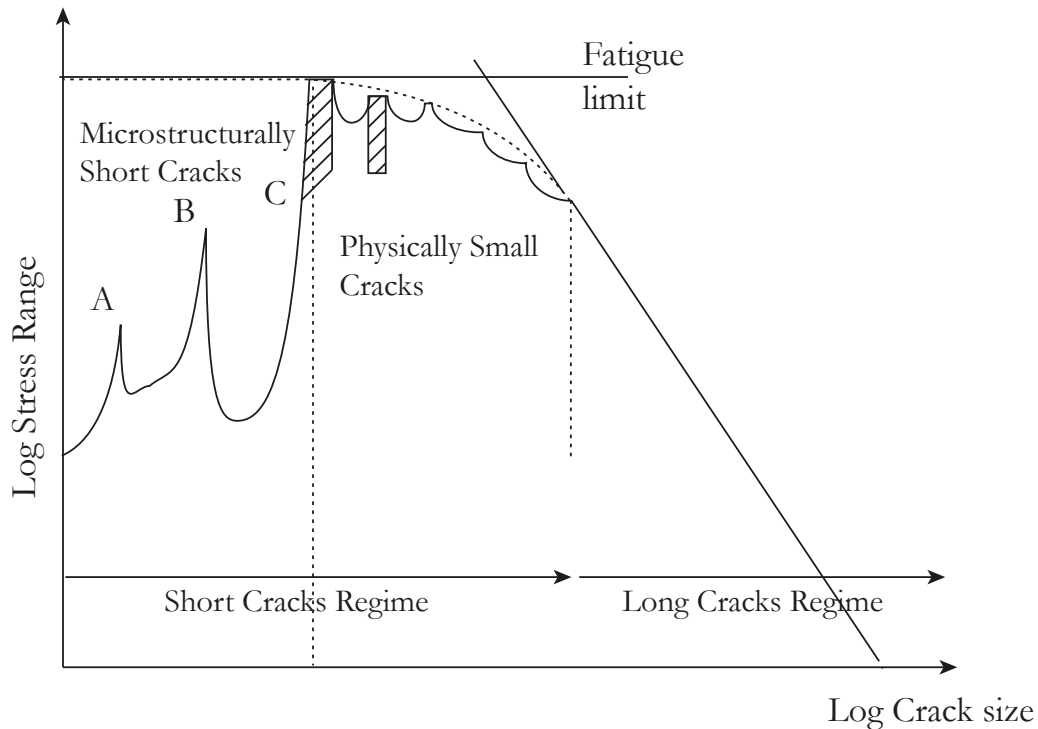


Figure 2.27: Fatigue stress limit function of the crack size.

The endurance limit can be defined as the stress amplitude below which microcracks can initiate but do not propagate to failure. If the cracks are sufficiently “short”, the endurance limit is independent of the size of the crack (Kitagawa and Takahashi 1976). This is called the “short crack” regime. Beyond a certain size, the endurance limit decreases as the crack grows, this represents the beginning of the “long crack” regime.

Fatigue cracks in most cases nucleates at free surfaces, usually external surfaces, but can also be initiated at sub-surfaces in the presence of defects such as voids and inclusions. Common surface defects include geometric notches and surface roughness. Fatigue crack nucleation and growth occurs in the following stages (Campbel 2008):

- Stage I: Crack initiation usually starts on a surface discontinuity such as a notch, which acts as a stress riser. In the absence of a surface defect, crack initiation will eventually occur due to the formation of persistent slip bands. Slip bands result from the systematic build-up of fine slip movements of approximately one nanometer. Therefore, the relative movement of the slip bands over each other results in the formation of intrusions and extrusions at the surface, which possibly leads to the formation of a crack. This phenomenon is essentially controlled by the

shear and the microstructure of the material. The crack propagation rate during stage I is very low. For uniaxial loading, the crack initially follows the slip bands at approximately  $45^\circ$  to the principal stress direction as illustrated schematically in FIG.2.28.

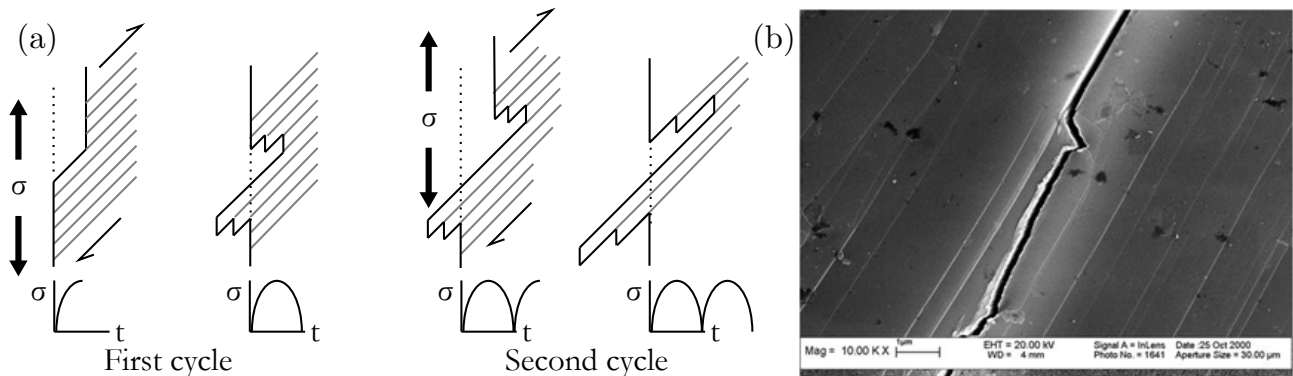


Figure 2.28: (a) Illustration of persistent slip bands phenomenon (Pommier 2001) (b) Initiation of a fatigue crack parallel to the grain slip bands (Le Biavant et al. 2002).

In industrial alloys, other nucleation processes can occur, depending on the microstructure and stress conditions. Figure I-8 illustrates some potential initiation sites (FIG.2.29a). At the surface, the initiation can be transgranular (i) or intergranular (ii), but can also develop from a defect such as porosity, shrinkage or inclusion (iii). In some cases, nucleation can be internal on sites such as inclusions (iv) micro space at grain boundary (v) or intersections of grain boundaries (vi) (Hénaff and Morel 2005).

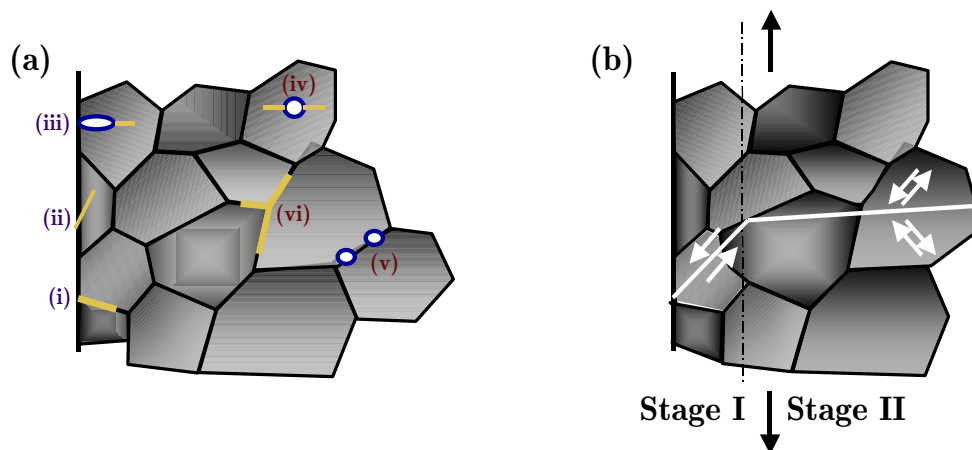


Figure 2.29: (a) Different initiation sites (b) Transition between Stage I and Stage II (Hénaff and Morel 2005).

- Stage II: When the crack length becomes sufficient for the stress field at the tip to become dominant, the overall crack plane changes and becomes perpendicular to the principal stress, and the crack enters stage II (FIG.2.29b). Fatigue crack growth proceeds by a continual process of crack sharpening followed by blunting (Laird 1967; Pelloux 1969), as shown in FIG.2.30.
- Stage III: Eventually, sudden failure occurs when the fatigue crack becomes long enough so that

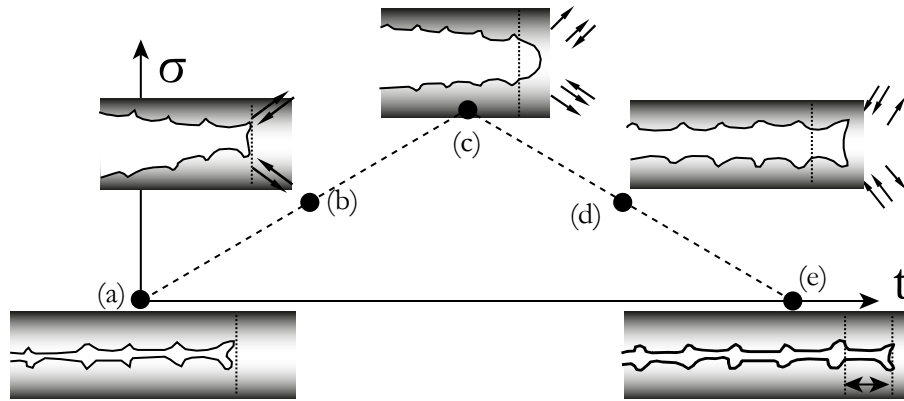


Figure 2.30: Fatigue crack growth mechanisms (a) no load (b) loaded (c) maximum load (d) load reduced (e) no load (Pelloux 1969).

the remaining cross section can no longer support the applied load, which is also called tensile fracture.

The effect of the fretting on the fatigue of the specimen is very located and particularly affect the short crack regime. Crack initiation and the stage I of the propagation are principally governed by the shear stress, while the later stage of the propagation is more affected by the normal stress.

### 2.3.2 Uniaxial tests and influence of the loading ratio.

In general, fully reversed push-pull fatigue tests are used to generate a S-N curve. The classical results of Goodman (1899) and Haigh (1917) have shown that the addition of an mean tensile stress leads to a decrease of the fatigue limit, whereas superimposition of a mean compressive stress significantly increases the fatigue limit. The Haigh diagram is a common method of representing the fatigue limit or endurance limit stress of a material in terms of alternating stress (the vibratory stress amplitude) and the mean stress (Nicholas 2006). Different equations were proposed to represent the effect of the mean stress:

- Goodman equation (or Modified Goodman equation):

$$\sigma_a = \sigma_{-1} \left( 1 - \frac{\sigma_m}{\sigma_u} \right) \quad (2.26)$$

- Soderberg equation (Soderberg and Sweden 1930):

$$\sigma_a = \sigma_{-1} \left( 1 - \frac{\sigma_m}{\sigma_y} \right) \quad (2.27)$$

- Gerber equation (Gerber 1874):

$$\sigma_a = \sigma_{-1} \left[ 1 - \left( \frac{\sigma_m}{\sigma_u} \right)^2 \right] \quad (2.28)$$

Where subscripts  $a$ ,  $m$ ,  $u$  and  $y$  refer to the alternating, mean, ultimate stresses, and yield stress, respectively, and  $\sigma_{-1}$  represents the experimental value of the alternating stress under fully reversed cyclic loading ( $R = -1$ ). FIG.2.31 gives an example of Haigh diagram obtained for a tensile loading with a target life of  $10^6$  cycles for a titanium alloy Ti-6Al-4V (Lanning et al. 2005).

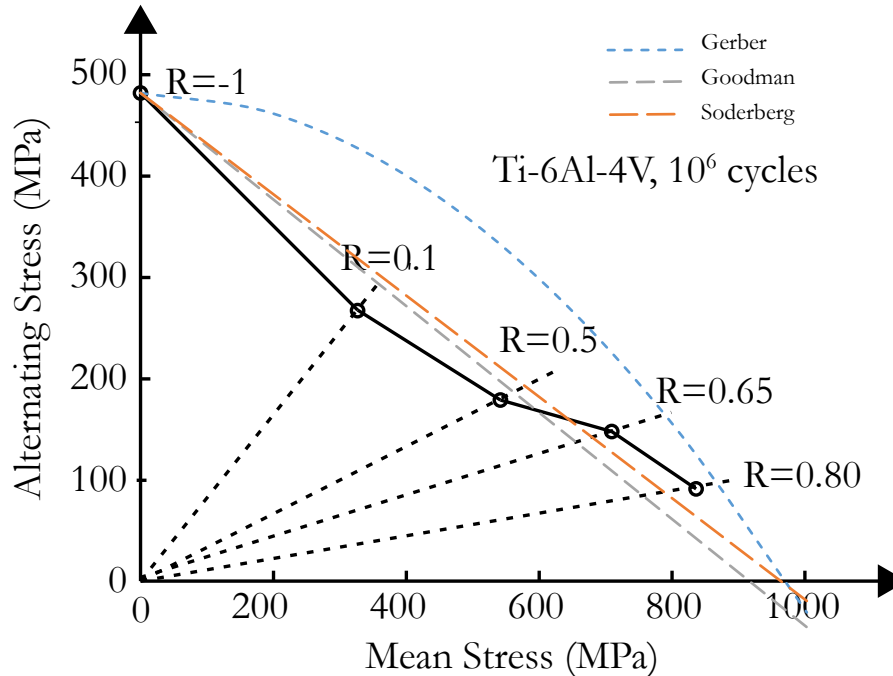


Figure 2.31: Haigh diagram for a constant life of  $10^6$  cycles smooth Ti-6Al-4V specimens (Lanning et al. 2005).

In cyclic torsion, Sines (1959) showed that endurance limit mostly depends on the magnitude of the shear and not the mean shear. The results of several authors, such as Gough (1949) and more recently Davoli et al. (2003) confirm this result.

When the fretting fatigue problem is studied for the disc/blade contact, the bulk load is generally applied with a loading ratio close to 0, which reflect the cycle of take off/landing and the centrifugal force generated. The fretting load, however, is usually applied with a loading ratio of -1, reflecting a simplification of the aerodynamic vibration on the blade. Therefore, initiated cracks will experience a variable ratio as they grow away from the contact. This evolution of the loading ratio should be taken into account by the fatigue criteria.

### 2.3.3 Criteria based on stress invariants

In order to deal with the multiaxiality of the problem, other authors presented a criterion based on stress invariants. Sines (1959) and Crossland (1956) proposed respectively the following criterion:

$$\frac{\sqrt{J_a} + \alpha_1 \cdot I_{moy}}{\beta} \leq 1 \quad (2.29)$$

$$\frac{\sqrt{J_a} + \alpha_2 \cdot I_{max}}{\beta} \leq 1 \quad (2.30)$$

where  $I_{moy}$ ,  $I_{max}$  are the mean and maximum of the hydrostatic stress during the loading cycle, and  $J_a$  is the amplitude of the second invariant which is defined as:

$$J_2 = \frac{1}{2} \cdot S : S \quad (2.31)$$

where  $S$  is the deviatoric part of the stress tensor. In torsion, the hydrostatic stress is null and the parameter  $\beta$  can be identified as:

$$\beta = \tau_{-1} \quad (2.32)$$

The major difference between these two formulations comes from the way the hydrostatic pressure is taken into account. In the case of a load in reverse bending, the average hydrostatic pressure is zero during the cycle, which results in a fixed ratio between the endurance limits in torsional and bending fatigue with the criterion of Sines, which is not realistic:

$$\frac{f_{-1}}{\tau_{-1}} = \sqrt{3} \quad (2.33)$$

The criterion of Crossland does not have this drawback since the hydrostatic pressure has a role to play in reverse bending. The parameters  $\alpha_1$  and  $\alpha_2$  are respectively identified with the bending fatigue limit with a load ratio -1 and 0:

$$\alpha_1 = 3 \cdot \frac{\tau_{-1}}{f_0} - \sqrt{3} \quad (2.34)$$

$$\alpha_2 = 3 \cdot \frac{\tau_{-1}}{f_{-1}} - \sqrt{3} \quad (2.35)$$

These two criteria ensure non-influence of the average torsional stress on the endurance limit, and reflect well the influence of mean stress on the endurance limit.

However these approaches are only valid when the loading is proportional (i.e. radial). As an example, a fully reverse out of phase bending-torsion test can be considered. In this case the stress tensor can be written as follow:

$$\Sigma(t) = \sigma_a \cdot \begin{bmatrix} \sin(\omega \cdot t) & \sin(\omega \cdot t + \frac{\pi}{2}) & 0 \\ \sin(\omega \cdot t + \frac{\pi}{2}) & \sin(\omega \cdot t) & 0 \\ 0 & 0 & 0 \end{bmatrix} \quad (2.36)$$

and the second invariant has a constant value :

$$J_2(t) = \sigma_a^2 \quad (2.37)$$

This result shows that the amplitude of the second invariant can be zero even though the stress field varies cyclically over time. As the hydrostatic pressure is null for this loading, the expressions of the Sines and Crossland criterion remains null even when  $\sigma_a$  tends to infinity.

Because of the non-linear nature of the friction at the contact interface, loading is likely to be non-proportional in the neighbourhood of the contact, even if the external loads are applied in a proportional fashion. Therefore, the criteria based on stress invariants cannot be used for fretting fatigue.

### 2.3.4 Critical plane approach

Limiting his study to proportional cases, Findley (1959) proposed a stress based multiaxial fatigue criterion considering a combination of the shear stress amplitude  $\tau_a$  and the maximum normal stress  $\sigma_{n_{max}}$  during a loading cycle. The general background follows the assumption that, fatigue crack nucleation and early growth is a process that is driven by shear stresses, but once nucleated, a crack tends to grow in perpendicular to the maximum principale stress direction.

$$(\tau_a + k\sigma_{n_{max}})_{max} = FN \quad (2.38)$$

Here  $k$  is a material constant that is related to the materials' sensitivity to normal stresses and  $FN$  is directly related to the materials' fatigue strength. For ductile materials,  $k$  typically varies between 0.2 and 0.3.

Under cyclic uniaxial traction with mean stress, characterized by the loading ratio  $R = \sigma_{min}/\sigma_{max}$ , it can be shown that Findley's criterion can be written as

$$0.5\sigma_a \left[ \sqrt{1 + \left( \frac{2k}{1-R} \right)^2} + \frac{2k}{1-R} \right] = FN \quad (2.39)$$

which quantifies the mean stress effect. The weakness of the Findley criterion appears when cyclic torsion with static mean shear stress is considered. Indeed, Sines (1959) showed that endurance limit mostly depends on the magnitude of the shear and not the average shear. The results of several authors, such as Gough (1949) and more recently Davoli et al. (2003) confirm this result. However, the application of the Findley criterion to cyclic torsion with static mean shear stress,  $\tau_{max} = \tau_a(2\pi t/T) + \tau_m$ , leads to the relation:

$$\tau_a \leq \sqrt{\frac{k^2\tau_m^2}{(1-k^2)^2} - (k^2\tau_m - FN^2)} - \frac{k\tau_m}{1+k^2} \quad (2.40)$$

that, erroneously, anticipates a dependence of the fatigue limit on the static mean shear stress.

In the 70's, observations on fatigue specimen showed that crack initiation tends to favor specific planes where the shear is maximum. It is from these observations that fatigue criteria formulated from mechanical quantities determined on these planes began to emerge.

For example, Brown and Miller (1973) noticed that the fatigue cracks propagate with the assistance of the normal strain and proposed a criterion taking into account the effect of both the shear strain,  $\gamma_a$ , and the tensile strain, normal to the plane of maximum shear,  $\epsilon_{aN}$ :

$$\gamma_a + \alpha.\epsilon_{aN} \leq \beta \quad (2.41)$$

Kandil et al. (1982) used a combination of the Manson and Coffin law and of the Basquin law to propose an explicit equation showing the number of cycles to failure (KBM model).

Later, Socie et al. (1985) proposed a similar criterion which considers the parameter  $\alpha$  equal to 1 and introduced a third term which involves the average normal stress,  $\sigma_{n_{moy}}$  in order to consider its influence on the opening of the crack:

$$\gamma_a + \epsilon_a N + \alpha \cdot \sigma_{n_{moy}} = \frac{\tau_0}{G} \cdot (2 \cdot N_r)^b + \gamma_0 \cdot (2 \cdot N_r)^c \quad (2.42)$$

where  $G$  is the shearing mode and  $\tau_0$ ,  $\gamma_0$ ,  $b$  and  $c$  are parameters which are identified from an SN curve.

The authors however found that this test ignores the hardening of metallic materials under non-proportional loading (Fatemi and Socie 1988). They deduced that the maximum normal stress at the maximum shear plane  $\sigma_{n_{max}}$  is a more representative parameter of the fatigue phenomenon than normal deformation. The latest version of their fatigue criterion is written as follows ( $\sigma_y$  being the yield strength of the material):

$$\gamma_a \cdot \left( 1 + \alpha \cdot \frac{\sigma_{n_{max}}}{\sigma_Y} \right) = \frac{\tau_0}{G} \cdot (2 \cdot N_r)^b + \gamma_0 \cdot (2 \cdot N_r)^c \quad (2.43)$$

These approaches knew a great success and are the basis of many criteria used today. However, their formulations is based on macroscopic parameters whereas the fatigue is also related to physical phenomena mesoscopic. Dang Van (1973) introduces a mesoscopic approach using the elastic shakedown principle and the Schmid's law to provide a non initiation criterion. It assumes that crack initiation occurs if a grain is not able to adapt elastically in all the crystal orientation possible. Assuming that the surrounding of the grain has an elastic behavior, it is possible to establish relations between the loading at the mesoscopic scale of the grain and the macroscopic loading. In this setting, the Dang Van criterion can be expressed by the following equation:

$$\max_{t \in [0; T], \vec{n}} (\tau(\vec{n}, t) + \alpha \cdot P(t)) \leq \beta \quad (2.44)$$

where  $\tau(\vec{n}, t)$  is the instantaneous amplitude of the shear stress on the plane defined by the normal  $\vec{n}$  and  $P(t)$  the instantaneous hydrostatic component of the stress tensor. Using torsion and bending test, the parameters can be defined as  $\alpha = 3 \left( \frac{\tau_{-1}}{f_{-1}} - \frac{1}{2} \right)$  and  $\beta = \tau_{-1}$ .

Later, Dang Van (1989) simplified the double maximization and proposed the following expression:

$$\max_{t \in [0; T]} (\tau_C(t) + \alpha \cdot P(t)) \leq \beta \quad \text{where} \quad \tau_C(t) = \max_{\vec{n}} \|\vec{\tau}(\vec{n}, t)\| \quad (2.45)$$

Papadopoulos (1997) showed that this criterion does not give good agreement with out-of-phase bending and torsion experimental result. In the case of soft metals ( $0.5 \leq \tau_{-1}/f_{-1} \leq 0.577$ ), he proposed to change the amplitude of shear stress by the generalised shear stress amplitude  $T_{ra}(\varphi, \theta)$ .

$$\max_{(\varphi, \theta)} [T_{ra}(\varphi, \theta)] + \alpha \cdot P_{max} \leq \beta \quad (2.46)$$

where the generalised shear stress amplitude is given by :

$$T_{ra}(\varphi, \theta) = \left( \int_0^{2\pi} \frac{1}{\pi} \tau_a^2(\varphi, \theta, \psi) d\psi \right)^{1/2} \quad (2.47)$$

where  $\tau_a(\varphi, \theta, \psi)$  is the amplitude of the projection of the tangential stress vector on the plane given by the angles  $\varphi$  and  $\theta$ , on the affine line oriented thanks to the angle  $\psi$ . The setting parameters of this criterion are the same as in the previous one.

The main difference among the many multiaxial fatigue endurance criteria proposed in the literature concerns the definition of the equivalent shear stress amplitude,  $\tau_a$ . Indeed, for complex paths, a number of different amplitudes may be defined for a same critical plane (FIG.2.32).

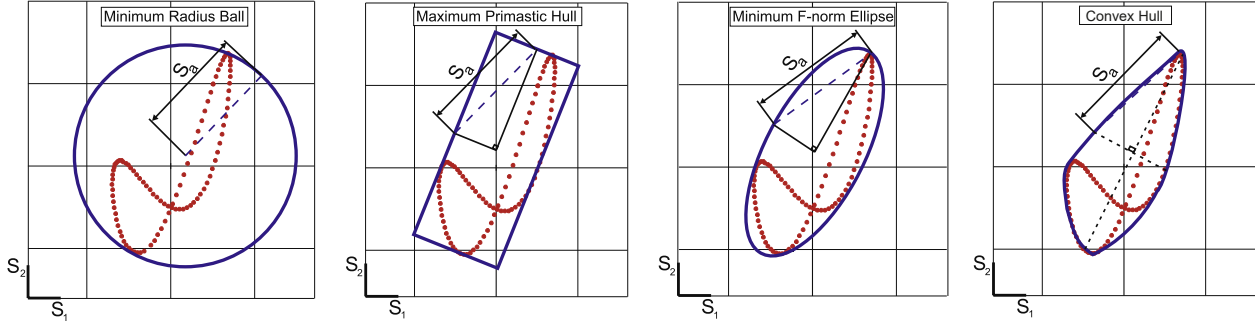


Figure 2.32: Definitions for the shear stress amplitude (Castro et al. 2009b)

Li et al. (2007) considered the minimum ellipsoid enclosing the deviatoric stress path as a measure of the shear stress amplitude. Nevertheless their procedure to compute the minimum ellipse may fail for some paths (e.g. rectangular paths).

Mamiya and Araújo (2002) proposed a definition of the minimum ellipsoid based upon its Frobenius norm. For elliptical paths, it was shown that this norm can be easily computed from the axes of any arbitrarily oriented rectangular hull. From this observation Mamiya et al. (2009) proposed to measure the shear stress vector path  $\Psi$  in a material plane  $\Delta$  with the Maximum Rectangular Hull (MRH) enclosing the deviatoric stress history. The halves of the sides of a rectangular hull with orientation

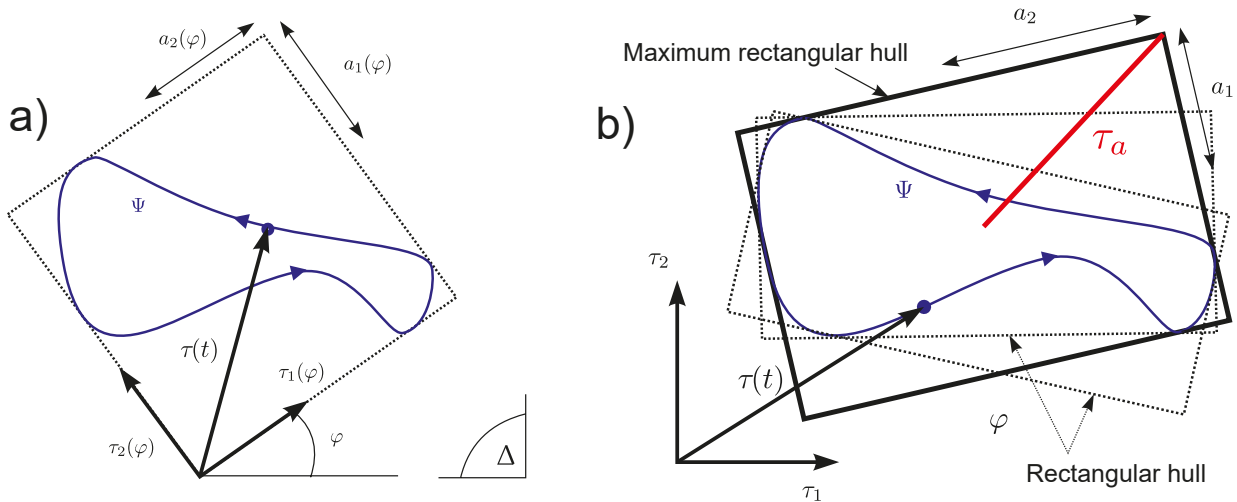


Figure 2.33: a) Half sides  $a_1(\varphi)$  and  $a_2(\varphi)$  of a rectangular hull with orientation  $\varphi$  bounding the shear stress path  $\Psi$  in a material plane and (b) the Maximum Rectangular Hull (MRH) for  $\Psi$ .

$\varphi$  (with respect to  $\tau_i$ ) bounding the shear stress path  $\Psi$ , can be defined as follows (FIG.2.33a):

$$a_i(\varphi) = \frac{1}{2} \left[ \max_t \tau_i(\varphi, t) - \min_t \tau_i(\varphi, t) \right] \quad i = 1, 2 \quad (2.48)$$

For each  $\varphi$ -oriented rectangular hull one can define its amplitude as

$$\tau_a(\varphi) = \sqrt{a_1^2(\varphi) + a_2^2(\varphi)} \quad (2.49)$$

Then, the equivalent shear stress amplitude is the one which maximizes Eq.2.49, as is illustrated in FIG.2.33b:

$$\tau_a = \max_{\varphi} \sqrt{a_1^2(\varphi) + a_2^2(\varphi)} \quad (2.50)$$

Carpinteri and Spagnoli (2001) proposed to correlate the critical plane orientation with the averaged principal stress directions deduced through the weight function method and formulated the following criterion:

$$\left(\frac{N_{max}}{\sigma_{-1}}\right)^2 + \left(\frac{C_a}{\tau_{-1}}\right)^2 < 1 \quad (2.51)$$

where  $\sigma_{-1}$  and  $\tau_{-1}$  are respectively the normal and shear stress fatigue limits for fully reversed bending and torsion,  $N_{max}$  is the quadratic combination of the maximum normal stress and  $C_a$  the shear stress amplitude acting on the critical plane.

Susmel and Lazzarin (2001) presented a fatigue damage parameter based on the theory of cyclic deformation in single crystals and proposed to estimate fatigue life by means of a modified Wöhler curve. Accuracy of the method was checked on 450 experimental data taken from the literature. This modified Wöhler curve method (MWCM) can be formalized as follows:

$$\tau_a(\phi^c, \theta^c) + \kappa \frac{\sigma_{n,max}}{\tau_a}(\phi^c, \theta^c) \leq \lambda \quad (2.52)$$

where  $\tau_a(\phi^c, \theta^c)$  is the equivalent shear stress amplitude in the critical plane  $(\phi^c, \theta^c)$ ,  $\sigma_{n,max}$  is the maximum stress perpendicular to this plane, and the parameters  $\kappa$  and  $\lambda$  are material constants that can be obtained from two fatigue strengths generated under different loading conditions (Susmel et al. 2005).

$$\kappa = \frac{\sigma_{-1} - \sigma_0/2}{2} \quad \lambda = \sigma_{-1} - \frac{\sigma_0}{4} \quad (2.53)$$

$$\kappa = \tau_{-1} - \frac{\sigma_{-1}}{2} \quad \lambda = \tau_{-1} \quad (2.54)$$

where  $\sigma_{-1}$  and  $\sigma_0$  are respectively the uniaxial fatigue limits under fully-reversed and under repeated load and  $\tau_{-1}$  the torsional fully-reversed plain fatigue limits. Note that expressions are different from the ones presented by Araújo et al. (2007) because of the different definition of the fatigue limit.

Araújo et al. (2011) used the MWCM with the MRH to determine the amplitude of the shear stress on experimental data involving proportional and nonproportional stress paths. It states that when, on certain planes, the shear stress amplitudes are similar, the crack prefers to nucleate and grow in the plane, where  $\sigma_{n,max}$  is the highest. The following procedure for identification of the critical plane was proposed:

1. Find the maximum equivalent shear stress amplitude (FIG.2.33b:) among all material planes:

$$\tau_a^{\max} = \max_{\phi, \theta} [\tau_a(\phi, \theta)] \quad (2.55)$$

2. Select the candidate planes within a tolerance:

$$(\phi^*, \theta^*) \in (\phi, \theta) \quad / \quad \tau_a^{\max} - tol \leq \tau_a(\phi, \theta) \leq \tau_a^{\max} \quad (2.56)$$

3. Identify the critical plane among the candidate planes as the one where the maximum normal stress is maximized:

$$(\phi^c, \theta^c) = \max_{\phi^*, \theta^*} [\sigma_{n,max}(\phi^*, \theta^*)] \quad (2.57)$$

Used locally on the contact surface, the critical plane approach has shown a reasonably good prediction of the crack initiation risk (Nowell 1988). However, the local approach fails to predict the life of the fretting fatigue sample. This is explained by the severity of the stress gradient due to the localized stress concentration at the contact. To overcome this difficulty, averaging of the parameters over a critical volume might be considered.

### 2.3.5 Gradient effect - Local vs Non local approach

Until now, plain specimens with uniform loading were implicitly considered, but structural components generally present stress concentrations promoting crack initiation. From the beginning, notched specimens were considered to study the effect of stress concentration. The effect of notches having a finite tip radius on the linear-elastic stress field distribution is usually quantified through the stress concentration factor,  $K_t$ . The S-N curve of FIG.2.34, adapted from the results of MacGregor and Grossman (1952), presents the fatigue test data for an unnotched bar ( $K_t = 1$ ) and for a notched specimen with  $K_t = 3.1$ . The blue plain line represents estimated data for the corresponding notched geometry. Notice that the experimental results are above this prediction.

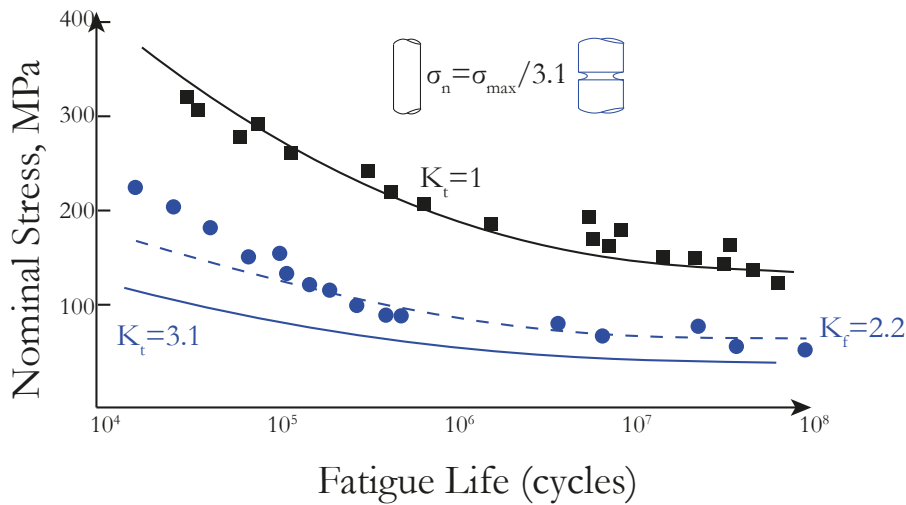


Figure 2.34: Notch effect. Figure adapted from result MacGregor and Grossman (1952).

Different formulas were proposed to define  $K_f$ , the fatigue strength reduction factor (Peterson 1959), which would better predict the detrimental effect of the notch (FIG.2.35 from Frost and Dugdale (1957)). In particular, Neuber (Neuber 1936, 1958) suggested estimating  $K_f$  by using the following well known relationship:

$$K_f = 1 + \frac{K_t - 1}{1 + \sqrt{\frac{a_N}{r_n}}} \quad (2.58)$$

where  $a_N$  is a constant depending on the ultimate tensile strength and  $r_n$  is the root radius of the notch contained in the component to be assessed. The concept of critical distance or process zone for notch fatigue was born.

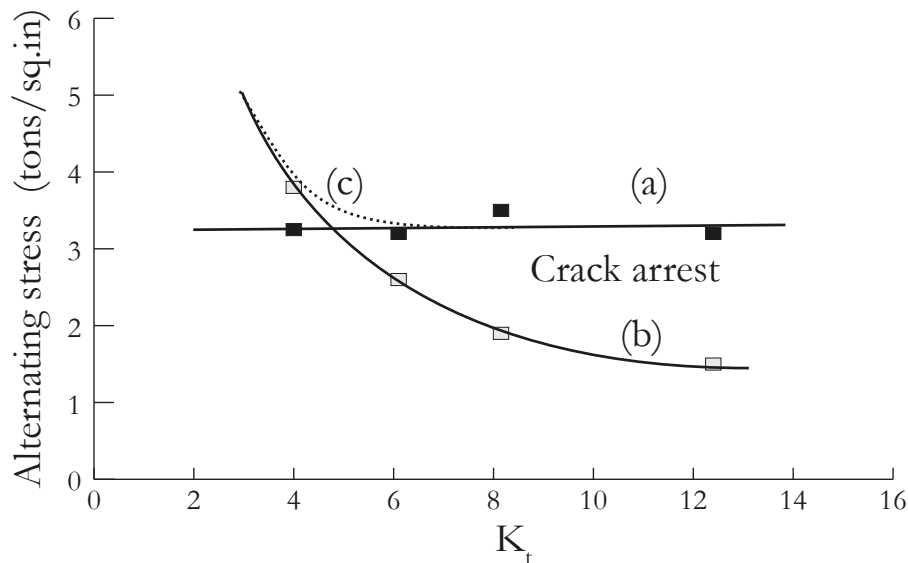


Figure 2.35: Fatigue strength and  $K_t$  for zeros mean load. a) Stress to propagate crack b) Stress to initiate crack c) nominal fatigue limit based on broken specimens (Frost and Dugdale 1957).

Later Tanaka (1983) showed that similar theory could be applied to sharp crack, and in this case, the length of the line over which stresses must be averaged could be calculated to be twice the material constant  $a_0$ , proposed by El Haddad et al. (1980). Taylor (1999) demonstrated that this value could also be used to predict the behavior of notches and short cracks. This theory, using linear fracture mechanic quantity, will be described in more detail in SEC.2.4.9.

In order to account for the high-stress gradients, non-local approach is necessary to predict the fatigue life in fretting fatigue.

Fouvry et al. (2003) have shown that averaging the Dang Van's mesoscopic parameter over a dimension of  $6\mu m$  allows to compare the fretting results of an low alloy steel spherical/plane contact with parameters from plain fatigue. But here, the optimum dimension was calibrated so that the prediction agrees for a set of tests. Nothing proved that the same method would work for a different contact geometry, a different loading (and loading ratio) or even contact size.

A better solution would be to have a dimensional parameter only dependent of the material considered. Taylor's critical distance, based only on linear fracture mechanic quantity and fatigue properties may offer this solution.

### 2.3.6 Scale effect - Probabilistic approach

It is admitted that scale effects are related to the probability of initiating a fatigue crack at a privileged location. When the volume of material increases, the probability of encountering a site favoring initiation also increases. The classical probabilist approach uses the Weibull model (Weibull 1951). It establishes a relationship between the probability of failure and the maximum principal stress. It uses

the hypothesis of the weakest link (Freudenthal 1968) assumes that the breaking of the weakest link leads the global failure.

The scale effect affects the fretting fatigue because of its role in the initiation of cracks. However, if the small cracks can stop to propagate because of a strong stress gradient, the hypothesis of the weakest link is no longer valid to describe entirely the life of the fretting fatigue test.

## 2.4 Fracture mechanics.

### 2.4.1 Introduction.

Historically, the mechanics of fracture became an engineering discipline after the famous story of the Liberty ships during the World War II. The Liberty ships had an all-welded hull, as opposed to the riveted construction of traditional ship designs. After a ship broke completely in 1946, inspection revealed that more than 400 of the 2700 Liberty ship built presented serious cracks. Fracture mechanics was born as the field of solid mechanics that deals with the mechanical behaviour of cracked bodies. The first major step in the direction of quantification of the effects of cracks as defects was taken by Inglis (1913). He published a stress analysis for an elliptical hole in an infinite linear elastic plate loaded at its outer boundaries.

Griffith (1921), who was carrying out tests on cracked glass spheres, showed that a simple elastic analysis could be applied to describe the propagation of different size cracks at different stress levels. He transformed the Inglis analysis by calculating the effect of the crack on the strain energy stored in an infinite cracked plate. He also proposed that this energy, which is a finite quantity, should be taken as a measure of the tendency of the crack to propagate.

But the birth of the modern fracture mechanics is often credited as beginning with George Irwin, sometimes named the “father of fracture mechanics” and his paper in the *Journal of Applied Mechanics* (Irwin 1957). There, he presented the idea of the equivalence of a crack-tip stress field parameter with an energy release parameter, and the idea that the crack-tip stress field parameters give the best approach for characterizing fracture behavior.

### 2.4.2 Fracture modes

Depending on the forces applied on a cracked plate, the crack can propagate in different ways. Irwin (1958) proposed a classification corresponding to three situations, or fracture modes, represented in FIG.2.36. Mode I is mainly connected to the traction states, whereas modes II and III correspond to the loading conditions of shearing type. In a more general situation, typically a mixed mode situation can be observed, where there is a superposition of the modes. In a linear elastic mixed mode

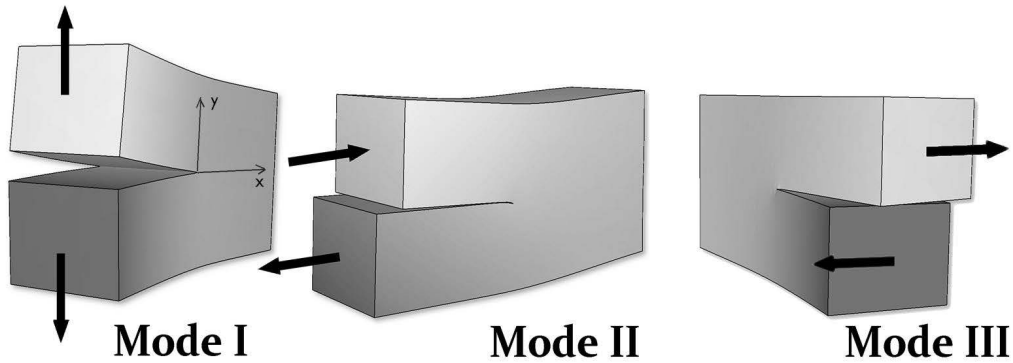
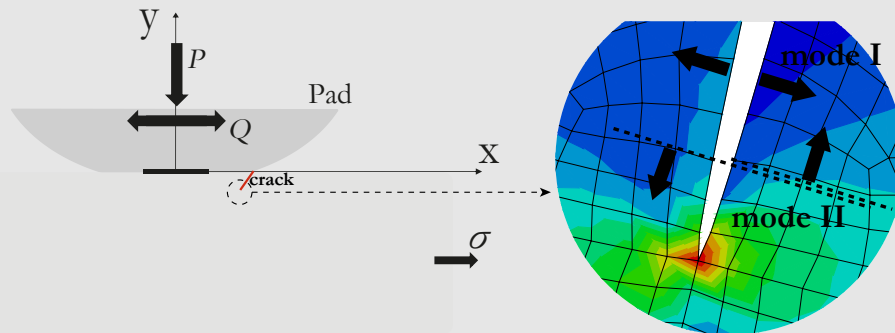


Figure 2.36: Fracture modes.

problem, the principle of stress superposition states that the individual contributions to a given stress component are additive, and can be written as:

$$\sigma_{ij} = \sigma_{ij}^I + \sigma_{ij}^{II} + \sigma_{ij}^{III} \quad (2.59)$$

In the cylinder/plane fretting fatigue configuration used in this study, a crack propagating is subjected to a combination of mode I and mode II.



### 2.4.3 Asymptotic solution

Kirsch (1898) has been one of the first to analyze elasticity based solutions for crack problems. He described the elastic stresses around a circular hole of radius  $a$  in an infinite plate under the unidirectional stress  $\sigma$ . Inglis (1913) also worked on a solution for an elliptical hole in a uniformly stressed plate adopting a curvilinear coordinate system.

Focusing on the case of mode I, Irwin (1957) analyses the problem of a crack in an infinite media. The problem is illustrated in FIG.2.37. It's a 2D problem, with symmetry with the axes  $x$  and  $y$ . Far

from the crack, the load is equibiaxial ( $\sigma_{xx} = \sigma_{yy} = S$  and  $\sigma_{xy} = 0$ ), and stress presents a singularity at the tips of the crack at  $(+a, 0)$  and  $(-a, 0)$ .

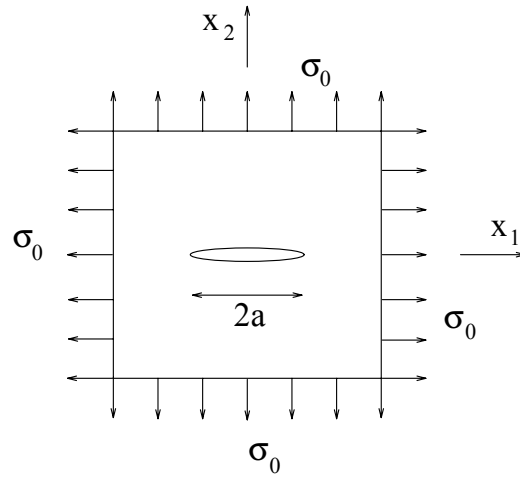


Figure 2.37: Crack in an infinite plate.

Before that, Westergaard (1939) proposed an exact solution using the Airy function.  $Z(z)$  is the assumed solution of the problem and the Airy function  $F$ , is written as:

$$F = \text{Re}\phi(Z) + y\text{Im}\phi'(Z) \quad (2.60)$$

And the stresses are expressed as:

$$\sigma_{xx} = \frac{\partial^2 F}{\partial x^2} ; \quad \sigma_{yy} = \frac{\partial^2 F}{\partial x^2} ; \quad \tau_{xy} = -\frac{\partial^2 F}{\partial x \partial xy} \quad (2.61)$$

Which leads to:

$$\begin{aligned} \sigma_{xx} &= \text{Re} \left( \frac{\partial^2 Z}{\partial z^2} \right) - y \text{Im} \left( \frac{\partial^3 Z}{\partial z^3} \right) \\ \sigma_{yy} &= \text{Re} \left( \frac{\partial^2 Z}{\partial z^2} \right) + y \text{Im} \left( \frac{\partial^3 Z}{\partial z^3} \right) \\ \sigma_{xy} &= -\text{Re} \left( \frac{\partial^3 Z}{\partial z^3} \right) \end{aligned} \quad (2.62)$$

While the singularity at the crack tips suppose that the expressions  $\frac{1}{z+a}$  and  $\frac{1}{z-a}$  are part of the solution. And the symmetry and far boundary condition lead to the expressions:

$$Z^\infty = \frac{S}{2} z^2 + \text{constant} \quad ; \quad \frac{\partial Z^\infty}{\partial z} = Sz \quad (2.63)$$

The exact solution found by Westergard is then:

$$\frac{\partial Z^\infty}{\partial z} = S(z^2 - a^2)^{1/2} \quad (2.64)$$

Irwin (1957) used this exact solution, and by expressing it in local coordinate ( $z = a + re^{i\theta}$ ) gave the the first order of the asymptotic expansion:

$$\begin{aligned}\sigma_{xx}(r, \theta) &= \frac{S\sqrt{\pi a}}{\sqrt{2\pi r}} \cos \frac{\theta}{2} \left( 1 - \sin \frac{\theta}{2} \sin \frac{3\theta}{2} \right) \\ \sigma_{yy}(r, \theta) &= \frac{S\sqrt{\pi a}}{\sqrt{2\pi r}} \cos \frac{\theta}{2} \left( 1 + \sin \frac{\theta}{2} \sin \frac{3\theta}{2} \right) \\ \sigma_{xy}(r, \theta) &= \frac{S\sqrt{\pi a}}{\sqrt{2\pi r}} \left( \cos \frac{\theta}{2} \sin \frac{\theta}{2} \cos \frac{3\theta}{2} \right)\end{aligned}\quad (2.65)$$

where  $r$  and  $\theta$  are still the polar coordinates centred at the crack tip (FIG.2.38).

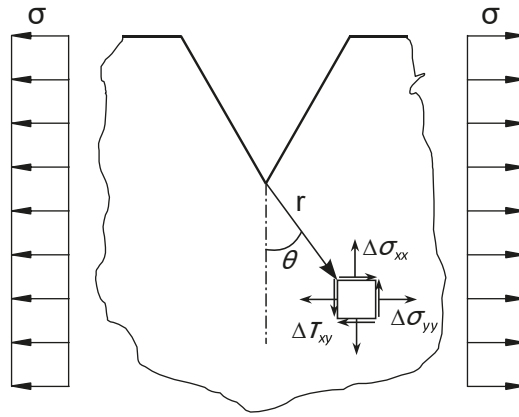


Figure 2.38: Stress components at a material point positioned at  $r, \theta$  from the crack like notch root.

Still in mode I, the non equibiaxial case may be reproduced by superimposing a pressure in the  $x$  direction equal to  $T = S_{xx} - S_{yy}$  and formulation for the stress field around a crack tip in a plate subjected to far-field shear stresses or antiplane shear stresses can as well be found.

Williams (1957) used a different approach. Starting from the equation of compatibility, he directly looked for a self similar solution:

$$F(r, \theta) = r^{\lambda+2}g(\theta) \quad (2.66)$$

and found that  $g(\theta)$  needed to be in the form of  $Ae^{ip\theta}$ . After applying the boundary conditions on the crack faces he found that

$$F(r, \theta) = r^{n/2+1}g(\theta) \quad \text{with } n \text{ a integer} \quad (2.67)$$

Irwin (1957) introduced the concept of Stress Intensity Factor (SIF) defined as:

$$\left\{ \begin{array}{c} K_I \\ K_{II} \\ K_{III} \end{array} \right\} = \lim_{r \rightarrow 0} \sqrt{2\pi r} \left\{ \begin{array}{c} \sigma_{yy}(r, 0) \\ \tau_{yx}(r, 0) \\ \tau_{yz}(r, 0) \end{array} \right\} \quad (2.68)$$

where  $\sigma$  are the near crack tip stresses, and  $K_i$  are associated with the three independent kinematic movements defined in the previous subsection.

The strain energy release rate,  $G$ , is the energy dissipated during fracture due to the formation of new surfaces and other dissipative processes such as plasticity. In other words, it is the energy that must

be supplied to a crack tip for it to grow . This energy may be related to the stress intensity factors. In plane strain, the relationship is:

$$U = K_I^2 \left( \frac{1 - \nu^2}{E} \right) + K_{II}^2 \left( \frac{1 - \nu^2}{E} \right) + K_{III}^2 \left( \frac{1}{2\mu} \right) \quad (2.69)$$

#### 2.4.4 J-integral

The J-integral was introduced by Eshelby (1956) and Rice (1968) who noticed the importance of this quantity for the analysis of the mechanical fields near crack tips. Path independence of J-integral allows for evaluation of the energy release rate.

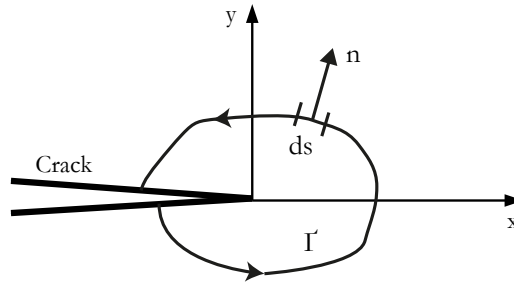


Figure 2.39: J-integral around the crack tip.

For a crack in the plane  $(x, y)$ , the J-integral can be written as :

$$J = \oint_{\Gamma} \left( W n_x - T_i \frac{\partial u_i}{\partial x} \right) ds \quad (2.70)$$

Where  $\Gamma$  is a closed counter-clockwise contour,  $ds$  is the differential element of the arc along the path  $\Gamma$ ,  $u$  is the displacement vector,  $T_i = \sigma_{ij} n_j$  is the traction vector on a plane defined by the outward normal vector  $\vec{n}$  and  $W$  is the strain energy density.

$$W = \int_0^{\epsilon} \sigma_{ij} d\epsilon_{ij} \quad (2.71)$$

in which  $\epsilon_{ij}$  is the strain tensor. Therefore J-integral can be rewritten as:

$$J = \int_0^{\epsilon} \sigma_{ij} d\epsilon_{ij} - \oint_{\Gamma} \left( (\sigma_x n_x + \sigma_{xy} n_y) \frac{\partial u_x}{\partial x} + (\sigma_y n_y + \sigma_{xy} n_x) \frac{\partial u_y}{\partial x} \right) ds \quad (2.72)$$

The J-integral is a way to calculate the strain energy release rate. Then, it is also a great tool to the computation of the stress intensity factor at the crack tip without considering the divergent stress field, but the finite strain and stress along a contour in the neighboring of the tip. This method is used to compute the stress intensity factor in most common finite element software.

### 2.4.5 Method of distribution of dislocations.

The stress intensity factor at the crack tip might also be obtained by the method of distribution of dislocations, which is described in detail by Hills and Nowell (1993). A rapid description of the method will be presented here.

The technique is based on the principle developed by Bueckner (1958), which is basically a superposition principle. Let suppose a body with a crack subjected to a contact loads as shown in Fig.2.40. Equivalence of the original problem can be obtained by superposition of (a) and (b) where (a) represents the body without the crack subjected to contact loads and (b) represents a cracked body in the absence of external loads but stress on the crack faces has inversely equal to the stress obtained on the line of (a), so that when adding the two problems, the crack surfaces are free of stresses.

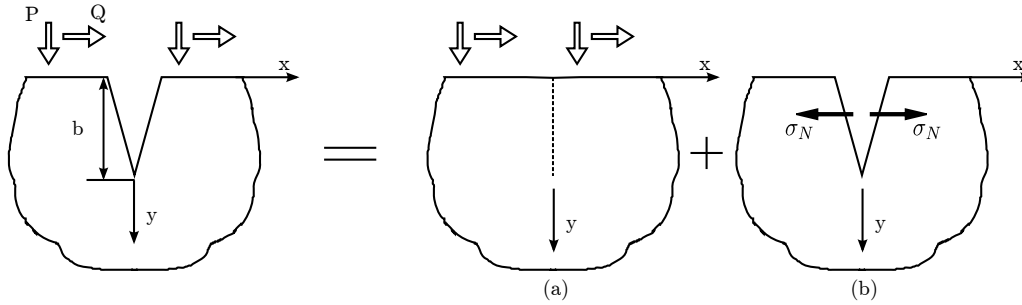


Figure 2.40: Schematic illustration of the Bueckner principe.

Let's assume that stress along the imaginary crack path are known. Dislocation distribution is applied on the face of the unloaded crack in order to generate stress on its faces. The first step consist to determine the stress  $\sigma_N$  induced by the shift of a point initially in  $(0, y)$  to the position  $(0, e)$  by a vector  $b_x$  (Burgers vector). A solution of the problem was proposed by Dundurs and Sendecyj (1965):

$$\sigma_N = \frac{2\rho b_x}{\pi(k+1)} G(y, e) \quad (2.73)$$

where  $\rho$  is the material stiffness,  $k = 3 - 4\nu$  in plane strain condition and the Kernel  $G(y, e)$  is defined by :

$$G(y, e) = \frac{1}{y-e} - \frac{1}{y+e} - \frac{2e}{(y+e)^2} + \frac{4e^2}{(y+e)^3} \quad (2.74)$$

A continue distribution of displacement  $B_x(e)$  is now considered along the crack. The free stress condition at the the crack faces leads to:

$$\sigma_{xx} + \frac{2\rho}{\pi(k+1)} \int_0^b B_x(e) G(y, e) de = 0 \quad \text{where} \quad B_x(e) = \frac{\partial b_x}{\partial e} \quad (2.75)$$

where  $b$  is the crack size and  $\sigma_{xx}$  the normal stress from the external loads. A discretization using a Gaussian quadrature generates a linear algebra system:

$$\begin{aligned} \frac{\rho}{\pi(k+1)} \sum_{i=1}^n \frac{2\pi(1+r_j)}{2n+1} G(s_i, r_j) \phi(r_j) &= -\sigma_{xx}(s_i) \\ r_j &= \cos\left(\frac{2j-1}{2n+1}\pi\right), \quad j = 1, 2, \dots, n \\ s_i &= \cos\left(\frac{2j}{2n+1}\pi\right), \quad j = 1, 2, \dots, n \end{aligned} \quad (2.76)$$

where  $r_j$  and  $s_i$  are respectively the discrete and normalized variables  $y$  and  $e$  and  $\phi$  are the function unknown. This system may be solved numerically and the mode I stress intensity factor is given by:

$$K_I = 2\sqrt{2}\sqrt{\pi b} \frac{\rho}{k+1} \phi(1) \quad (2.77)$$

The values of  $\phi$  obtained by Eq.2.76, are only valid at the integration points  $r_j$ . Krenk (1975) defined  $\phi$  for the rest of the domain by using a polynomial formulation:

$$\phi(1) = \frac{2}{2n+1} \sum_{j=1}^n \cot\left(\frac{2j-1}{2n+1} \frac{\pi}{2}\right) \sin\left(\frac{n}{2n+1}(2j-1)\pi\right) \phi(r_j) \quad (2.78)$$

A similar formulation is used to compute the stress intensity factor in mode II.

The method of distribution of dislocations presented here was coded in Python for the mode I and the mode II. This analytic formulation has the advantage to compute the SIF very fast compared to the computation with finite elements. However, it inherits the limitations of the analytical fretting fatigue formulation (SEC.2.1.3). Furthermore, unlike a finite element computation, the method is unable to update the external geometrical deformations that may occur when a long crack is considered (discussed in SEC.3.3.3.ii). Therefore, this method will only be used in the study of short cracks.

#### 2.4.6 Paris Law

Paris et al. (1961) postulated that the range of stress intensity factor might characterise crack growth under fatigue loading. He examined a number of alloys and realised that plots of crack growth rate against a range of stress intensity factor gave straight lines on log-log scales.

$$\frac{da}{dN} = C \Delta K^m \Leftrightarrow \log\left(\frac{da}{dN}\right) = m \log(\Delta K) + \log(C) \quad (2.79)$$

where  $a$  is the crack length,  $N$  is the number of load cycles,  $m$  and  $C$  are material constants, and  $\Delta K$  is the range of the stress intensity factor. This law is only valid in mid-growth rate, also called the Paris regime, as depicted in FIG.2.41.

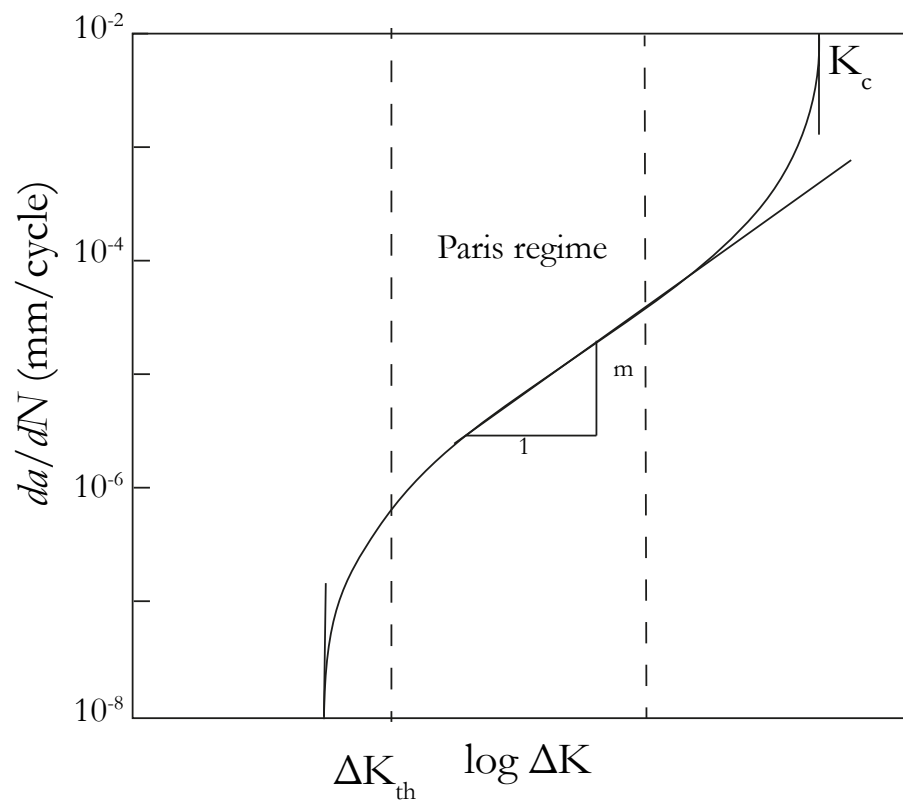
When  $\Delta K$  is below to the threshold stress intensity factor,  $\Delta K_{th}$ , the crack growth rate is so slow that the crack is often assumed to be dormant or growing at an undetectable rate. The growth rate often used to define  $\Delta K_{th}$  is  $10^{-10}$  mm/cycle. When the load exceeds the fracture toughness, the growth rate becomes unstable and can lead to sudden failure.

#### 2.4.7 The Kitagawa–Takahashi (K–T) diagram

Kitagawa and Takahashi (1976) noted that many materials exhibit a long crack threshold  $\Delta K_0$  independent of crack length. For short cracks, however, they observed that cracks may propagate at  $\Delta K < \Delta K_0$ . This means that the tensile stress range experienced by the crack,  $\Delta\sigma$ , is greater than the fatigue limit for the material,  $\sigma_{fl}$ .

For the majority of the metals, the transition between short and long crack behavior is not sharp. El Haddad et al. (1979) introduced the intrinsic crack length,  $b_0$ , defined as:

$$b_0 = \frac{1}{\pi} \left( \frac{\Delta K_{th}}{Y \Delta \sigma_{fl}} \right)^2 \quad (2.80)$$

Figure 2.41: Schematic  $da/dN - \log \Delta K$  Paris curve.

Although,  $b_0$  might be considered to be a material constant, it does not correspond to any physical dimension within the material and depends on the loading ratio and the crack geometry ( $Y$  is the correction factor depending on crack shape). In the short crack regime, the smooth transition of the threshold is described by:

$$\sigma_{th} = \frac{\Delta K_{th}}{F \sqrt{\pi(b + b_0)}} \quad (2.81)$$

Another description was proposed by Murakami and Endo (1994), the  $\sqrt{area}$  parameter.

The K-T diagram, which shows the variation of the crack growth threshold with crack size, may be plotted in two forms: (i)  $\Delta K$  against crack length  $b$ , or (ii)  $\Delta \sigma$  against  $b$  (FIG.2.42). In the first plot, the curve 1 illustrates a crack propagating while the curve 2 illustrates a short crack arrest.

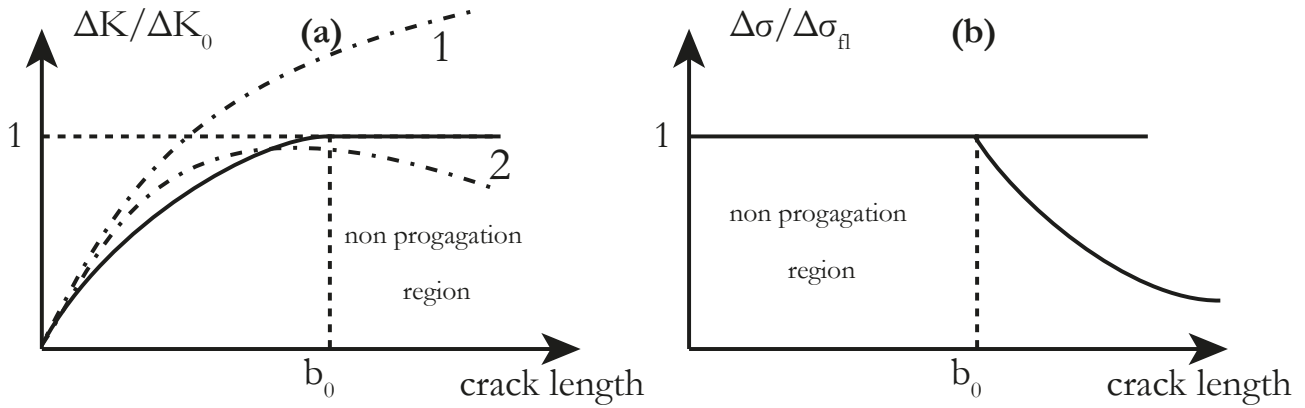


Figure 2.42: Schematic K-T diagrams showing the threshold for crack propagation: (a) in terms of  $\Delta K$ ; (b) in terms of  $\Delta \sigma$  (Araújo and Nowell 1999).

#### 2.4.8 Crack closure or effect of the loading ratio.

At a given applied cyclic stress intensity,  $\Delta K$ , an increase in load ratio results in an increase of the crack growth rate. In other words, the observed threshold stress-intensity range for fatigue-crack propagation,  $\Delta K_{th}$ , decreases as the loading ratio is increased. A common conception of this variation is illustrated in FIG.2.43a. Schmidt and Paris (1973) explained this behavior with the crack closure concept. Below a certain load ratio,  $R_c$ , crack closure occurs, and the closure-corrected effective fatigue threshold,  $\Delta K_{eff,th}$  may be defined as:

$$\Delta K_{eff,th} = \begin{cases} K_{max,th} - K_{cl} < \Delta K_{th} & \text{if } R < R_c(K_{min,th}) < K_{cl} \\ K_{max,th} - K_{min,th} = \Delta K_{th} & \text{if } R > R_c(K_{min,th}) > K_{cl} \end{cases} \quad (2.82)$$

where  $K_{cl}$  is the closure stress intensity factor. However, in some cases, the value of  $\Delta K_{th}$  is not invariant at  $R_\sigma > R_c$  as illustrated in FIG.2.43b.

Boyce and Ritchie (2001) carried out tests on Ti-6Al-4V turbine blade alloy, from a loading ratio  $R_\sigma = 0.1$  to 0.94. The ratio limit  $R_c = 0.5$  for detection of the crack closure was identified. For low loading ratio,  $\Delta K_{eff,th}$  does tend to normalize the results. These curve may be extended for negative loading ratio. Then, for  $R_\sigma = -1$ , extrapolation of those results would give  $\Delta K_{th,R_\sigma=-1} = 7.88 MPa.m^{1/2}$ , while  $\Delta K_{eff,th}$  should remain around the value  $3.6 MPa.m^{1/2}$ .

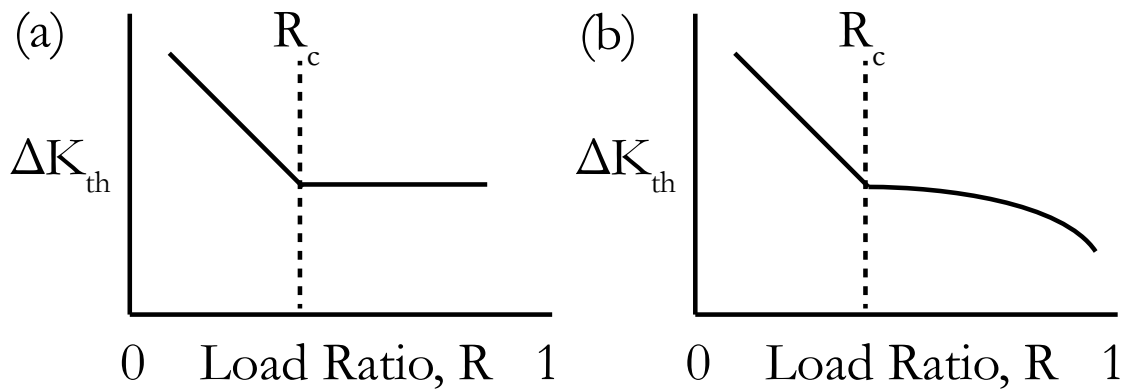


Figure 2.43: (a) Classic representation of the influence of the load ratio,  $R_\sigma$ , on the fatigue threshold,  $\Delta K_{th}$ . (b) Many data sets, however, exhibit decreasing threshold even beyond the transition,  $R_\sigma > R_c$ . (Boyce and Ritchie 2001)

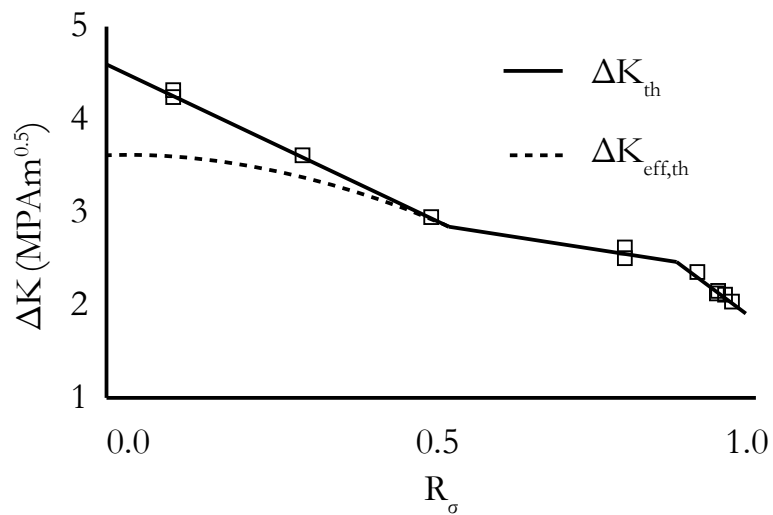


Figure 2.44:  $\Delta K_{th} - R_\sigma$  for Ti-6AL-4V (Boyce and Ritchie 2001)

### 2.4.9 Gradient effect - Critical distance.

It is well established that the hot-spot approach provides underestimated predictions of the fatigue limit for geometrical features under high-stress gradients. In order to consider the effect of the stress gradient on the fatigue limit, Neuber (1958) and Peterson (1959) assume that the effective stress which is expected to govern at the notched tip should be an average of the stress distribution around the stress concentration.

This idea was then generalized for any geometric feature presenting high stress concentration (e.g. cracks, fretting fatigue) and presented as the theory of critical distances (TCD) (Taylor 1999).

Under a general framework, which is denominated as the volume method, the TCD assumes that fatigue endurance occurs when:

$$\frac{1}{V} \int_V F(\sigma) dV \leq c \quad (2.83)$$

where  $\sigma$  is the elastic Cauchy's stress tensor at an arbitrary point within a volume of material  $V$  around the stress raiser, while  $F(\cdot)$  denotes an effective stress that appropriately characterizes the fatigue loading and  $c$  is a material parameter associated with its fatigue resistance. The TCD can be expressed in simplified versions by substituting the material volume in Eq. 2.83 by an area, a line or a point. Which leads respectively to the following expression:

$$\frac{4}{\pi l_{AM}^2} \int_0^{\pi/2} \int_0^{l_{AM}} F(\sigma) r dr d\theta \leq c \quad (2.84)$$

$$\frac{1}{l_{LM}} \int_0^{l_{LM}} F(\sigma) dl \leq c \quad (2.85)$$

$$F(\sigma, l_{PM}) \leq c \quad (2.86)$$

Considering the elastic stresses ahead of a crack under mode I loading (FIG.2.38) given by the EQ.2.65, the maximum principal stress range  $\Delta\sigma_1$  at a distance  $r$  on the bisector line ( $\theta = 0$ ), is:

$$\Delta\sigma_1(r, 0) = \Delta\sigma_{yy}(r, 0) = \frac{\Delta K_I}{\sqrt{2\pi r}} \quad (2.87)$$

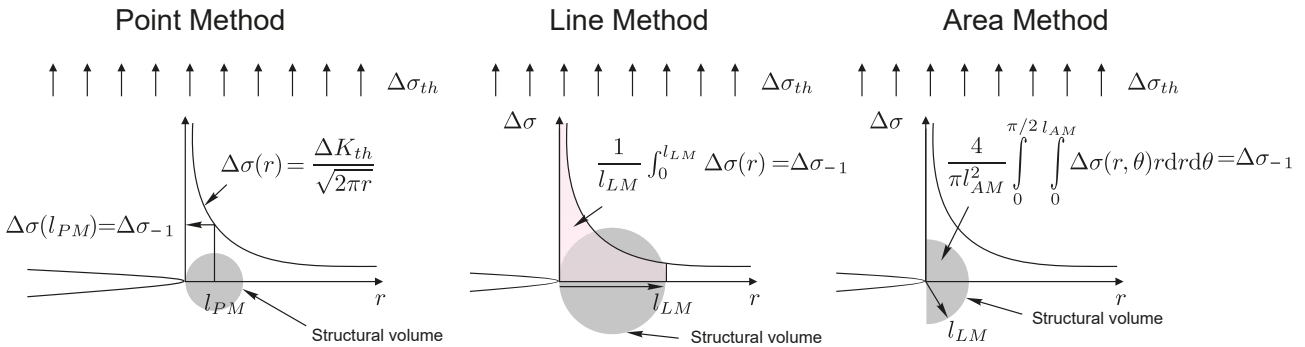


Figure 2.45: Schematic formalization of different methods.

Taylor proposed that the endurance occurs if the range of the maximum principal stress at the critical distance (in term of point method) is inferior to a material fatigue resistance parameter. Then, from

$$\Delta\sigma_1(l_{PM}) = \frac{\Delta K_I}{\sqrt{2\pi l_{PM}}} \quad (2.88)$$

the critical distance (PM) can be written:

$$l_{PM} = \frac{1}{2\pi} \left( \frac{\Delta K_I}{c} \right)^2 \quad (2.89)$$

In the case of the line method the maximum principal stress range  $\Delta\sigma_1$  is average along a line. From:

$$\frac{1}{l_{LM}} \int_0^{l_{LM}} \Delta\sigma_{yy}(r,0)dr = \frac{1}{l_{LM}} \int_0^{l_{LM}} \frac{\Delta K_I}{\sqrt{2\pi r}} dr = \frac{\Delta K_I \sqrt{2}}{l_{LM} \sqrt{\pi}} \quad (2.90)$$

the critical distance (LM) can be written:

$$l_{LM} = \frac{2}{\pi} \left( \frac{\Delta K_I}{c} \right)^2 \quad (2.91)$$

It is important to notice that EQ.2.89-2.91 establish a relation among a critical distance ( $l_{PM}$  or  $l_{LM}$ ), a fracture mechanics ( $\Delta K_I$ ) and a fatigue resistance parameter ( $c$ ). This essentially means that knowing any pair of these three parameters, one can extract the other. Therefore, under threshold conditions one can consider a fracture mechanics test (on a cracked specimen) and a fatigue limit test (on a smooth specimen) to determine the critical distances:

$$l_{PM} = \frac{1}{2\pi} \left( \frac{\Delta K_{th}}{\Delta\sigma_{-1}} \right)^2 \quad (2.92)$$

$$l_{LM} = \frac{2}{\pi} \left( \frac{\Delta K_{th}}{\Delta\sigma_{-1}} \right)^2 \quad (2.93)$$

EQ.2.92-2.93 show that  $l_{LM}$  is four times greater than  $l_{PM}$  although the function which defines the effective stress for the fatigue loading,  $F(\sigma)$ , is the same in both cases (PM and LM).

Araújo et al. (2007) attempted to predict fretting fatigue strength in the high-cycle fatigue regime by using the Modified Wöhler Curve Method and Dang Van's Mesoscopic Model re-interpreted in terms of the Theory of Critical Distances. In particular, the devised procedure took as its starting point the idea that high-cycle fretting fatigue strength can correctly be predicted, provided that two different aspects are simultaneously taken into account: the presence of the stress gradients that govern the size effect phenomenon and the degree of multiaxiality of the stress field damaging the process zone which leads to the initial mixed-mode crack nucleation. In order to assure the above two conditions, the TCD was then used to manage the presence of stress concentration phenomena, whereas the multiaxiality of the stress field was accounted for by using the MWCM and the Mesoscopic model.

It is worth noticing here that one of the main features of the TCD is that it can be used in conjunction with any conventional multiaxial fatigue criterion (Susmel and Taylor 2006). However, care must be exercised, as Castro et al. (2009a) proved that the Critical Distance depends on the multiaxial model under consideration, and not only on material data such as the fatigue limit and threshold stress intensity factor range. Moreover, Meggiolaro et al. (2007) showed from fracture mechanics and short crack models that notch sensitivity (and thus the critical distance) also depends on the notch shape.

#### 2.4.10 T-stress.

As said before, the Williams solution (Williams 1957) describes the stress state at any material point ahead the crack tip for an isotropic elastic material. It can be expressed as:

$$\sigma_{ij}(r, \theta) = A_1 r^{-1/2} f_{ij}^1(\theta) + A_2 f_{ij}^2(\theta) + A_3 r^{1/2} f_{ij}^3(\theta) + \dots \quad (2.94)$$

where  $r$  and  $\theta$  are polar coordinates centred at the crack tip. Functions  $f_{ij}^n$  can be normalised so that  $A_1$  is defined as the stress intensity factor,  $K$ , and  $A_2$  represents a uniform, non-singular stress,  $T$ . At the crack tip and within a region whose size is of the same order of the size of the plastic zone, the third and higher order terms are still negligible but not  $K$  and  $T$ . As a matter of fact, for such small region a two parameter formulation (K-T) has been shown to describe the fracture process better than the K based approach for several cracked geometries (Larsson and Carlsson 1973; Tong 2002).

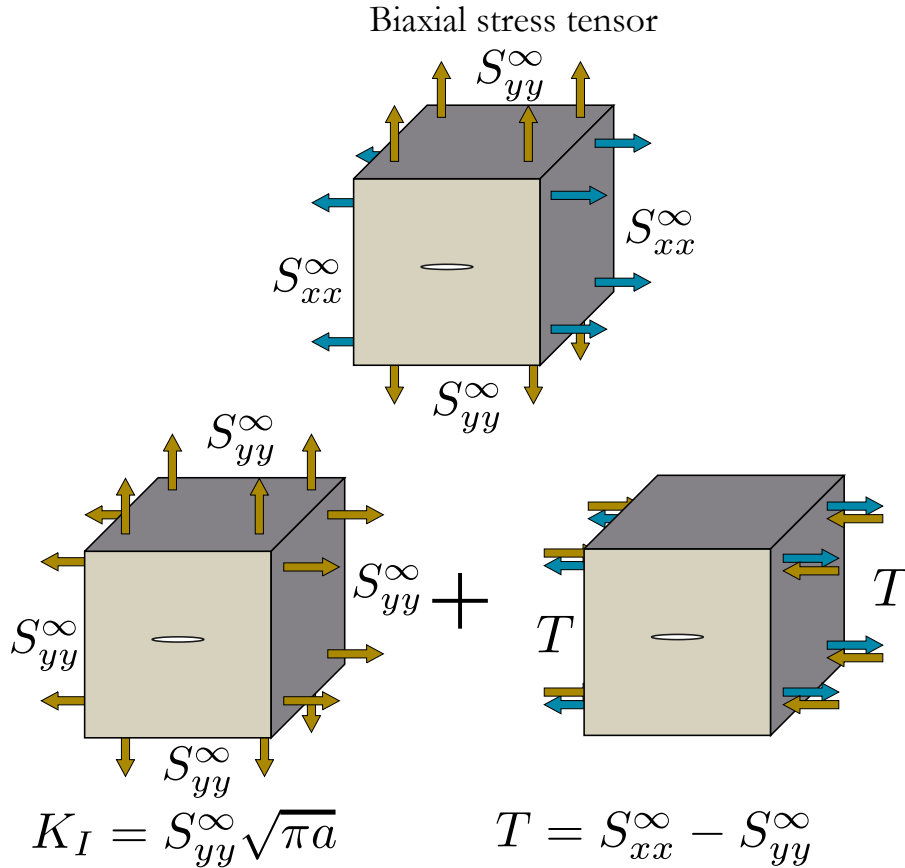


Figure 2.46: Illustration of the significance of the  $T$ -stress components in plane strain.

To clarify the significance of the  $T$ -stresses, let us consider a media subjected to a biaxial stress tensor  $\mathbf{S}^{\infty}$ . Let now consider that a small crack with a length  $2a$  is inserted in that media, lying in the plane normal to  $y$  and with its straight front directed by  $\mathbf{z}$ . In linear elastic conditions, the solution of this problem can be obtained by superposition (Fig.2.46). At the crack tip, the mode I exact solution corresponds to an equibiaxial plane strain loading case. Within a boundary of approximately the size of the plastic zone, the  $T$ -stress component is then superimposed to the mode I plane strain solution to restore the non-equibiaxial remote loading condition.

Expressions of the  $T$ -stresses for various crack geometries and non-uniform loading cases can be found in the literature (Schütte and Molla-Abbasi 2007; Wang and Bell 2004), or can be determined from FE computations using fracture mechanics routines.

The contribution of the  $T$ -stress to the crack tip stress and strain fields is usually neglected because long cracks are considered. However, it becomes non-negligible when short cracks are considered. A new criterion, initially proposed by Thieulot-Laure et al. (2007) and later modified by De Moura Pinho et al. (2012) will be applied to the fretting fatigue problem. This criterion is using linear elastic fracture mechanics quantities and accounts for the  $T$ -stresses, so as to get a dependency of the non-propagation threshold to the crack length and to the stress multiaxiality.

## 2.5 Summary of the literature review.

The simplified Coulomb law is generally used to describe the friction between two bodies in contact. While it has been shown that the friction coefficient varies in the different zone of the mixed-slip regime, a constant coefficient is often considered to allow the use of the Mindlin analytic formulation, of simple finite elements models.

Relative to plain fatigue, fretting fatigue displays a number of important features which must be considered in any analysis of experimental results or design situations (Nowell et al. 2006b):

- Stress gradients are likely to be very high, due to the localized stress concentration at the contact. This can favor the formation and the initial growth, of small cracks, whose subsequent propagation can be accelerated by the presence of external cyclic loading leading to the final breakage by fretting fatigue.
- Loading is likely to be non-proportional in the neighborhood of the contact, even if the external forces are applied in a proportional fashion. This feature is caused by the non-linear nature of the friction at the contact interface.
- Initiated cracks will experience a variable R-ratio as they grow away from the contact.
- Localized surface damage at the asperity level may play a role in accelerating the initiation of cracks at the asperity scale.

The state of the art shows that many different attempts have been already made by different researchers in order to propose sound methodologies suitable for predicting damage due to fretting fatigue. According to the idea that fretting fatigue damage is mainly a multiaxial fatigue problem, many authors have already attempted to use conventional multiaxial fatigue criteria to predict fretting fatigue strength by considering the stress states calculated at the contact point experiencing the maximum stress range. The main limitation in the use of such an idea is that hot-spot stresses alone were seen not to be capable of completely capturing the gradient effect phenomenon.

The theory of the critical distance proposes to overcome the above limitation using elastic stress information in a critical region close to the stress concentration.

The observation of crack arrests in fretting fatigue suggests that the scale effect and probabilist approach of the weakest link is not suitable to predict the failure risk.

Using the Kitagawa–Takahashi diagram, it is possible to predict the short crack arrest with quantities of the linear fracture mechanic. However, it has been showed that the stress intensity threshold varies

with the loading ratio. Therefore, in the fretting fatigue problem, the threshold will vary as the crack grows away from the contact.

## Chapter 3

# Test design and experimental protocol

### 3.1 Introduction

The general objective of the experimental campaign of this study was to quantify the effect of the gradient in fretting fatigue. The contact cylinder/plane will be taken as the study case. In order to vary the stress gradient, two pad radii will be considered.

A secondary goal was to design a fretting fatigue test using a different contact geometry and complex loading. The access to 6 actuators fatigue machine allowed us to envisage the fretting of spherical-ended indenters on a cruciform sample loaded with a multiaxial fatigue load.

In this section, we will present the sample and test machines which will be used in the experimental campaign. As the friction coefficient is an important parameter for the analysis of the contact problem, tests will be carried out to estimate the friction coefficient within the slip zones using two different methodologies. The analytical formulation of the fretting problem was described in the previous chapter. Here, we will present and discuss a finite element model of the cylinder/plane contact and compare the results with the analytic formulation.

### 3.2 Apparatus configuration and preliminary test

#### 3.2.1 Pads and Specimen

**Cylinder/Plane contact:** Pads and specimens were machined from a turbine disk and delivered by Snecma (FIG.3.1). Specimen used in this work have a shape of a dogbone. Two set of pad were machined with radius of  $70mm$  and  $20mm$ . Geometric detail are given in the FIG.3.1. Machined surfaces were observed using a STIL optical measurement station. Profiles were measured following the fatigue loading direction  $x$  and the perpendicular direction  $y$  over a line of  $2mm$ . Software MountainsMap 7.2 was used to estimate the roughness parameters which are presented in FIG.3.2.

**Sphere/Plane contact:** Pads and specimen were machined by the company UTF Meca and geometric detail are given in the FIG.3.3.

Surface observation reveals machining defects of the spherical surface of the pads. First, radius measured were around  $51mm$  and not  $70mm$  as ordered. Moreover, miss machining resulting from the spinning process was observed at the tip of the sphere (FIG.3.4).

Measure of the specimen roughness is detailed in FIG.3.5. Note that both  $R_a$  and  $R_q$  are higher than the roughness measured on the dog-bone specimens machined by Snecma.

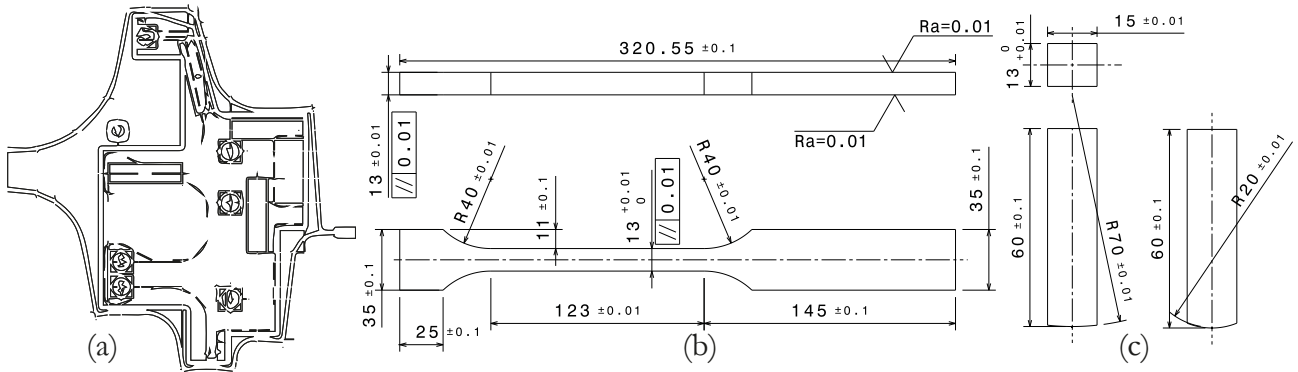


Figure 3.1: (a) Scheme of a disk (b) specimen (c) pads.

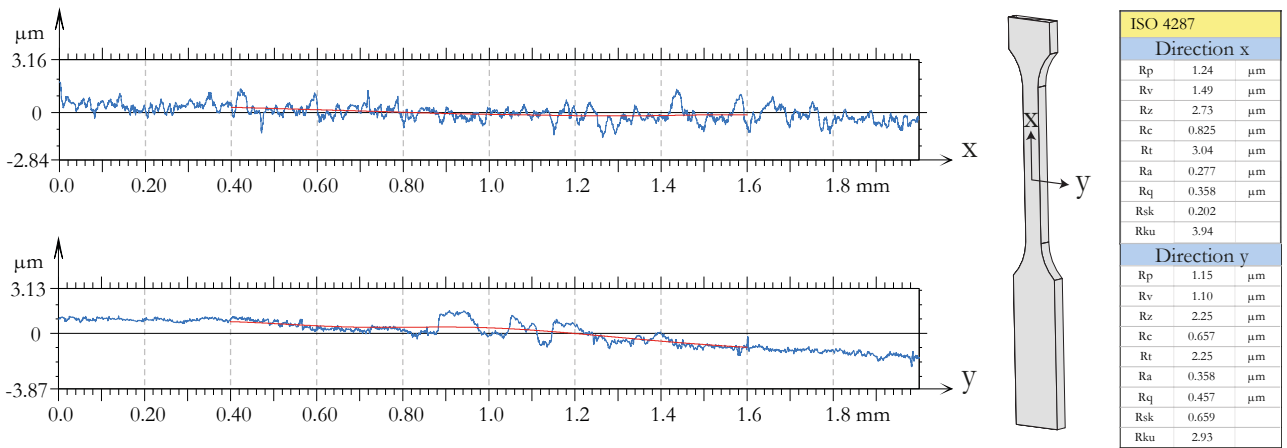


Figure 3.2: Profiles of the specimen surface and roughness parameter.

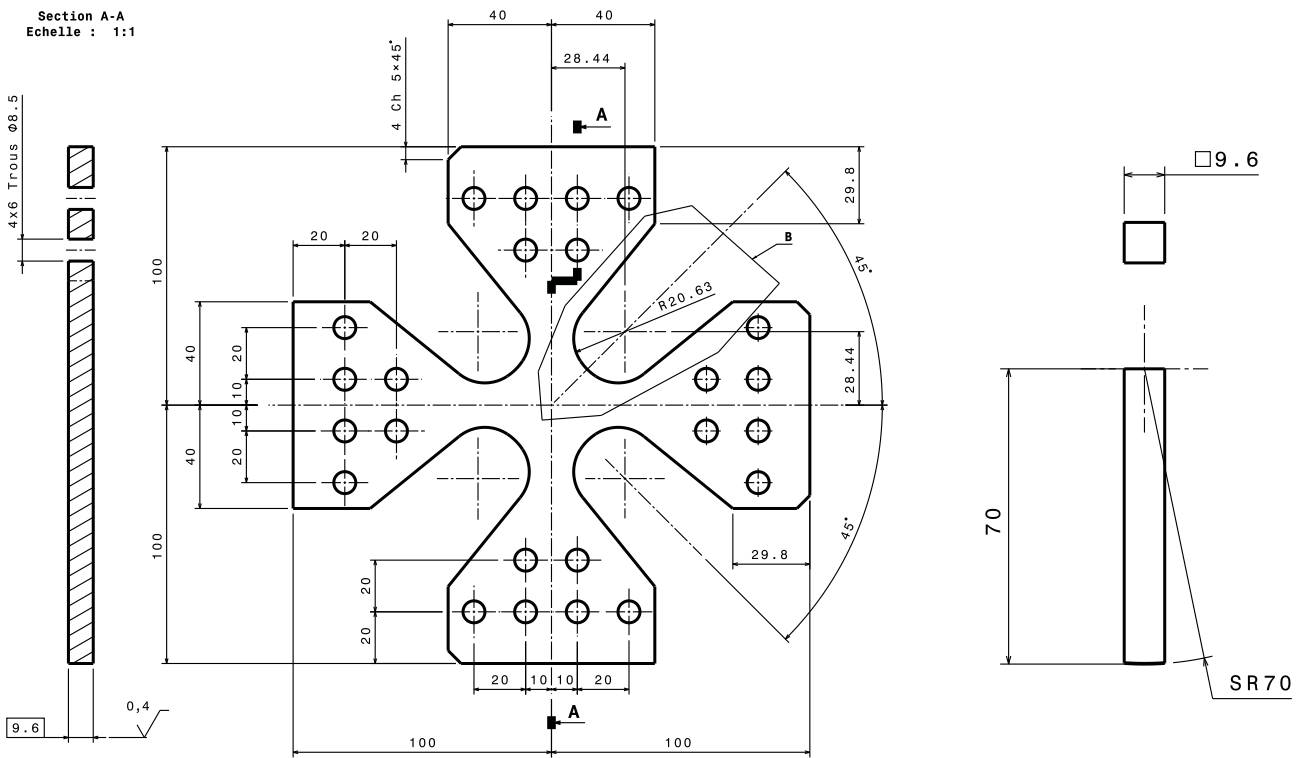


Figure 3.3: Specimen and pad used for fretting and bi-axial fatigue.

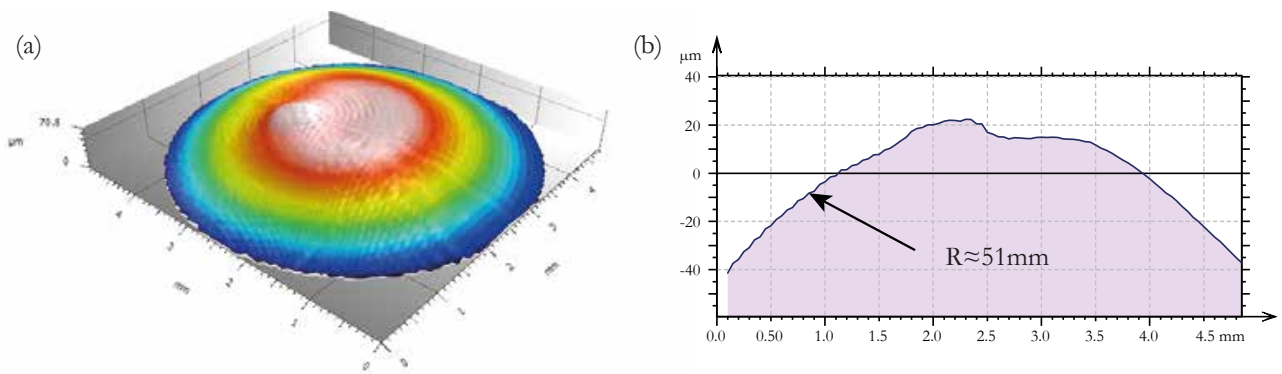


Figure 3.4: (a) 3D topography of the pad extremity (b) profile at the middle section.

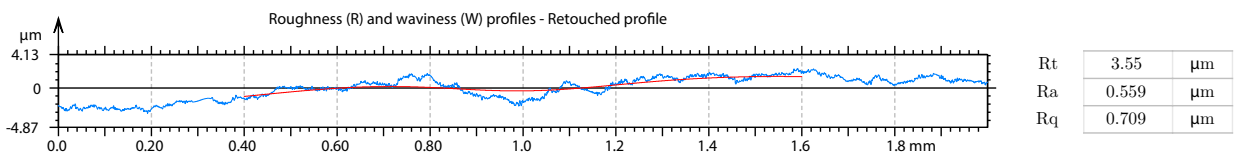


Figure 3.5: Roughness of the cross shape specimen.

### 3.2.2 Experimental set-up used for cylinder-plane fretting fatigue research

In this work, fretting fatigue tests are carried out using two cylindrical fretting pads, which were loaded against a flat dogbone tensile test piece. The apparatus used to carry out test were inspired by a device initially proposed by Nowell (1988).

The apparatus is attached to a servo-hydraulic fatigue test frame and works as a spring that reacts to the motion of the pads, which are pressed by a static force against the dog bone fatigue specimen. This motion arises when the specimen is subjected to a cyclic bulk load and then experiences a deformation that the pads do not. Due to the interfacial friction and to the fact that the pads are attached to the apparatus/spring, material points in the pads contact surface are not allowed to displace together with their counterparts in the specimen surface. The reaction of the spring results in the cyclic tangential load,  $Q$ , which is hence proportional and iso-frequency to the bulk load,  $B$ . Using the scheme depicted in FIG.3.6(b), the vertical forces are related by:

$$Q = 1/2(B - B_T) \quad (3.1)$$

In partial regime, the relation between  $Q$ ,  $B$ , and  $k_A$  and  $k_D$ , which are respectively the stiffness of the specimen portion above the contact and the half stiffness of the whole apparatus, is given by the following equation:

$$Q = B/(2 + k_A/k_D) \quad (3.2)$$

The determination of the exact stiffness of the whole apparatus is complicated because it involves assemblies of components having complex shapes and bolted joints. Usually, it is assumed that the flexible beams provide such stiffness being all other components considered as rigid bodies. Complete analysis of the stiffness of this apparatus can be found in (Martins et al. 2008).

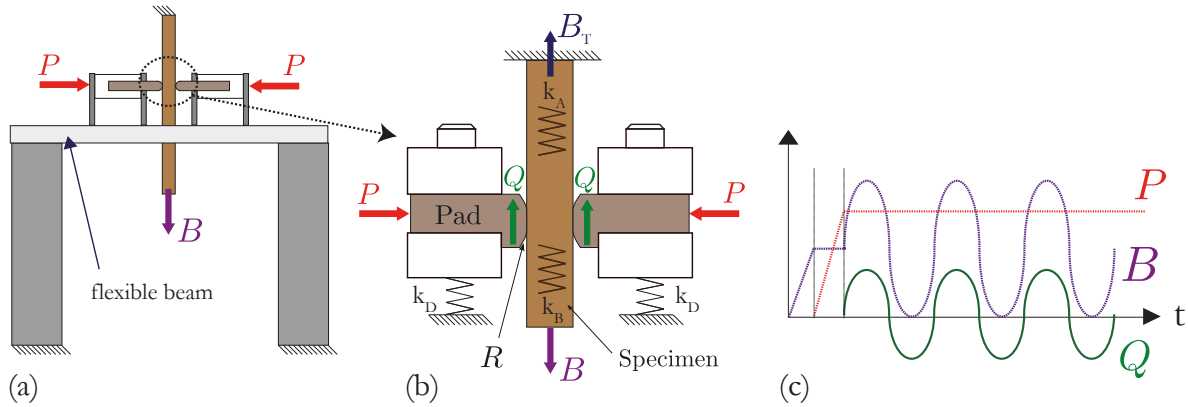


Figure 3.6: (a) Scheme of the fretting fatigue apparatus (b) equivalent spring arrangement and forces in the contact region (c) diagram of the loading cycle.

The auxiliary hydraulic system is composed of a hand pump, a pressure accumulator with a manometer, a Y hose, two valves and two single acting cylinders. In order to avoid pressure drop in the auxiliary hydraulic line, which can be caused the loss of material in the contact interface, a pressure

accumulator was connected to this line. This will assure that the normal load  $P$  will be kept constant in long lasting tests. A pad alignment consists of four small pitch screws on the sides of the pads carrier which allow careful control of the angular position of the pads (FIG.3.7).

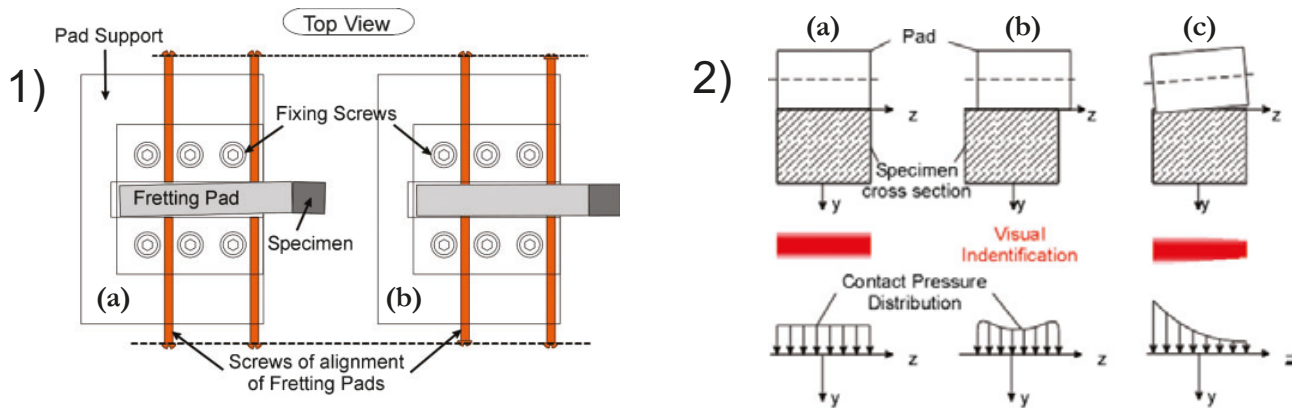


Figure 3.7: 1) Scheme of pad alignment system ((a) not aligned; (b) aligned pad) 2) Alignment conditions, types of pad impressions on pressure sensitive film and pressure distribution (Martins et al. 2008).

Before testing, pads and specimen are chemically degreased and, to assure the alignment of the contact between the cylindrical pads and the flat specimen was correct across the width of the specimen, a Pressure Measuring Film (Fuji Prescale Film - Medium Pressure - Mono Sheet Type) is used. FIG.3.8 depicts a photograph of a pair of pads together with impressions made on the pressure sensitive paper after a correct alignment was performed.

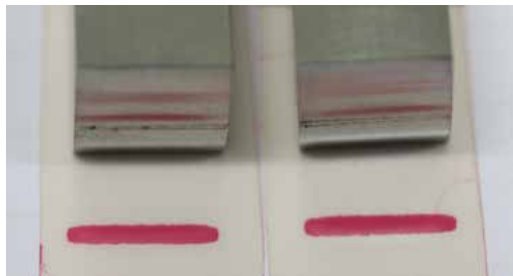


Figure 3.8: Set of pads with their respected prints on the pressure sensitive paper.

At the beginning of this work, the apparatus well described by Martins et al. (ibid.) was used (FIG.3.9), later on, a new one was designed and produced. The general objective of this new design was to allow higher tangential loading on the specimen, and for that, a more robust apparatus was needed.

At the same time, other improvements have been included. The pad holders have been totally re-designed. A slideway allows a rough adjustment of the pad holder to allow a large range of pad geometry, and a screw at the rear of the pad allows a fine adjustment of the contact and deformation of the plates. A new miniature load cell has been inserted at the rear of the pad and allow a direct reading of the normal force  $P$  before clamping of the pad. A laser has also been added to the apparatus. Its base is fixed to one of the pad holders and the laser point to a marker fixed at the contact

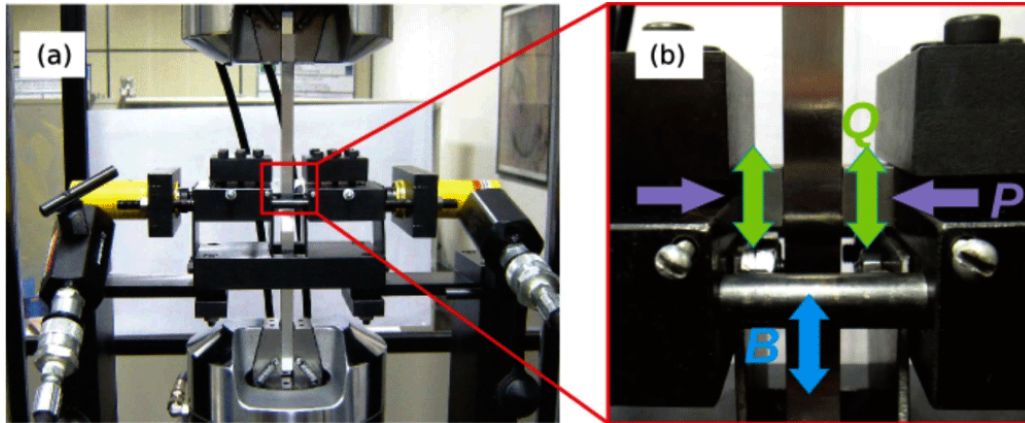


Figure 3.9: (a) photo of the initial apparatus (b) zoom of specimen/pad contact.

position on the specimen. This measure gives the relative displacement  $\delta^*$  between the pad and the specimen. By monitoring this relative displacement, the transition between partial and total sliding is easily spotted.

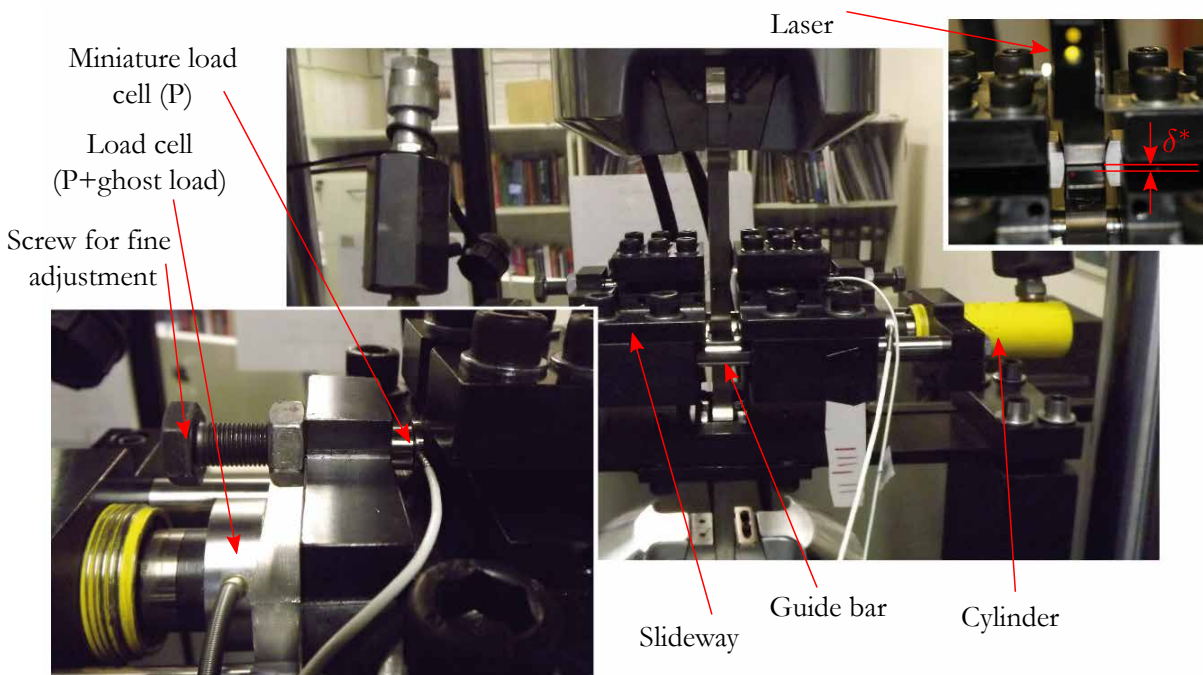


Figure 3.10: Picture of the fretting fatigue apparatus and its instrumentation.

The fatigue force  $B$  applied and the resulting tangential force  $Q$  are monitored by the load cell of the servo-hydraulic fatigue test frame and their precisions are around 2%. The constancy of the normal force  $P$  depends on the leaks of the hydraulic circuit and the relaxation of the apparatus. It has been observed that for long test ( $> 1$  day) the normal pressure may drop, losing around 5% of its initial value. Adding the precision of the load sensor, it can be assumed that the general precision of the

normal force  $P$  is around 7%.

With the test rig used in this study, two fretting pads are pushed against a specimen by a constant contact force. The fatigue specimen is subjected to cyclic axial stress and the tangential forces are controlled by the stiffness of the fretting apparatus and the position of the contact. The alignment of the pads is controlled before testing while the normal, tangential and bulk load are monitored during all the test.

### 3.2.3 Digital Image Correlation applied to fretting fatigue

The fretting apparatus is composed of several part screwed one to another, which affect the overall rigidity of the assembly. In order to verify that the pads remain perpendicular to the sample surface, the displacement of the pad holder was observed during a cycle fretting cycle.

The use of the digital image correlation appeared to be perfectly adapted for this analysis. Picture of the pad holders were taken with a camera Canon and the software Corelli V4 was used to compute the displacements and rotation for different loadings. Particular attention was taken to the twisting or rotation of the pad holder.

FIG.3.11 presents the rotation of the two pad holders for different tangential forces ( $2Q$ ). The linearity and symmetry of the pad holder twist appear clearly but the range of the rotation observed appeared to be small enough to be discarded. However when the deformation of the pad extremity is observed,

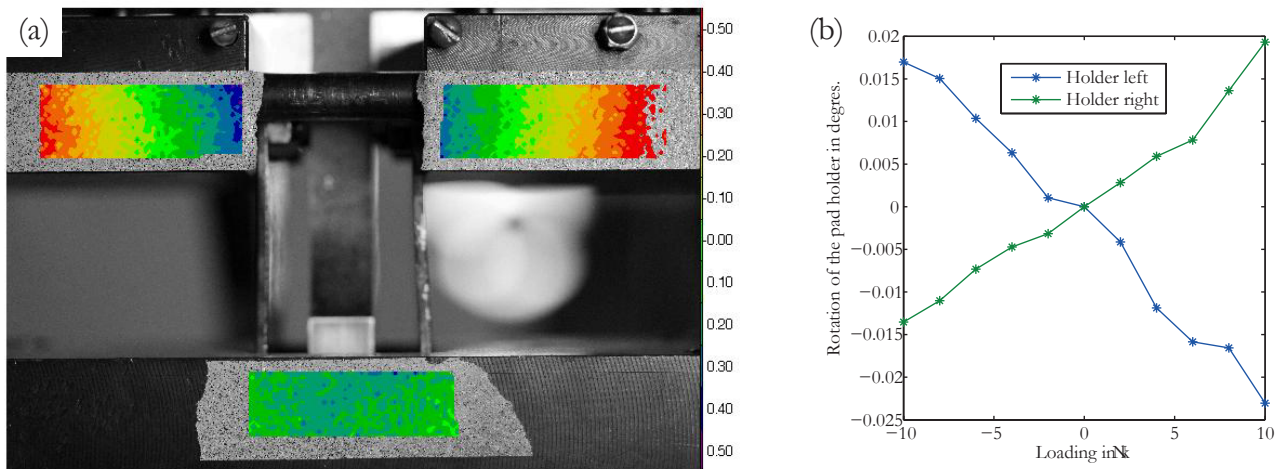


Figure 3.11: a) displacement field in the vertical direction b) rotation of the pad holder during a fretting cycle.

larger rotations are observed. FIG.3.12 illustrates the deformation (with a factor 100) of the pad extremity, loaded with a tangential force  $2Q = 6kN$ . In this case the rotation observed is about  $0.14^\circ$ .

In the light of those observations, several improvements have been made to limit the deformation of the pad extremity to a minimum. First, as said before, the new fretting apparatus designed has a higher stiffness. Secondly, the moment of inertia of the pad cross-section was increased. And finally

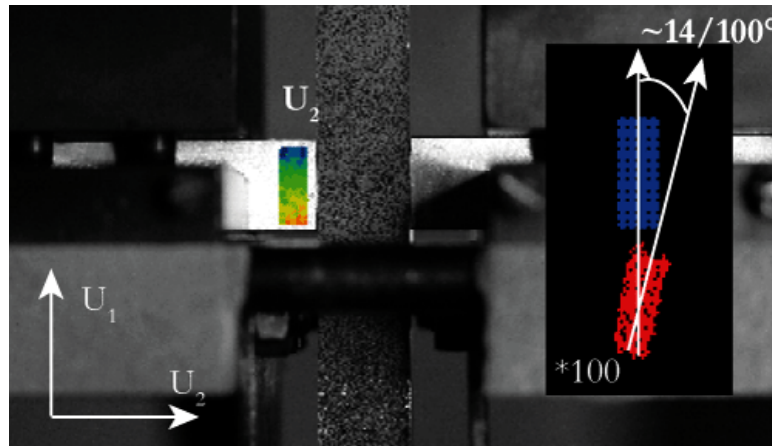


Figure 3.12: DIC on the extremity of the pad, for a tangential force  $2Q = 6kN$

the free extremity of the pads was limited to a few millimeters. With this setting, no rotation of the pad extremity could have been observed using the available correlation image technical.

More recently, Hojjati Talemi (2014) used the DIC to detect the transition between partial and relative sliding and calculate the coefficient of friction (FIG.3.13). The methodology used to estimate the coefficient of friction is based on the work of Hills (1994) which will be presented in the next subsection.

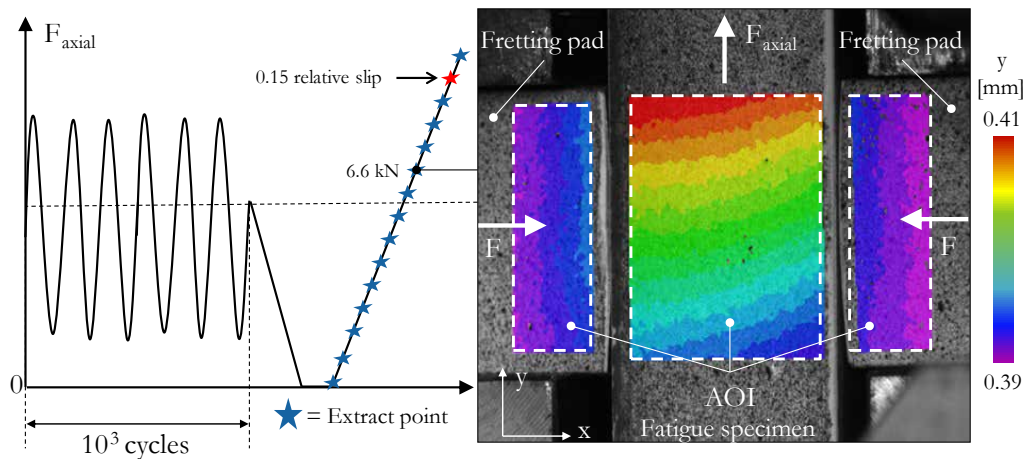


Figure 3.13: Loading sequence for calculating COF using DIC technique (Hojjati Talemi 2014).

Because of the obstructions and vibration of the test machine, contactless monitoring is necessary to monitor local displacement at the contact and the image correlation appears to be an excellent way to measure displacements of the free surface during the fretting cycle. The observations are of course limited to the external surface of the contact, but this first attempt and other recent works from the literature suggest that DIC applied to the fretting test has an interesting potential.

### 3.2.4 Experimental set-up for spherical-plane fretting bi-axial fatigue research

#### 3.2.4.i Set up and methodology

ASTREE (FIG.3.14a) is a three axis fatigue machine which is the result of reflection and joint work between the LMT-Cachan and SCHENCK company and was developed in early 1990. Two vertical cylinders respectively mounted on the base and on a moving crosshead have a capacity of 250 kN. The four horizontal cylinders have a capacity of 100 kN. The management of enslavement allows a control of the three axes by force/displacement difference and average.

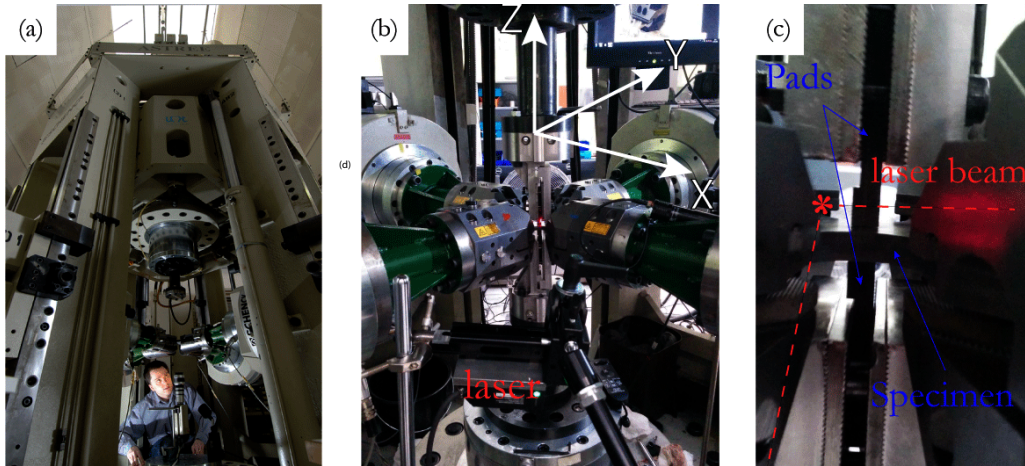


Figure 3.14: (a) Astree fatigue machine (b) fretting fatigue set up (c) zoom on the contact.

FIG.3.15 illustrates the deformation of the specimen and the force applied on each of its arms. The fatigue force is controlled by the average command on the horizontal arm. Here, a equibiaxial load was applied with a load ratio  $R_\sigma = -1$ . Non equibiaxial load can also be applied, but resulting fatigue stress can not be easily deduced without FEM computation. After applying the mean load on the specimen (here null), pads are pressed against the specimen by controlling the average of the z-axis, while the difference is forced to 0. The fretting load is generated by applying a difference between the forces of each cylinder on the horizontal axis. Indeed, this difference generates a displacement of the central zone of the specimen, counter by the fretting of the pads, bounded to the z-axis.

The force difference was applied equally on the axis  $x$  and  $y$ , the resulting tangential force lie in the bisector of the two axes, illustrated in red in FIG.3.15, while the cyclical fatigue load at the center of the specimen is equi-biaxial. A second referential  $(x', y', z)$  may be attached locally to the contact. In the referential, we have the tangential force in the direction  $x'$ , while the fatigue out of the contact is  $\sigma_{x'x'} = \sigma_{y'y'}$ .

#### 3.2.4.ii Limitations.

**Centering and alignment of the pads.** Because of the spherical shape of the pad, vertical alignment is not as complicated as for the cylinder/plane contact. However, because of the defect at the extremity of the pads (see SEC.3.2.1), the pads were slightly tilted to make sure that contact occurs with the perfectly spherical part of the pad. Here, positioning was performed with markers on the surface of the specimen, but it could also be done with Pressure Measuring Film.

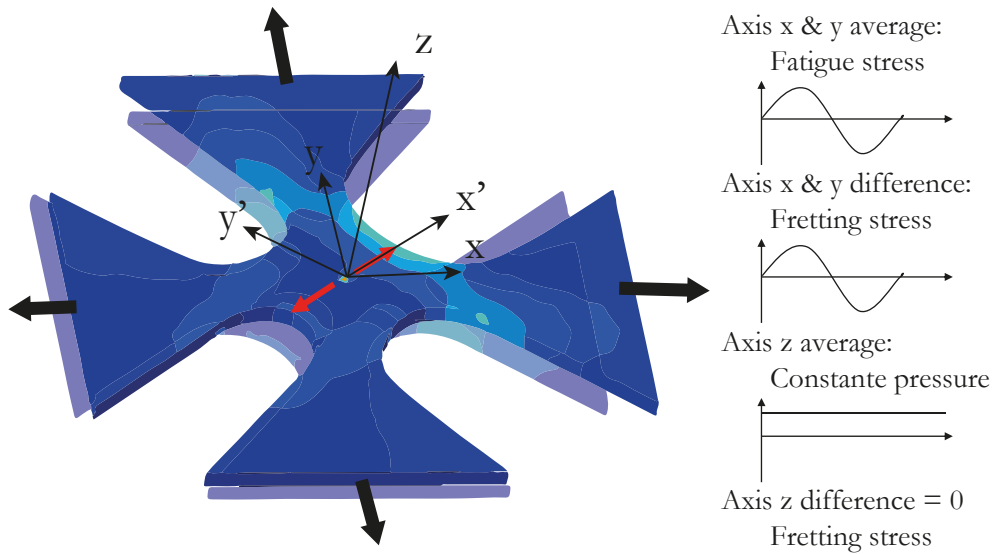


Figure 3.15: Illustration of the deformed cross shape specimen and forces applied.

**Poisson effect and control of the normal load.** As the fatigue load modifies the thickness of the central section by Poisson effect, the enslavement of the vertical axis has to compensate the micro-displacement and maintain the normal force as constant. In our tests, the normal force was around  $1kN$ , while the capacity of the vertical cylinders is  $250kN$ . This results in a very sensitive adjustment of the PID controller. Here, fatigue load led to a vertical displacement of the pad around  $1\mu m$ , resulting in a variation of 12% of the normal load (FIG.3.16).

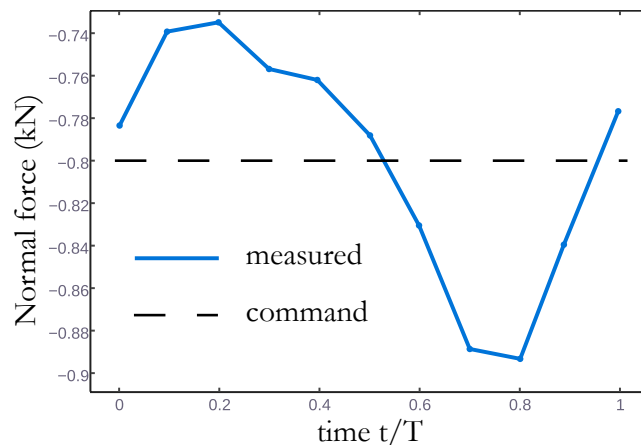


Figure 3.16: Variation of the normal force applied by the pads.

**Rigidity of the vertical axis.** Because of the fretting load, the cylinder/holder/pads assembly is subjected to flexure. Because the global area moment of inertia of the assembly is difficult to estimate, laser were installed to quantify the displacement of the pad extremity (FIG.3.17).

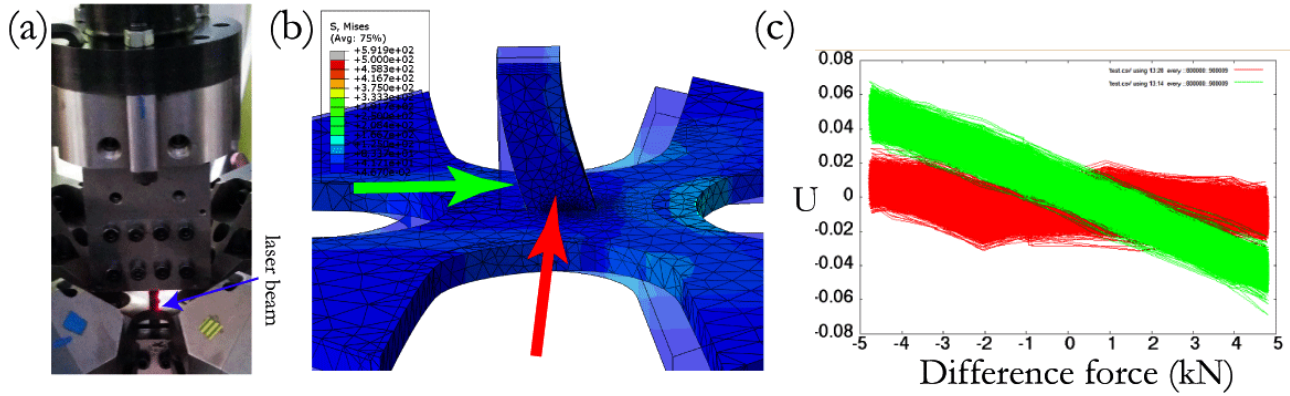


Figure 3.17: (a) Picture of the test zone (b) Illustration of the pad deformation computed by FEM (c) Typical signal of the laser during a test.

**Limitation of the loading.** Because of the specimen geometry, a stress concentration appears in the arm of reduction of the specimen arms. Fatigue stress in the central zone where the fretting phenomenon occurs is then limited. With the current shape of the specimen, FEM was used to estimate the maximum forces for not breaking the arm of the specimen. Calling respectively  $F_A$  and  $F_D$  the force amplitude and difference equally applied on the horizontal axis and considering the fatigue limit  $\sigma_{-1} = 480MPa$ , we obtain the condition:

$$8 * F_A + 15 * F_D < 480 \quad (3.3)$$

For a decade, the six actuators servo-hydraulic machine ASTREE is used to study the propagation of crack under complex multiaxial load. For the first time, we used this expertise to develop an original fretting fatigue test. Despite some challenges, we showed that it is possible to generate a fretting load coupled with a multiaxial fatigue load.

### 3.2.5 Coefficient of friction

In SEC.2.1.2.iii, the complexity of the concept of coefficient of friction was discussed. In this work, and for the simplicity of the analytic and numerical modeling of the fretting problem, a constant coefficient of friction will be assumed.

Two methods were used to estimate the coefficient of friction. A first technique for estimating the slip zone friction coefficient has been developed by Hills (1994). In partial slip, the central stick zone is defined as  $|x| \leq c_0$  and the two slip zones as  $c_0 < |x| \leq a$ . After  $n$  cycles, it is assumed that surface modification will raise the coefficient of friction within the slip zones to  $\mu_s$ , independently of the pressure. The stick zone size being a function of  $\mu_s$ , it will also increase its size to  $|x| \leq c_s$ , as shown in FIG.3.18.

Notice that for  $c_0 < |x| \leq c_s$  the value of  $\mu(x)$  is unknown although it has to lie between  $\mu_0$  and  $\mu_s$ .

$$\frac{c_s}{a} = \sqrt{1 - \frac{Q}{\mu_s P}} \quad (3.4)$$

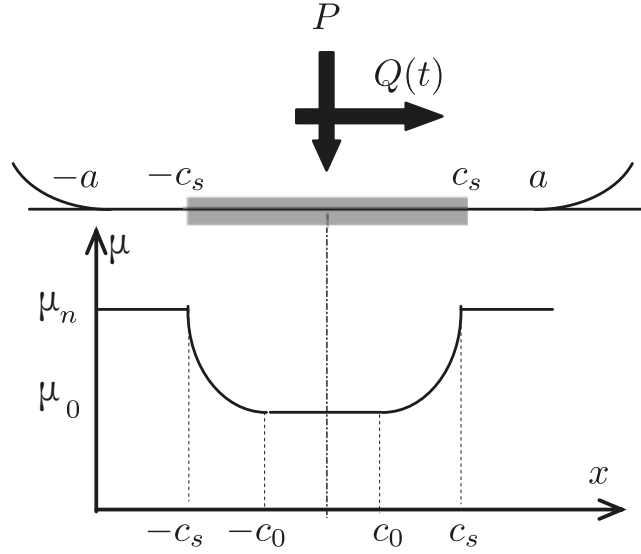


Figure 3.18: Model of variation of the coefficient of friction across contact.

At this stage of the experiment, the average coefficient of friction,  $\mu_m$ , may be measured by stopping the oscillatory fretting load and sliding the cylinders by a minute distance under displacement control. The value of this measured average coefficient is function of the local coefficient of the stick and slip zone:

$$\frac{\pi a \mu_m}{4} = \int_0^{c_0} \mu_0 \sqrt{1 - \left(\frac{x}{a}\right)^2} dx + \int_{c_0}^{c_n} \mu(x) \sqrt{1 - \left(\frac{x}{a}\right)^2} dx + \int_{c_n}^a \mu_s \sqrt{1 - \left(\frac{x}{a}\right)^2} dx \quad (3.5)$$

Which after differentiation with respect to the number of cycles  $n$  yields:

$$\frac{\pi a}{4} \frac{\partial \mu_m}{\partial n} = \frac{\partial \mu_s}{\partial n} \left[ \frac{\pi}{4} - \frac{c_s}{2} \sqrt{1 - \left(\frac{x}{a}\right)^2} + \frac{1}{2} \sin^{-1} \left(\frac{c_s}{a}\right)^2 \right] \quad (3.6)$$

The Eq.3.4 is used to write:

$$\mu_m = \mu_s - \frac{2}{\pi} \int_{\mu_0}^{\mu_s} \left[ \sqrt{\frac{Q}{\mu_s P}} \sqrt{1 - \frac{Q}{\mu_s P}} + \sin^{-1} \sqrt{1 - \frac{Q}{\mu_s P}} \right] d\mu_s \quad (3.7)$$

In most fretting tests the initial coefficient of friction is quite low, hence initial sliding may be anticipated. If this is so then  $\mu_0 = Q/P$  and the evaluation of the integral in eq.3.7 yields:

$$\mu_m = \mu_s - \left\{ \frac{4Q}{\pi P} \left[ \frac{\pi}{2} - \cot \theta_s - \theta_s \right] - 2 \frac{2}{\pi} \left[ \mu_s \phi_s - \frac{Q}{P} \tan \phi_s \right] \right\} \quad (3.8)$$

where

$$\theta_s = \sin^{-1} \sqrt{\frac{Q}{\mu_s P}} \quad \text{and} \quad \phi_s = \cos^{-1} \sqrt{\frac{Q}{\mu_s P}} \quad (3.9)$$

Thus it is possible to estimate the coefficient of friction at the slip zones,  $\mu_s$ , if a measurement of the average coefficient,  $\mu_m$ , is taken after  $n$  fretting cycles. Fig.3.19 depicts the relationship between these

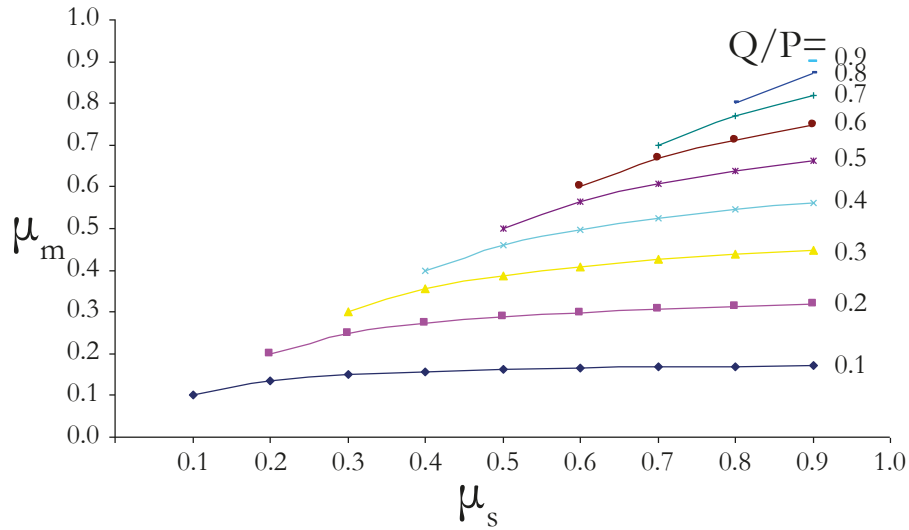


Figure 3.19: Prediction of the coefficient of friction within the slip zones from measured average values Araújo 2000.

quantities for different values of  $Q/P$ . An interesting phenomenon revealed by this graphic is that for lower  $Q/P$  values the value of  $\mu_s$  may vary significantly with small variations in the values of  $\mu_m$ . A value of the coefficient of friction was estimated after 10000 cycles and for a ratio  $Q/P = 0.29$  and a peak pressure  $p_0 = 700MPa$ . Fig.3.20a shows the results of the tangential force  $Q$ , function of the displacement of the chuck during the traction of the specimen still clamped between the pad. Total sliding is observed at  $Q = 2.32kN$ , which gives a average coefficient  $\mu_m = 0.38$ . When the Eq.3.9 is plotted (Fig.3.20b), the predictions for the slip zone friction coefficient gives  $\mu_s = 0.49$ .

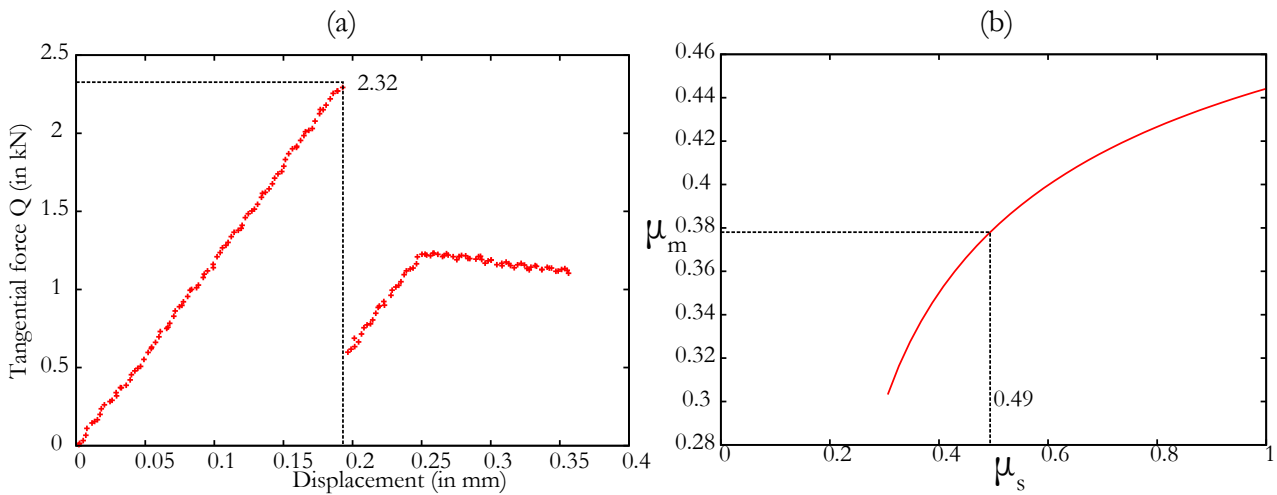


Figure 3.20: (a) Tangential force function of the displacement command, (b) determination of the slip zone friction coefficient.

A second technique for estimating the slip zone friction coefficient consists to assume that friction coefficient measured at the transition between partial and gross slip conditions ( $\mu_t$ ) may be used to

provide a representative value of the friction under partial slip condition (i.e.,  $\mu_s \approx \mu_t$ ). To determine the sliding transition of the studied contact, a variable displacement method can be used: the normal load is kept constant whereas the relative displacement amplitude ( $\delta^*$ ) starts from a very low value, imposing a clear partial slip condition (with  $Q < fP$ ). When stabilized conditions are reached,  $\delta^*$  is increased and then maintained constant until a new stable situation is reached. The imposed displacement,  $\delta^*$ , is increased in this way, step by step until the contact makes the transition to sliding ( $Q_t = \mu_s P$ ). FIG.3.21 presents the results obtained by Proudhon et al. (2005), and shows a value of the fretting coefficient equal to  $\mu_s = 0.8$ .

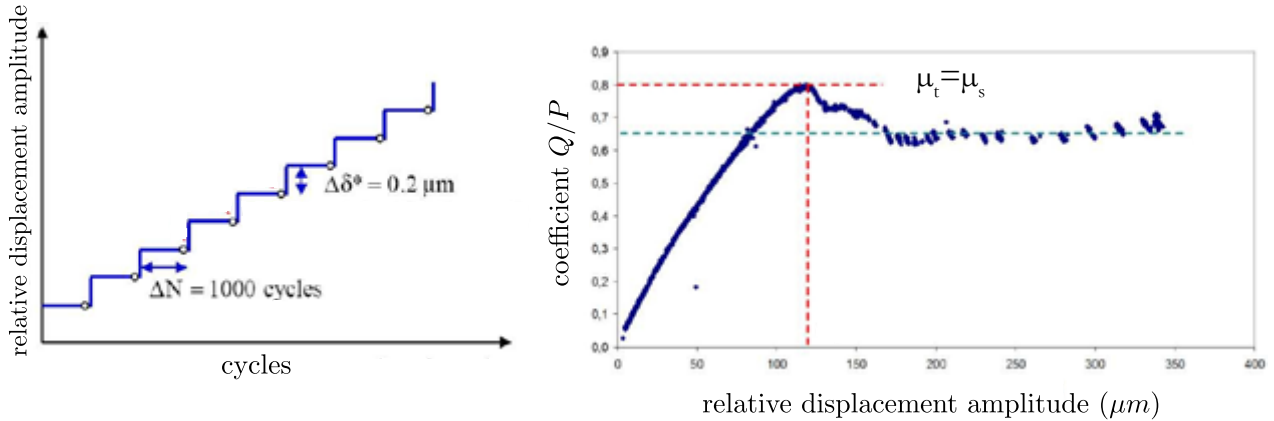


Figure 3.21: a- Illustration of the variable displacement method, b- results obtained using Ti-6Al-4V alloy in a complete-contact (plane/plane) fretting problem with a normal force of  $9.4kN$ .

This methodology was also used to determine the fretting coefficient with the pad of  $20mm$  radius and under the normal load  $P = 3140N$ . To carry out a fretting test, the specimen is clamped between the pad while its upper part is left free. In the current apparatus configuration, it is not possible to control the relative displacement  $\delta^*$  between the pad and the specimen. Instead, incremental displacement  $\delta$  is imposed at the bottom part of the specimen. Because of the elasticity of the apparatus and of the bottom part the specimen,  $\delta^*$  is proportional to  $\delta$ , while the partial slip condition is maintained. The increment  $\Delta \delta = 7 \mu m$  was added every 250 cycles, which gave  $\Delta \delta^* \approx 0.06 \mu m$ . The relative displacement  $\delta^*$  is registered thank to a laser. FIG.3.22 illustrates the relative displacement  $\delta^*$  during the fretting test. The transitions between partial slip and gross sliding can clearly be identified. Just before this transition the amplitude of the tangential force observed was  $\Delta Q_{obs} = 2.2kN$ . When the transition occurs, the fretting coefficient observed is then  $\mu_s = Q/P = 0.40$ . The method was repeated with a pad radius of  $R = 70mm$  and a normal load  $P = 11kN$ . In this case, the ratio  $Q/P$  at the transition was equal to  $\mu_s = Q/P = 0.5$ .

The fretting fatigue coefficient in the slip zone was determined using two different methodologies. The results were between  $\mu_s = 0.40$  and  $\mu_s = 0.50$ . As a matter of comparison, Araújo (2000) found valor between  $\mu_s = 0.55$  and  $\mu_s = 0.59$  when using a ratio  $Q/P = 0.45$ , while Proudhon et al. (2005) found a coefficient of friction  $\mu_s = 0.8$ . In the following, and for the different models, we will assume a unique coefficient of friction  $\mu = 0.5$ .

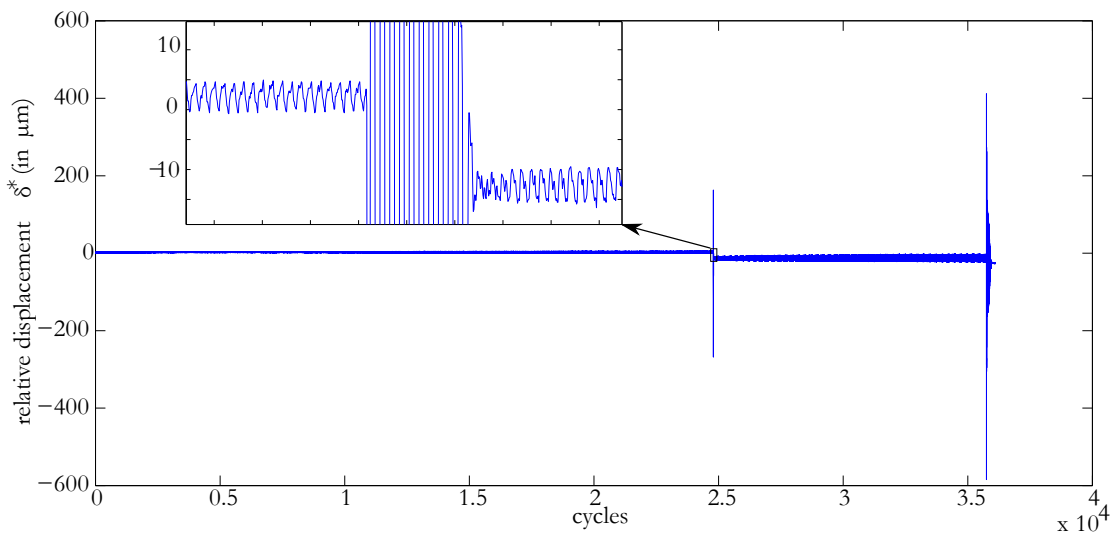


Figure 3.22: Relative displacement  $\delta^*$  estimated by laser.

### 3.3 Finite element modelling of fretting fatigue tests

The fretting-fatigue configuration of the cylinder/plane was modeled with finite elements using the commercial software ABAQUS. First a basic elastic 2D plane strain model of the cylinder against a flat specimen is presented. There follow an analysis of the pad deformation and its influence on the stress distribution at the surface and a comparison of the 2D model with a 3D model. Finally, using the intern tool of the ABAQUS software, a model including a crack is used to compute stress intensity factors.

#### 3.3.1 Basic 2D model

Basic geometries and boundary conditions of the model are illustrated in FIG.3.23. Using the symmetry of the experimental set-up, only one pad and half of the specimen are modeled and symmetry boundary conditions are imposed on the middle of the specimen. Three reference points are used to apply the rest of the boundary conditions. Displacement of the specimen and pad extremities are coupled to these reference points. Rotation around the out of plan axis is forbidden at these points from the initial step. With this method, forces corresponding to the fatigue and normal and tangential load are applied locally. The boundary conditions applied to the referential point is illustrated in on the FIG.3.23 and consist in four steps:

- Step 1: The mean load of the fatigue cycle is applied to the specimen. Opposition forces are applied to reference points 1 and 2 while infinitesimal displacement is imposed on the pad. The displacement of the pad in the direction  $y$  is also fixed. The infinitesimal contact of the pad on the specimen allows to omit a control of the x-displacement of the specimen and insure the position of the center of the contact to come. Displacement of  $1\mu m$  appears to be enough to ensure the convergence without affecting the stress distribution in the specimen.
- Step 2: Reference point 1 is fixed at its current position while the mean force is maintained at

the other extremity of the specimen. The normal force  $P$  is applied on the y-axis of the pad and will be maintained in the following.

- Step 3-4-...: Fatigue force and tangential force are applied respectively on RP2 and RP3.

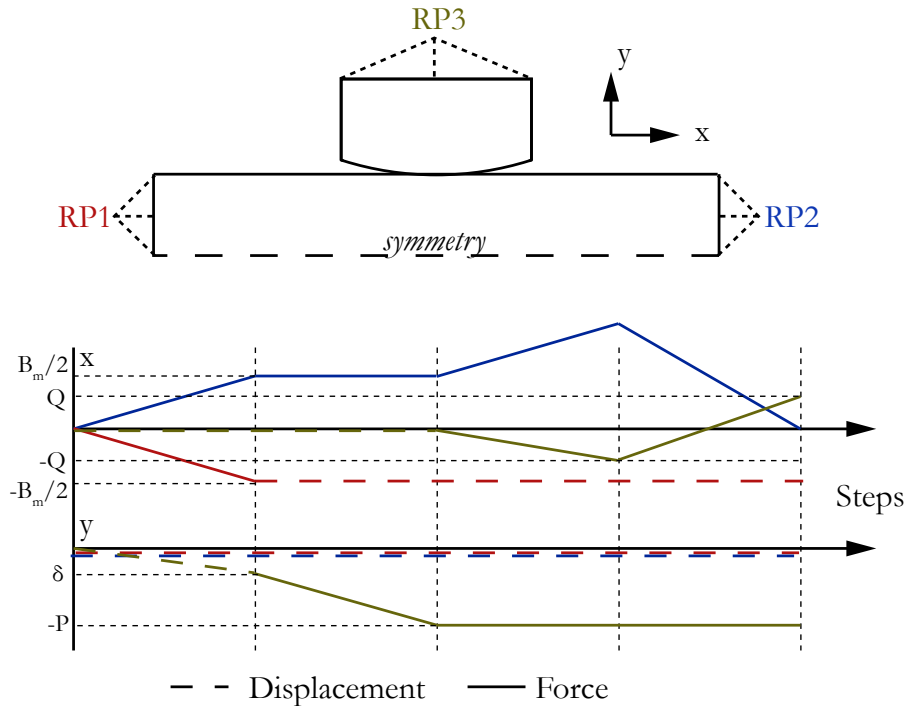


Figure 3.23: Illustration of the FEM modelling.

In order to depict precisely the effect of the fretting, a refinement of the mesh is necessary at the pad/specimen interface. Affonso (2012) studied the convergence of the model for diverse element types under plain strain conditions (CEP4, CEP8,...) and shows that the best balance between element density and computation cost is obtained with linear elements. Moreover, with a number of 160 elements to describe the contact size, the results reach the convergence. The present model use linear quadrilateral plane strain elements CEP4. The element size away from the contact interface is  $500\mu m$ , and in the contact zone, the refined mesh required  $5\mu m$  elements.

In order to model the contact between the round pad and the flat specimen, a Surface-to-Surface discretization type is used. The pad is defined as the master surface and the specimen as the slave surface, the distribution of pressure is ensured to remain under an error threshold of 1%. Concerning the formulation of the friction, two methods proposed by Abaqus are suitable for the configuration of fretting-fatigue: the penalty method and the Lagrange multiplier. The penalty method has a lower computational cost than Lagrange multiplier method, with the disadvantage of admitting the interpenetration of the bodies, which slightly alter the results. Abaqus also proposes to choose between the option Small or Finite sliding. When the small sliding option is used, the plans where the slave nodes may slide are never updated after the first increment. In the configuration presented here, the normal force, primarily applied, can lead to different plans from those preferred for the fretting when the bulk load is applied. Then Finite sliding is the only option providing understandable results.

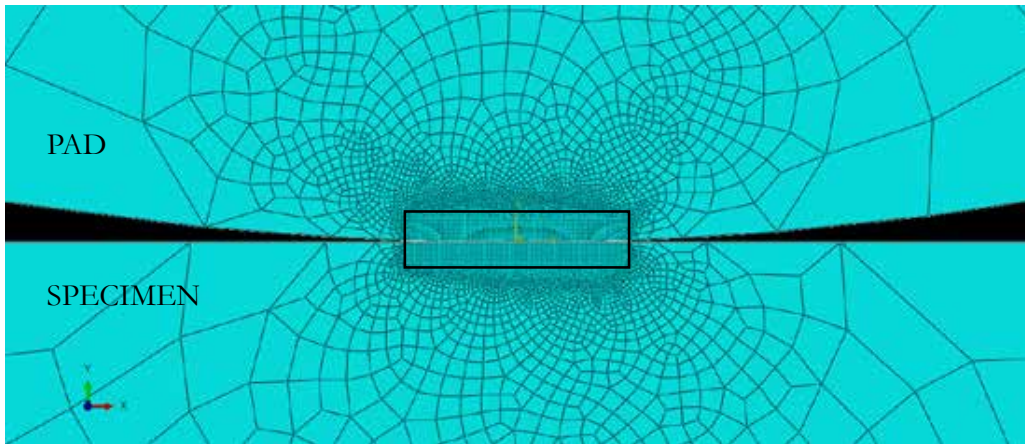


Figure 3.24: 2D mesh using CEP4 elements around the contact zone.

FIG.3.25 compares the analytical shear distribution with the result obtained with finite element using the Lagrange multiplier method.

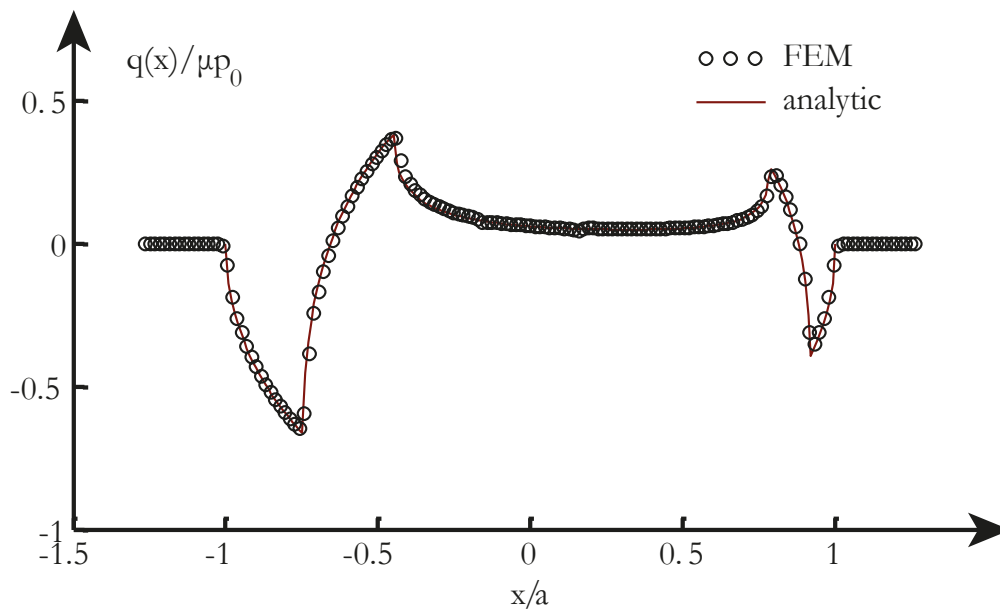


Figure 3.25: Distribution of the shear stress at the surface during unloading for  $\sigma_{Bmax}/p_0 = 0.7$  and  $Q_{max}/\mu P = 0.62$ .

FIG.3.26 presents the gradient of the  $\sigma_{xx,max}$  from the trailing edge of the contact until the middle of the sample, computed with the analytical formulation and with FEM. This figure illustrates clearly the domain of influence of the fretting. For the loading considered here, this domain is limited to 2mm. And the little difference between the two stress gradients suggests that the assumption of infinite half-plane like used by the Muskhelishvili's potential theory is legit (Fellows et al. 1995).

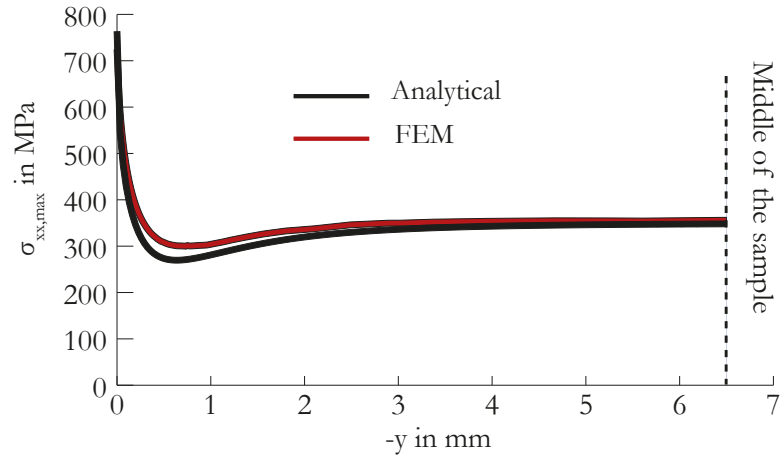


Figure 3.26:  $\sigma_{xx,max}$  from the trailing edge of the contact until the middle of the sample, computed with the analytical formulation and with FEM. ( $\sigma_{Bmax}/p_0 = 0.7$  and  $Q_{max}/\mu P = 0.62$ ).

A simple 2D elastic finite element model describing the experimental fretting fatigue problem of the cylinder/plane configuration. At the convergence of the model, the traction fields are exactly the same as the Mindlin analytical description. In the range of loading considered in this study, the subsurface fields are also very close. Therefore, the analytical model, faster, will be always preferred to access the stress field below the contact.

### 3.3.2 Comparison with 3D model

Only one of the symmetries of the problem cylinder against flat specimen, a quarter of the geometry is modeled (FIG.3.27). Other boundary conditions and loads are identical to the 2D model detailed previously, three reference points are used and coupled with the faces of the specimens and the superior section of the pad. 8-node linear brick are used with a sweep method in the direction  $z$ . Standard surface-to-surface contact is used with the same interaction properties used for the 2D model.

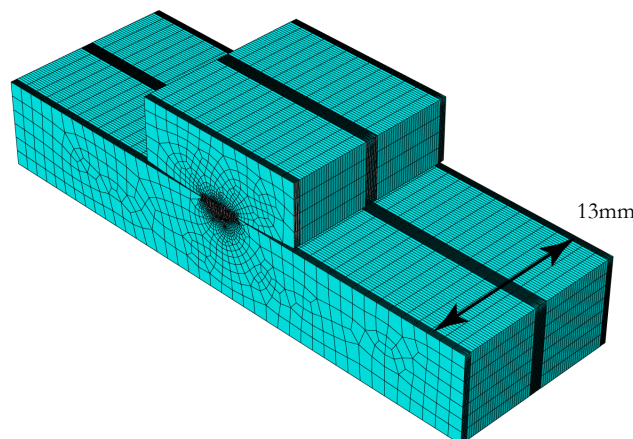


Figure 3.27: Geometries and Mesh of the 3D FEM.

FIG.3.28 presents the tractions distribution at the surface for a pad radius  $R = 70\text{mm}$  under the loading  $Q/\mu P = 0.62$  and  $\sigma_{Bmax}/p_0 = 0.7$  with a normal force giving in theory  $p_0 = 500\text{MPa}$ . The normal force is given by the formula:

$$P = \int p(x, z) dA = \frac{\pi}{2} W a p_0 \quad (3.10)$$

The distribution is compared with the analytic result. On the free edge of the specimen, a significant drop of the normal pressure is observed while at the middle of the specimen the peak pressure is 4% superior to the theoretic one.

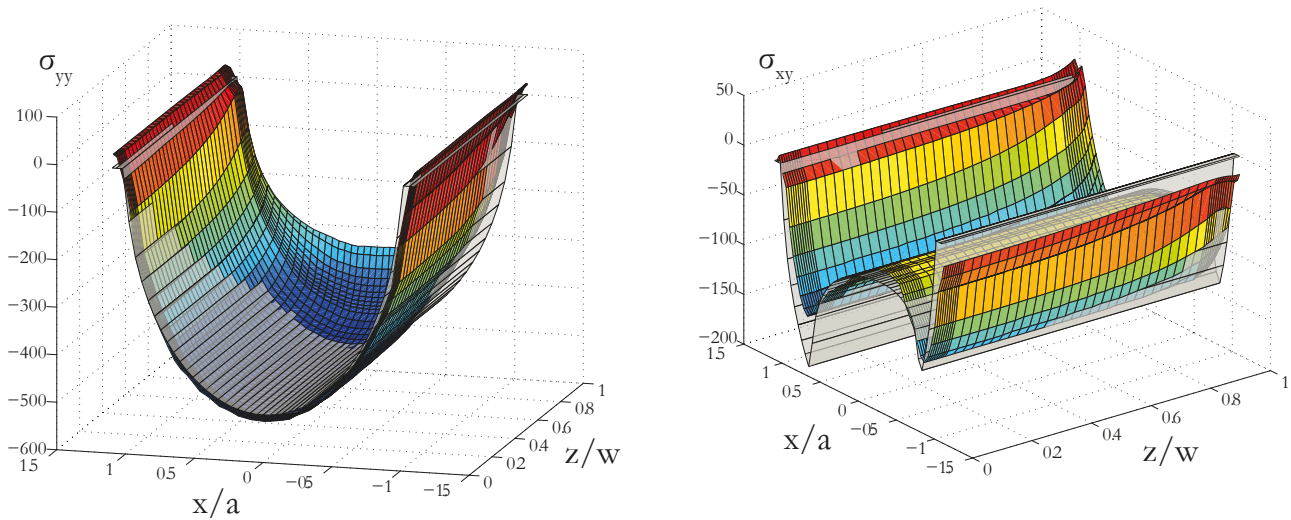


Figure 3.28: Normal and tangential tractions computed with a 3D FEM, compared with the plain strain 2D distribution.

The 3D model allows to verify the assumption of plane strain condition at the middle of the contact. FIG.3.29 present the ratio  $\frac{\sigma_{zz}}{\nu(\sigma_{xx} + \sigma_{yy})}$  at the contact surface at the maximum loading. The load considered is the same as previously. When this ratio is null, it indicates pure plane stress condition, while a ratio equal to 1 reflects pure plain strain conditions. At the center of the contact, the ratio has a maximum value of 0.8.

3D modeling of the cylinder/plane, shows that in the contact width direction, the pressure profile decrease as compared to the values at the symmetry plane. Thus, at the specimen sides, the contact width decreased. The redistribution of the pressure increases the maximum contact pressure and the contact size on the remaining imprint. Moreover, it appears that the stress out of plane is lower than with the assumption of plane strain.

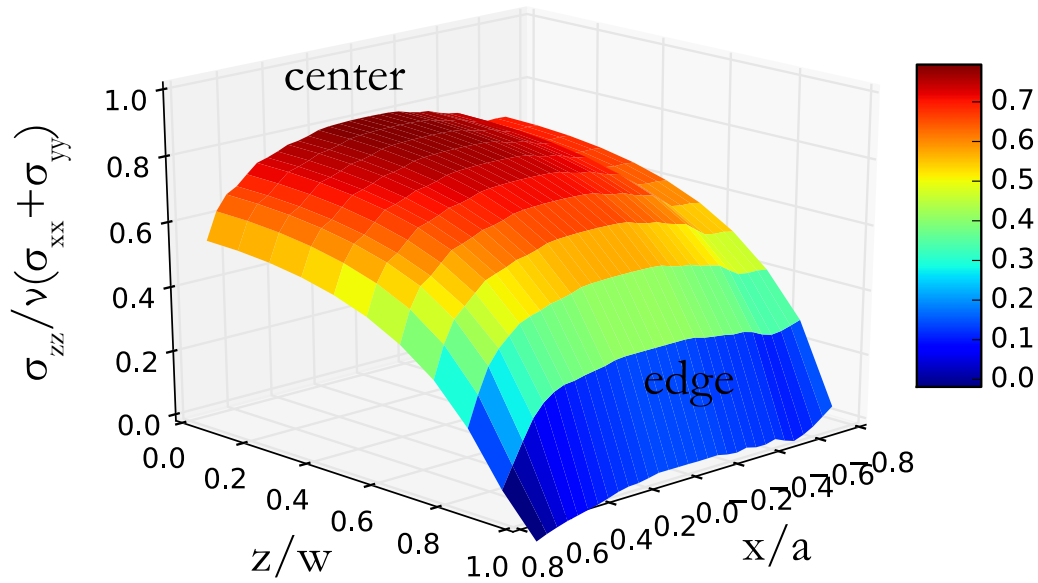


Figure 3.29:  $\frac{\sigma_{zz}}{\nu(\sigma_{xx} + \sigma_{yy})}$  at the surface of the contact at maximum loading.

### 3.3.3 Crack modeling

From the Interaction module of Abaqus, a crack may be introduced into the model with a seam. A seam is defined in the model as an edge that is originally closed but can open during an analysis. Abaqus/CAE places overlapping duplicate nodes along a seam when the mesh is generated. The virtual crack extension direction is specified with the q-vector as illustrated in FIG.3.30.

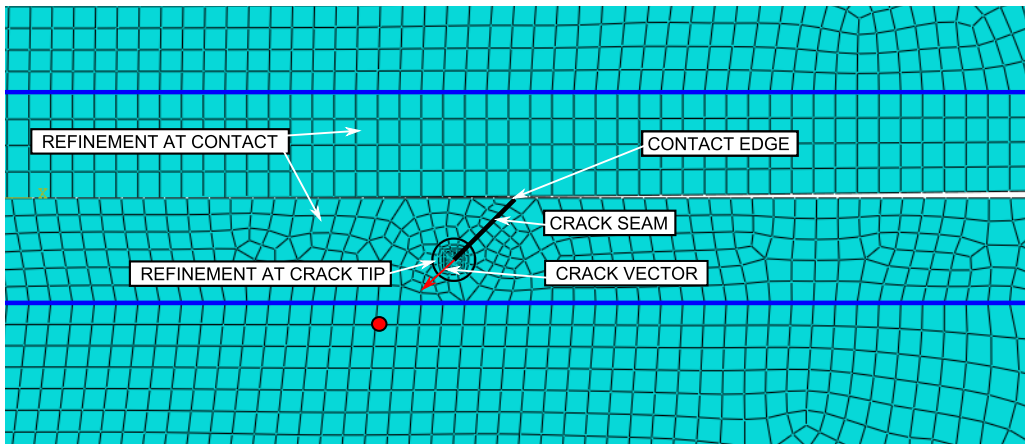


Figure 3.30: Crack modelling in FEM.

For a sharp crack, the strain field becomes singular at the crack tip. Including the singularity at the crack tip for a small-strain analysis improves the accuracy of the J-integral, stress intensity factors, and the stress and strain calculations. The partitioning of the geometry is defined by the circular

lines centered on the crack tip. This partitioning strategy facilitates the generation of a focused mesh. Usually, the value of  $K_I$ ,  $K_{II}$  and T-stress resulting from the calculation of the J-integral for the first contours are ignored because of numerical inaccuracies in the stresses and strains at the crack tip. Convergence was here obtained at the third contour.

### 3.3.3.i Effect on the surface traction

To study the influence of a fretting crack on the contact traction distributions, we have modeled normal cracks to the surface located at the trailing edge of contact zone, for the fretting fatigue parameter  $\sigma_{Bmax}/p_0 = 0.7$ ,  $Q/\mu P = 0.62$  and  $R = 70mm$ . Four models including a straight crack of length  $b = 10\mu m$ ,  $b = 50\mu m$ ,  $b = 100\mu m$  and  $b = 1mm$  were computed. FIG.3.31 shows the normal and tangential traction distribution  $p(x)$  and  $q(x)$  along the contact surface. For the small cracks ( $b \leq 100\mu m$ ) the tractions are perturbed for  $x/a = 1$  but the redistribution of the stress does not generate significant variation on the rest of the contact surface. When a long crack is considered ( $b = 1mm$ ), redistribution is clearly visible. The contact zone extends to the other side of the crack due to the loss of local stiffness originated by the crack discontinuity. The loss of stiffness under the normal load causes that the indenter tends to penetrate more deeply. As a consequence, the right lip of the crack enters into contact, bearing part of the indenter vertical load and showing local peaks at points  $x/a > 1$ . The redistribution extends to the left side of the contact, causing a shifting of the contact zone to the right.

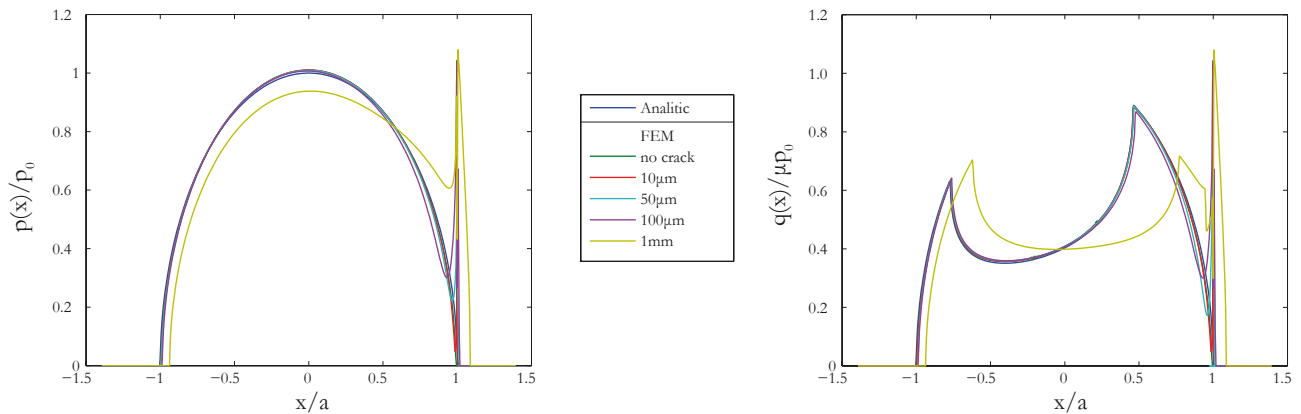


Figure 3.31: Effect of a short crack normal to the surface at  $x = a$  on  $p(x)$  and  $q(x)$ .

The overall traction distribution is almost not affected by the presence of a short crack at the edge of the contact. But a perturbation of the traction distribution is observed at the exact position of the crack initiation point.

### 3.3.3.ii Comparison with distributed dislocation method

We consider here a straight crack, initiating at the trailing edge of the contact and in a direction perpendicular to the contact surface. We compared the stress intensity factor in mode I,  $K_{Imax}$ , computed by FEM with the value calculated with the method of distribution of dislocations using the analytic formulation of the problem. Results are presented in FIG.3.32. For short cracks, the

method of distribution of dislocations shows good agreement with the FEM, while, for the 1mm crack, the difference is about 4%. At the light of this result, in the following, when the SIF in mode I will be computed at for a straight crack perpendicular to the surface, the method of distribution of dislocations, will be used because of its easiest computation. We can compare these results to the simplistic approach of considering the bulk stress alone as in plain fatigue. These values were computed using the geometric function for a double-edge notch in tension given in (Tada et al. 2000). For short crack, the difference represents the contribution of the contact stresses. The longer the crack is, the closer the FEM result will tend to the plain fatigue results.

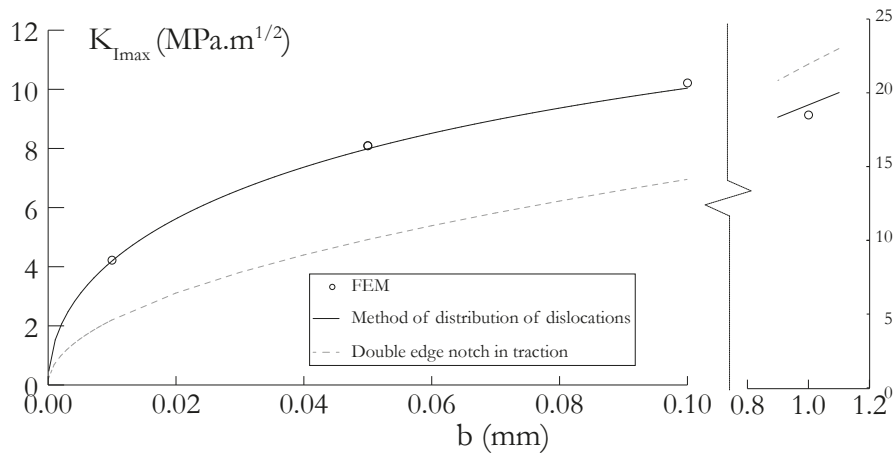


Figure 3.32: Values of SIF obtained via FEM for different crack lengths. Comparison with the method of distribution of dislocations.

We consider now an inclined crack at  $115^\circ$ . The fretting fatigue load is the same as considered before. The size of the crack,  $b$ , is accounted as the projection of the crack on the y-axis, as illustrated in FIG.3.33, which presents the von Mises distribution around a  $100\mu\text{m}$  crack. When the crack is inclined, the SIF in mode II,  $K_{II}$  can no more be negligible.

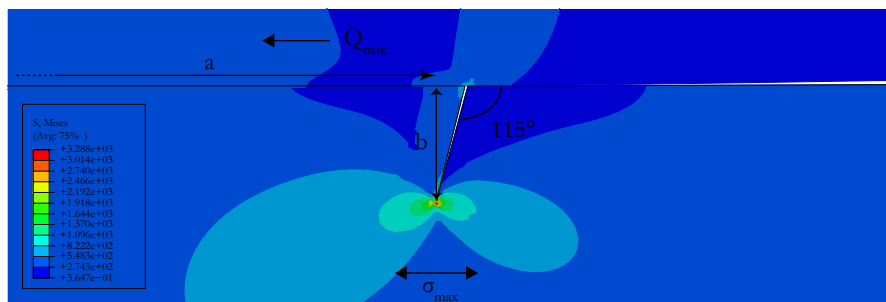


Figure 3.33: Von Mises distribution around a inclined crack at maximum loading.

FIG.3.34 presents the comparison of the SIF  $K_I$  and  $K_{II}$  computed with FEM and with the method of distribution of dislocations. Value are taken at the instant of maximum fatigue force.

As before, values of  $K_{I_{max}}$  are matching very well. For the SIF in mode II, however, significant difference appear. The distributed dislocation method uses the analytical formulation of the stress field. Unlike in the finite element model, the surface tractions are not updated with the perturbation of

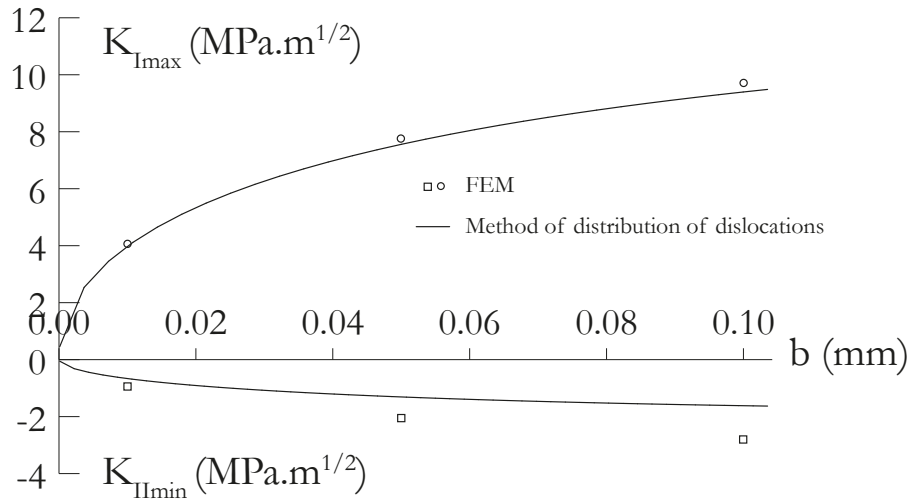


Figure 3.34: Values of SIF obtained via FEM for different crack lengths inclined at 115°.

the crack presence. With the FEM, the contact pressure generates a discontinuity of the  $\sigma_{yy}$  between each side of the crack faces (FIG.3.35). This results in a constant mean shear at the crack tip during the cycle. The release of this stress component is not represented in the analytical field which may explain the absence of a mean component in the  $K_{II}$ . The presence of a mean  $K_{II}$  with the FEM is clearly visible in FIG.3.36.

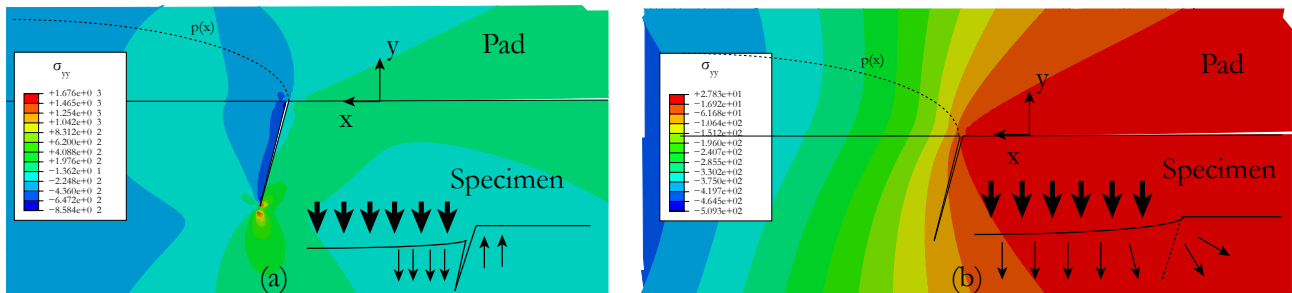


Figure 3.35:  $\sigma_{yy}$  distribution (a) with a crack modeled (b) without crack (analytic field used in the method of distribution of dislocations).

During the unloading, negative values of  $K_I$  are observed, which indicates a closure of the crack. The fatigue force has a load ratio  $R_\sigma = 0$ . While the bulk favors an opening of the crack ( $R_\sigma = 0$ ), the constant normal force and the tangential force during unloading tends to favor the closing, in particular if the crack is inclined toward the contact. Contact interaction can be defined between the crack face of the FEM model. The difficulty is to characterize the tangential behavior of the sliding between the crack faces. FIG.3.36 includes the SIFs computed when no sliding is allowed when crack faces are in contact. It is good to remind that the analyze of a straight crack is purely academic. Experimentally, the crack fracture surfaces show variation in the direction of propagation and the roughness of the fracture surface depends on the micro structure of the material. Theses phenomena tend to prevent a sliding between the crack faces and then directly affect the stress intensity factor  $K_{II}$ .

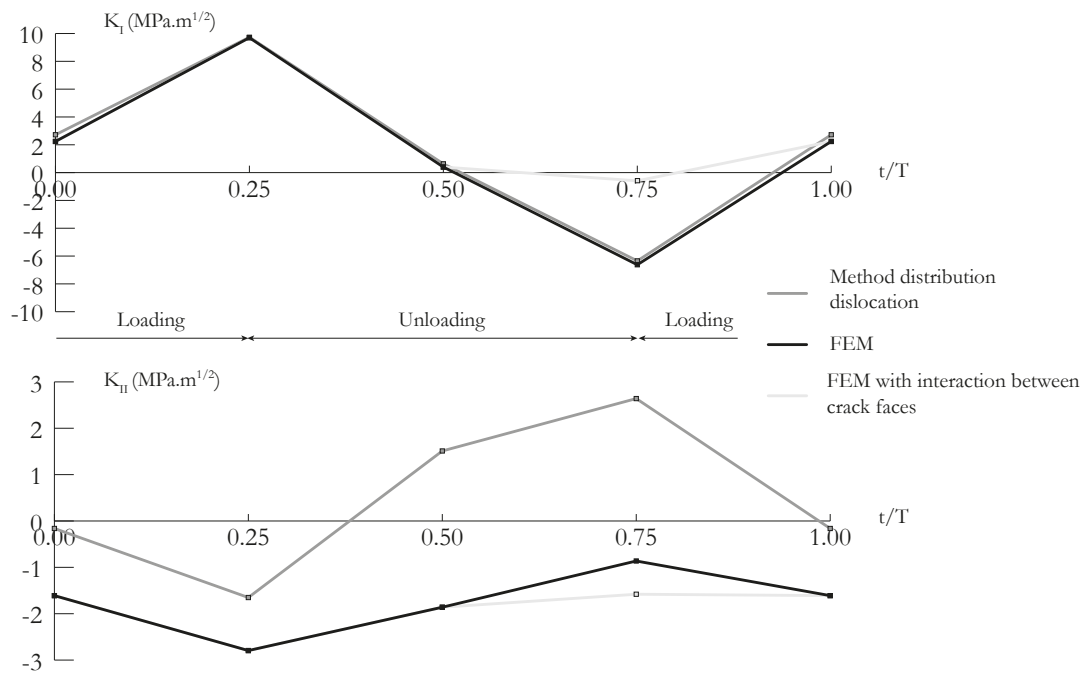


Figure 3.36: Time history of the SIF computed for an inclined crack.

For short cracks, the distributed dislocation method accurately predicts the stress intensity factor at the tip of a crack initiating at the edge of the contact. However, the method does not update the exterior geometrical perturbation generated by the crack presence, which particularly affect the calculation of the mode II stress intensity factor. Because of the crack closure phenomenon, assumptions are necessary to model the interaction between the crack faces. Because of the roughness of the fracture surface, it might be assumed that no sliding occurs when crack faces are in contact, which would limit the variations of  $K_{II}$  during the crack closure.

## Chapter 4

# Experimental results

### 4.1 Results of cylinder/plane fretting fatigue test

On the initial stage on the project, fretting fatigue test with dogbone specimen and a cylindrical indenter with a 20mm radius was carried out using the initial set up described in SEC.3.2.2 and by Martins et al. (2008). The pick pressure was fixed to  $p_0 = 700MPa$  and the fatigue and tangential load were changed to determine the strength limit. The main objective of this study was to compare these results with equivalent tests but with a 70mm pad radius. In this setting, the fretting apparatus initially used happened to be unable to provide the tangential force necessary to equal both conditions  $p_0$  and  $Q/\mu P$  of the test with 20mm pad radius. In other words, the apparatus was not stiff enough to allow such forces. A more robust fretting set up was designed and the pick pressure was decreased to  $p_0 = 500MPa$  to ensure the feasibility of the comparison between the two gradients considered. At last, a new type of fretting fatigue test using a spherical contact and a tri-axial set up was designed.

#### 4.1.1 First set of tests

The aim of these tests was to find the fretting condition threshold separating failure from infinite life (here defined by tests which reached  $10^6$  cycles). To achieve this, the pick pressure,  $p_0$ , was fixed for all tests at 700MPa (as  $P$  and the pad radius ( $R = 20mm$ ) are constants), and an initially high fatigue load was decreased from test to test until the run out condition was achieved. Test frequency was fixed to 10Hz.

#### Dependence between tangential and fatigue force

As detailed in SEC.3.2.2, the shear load depends not only on  $B$  and the stiffness of the apparatus, but also on the length of the specimen above the contact line. Here, the horizontal flexible beam of the fretting apparatus and the position of the pads along the specimen were defined so that the ratio between the bulk and the tangential force  $B/Q$  was set to be around 10.

#### Procedure

After the specimen was mounted on the servo-hydraulic machine, the first step in the loading program was to apply the mean bulk load, so that the load ratio was set to 0. The fretting pads were then clamped by a constant normal contact load,  $P$ . This procedure means that the mean load/stress provokes no disturbance on the contact setting. The sinusoidal (fatigue) bulk load,  $B$ , was finally

applied in small steps until reaching the prescribed value for each test. The gradual increase of the bulk load and its frequency is necessary to avoid the pads sliding at the beginning of the test when the coefficient of friction,  $\mu$ , is still very low. Therefore, as the shear load is proportional to the bulk load, its gradual increase will allow the slip zones to grow smoothly together with  $\mu$ .

## Results

FIG.4.1 contains the experimental points in a  $\sigma_{Bmax}/p_0 \times Q/\mu P$  diagram. Notice that the loading threshold is somewhere between  $0.242 < \sigma_{Bmax}/p_0 < 0.258$  and  $0.48 < Q/\mu P < 0.53$ . Also worth of notice is the fact that for each of these limiting values of this  $\sigma_{Bmax}/p_0$  range, at least three tests were carried out to evaluate the repeatability of such conditions.

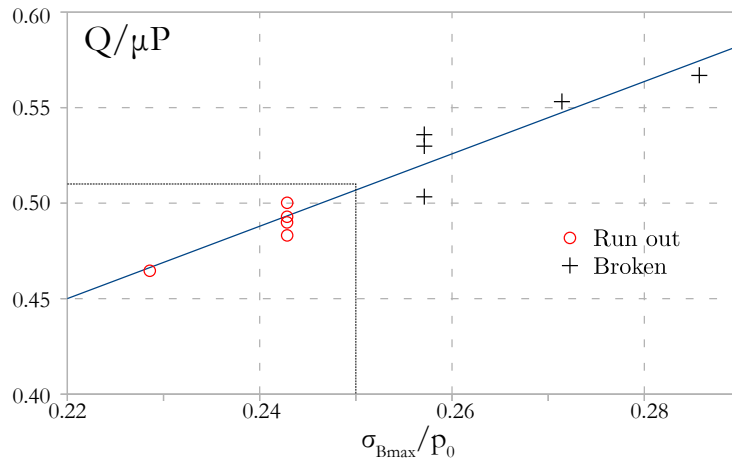


Figure 4.1: Experimental result, determination of the limit broke/last  $10^6$ .

Note that for the same  $\sigma_{Bmax}/p_0$ , these tests have slightly different values for  $Q/fP$ . This is mainly due to the fact that it is not possible to guarantee from test to test that the pads will be placed at the same position along the specimen length and this will interfere in the measured value of the shear load. Table 4.1 reports the salient parameters for the tests carried out and the registered lives.

Test	$\sigma_{Bmax}/p_0$	$Q/\mu P$	Nb cycles
1	0.228	0.464	1000000
2	0.284	0.566	358681
3	0.256	0.503	593547
4	0.250	0.512	1000000
5	0.256	0.536	509677
6	0.241	0.492	1000000
7	0.256	0.529	775445
8	0.242	0.500	1000000
9	0.272	0.553	645763
10	0.242	0.489	1000000

Table 4.1: Test parameters and results.

Because we have two parameters varying at the same time, is it difficult to analyze the result in terms of life. A 3D representation of the results is presented in FIG.4.2. In the range of load used, it seems possible to fit the results linearly if the life is considered with a log-scale. Note that tests stopped at  $10^6$  cycles are not considered for the calculus of the plane, and the fit is realized by minimizing the normal quadratic distance.

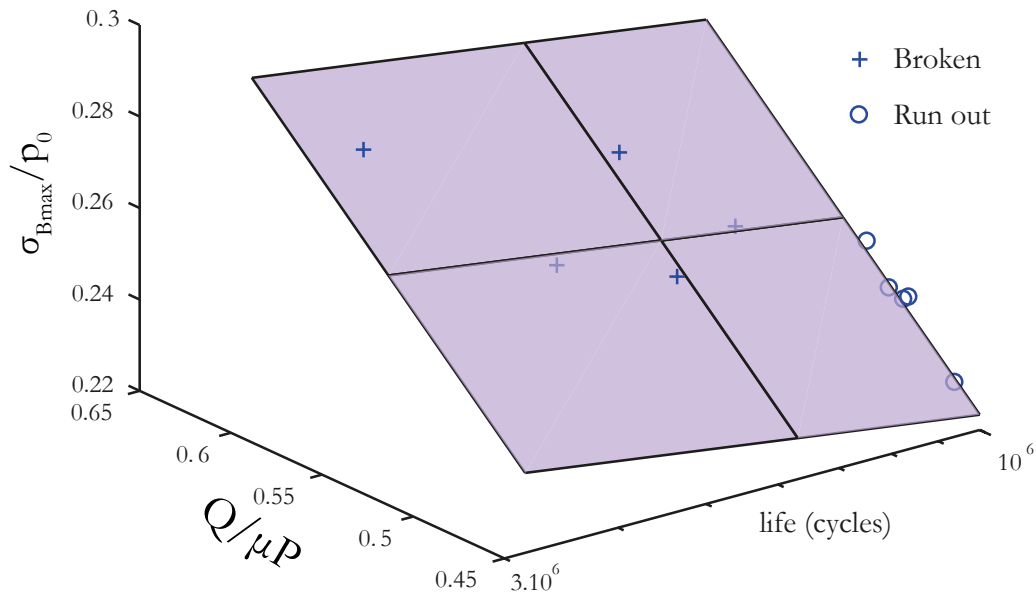


Figure 4.2: 3D representation of the results in a  $\sigma_{Bmax}/p_0 - Q/\mu P - \text{life}$  graphic.

As follows, one will assume that the threshold condition between complete fracture of the specimen and run out is obtained by setting  $Q/fP = 0.51$ ,  $\sigma_{Bmax}/p_0 = 0.25$ .

### Post failure investigation

From fracture surface observations under a spectrum electron microscope (SEM), the crack initiation and growth mechanisms for the fretting fatigue conditions here imposed were investigated. FIG.4.4a shows an example of the damage caused on the specimen surface by the fretting mechanism, which is typical of the partial slip regime. It is clear that there are two slip/fretted zones around a preserved/stick zone. In this figure, the theoretical dimensions of the contact,  $a$ , the stick zone,  $c$ , and the offset,  $e$ , are indicated, and a scaled representation of the slip/fretted zones is represented. The contact size appears to be slightly larger than the dimension predicted by the Hertz theory.

FIG.4.3a shows a picture of the edge of the specimen from test number 4. The drop of the local pressure on the edge of the contact looks even more severe than computation with 3D FEM (FIG.4.3b).

Crack initiation invariably started inside of the fretting damage zones (slip zones) from either of the two specimen sides. Further on, multiple crack initiations usually occurred within one of these slip zones somewhere close to the trailing edge of the contact, as illustrated in FIG.4.4b and FIG.4.4c. Initially, these cracks grew inwards the contact zone. For a very short distance, they propagated a plane nearly perpendicular to the axial main fatigue load direction and then perpendicular to it, until one unique crack front appeared (see FIG.4.4c and FIG.4.4d). The inclination of the crack initiation plane was quantified by using a confocal optical microscope (Keyence VHX-5000). The crack plane

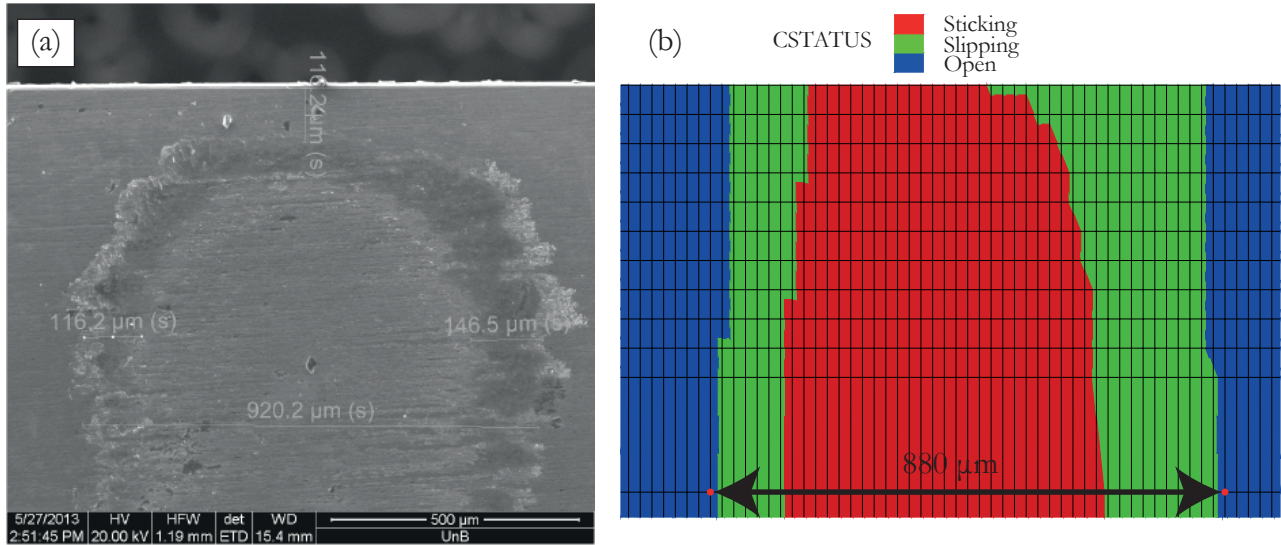


Figure 4.3: (a) Edge of the fretting mark of test number 4 (b) Contact status computed with a 3D FEM.

usually formed an angle with the specimen surface, which varied between  $-100^\circ$  and  $-115^\circ$  (FIG.4.4d). The transition to a mode I crack growth occurred after the crack reached a size varying between  $40\mu m$  and  $100\mu m$ .

In the first set of fretting fatigue test realized, the bulk load maximum for  $10^6$  cycles was  $175MPa$  which represents a reduction of about 75% of the fatigue limit in plain fatigue. Multiple crack initiation sites were observed in the slip band of the contact, but the cracks leading to failure of the specimens initiated at the vicinity of the trailing edge of the contact.

## 4.1.2 Comparison among different gradients

### 4.1.2.i Introduction

The objective of the test campaign is to quantify the influence of the stress gradient in fretting fatigue. For the analysis, the crack is assumed to initiate at the trailing edge of the contact and in a direction perpendicular to the contact surface. In order to generate two different gradients, the set of pads with radii  $R = 20mm$  and  $R = 70mm$  were considered. Indeed, when the peak pressure  $p_0$ , the bulk load  $s_B$  and the ratio  $Q/fP$  are constant, the different radii of the pads will affect the stress state neither at the surface, nor deep into the specimen. Only the decrease of the stress state will vary. FIG.4.5 illustrates as an example the amplitude and mean value of the stress  $\sigma_{xx}$ , along the vertical of the contact edge, for the two radii under the same conditions.

Constant peak pressure  $p_0 = 500MPa$  and ratio  $Q/fP = 0.46$  was chosen to ensure the feasibility of the test for both pad geometries, and the test frequency was fixed to 10Hz. In pure fretting, this loading condition would generate the surface mark illustrated in FIG.4.6a-b, while the fatigue load adds an asymmetry (FIG.4.6c-d), as detailed in SEC.2.1.3.ii.

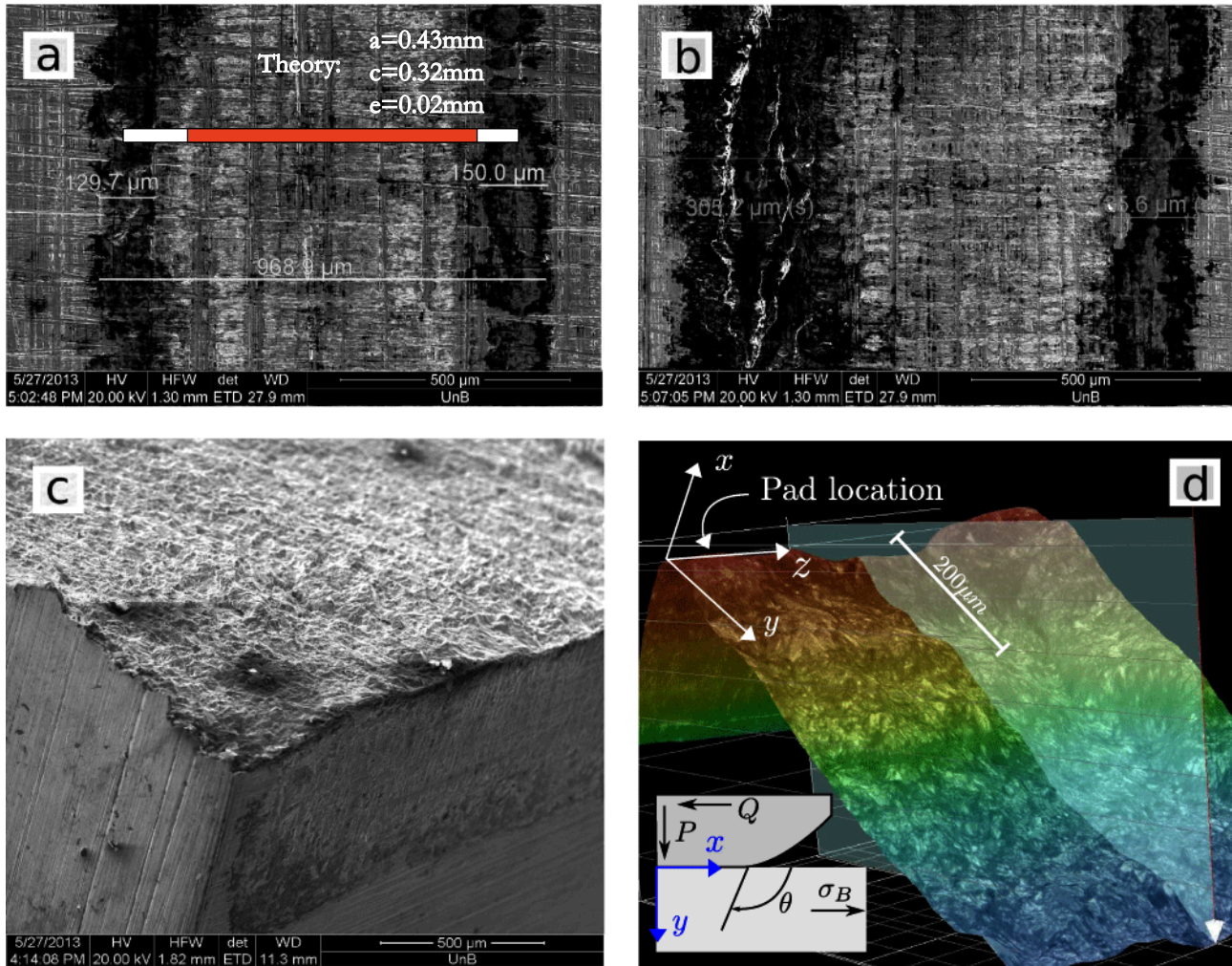


Figure 4.4: SEM photos tests of TAB.4.1 a) A typical fretting-fatigue mark on a unbroken specimen (test 1) b) Unbroken specimen at  $10^6$  cycles with presence of multiple crack initiation (test 4) c) fracture surface of a crack which initiates close to the trailing edge of the contact (test 3) d) Crack profil using a confocal optical microscope (test 7, initial angle of  $-110^\circ$ ).

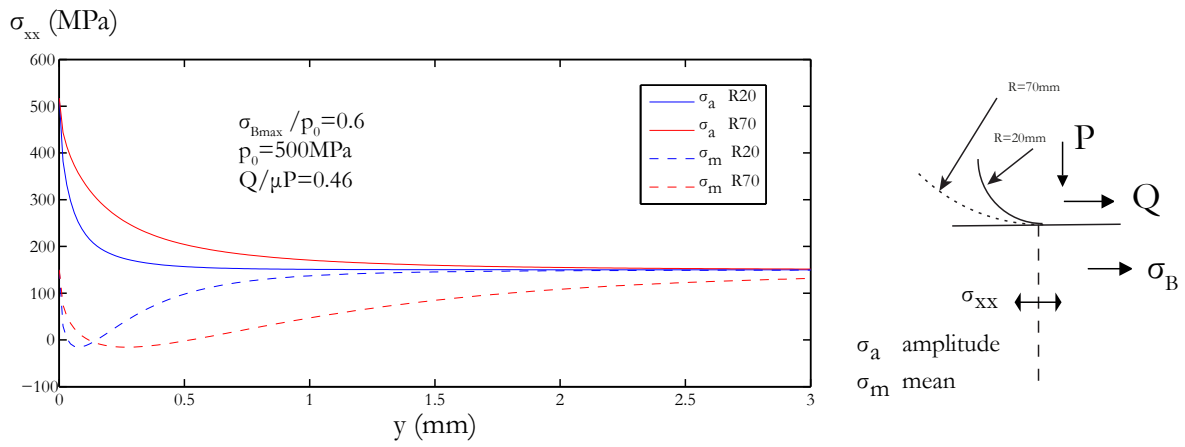


Figure 4.5: Illustration of the stress gradient:  $\sigma_{xx}$  for two pad radii ( $p_0 = 500\text{MPa}$ ,  $\sigma_{Bmax} = 300\text{MPa}$  and  $Q/fP = 0.46$ ).

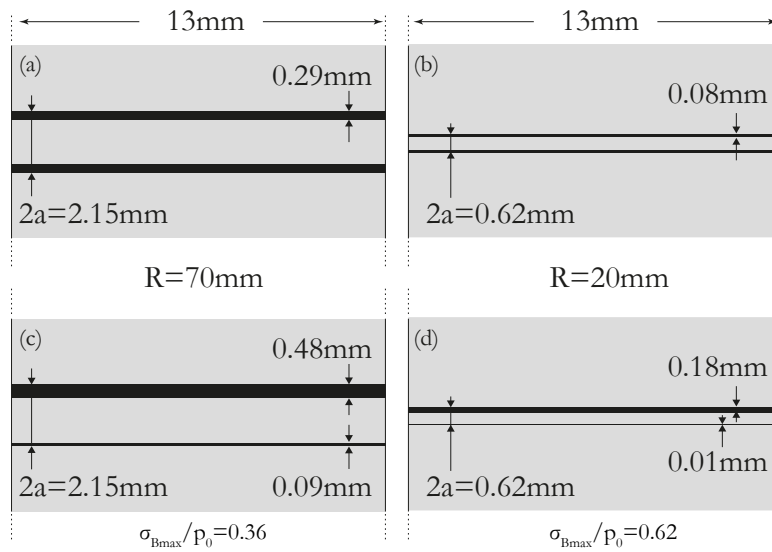


Figure 4.6: Scaled fretting contact mark for  $p_0 = 500\text{MPa}$  and  $Q/fP = 0.46$ , on the top in pure fretting, below, with a fatigue load added.

#### 4.1.2.ii Results

A staircase procedure was used to determine the critical fatigue load for running out conditions. In this setting and because of the dependence between tangential and fatigue forces, the position of the pads along the specimen had to be adapted so that the ratio  $Q/fP$  remained constant. Even if this dependence was a priori determined, it remains that small variations of the stabilized ratio  $Q/fP$  was observed between each test. TAB.4.2 reports the salient parameters for the tests carried out and the registered lives.  $P'$  is the normal force measured after stabilization of the fatigue cycles. The test surviving  $10^6$  cycles were stopped.

Test	Pad radius	$\sigma_{Bmax}/p_0$	$Q/\mu P$	Life (cycles)
11	20	0.6	0.45	$10^6$
12	20	0.6	0.46	$10^6$
13	20	0.612	0.46	$10^6$
14	20	0.62	0.47	$10^6$
15	20	0.62	0.47	$10^6$
16	20	0.64	0.47	$10^6$
17	20	0.68	0.46	225780
18	20	0.76	0.50	163840
19	20	0.64	0.46	478632
20	20	0.64	0.46	488632
21	20	0.62	0.46	723487
22	70	0.38	0.35	$10^6$
23	70	0.36	0.46	$10^6$
24	70	0.60	0.457	168266
25	70	0.56	0.465	248790
26	70	0.48	0.465	379841
27	70	0.40	0.40	398069
28	70	0.40	0.42	579954
29	70	0.38	0.505	583981
30	70	0.44	0.458	635177
31	70	0.42	0.45	696665
32	70	0.38	0.46	707132
33	70	0.36	0.47	971557

Table 4.2: Test parameters and results.

As before, results in a 3D ( $\sigma_{Bmax}/p_0 - Q/\mu P - \text{life}$ ) graph are presented in FIG.4.7. Even if this representation is difficult to analyze, it allows to compute a fit line on the plane  $Q/\mu P = 0.46$ , even such small variations of the tangential load, were measured from one test to another. Projection of the results on a 2D graph are presented in FIG.4.8.  $\sigma_{Bmax}/p_0 - Q/\mu P$  graph illustrates the scatter of the results while the  $\sigma_{Bmax}/p_0 - \text{life}$  graph shows the trend of the life reduction with the increase of the bulk load.

For the equivalent load setting,  $\sigma_{Bmax}/p_0 = 0.6$  and  $Q/\mu P = 0.46$ , results shows that with the high-stress gradient considered (R=20mm), the specimen survived  $10^6$  cycles whereas for the lower gradient (R=70mm), the failure occurred at  $1.7 * 10^5$  cycles. Moreover, and considering  $Q/\mu P = 0.46$ , the fit of the results indicates that  $10^6$  life cycles are obtained for a fatigue load equal to  $\sigma_{Bmax}/p_0 = 0.61$

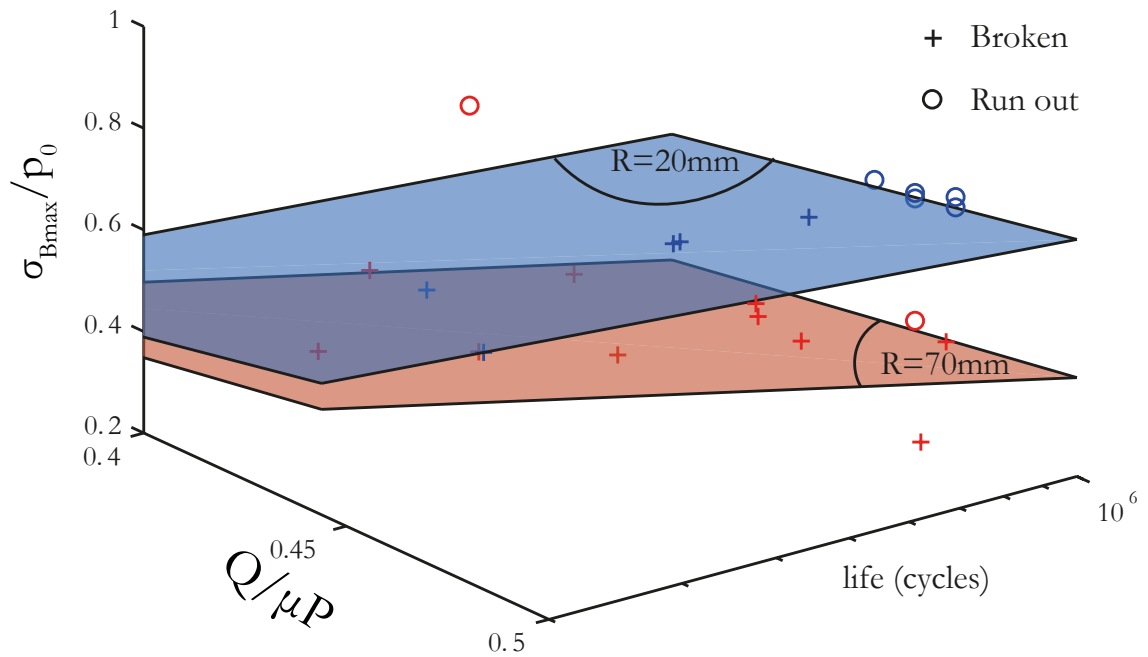


Figure 4.7: 3D representation of the results for both pad in a  $\sigma_{Bmax}/p_0 - Q/\mu P - \text{life}$  graphic.

with the 20mm pad radius, while it is only around  $\sigma_{Bmax}/p_0 = 0.35$  when the larger radius is used.

The effect of the stress gradient was clearly highlighted here. Under the same loading conditions, the tests with a strong stress gradient (20mm pad radius) survived five times longer than a test with a smoother gradient (70mm pad radius). Moreover, considering a constant tangential load ( $Q/\mu P$ ), the fatigue limit (i.e. the maximum bulk load) for test with  $R=70\text{mm}$  was reduced to 175MPa while for the one with  $R=20\text{mm}$  it was reduced to 305MPa.

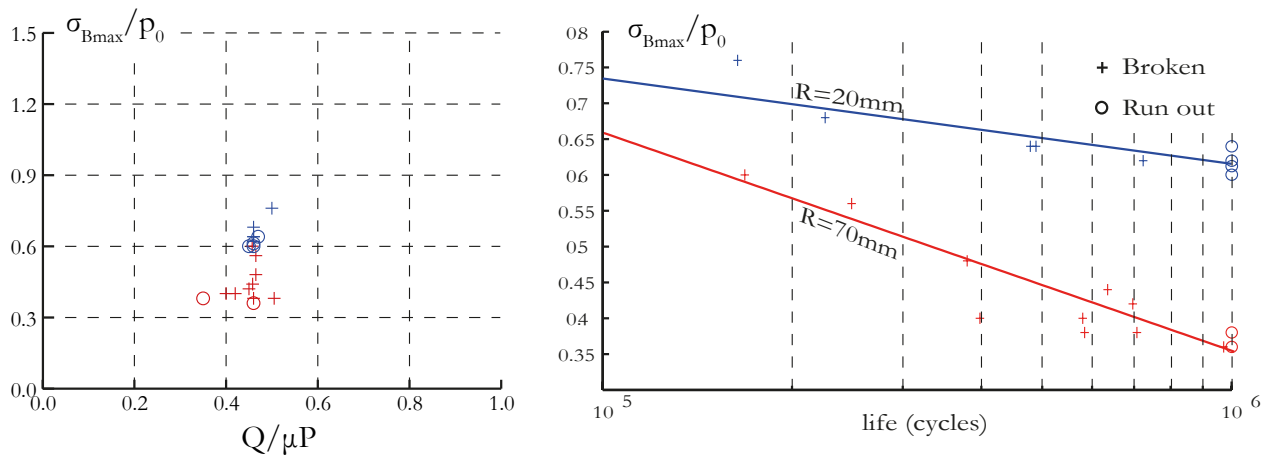


Figure 4.8: Representation of the results for both pads in a  $\sigma_{Bmax}/p_0$  – life graphic and projection of the fit computed in 3D.

4.1.2.iii Post failure investigation

**Fretting scar** FIG.4.9 presents pictures realized with a scanning electron microscope, of the fretting mark of the specimen used in tests number 14 and 24 of TAB.4.1. Contact size generally measured at the middle of the cross section are slightly superior to the analytical prediction illustrated in FIG.4.6. Limits of the sliding zones are not always clear nor regular, particularly with the 20mm pads.

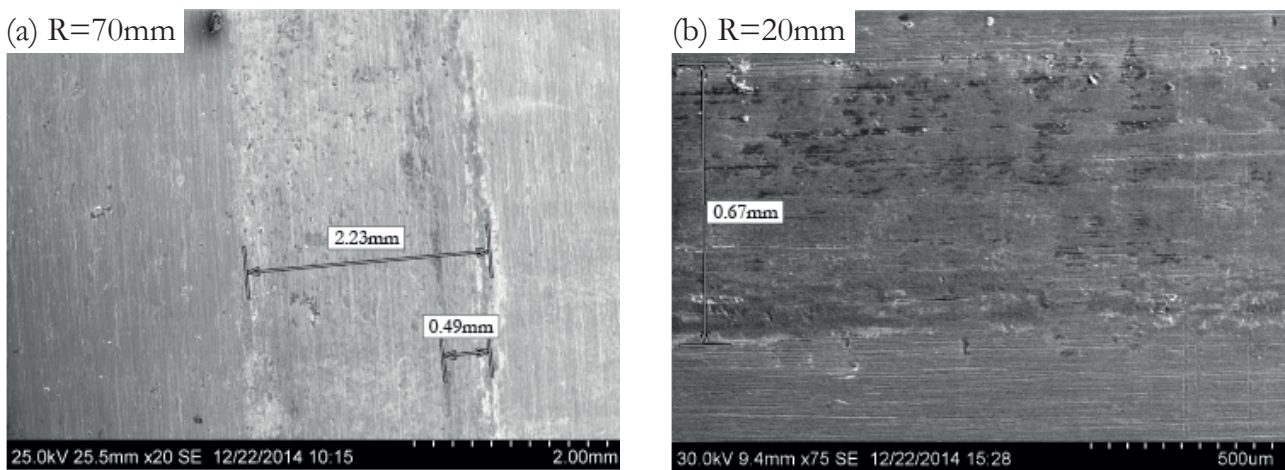


Figure 4.9: a) Fretting scar of unbroken specimen b) Contact status .

For the pictures presented here, the peak pressures,  $p_0$ , leading to this contact size would be respectively  $518MPa$  and  $540MPa$  in tests, using a pad radius of 70mm and 20mm. This variation may be caused by the 3D aspect of the contact (edge effect), discussed in SEC.3.3.2.

**Fracture surface** Most of the fracture surface has been observed with a confocal optical microscope and with a scanning electron microscope. Confocal microscope was used to analyze the topology of the initial stage of the crack while the SEM revealed the microscopic phenomenon of the crack growth. FIG.4.10 regroups the step of the observation and analysis of the broken specimen. The Keyence VHX-5000 microscope is first used to identified the possible initiation sites, and build the topology. The software MountainsMap (Digital Surf) was used to reoriented the coordinates and perform an average over 0.5mm of 10 profiles around the location of the possible initiation spots. For many fracture surface, multiple initiation spots are present.

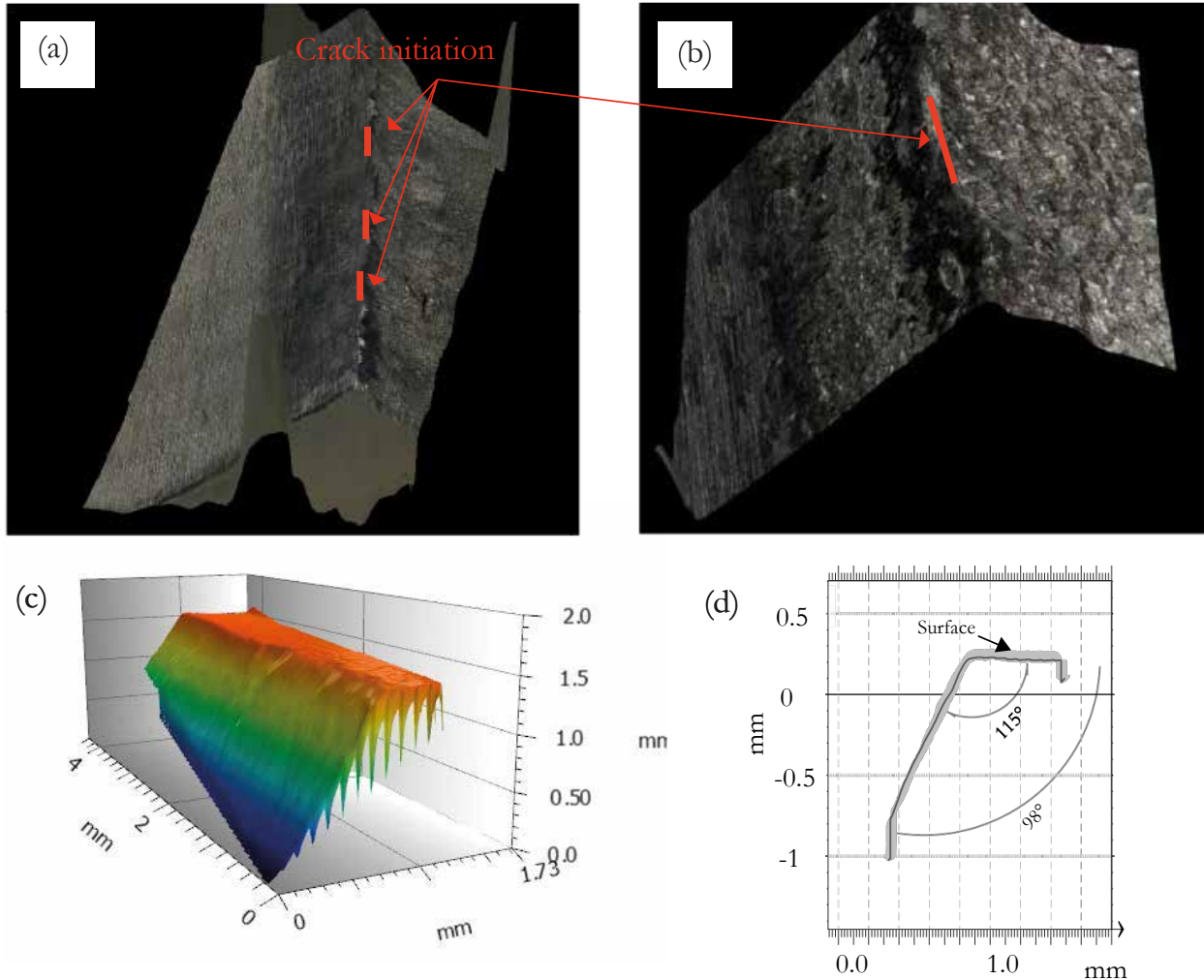


Figure 4.10: (a-b) topology of fretted part of the broken specimen of test 20 and 42 (c) 3D analysis of the topology of the out of contact part of the specimen 20 (d) estimation of the angular initiation by averaging over 1mm millimeter (out of contact-specimen 20).

Because of the variation of the results and imprecision of this method, few conclusions can be made:

- The initial angle between the surface and the crack is smooth, probably because the fretting and the contact damage the lips while the crack is propagating. As a result, estimation of an

inclination can only be made from about  $50 - 100\mu m$  to the surface.

- Fracture plane is always inclined toward the contact.
- From  $100\mu m$  until  $300 - 800\mu$  the angles measured were between  $-110^\circ$  and  $-130^\circ$  while after the direction tend to be perpendicular to the surface.

FIG.4.11 regroups images of the fracture surface of the broken specimen number 32. Several stages of the crack propagation can be identified:

- *The initiation in mode II.* A first initiation region can be observed. In this area, some zones of the crack surface are damaged or even polished. Some fatigue striations appear collinear to the crack propagation direction. This phase is then highly dominated by the mode II.
- *Mixed mode transition.* From  $200\mu m$  to  $1mm$ , the surface is typical of a cleavage fracture controlled by the mode I. Some grain are however still polished, which let us think that the mode II still plays a role, but their number decreases progressively. It is then a zone of transition between an initiation exclusively govern by the mode II and a propagation in mode I.
- *Propagation in mode I.* Fracture striations are orthogonal to the direction of propagation, with a distance between the striation increasing when going to the center of the sample.

Analysis of the fracture surface shows different stages in the growth of the fretting fatigue cracks. In the initial stage, the crack propagates under mixed mode condition up to a distance comparable to the contact width, and after that the crack propagation is governed by the axial stress perpendicular to contact interface.

#### 4.1.2.iv Crack growth

FIG.4.12 presents a picture of the crack present in the specimen of test number 23. While the test was stopped after reaching  $10^6$  cycles, visual observation reveals the presence of a long crack. In order to analyse the cracking evolution, the test was repeated and stopped at  $2.5 \cdot 10^5$ ,  $5 \cdot 10^5$  and  $7.5 \cdot 10^5$  cycles. Same procedure was realized for the critical load identified for 20mm pad radius. Loading conditions of the interrupted test are summarized in TAB.4.3.

Test	Pad radius	$\sigma_{Bmax}/p_0$	$Q/\mu P$	Stopped at:	crack/defect size observed ( $\mu m$ )
15	20	0.62	0.47	$10^6$	10
34	20	0.62	0.47	750000	no crack/defect
35	20	0.62	0.47	500000	6
36	20	0.62	0.47	250000	no crack/defect
23	70	0.36	0.46	$10^6$	$> 4mm$
37	70	0.36	0.47	750000	20
38	70	0.36	0.48	500000	10
39	70	0.36	0.50	250000	damage $< 5\mu m$

Table 4.3: Test interrupted.

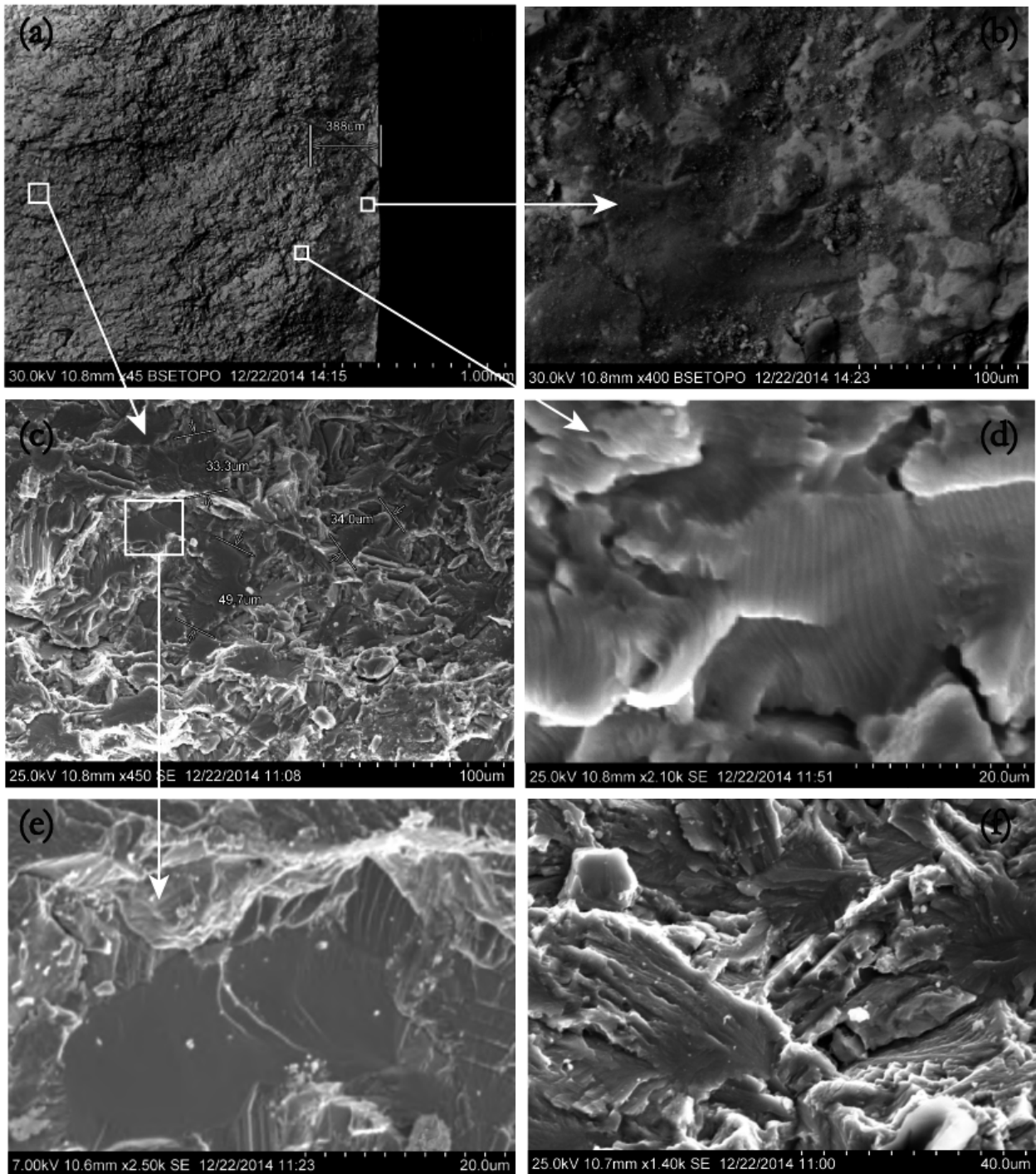


Figure 4.11: Fracture surface of test number 32.



Figure 4.12: SEM picture of specimen 23, after cutting and polishing.

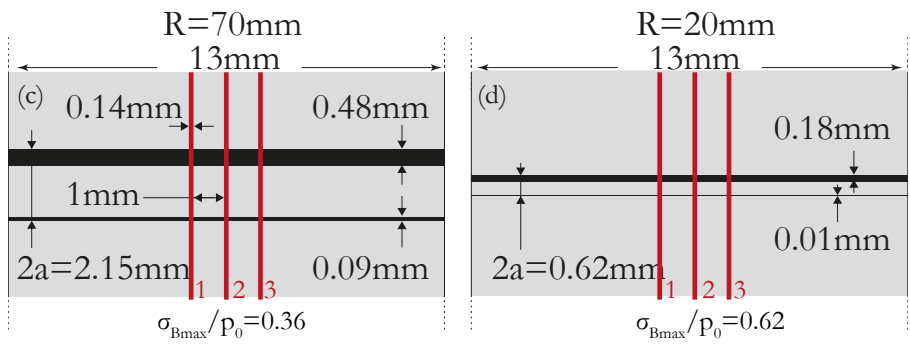


Figure 4.13: Fracture surface of test number 32.

Specimens were then cut at 3 different positions, using a diamond cutting wheel with a 0.14mm thickness. FIG.4.13 illustrates the position of the cuts. Surfaces were polished progressively with papers of grains size from 480 to 4000, then observed with a SEM.

FIG.4.14 compiles examples of pictures taken at the vicinity of the contact edges. Few cracks were clearly identified. Pictures (a) and (b) illustrate what could be a very short inclined crack. But in most cases, only surface defects were observed. Pictures (c) and (d) show examples of defects observed near the contact edges. The maximum size of the crack from defects for each specimen are referenced in TAB.4.3. For all tests, no crack larger than  $20\mu m$  were observed.

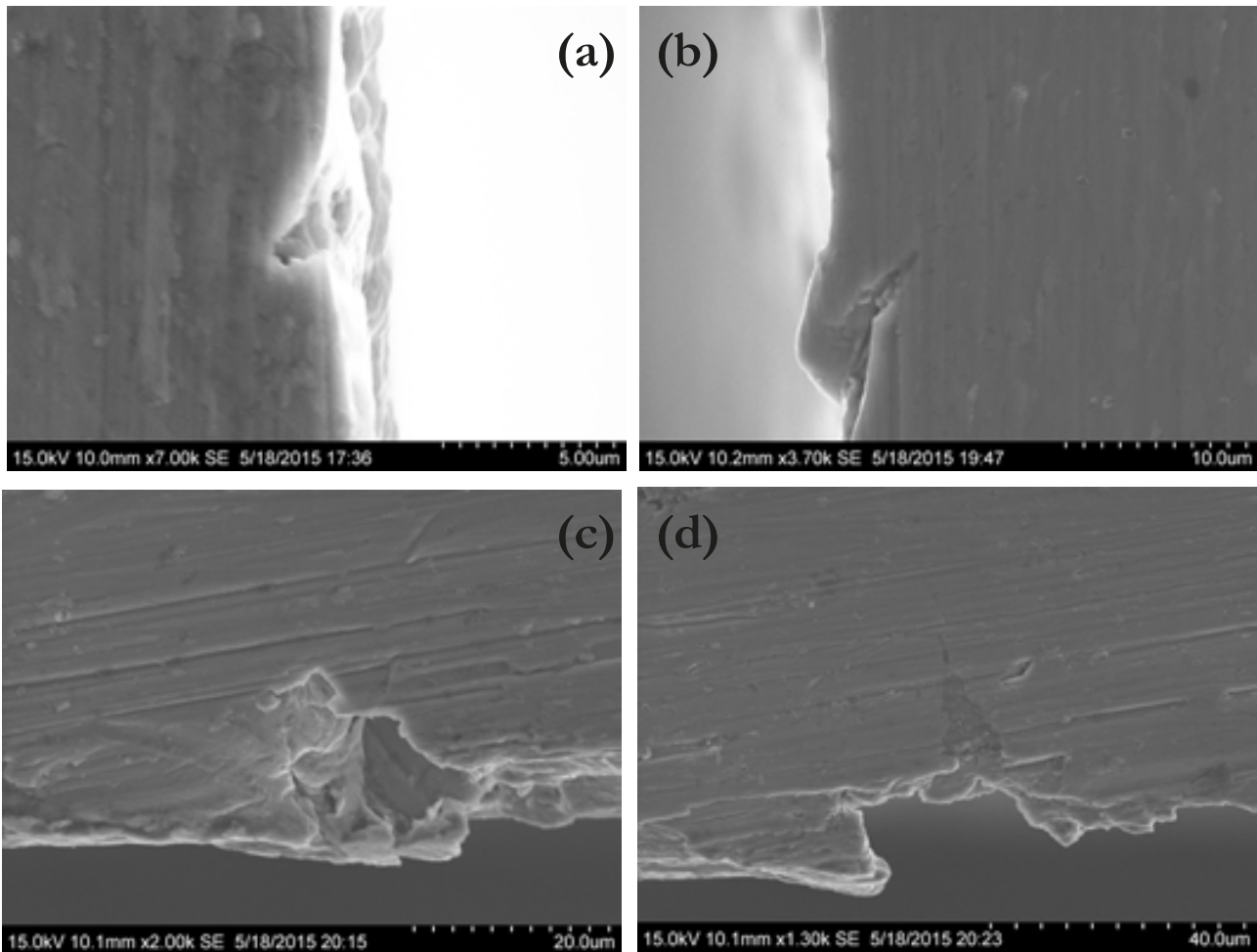


Figure 4.14: Example of crack observed on the cut specimen: (a-b) test 35, respectively on the cut 1 and 2 (c) test 38 on the cut 2 (d) test 37 on cut 2.

The analysis of the threshold test stopped at 1/4, 1/2 and 3/4 of total life did not reveal any clear crack growth. The cracks and defects observed at the vicinity of the trailing edge had dimensions inferior to  $20\mu m$ .

## 4.2 Results of spherical/plane fretting fatigue test

### 4.2.1 Objective

The initial objective was to experiment a different contact geometry and different loading condition than conventional cylinder/plane test, but with similar local stresses.

The relation between the peak pressure and the normal load is given :

$$p_0 = \frac{3P}{2\pi^2} \quad (4.1)$$

where  $a$  is the radius of the circular contact region:

$$a^3 = \frac{3PR}{3E^*} \quad (4.2)$$

Assuming a spherical pad radius of  $R = 70mm$ , a normal force  $P = 750N$  necessary to have  $p_0 = 500$ . The resulting radius of the contact is  $a = 0.846mm$ . As for the cylinder configuration, when the normal load  $P$  is maintained constant and the tangential force  $Q$  is cyclic, slip appears at the contact edge and covers an annular region with an outer radius  $a$  and an inner radius  $c$  with:

$$c^3 = a^3 \left( 1 - \frac{Q}{\mu P} \right) \quad (4.3)$$

If we keep the condition used beforehand, i.e.  $Q/\mu P = 0.46$  or  $Q = 172N$ , the radius of the central stick zone would be  $c = 0.69mm$ . If the cyclic bulk stress,  $\sigma_{Bmax} = 175MPa$ , is added in the direction of the tangential load, the distribution of the shear surface is no longer axially symmetric. Wittkowsky and Birch (2000) determine the offset,  $e$ , for plane strain conditions. However in the present objective, the fatigue stress is not uni-axial, but equi-biaxial, and a more modified analytic formulation would be needed. Finite element appeared to be a more simple methodology to compute the stress field of this contact.

A finite element model was then designed and used to determine the external force to apply on the arm of the cruciform specimen in order to obtain the local forces at the center of the specimen. FIG.4.15a presents a photo of the sphere on the cruciform specimen while FIG.4.15b-c shows its initial finite element model. Mesh size and contact formulation are very similar to the previous 3D model. The size of the 4-node linear tetrahedron elements under the contact are  $10\mu m$  and Lagrange formulation is used for the contact definition, with a fretting ratio  $\mu = 0.5$ . In this model, only the z-displacement of the pad is allowed, later in a second model the displacement along x and y were controlled to adapt to experimental measures (FIG.4.15d).

Note that with this FEM, we assume that pads cannot move in the plane of the specimen. In this setting, the force difference between cylinder of the axis  $x$  and  $y$  necessary to obtain a tangential amplitude  $Q = 172N$ , is  $F_D = 580N$ . On the other hand, a maximum average force  $F_{Amax} = 60kN$  was found necessary on each axis horizontal axis to obtain a fatigue stress  $\sigma_{max}^* = 175MPa$  in the direction tangential (and perpendicular) to the tangential load.

This initial test was realized and the sample broke in one of the arms after few thousand of cycles. And the contact surface did not show any visible fretting scar. It was concluded that the assembly cylinder/pad on the axis  $z$  was not 'resisting' to the displacement of the sample center, i.e. was acting as a string and not a rigid body. Other conclusions discussed in SEC.3.2.4.ii were done, and the objective were revisited.

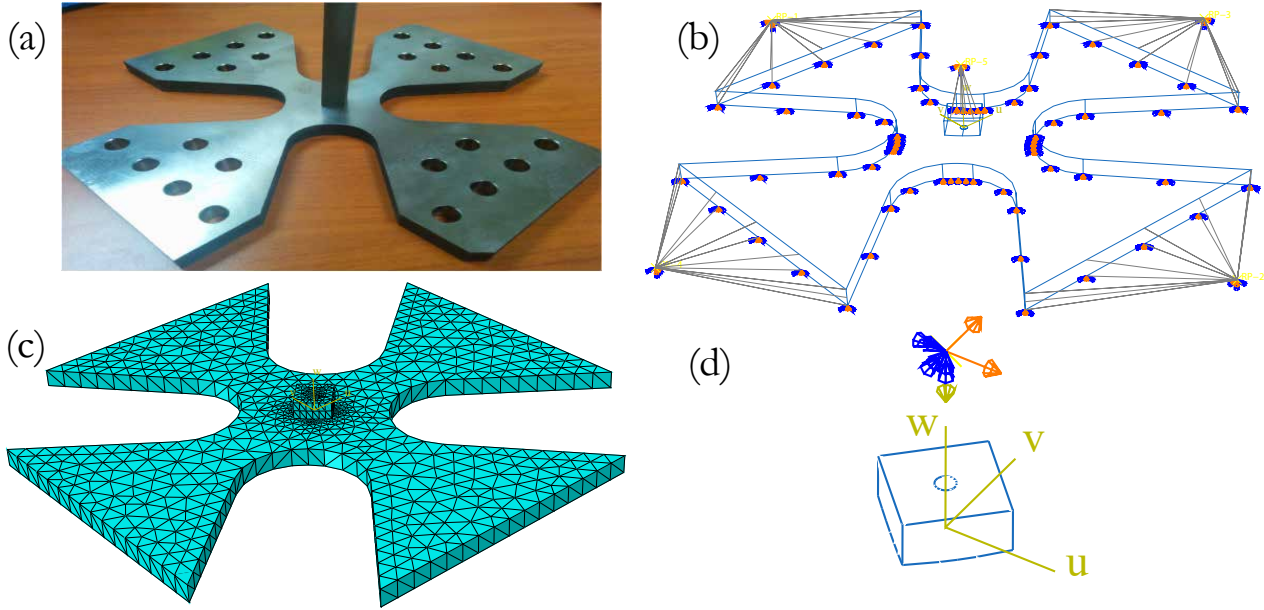


Figure 4.15: (a) Photo of the sample and a pad (b) Boundary conditions of the 3D FEM (c) Mesh (d) boundaries condition of the pad.

The design of the cruciform specimen and the experimental limitation of the set-up made impossible the realization of a test leading to fretting fatigue failure of the specimen. The analysis was limited to the study the fretting fatigue scars and the comparison with the FEM prediction.

#### 4.2.2 Experimental test realized

Test	$F_{Axy}$ in kN	$F_{Dxy}$ in kN	$F_{Az}$ in kN	$F_{Dz}$	$\delta_{x'}$ ( $\mu\text{m}$ )	Q (N)
40	10	3.2	0.8	0	13	246
41	10	3.8	0.8	0	15	302
42	10	4.8	0.8	0	20	329

Table 4.4: Parameters of the ‘fretting equi-biaxial’ tests.

The normal force applied on the specimen was fixed to  $F_{Az} = 0.8\text{kN}$ . The fatigue force,  $F_{Axy}$ , applied on the arms of the sample was fixed to  $10\text{kN}$ , applied with a ratio  $R_\sigma = -1$ . This insures that the sample will not break in the reduction of the arms section. The force difference  $F_{Dxy}$  was increased progressively, having for effect to increase the local tangential force  $Q$ .

The amplitude of displacement,  $\delta_{x'}$  and  $\delta_{y'}$ , of the one pad extremity were record by the laser in the direction along  $x'$  and  $y'$  (FIG.3.15). In the direction  $y'$ , the valor of displacement,  $\delta_{y'}$ , measured were so small that there will be considered null in the following.

Test setting and measure of the displacement of the upper pad are detailed in TAB.4.4. This displacement is inputted in the FEM model (FIG.4.15d), which allows a computation of the reaction tangential force,  $Q$ . The ratio  $Q/\mu P$  can be estimated for the three test. It gives respectively 0.62, 0.75 and 0.82. Moreover, FIG.4.16 illustrates presents the fretting scars of the upper contact of each

of the three tests. The dashed line represents the theoretical contact surface, while the transparent layer is the contact status computed with finite elements (blue= no contact, green = slipping and red = sticking) at the maximum loading.

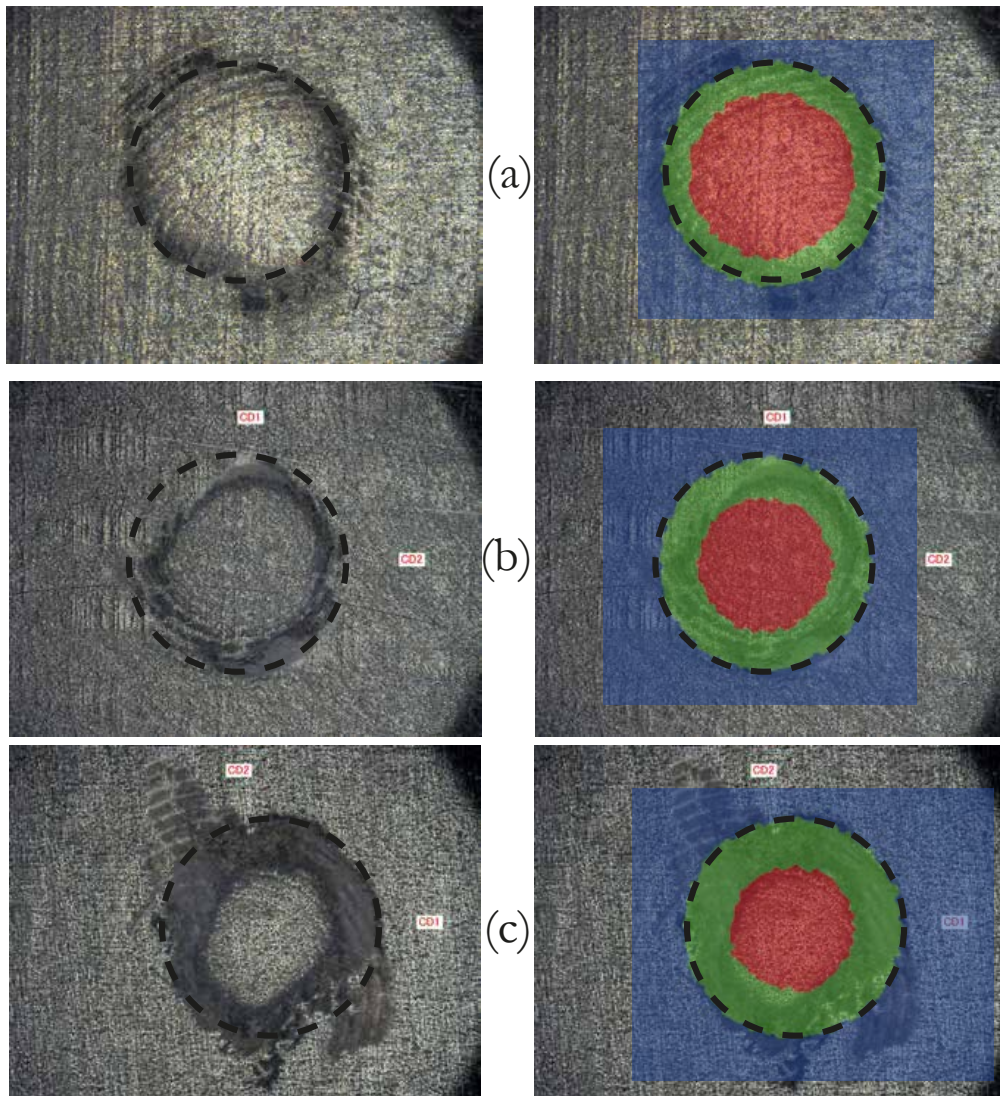


Figure 4.16: Fretting scars (upper contact) of the three fretting equi-biaxial tests.

The slip zone distribution around the central stick area was computed with a finite element model where the displacement of the pad was controlled by the experimental measurement. The good agreement between the contact status computed and observed strengthened our trust in the value of the coefficient of friction.

### 4.3 Conclusion of the experimental tests.

Three fretting fatigue test sets were carried out with a configuration cylinder/plane. FIG.4.17 illustrates the course of the campaign.

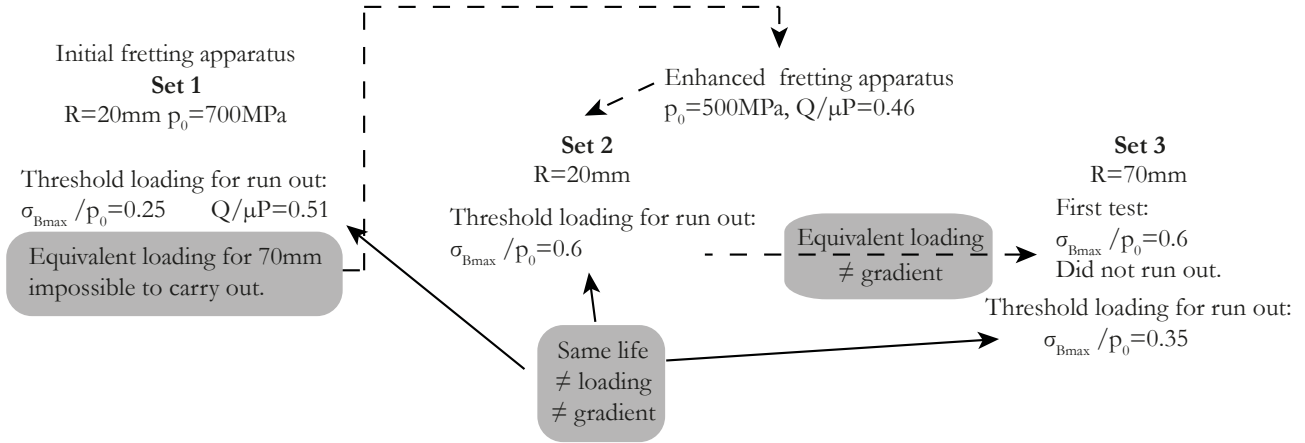


Figure 4.17: Methodology used for experimental tests.

The first set used a pair of 20mm radius cylindrical indenters loaded with a constant normal force calculated with the Hertz theory, so that a peak pressure  $p_0 = 700\text{MPa}$  should be obtained on the contact. The fatigue and tangential loading were decreased gradually and the threshold loading for run out was identified. We were unable to reproduce an equivalent loading for the 70mm pad radius cause of the limitation of the apparatus. An enhanced apparatus was designed, and the methodology was repeated with lower constant normal force. Moreover, in this second test set with the 20mm pad radius, we tried to maintain the same tangential test between each test, so that only the bulk load was decreased to identify the threshold loading for run-out.

The first test with 70mm pad radius was realized with a loading equivalent to this threshold. As the test broke, the test was repeated with lower fatigue loading, until reaching the run-out condition.

At the end, we highlight the effect of the stress gradient on the fatigue life of the sample. Indeed, under the same loading conditions, the tests with a strong stress gradient survived five times longer than a test with a smoother gradient.

Moreover, we identified three different loading thresholds presenting different stress gradient, but all leading to  $10^6$  cycles life:

Pad radius (mm)	$p_0$ in MPa	$\sigma_{Bmax}/p_0$	$Q/\mu P$
20	700	0.25	0.51
20	500	0.6	0.46
70	500	0.35	0.46

A new fretting fatigue test was designed around the Astree fatigue machine. This test configuration allows to realize fretting on a sample subjected to multiaxial fatigue load. The initial objective was to generate with similar stress gradient but using a spherical/plane contact geometry and a biaxial fatigue load. However, the design of the cruciform sample prevented us to reach local stress severe enough to brake the specimen by fretting fatigue and only three tests were carried out.



## Chapter 5

# Prediction of fretting fatigue life

### 5.1 Introduction

Two criteria will be analyzed and assessed. The objective being to see if they correctly evaluate the gradient effect and meet our experimental results. The first is the non-local multiaxial criterion proposed by Araújo et al. (2007). This model uses the Theory of Critical Distances and the Modified Wöhler Curve Method to predict the failure. The second method is  $\Delta K$ -based short crack arrest models. For both cases, the following statements will be initially assumed valid to describe the fretting fatigue problem:

- The material properties of the Ti-6Al-4V alloy of the literature can be used;
- The contact is in partial slip condition;
- The peak pressure is constant and defined by the Hertz formulation;
- The coefficient of friction is constant all over the contact surface and  $\mu = 0.5$ ;
- The stress field is elastic;
- The problem is 2D and in plane strain condition;
- The Mindlin analytical formulation of the surface traction can be used and the stress field and the sub-surface field can be calculated with the Muskhelishvili's potential theory;
- If a crack appears, it will initiate from the trailing edge of the contact and grow perpendicularly to the contact surface;

Some of those statements are discussed in the following subsections while others will be discussed after during the analyze of the criteria. In the last part of this chapter, a new criterion will be compared with the results of the first set of experimental results. This criterion has the particularity the LEFM classical quantities,  $K_I$  and  $K_{II}$  but also the T-stress.

#### 5.1.1 Material properties and coefficient of friction of Ti-6Al-4V alloy.

In SEC.2.2, we summarized the fatigue properties of the Ti-6Al-4V alloy observed in the literature. The fatigue limits,  $\sigma_{max}$ , adopted in this section are considered for  $10^6$  cycles life:

$$\sigma_{-1} = 480MPa \qquad \sigma_{0.1} = 640MPa \qquad (5.1)$$

The description of the stress intensity factor threshold from Boyce and Ritchie (2001) will be used here. By extrapolation on the line,  $\Delta K_{th}(R_\sigma)$ , of the FIG.2.44, the value  $\Delta K_{th,R_\sigma=-1} = 7.88 MPa.m^{1/2}$  will be used in the following.

### 5.1.2 On the use of the analytical formulation of the contact problem.

In order to be allowed to use the Mindlin analytical formulation of the fretting problem, the analysis has to be limited to the case of partial sliding, and the bulk stress has to be limited in order to avoid reverse sliding. Those two conditions may be written as:

$$\frac{Q}{\mu P} \leq 1 \quad (5.2)$$

$$\frac{\sigma_B}{\mu p_0} > 4 \left( 1 - \sqrt{1 - \frac{Q}{\mu P}} \right) \quad (5.3)$$

The Von Mises yield criterion might be used to verify the general elasticity of the fretting fatigue problem. FIG.5.1b illustrates the typical distribution of the maximum Von Mises Criterion encountered during a fretting fatigue cycle. Two critical zones appear clearly; zone 1 is directly associated with the normal force of the Hertz contact but is also influenced by the fatigue force; zone 2 is located around but not exactly at the trailing edge of the contact. While considering a fixed peak pressure equal to  $p_0 = 500 MPa$  the zone 2 will be the first to yield. The maximum of the Von Mises criterion was computed in this zone for various fatigue and tangential load, then compared to the yield point,  $R_{p0.2}$ . The elastic domain can be plotted in a  $\sigma_{Bmax}/p_0 - Q/\mu P$  map (FIG.5.1).

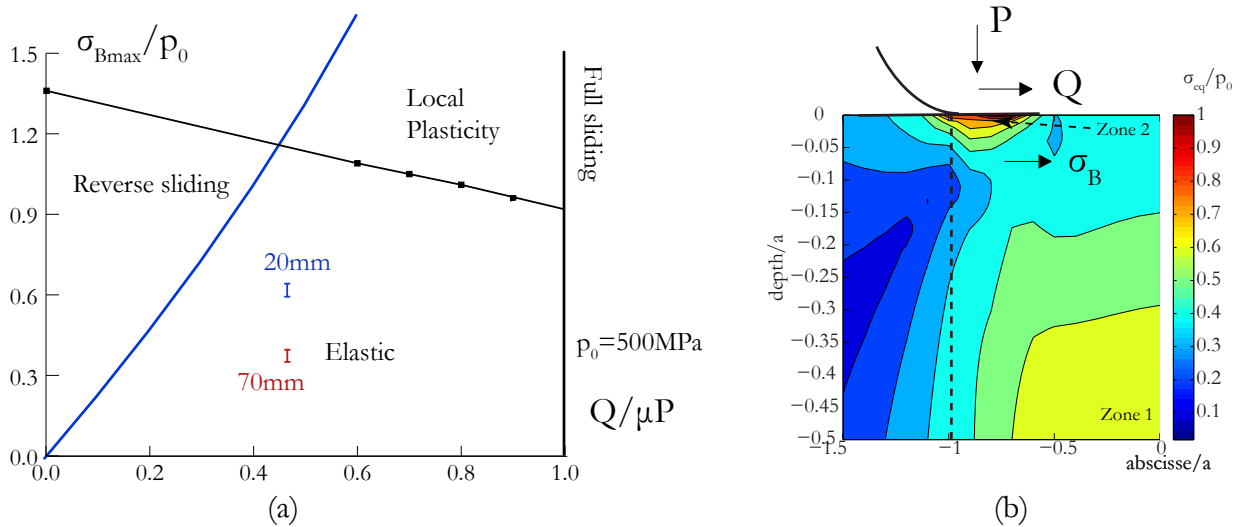


Figure 5.1: Elastic domain in a fretting fatigue map ( $\sigma_{Bmax}/p_0 - Q/\mu P$ ) under peak pressure  $p_0 = 500 MPa$ .

### 5.1.3 Location of the critical site for crack initiation.

It is known that crack initiation is mostly controlled by the shear amplitude. Using the Mindlin analytic plain stress formulation, we first attempt to characterize the shear amplitude distribution at

the fretting surface.

FIG.5.2 presents the maximum of the shear range at the surface for pure fretting condition and when fatigue is added. The dotted lines show the orientation of the plane maximizing the shear amplitude ( $\theta = 0^\circ$  when perpendicular to the surface). In pure fretting, the shear amplitude is constant in the two sliding zones, however, the direction maximizing the shear vary along the zones. In fretting fatigue, the maximum is localized at the trailing edge of the contact,  $x/a = -1$ .

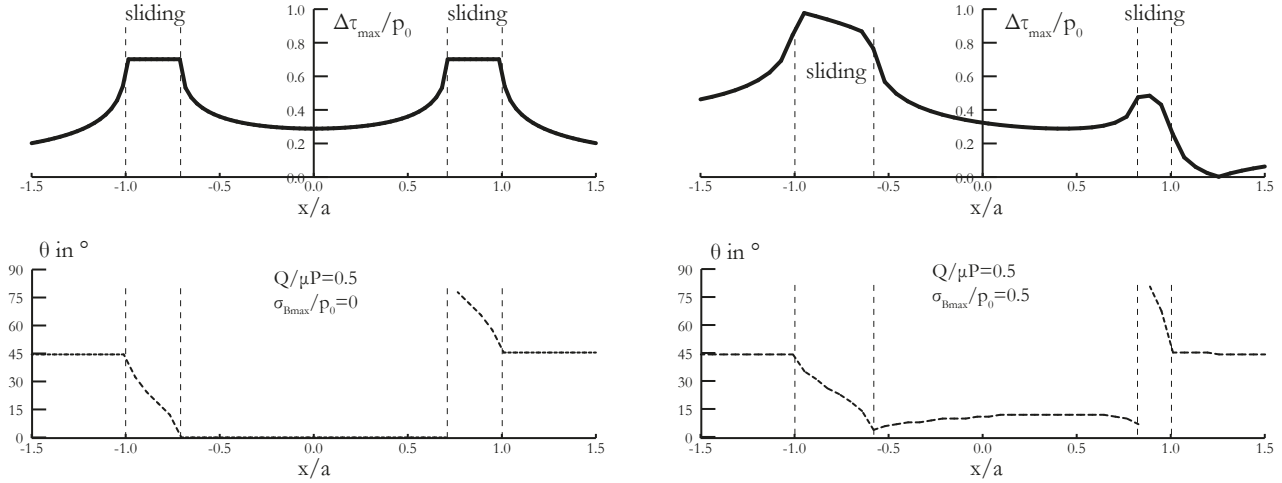


Figure 5.2: Distribution of the maximum shear range at the surface of a contact and the plane maximizing this shear for a pure fretting loading and for a fretting fatigue loading.

Brown and Miller described the influence of the slide plane orientation on initiation of fatigue cracks. If the angle between the surface and the Burgers vector is high, as shown in FIG.5.3, the ‘step height’ will allow formation of fatigue cracks through an irreversible sliding mechanism.

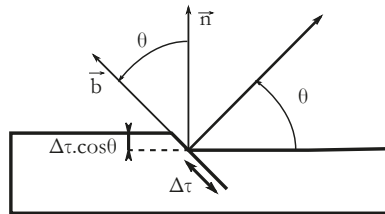


Figure 5.3: Effect of the plane orientation on crack initiation.

FIG.5.4 presents now the quantity  $\Delta\tau_{max} \cos \theta$  at the surface. In pure fretting this quantity is maximum at the limit stick/sliding, while in the fretting-fatigue load considered here, all the sliding zone (on the trailing side) presents a value relatively equal.

Other classical approach could be considered, for example Crossland criterion detailed in SEC.2.3.3. Parameter,  $\alpha_2 = 0.429$  and  $\beta = 412.0MPa$ , of the Crossland criterion, has been taken from a parallel study. The initiation risk, defined with the Crossland criterion can be expressed as:

$$d_c = \frac{\sqrt{J_a} + \alpha_2 \cdot I_{max}}{\beta} \quad (5.4)$$

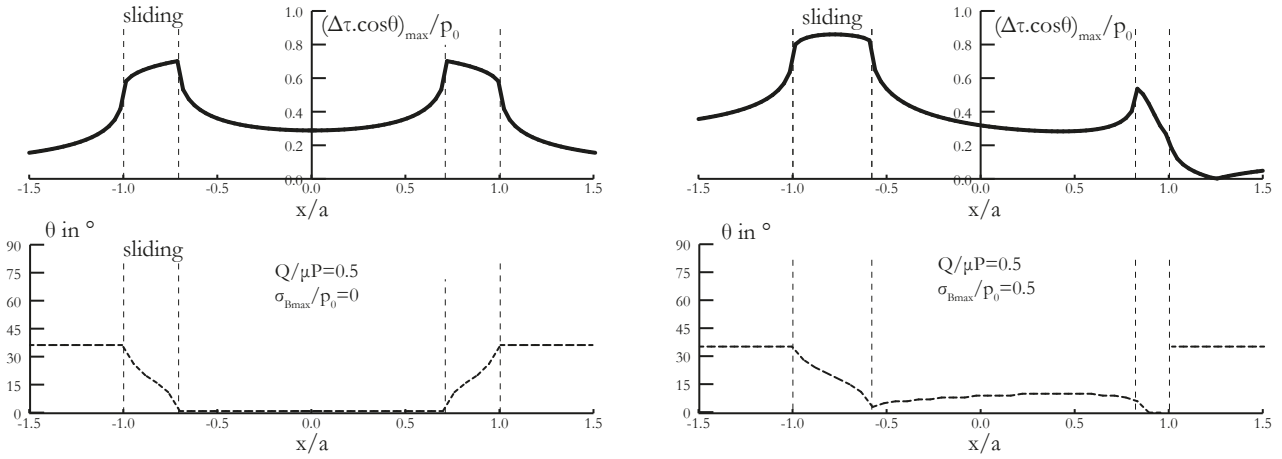


Figure 5.4: Distribution of  $\Delta\tau_{max} \cos \theta$  at the surface of a contact.

FIG.5.5 illustrates a typical distribution of the Crossland parameter, computed using the Mindlin analytic stress formulation, at the surface of the fretting fatigue contact. When the parameter is superior to 1, initiation is predicted. With this approach, the trailing edge of the contact,  $x/a = -1$ , will be the initiation point of the crack. Note that this curve is independent of the radius of the pad, and would should present the same tendency with other local criterion.

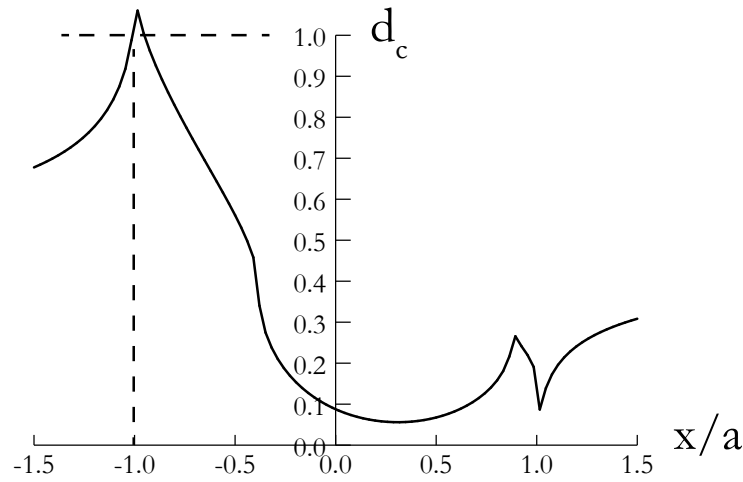


Figure 5.5: Distribution of the Crossland parameter at the surface of a contact with  $\sigma_{Bmax}/p_0 = 1$ ,  $Q/\mu P = 0.6$  and  $p_0 = 500MPa$ .

If the shear stress is considered to be the major actor in the crack initiation, the Brown and Miller approach suggests that risk of initiation is roughly the same in the sliding zone at the trailing side of the contact. When the influence of the normal load is also considered, the edge of the contact appears to be the most critical. These approaches agree with the experimental observation. Indeed, examinations of contact surfaces of the after fretting fatigue tests revealed

multiple crack initiations in the slip zone on the side of the trailing edge of the contact. However, the crack or the coalescence of cracks which propagated until the failure were initiating in the vicinity of the contact edge.

## 5.2 Multiaxial stress fatigue model.

In this section, we will use the conventional critical plane approach called modified Wöhler curve method (MWCM). The theory of critical distance (TCD) is used to manage the presence of stress concentration phenomena (i.e. the stress gradient), whereas the multiaxiality of the stress field was accounted for by using the MWCM.

### 5.2.1 Fretting map and comparison with experimental results.

Using the material properties from the literature, the critical distance (point method, see SEC.2.4.9) is calculated as:

$$l_{PM} = \frac{1}{2\pi} \left( \frac{\Delta K_{th-1}}{\Delta \sigma_{-1}} \right)^2 \quad (5.5)$$

leading to  $l_{PM} = 10.7\mu m$ .

The criterion is defined as :

$$\tau_a(\phi^c, \theta^c) + \kappa \frac{\sigma_{n,max}}{\tau_a}(\phi^c, \theta^c) \leq \lambda \quad (5.6)$$

where  $\tau_a$  is the equivalent shear stress amplitude in the critical plane  $(\phi^c, \theta^c)$  computed with the Maximum Rectangular Hull (Mamiya et al. 2009) enclosing the shear stress history,  $\sigma_{n,max}$  is the maximum stress perpendicular the critical plane, and the parameters  $\kappa$  and  $\lambda$  are material constants defined as:

$$\kappa = \frac{\sigma_{-1} - \sigma_0/2}{2} \quad \lambda = \sigma_{-1} - \frac{\sigma_0}{4} \quad (5.7)$$

or as we are using the fatigue limits  $\sigma_{-1}$  and  $\sigma_{0.1}$ , a alternative writing is used :

$$\kappa = \frac{\sigma_a(\sigma_{-1} - \sigma_a)}{2\sigma_m} = \frac{0.45}{1.1}(\sigma_{-1} - 0.45 * \sigma_{0.1}) = 78.5MPa \quad (5.8)$$

$$\lambda = \kappa + 0.5 * \sigma_{-1} = 318.5MPa \quad (5.9)$$

In the following, we will use the following index for simplification of the writing:

$$I(x, y) = [\tau_a + \kappa\rho] / \lambda \quad (5.10)$$

where  $(x, y)$  are the coordinates below the contact (FIG.5.6b) and  $\rho = \frac{\sigma_{n,max}}{\tau_a}$ .

To calculate this criterion for the fretting problem, the cyclic stress field is computed using the analytical formulation (Hertz + Mindlin + Muskhelishvili) detailed in SEC.2.1.3.

In this setting, FIG.5.6 presents the fretting fatigue map ( $\sigma_{Bmax}/p_0 - Q/\mu P$ ) for the two pad radii under the same peak pressure  $p_0 = 500MPa$ . The analyze is limited to the area where plasticity and reverse slip does not occur.

The threshold for crack for crack initiation correspond to the validation of the criterion at the initiation point,  $I(x/a = -1, y = 0) = 1$ . As expected, this local approach predicts the same limit for both pad radii.

When the index, computed at the critical distance, is inferior to 1 (i.e.  $I(x/a = -1, y = l_{PM}) \leq 1$ ), the criterion postulates that short crack will be contained in a zone of radius  $l_{PM}$ . If the index is superior to 1, a larger crack will appear, but the criterion can not predict if the propagation will lead to failure. Indeed, if the stress field crossed by the long crack strongly decreases, a long crack arrest may occur. In fretting fatigue, however, the bulk load will usually make a long crack propagate until failure.

The thresholds so that  $I(x/a = -1, y = l_{PM}) = 1$  were computed for the two pad radii. Two distinct threshold lines appear when represented in a  $\sigma_{Bmax}/p_0 - Q/\mu P$  map. As expected, the threshold for the highest gradient, with the 20mm pad radius, is above. However, the comparison with experimental results shows a significant difference.

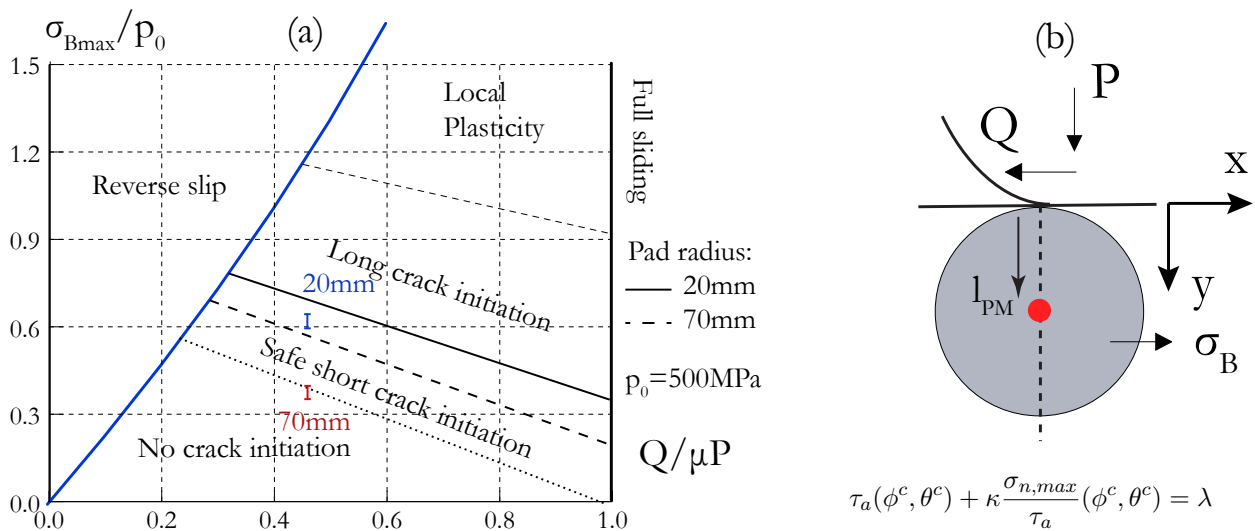


Figure 5.6: Fretting fatigue map ( $\sigma_B/p_0 - Q/\mu P$ ) for two pad radius under same peak pressure  $p_0 = 500MPa$ .

The multiaxial stress fatigue model presented here fails to predict accurately the experimental results produced earlier on. The difference between the critical loads obtained for the two gradients is larger than predicted here. Moreover, the predicted thresholds are clearly above those obtained experimentally.

Nonetheless, other authors obtained good agreement when using this method for fretting fatigue. Araújo et al. (2007) used a similar approach but on a different material. He was capable of predicting the results of fretting fatigue experiments with  $\pm 20\%$  degree of accuracy. The error obtained here may be linked to the material property used, which were not produced in this study but extracted from the literature.

### 5.2.2 Discussion on the model.

First, we will look at the experimental test loads. From condition  $p_0 = 500MPa$ , normal forces were calculated using the Hertz theory, which leads to  $P_{R=20mm} = 3.14kN$  and  $P_{R=20mm} = 10.99kN$ . The testing set up maintained these values of  $P$  with 5% precision. Because  $p_0 \propto \sqrt{P}$ , a precision of 2% may be expected on the peak pressure. However, we showed in SEC.3.3.2 that pressure distribution is affected by the edge effect. The peak pressure computed with FEM at the contact center for this sample width was 4% superior to predicted by the hertz theory.

Consequently, the actual peak pressure to be considered in the Mindlin formulation is  $520MPa$  and not  $500MPa$ . This correction slightly brings down the threshold line predictions in the previous  $(\sigma_{Bmax}/p_0 - Q/\mu P)$  map, but not enough to correct the difference with the experimental results.

More importantly, the model parameter,  $\lambda$ ,  $\kappa$  and  $l_{PM}$  were calculated using material plain fatigue properties averaged from the literature. Even if we assume that  $\Delta K_{th-1}$  is well known, the dispersion of the fatigue limits directly affects the model parameter. For example, from the test of Bellows (1999), the parameter  $\lambda = 51MPa$ ,  $\kappa = 251MPa$  and  $l_{PM} = 15\mu m$  are obtained, while results from Nagai et al. (1993) give  $\lambda = 94MPa$ ,  $\kappa = 367MPa$  and  $l_{PM} = 8\mu m$ . The threshold line defined by the criterion can be plotted in a  $(\tau_a, \rho)$  graphic. In this representation, the threshold lines are passing through the points  $(\tau_{-1}, 0)$ ,  $(\sigma_{-1}/2, 1)$  and  $(\sigma_0/4, 2)$ . FIG.5.7 illustrates the thresholds defined by the criterion when the parameters are calculated with the data from (Bellows 1999), (Nagai et al. 1993) and with the averaged material properties.

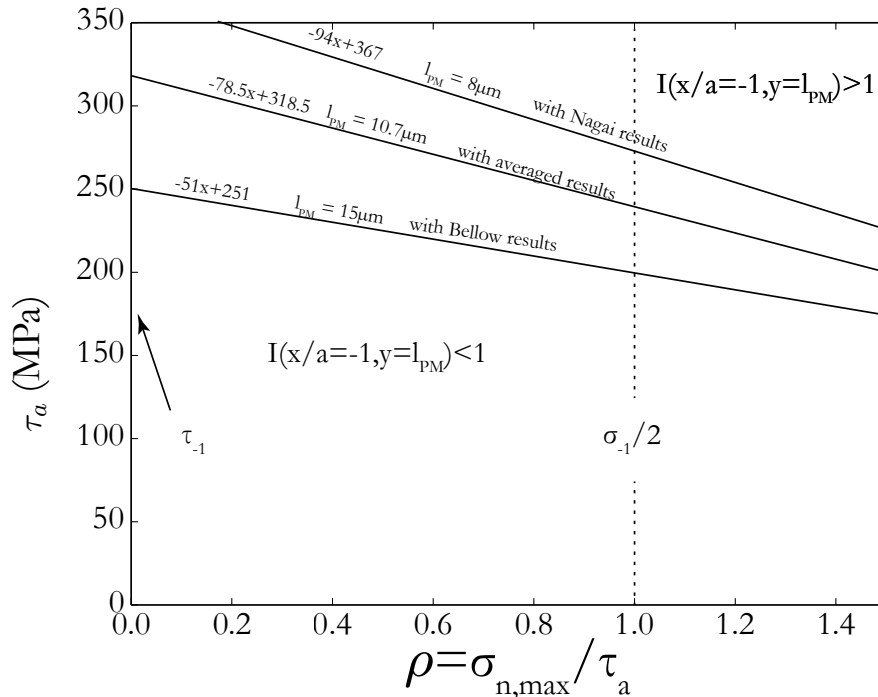


Figure 5.7: Representation of the multiaxial stress fatigue model in a  $(\tau_a, \rho)$  plot.

The assumption on the crack path may also be reconsidered. Indeed, here the criterion is computed

at a critical distance in a direction perpendicular to the surface, however, we observed experimentally that cracks tend to initiate along an inclined plane. Instead of calculate the criterion at the coordinate  $[x = -a, y = l_{PM}]$ , we may consider the position  $[x = -a + l_{PM}\sin(\theta), y = l_{PM}\cos(\theta)]$  where  $\theta$  is the angle from the perpendicular direction. In FIG.5.8, the quantities  $\tau_a$  and  $\rho$  are calculated for the critical loading identified for the 70mm pad radius. The parameter  $l_{PM}$  and  $\kappa$  are here taken from (Bellows 1999), and four angles  $\theta$  are considered.

The difference between the multiaxial model value  $\left( \tau_a + \kappa \frac{\sigma_{n,max}}{\tau_a} \right)_{l_{PM}=15\mu m}$ , computed for the straight and inclined planes are estimated.

For an inclination  $\theta = 0^\circ$  to  $\theta = 30^\circ$ , the weight of  $\tau_a$  and  $\rho$  is modified, but the value of the index is very little modified. It is them relevant to assume that the multiaxial criterion can be evaluated at the critical distance on the perpendicular direction of the contact.

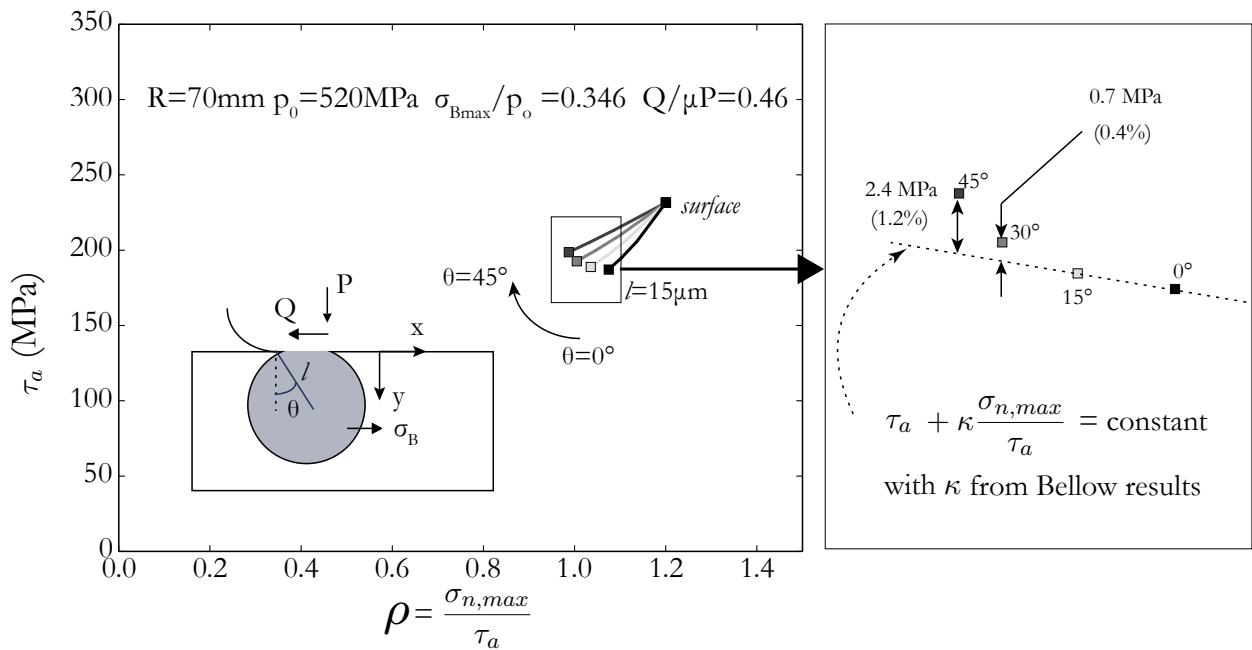


Figure 5.8: Effect of calculation position of multiaxial stress fatigue criterion.

Calibration of the criterion requires two plain fatigue limits and the long crack stress intensity factor threshold. Among all other assumptions considered in this model, the criterion parameter assessment appears to affect the most the prediction. The initial values averaged from literature data led to threshold load computation too high. It suggests that our material fatigue properties are lower than generally observed in the literature for the same TI alloy. This difference also includes the difference of surface machining and treatment of the samples.

### 5.2.3 Proposition of criterion parameter.

Using a reverse approach, we propose here to calibrate the model parameters with the fretting fatigue experimental results. Correcting the 4% error on  $p_0$ , the three threshold loadings identified are:

- $R = 20mm$   $p_0 = 728MPa$   $\sigma_{Bmax}/p_0 = 0.240$   $Q/\mu P = 0.51$
- $R = 20mm$   $p_0 = 520MPa$   $\sigma_{Bmax}/p_0 = 0.587$   $Q/\mu P = 0.46$
- $R = 70mm$   $p_0 = 520MPa$   $\sigma_{Bmax}/p_0 = 0.346$   $Q/\mu P = 0.46$

FIG.5.9 regroups the computation of  $\tau_a$  and  $\rho$  for those three loading conditions for different critical size,  $l_{PM}$ .

For the distance  $10\mu m$ ,  $15\mu m$  and  $20\mu m$ , linear fit are calculated. The equations of those lines represent the best criterion parameters  $\lambda$  and  $\kappa$  for each critical distance considered.

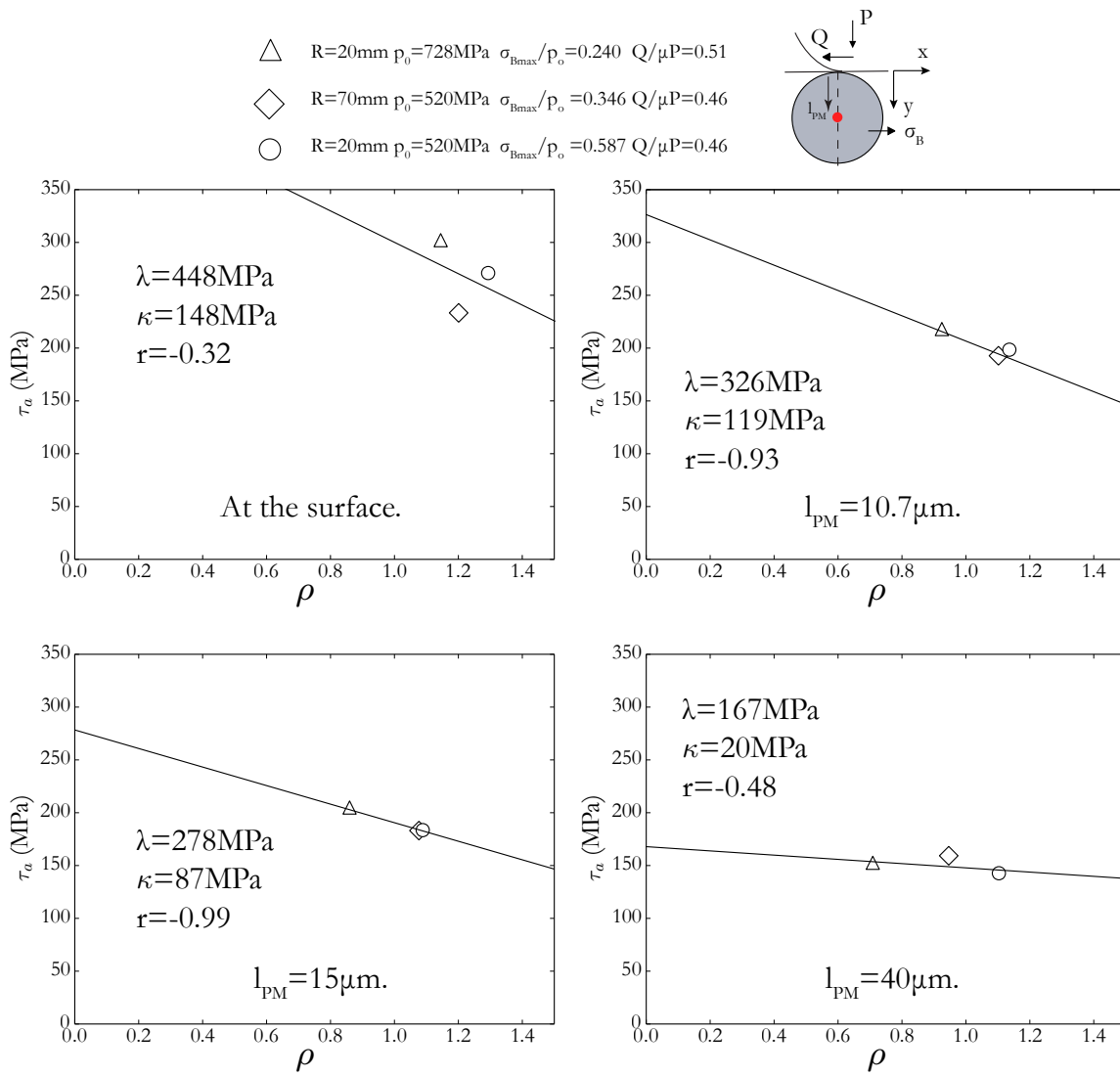


Figure 5.9: Reverse calibration of the model parameters, using the experimental load threshold.

The best regression coefficient is obtained for the distance  $15\mu m$ . This means that the set of parameters  $\lambda = 278MPa$ ,  $\kappa = 87MPa$  and  $l_{PM} = 15\mu m$  would be among the best set of parameters for the prediction of our experimental results.

FIG.5.10 compares the threshold defined with these optimized parameters with the threshold calculated with the data from (Bellows 1999), (Nagai et al. 1993) and with the averaged material properties. The threshold is very much alike the one calibrated with the data of Bellows (1999).

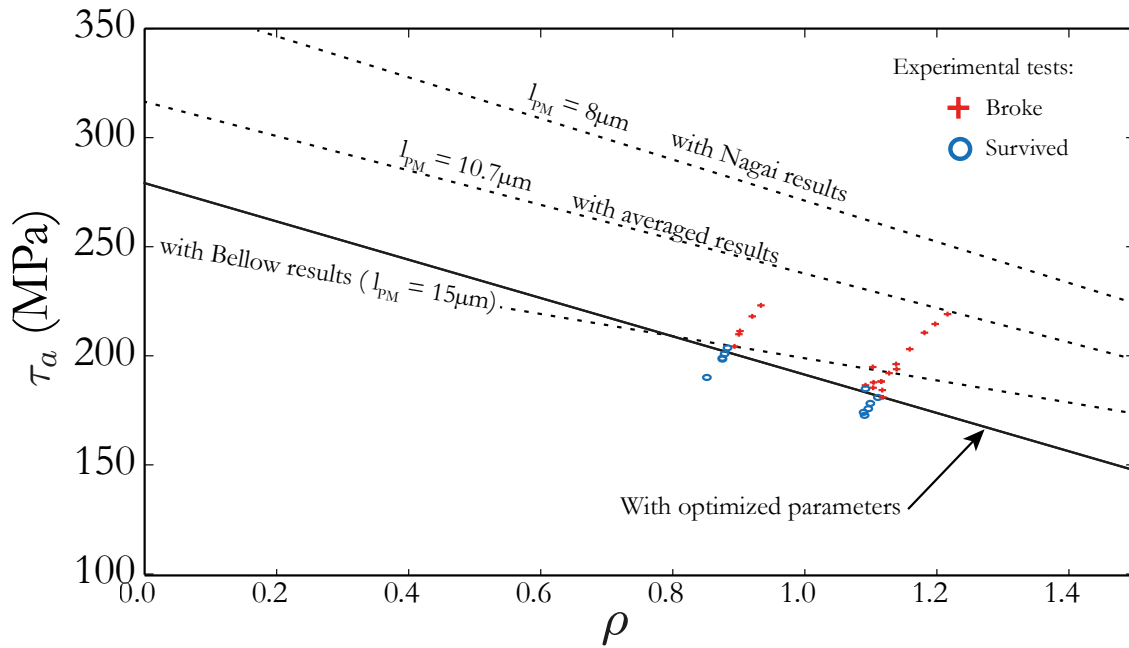


Figure 5.10: Reverse calibration of the model parameters, using the experimental load threshold.

Using the proposed set of parameter, FIG.5.11 shows the gradients of the criterion index for the three threshold loadings identified.

A calibration of the criterion was proposed using the fretting fatigue test results. The parameters  $\lambda = 278MPa$ ,  $\kappa = 87MPa$  and  $l_{PM} = 15\mu m$  was identified. Using the EQ.5.8 and EQ.5.9, the plain fatigue limits  $\sigma_{-1} = 382MPa$  and  $\sigma_{0.1} = 376MPa$  may be guessed. These fatigue limits are lower than the fatigue limits referenced in the literature.

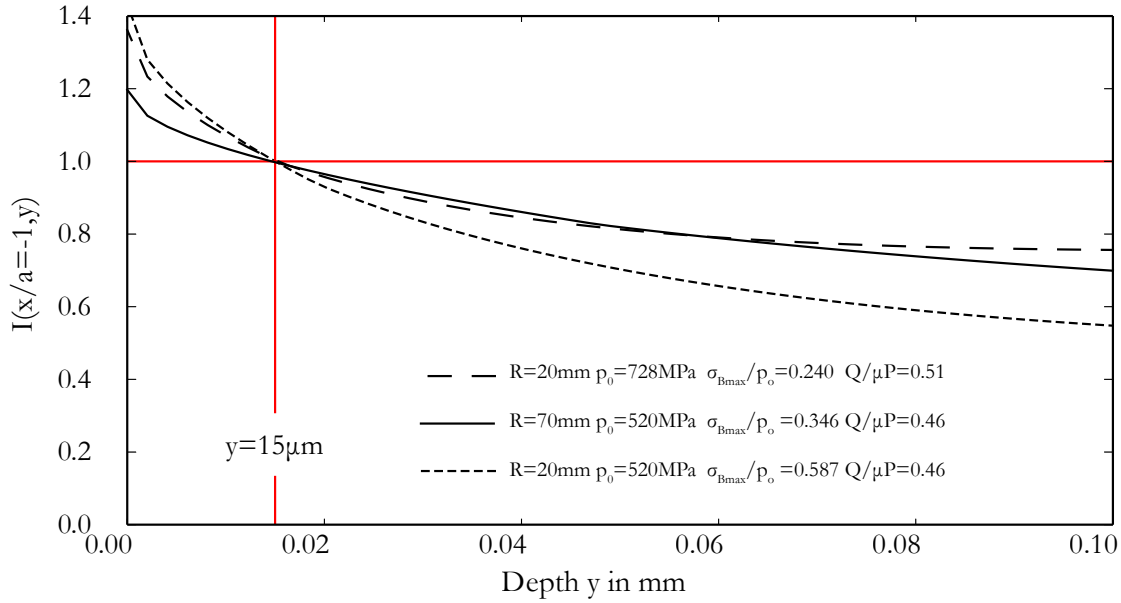


Figure 5.11: Criterion index of three threshold loadings identified, using criterion parameters from the reverse analysis.

### 5.3 Short crack arrest approach.

#### 5.3.1 Introduction.

In this section, we will evaluate a short crack methodology proposed by Araújo and Nowell (1999), based on the Kitagawa-Takahashi (K-T) diagram.

The analysis carried out by Kitagawa and Takahashi (1976) showed that the minimum crack length for which classical Linear Elastic Fracture Mechanics applies is given by:

$$b_0 = \frac{1}{\pi} \left( \frac{\Delta K_0}{Y \Delta \sigma} \right) \quad (5.11)$$

where  $\Delta K_0$  is the long crack threshold stress intensity factor range and  $\Delta \sigma$  is the plain fatigue limit, both under the same load ratio, while  $Y$  is a geometric correction factor. For a crack initiating from an edge, the geometric correction factor is usually  $Y = 1.12$ .

The method assumes that below the transition crack size,  $b_0$ , the short crack behavior occurs. The threshold  $\Delta K_{th}$  is then defined as:

$$\begin{aligned} \Delta K_{th} &= \Delta K_0 \sqrt{\frac{b}{b_0}} & \text{for } b \leq b_0 \\ \Delta K_{th} &= \Delta K_0 & \text{for } b > b_0 \end{aligned} \quad (5.12)$$

If this setting, the crack will grow until a size  $b_1$  and arrest if the following condition are satisfied:

$$\begin{aligned} \Delta K &> \Delta K_{th} & \text{for } b < b_1 \\ \Delta K &= \Delta K_{th} & \text{for } b = b_1 \end{aligned} \quad (5.13)$$

For the fretting fatigue loading range considered in this work, the mode I stress intensity factor range obtained for a crack starting at the trailing edge of the contact, and growing normal to the surface have usually the form of the curve illustrated in FIG.5.12. In this example, the crack is predicted to grow until a size  $b_1$  and arrest.

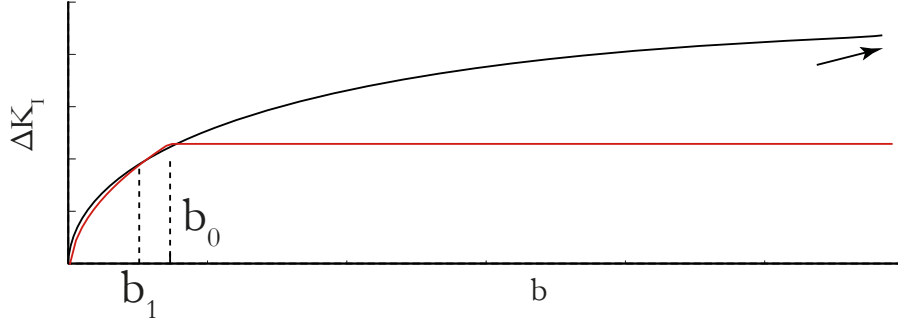


Figure 5.12: Schematic example of  $\Delta K_I$  typically obtained for fretting fatigue.

Based on the observation that in this fretting fatigue loading range, crack arrest generally occurs in the short crack regime, Araújo and Castro (2012) reinterpreted this model and proposed to simplify the approach. If the fatigue crack driving force  $\Delta K$  is less than  $\Delta K_0$  at a distance  $b_0$  from the trailing edge of the contact, short cracks are expected to lie within a surface layer of depth  $b_0$ :

$$\Delta K \leq \Delta K_{th} \quad \text{at } (x, y) = (-a, b_0) \quad (5.14)$$

The threshold condition occurs when the equality is verified.

### 5.3.2 Comparison with experimental results.

In order to implement the model to the fretting fatigue problem, the mode I stress intensity factor was calculated by means of the Distributed Dislocation Method, detailed previously in SEC.2.4.5. For the sake of simplicity, the short crack methodology described here assumes that a single major crack starts at the trailing edge of the contact,  $x = -a$ , and grows normal to the surface under pure Mode I. The stress intensity factor range  $\Delta K$  is considered here from a numerical aspect, defined as  $\Delta K_I = K_{I_{max}} - K_{I_{min}}$ , where  $K_{I_{min}}$  may be negative.

We will assume here that  $b_0$  is a material parameter. Using the material parameters at  $R_\sigma = -1$  defined in the introduction of this chapter, the value  $b_0 = 17.1 \mu m$  is calculated.

FIG.5.13 presents in Kitagawa–Takahashi diagram the mode I stress intensity range of the three critical experimental loading, labeled (a), (b) and (c). Note that the edge effect correction has been included in the loadings (SEC.3.3.2). For the configuration (a),  $\Delta K_I > \Delta K_{th}$  for any  $b$ , so the crack is predicted to growth until failure. We can see that the curve passes close to the point  $(b_0, \Delta K_0)$ . If the loading is slightly decreased, a crack arrest will be predicted in the short crack domain. For this configuration, the prediction of  $\Delta K_{th}$  may look correct. For the configuration (b) and (c),  $\Delta K_I < \Delta K_{th}$  even for very short crack. These configurations also correspond to experimental loading threshold. This means that a small increase of the load should lead to  $\Delta K_I > \Delta K_{th}$  for all crack size  $b$ . In other words, the plot of  $\Delta K_I$  should be tangent to the predicted threshold  $\Delta K_{th}$ .

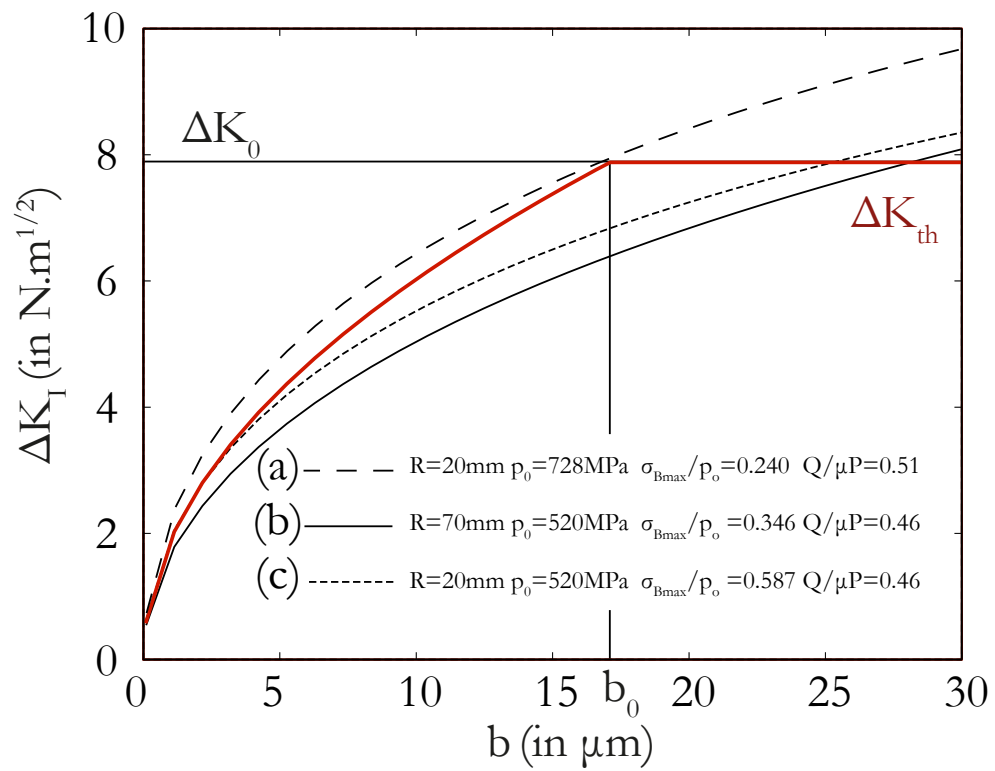


Figure 5.13: Experimental loading threshold in a Kitagawa–Takahashi diagram.

The quality of the results provided by this method may be assessed in terms of a relative error measured at the critical size  $b_0$ :

$$E_{\Delta K_{th}} [\%] = \frac{\Delta K_0 - \Delta K_{I,experimental}(b_0)}{\Delta K_{I,experimental}(b_0)} \quad (5.15)$$

The errors obtained for the configurations (a), (b) and (c) are respectively 1%, 15% and 23%.

The  $\Delta K_I$ -based short crack arrest model presented here fails to predict correctly all our fretting fatigue experimental results. The prediction error is not the same for the three configurations.

### 5.3.3 Effect of the loading ratio.

Whereas the previous multiaxial criterion, this model does not account for the effect of the loading ratio variation under the contact. However, it is well known that the threshold stress intensity factor depends on the loading ratio (Moshier et al. 2001). Indeed, when plasticity occurs, if the plastic zone is confined, residual stresses arise in the vicinity of the crack front. These constraints produce a shielding effect, which is superimposed on the applied load (Rice 1974).

We propose here to modified the long crack threshold stress intensity factor  $\Delta K_0$  as a function of the  $R_\sigma$  which can be estimated for each crack size  $b$  as:

$$R_\sigma = \frac{K_{min}}{K_{max}} \quad (5.16)$$

The threshold stress intensity factor would then be defined as:

$$\begin{aligned} \Delta K_{th} &= \Delta K_0(R_\sigma) \sqrt{\frac{b}{b_0}} & \text{for } b \leq b_0 \\ \Delta K_{th} &= \Delta K_0(R_\sigma) & \text{for } b > b_0 \end{aligned} \quad (5.17)$$

Note that we still assume here that  $b_0$  is a material parameter, independent of the load and loading ratio.

In the domain of crack size considered, i.e.  $b < 30\mu m$ , the loading ratio calculated for the fretting fatigue configuration (a-b-c) varies between -0.5 and -1.5. We choose to correlate  $\Delta K_0$  to  $R_\sigma$  using a linear extrapolation of Boyce and Ritchie (2001) results, which were presented in SEC.2.4.8:

$$\Delta K_0 = 4.5 - R_\sigma * 3.38 \quad (5.18)$$

FIG.5.14 presents the same configurations (a), (b) and (c) in a  $(\Delta K_I, b)$  graphic, and for each setting, the modified  $\Delta K_{th}$  is plotted. Errors of 6%, 10% and 8% are respectively observed for the configurations (a), (b) and (c).

By taking in account the variation of the loading ratio see by the crack while growing, the errors between  $\Delta K_{I,experimental}(b_0)$  and  $\Delta K_{th}(b_0, R_\sigma)$  are very similar. We believe that this model could be calibrated using a different distance  $b_0$  (i.e. if different material parameters are considered), so that the error would be reduced.

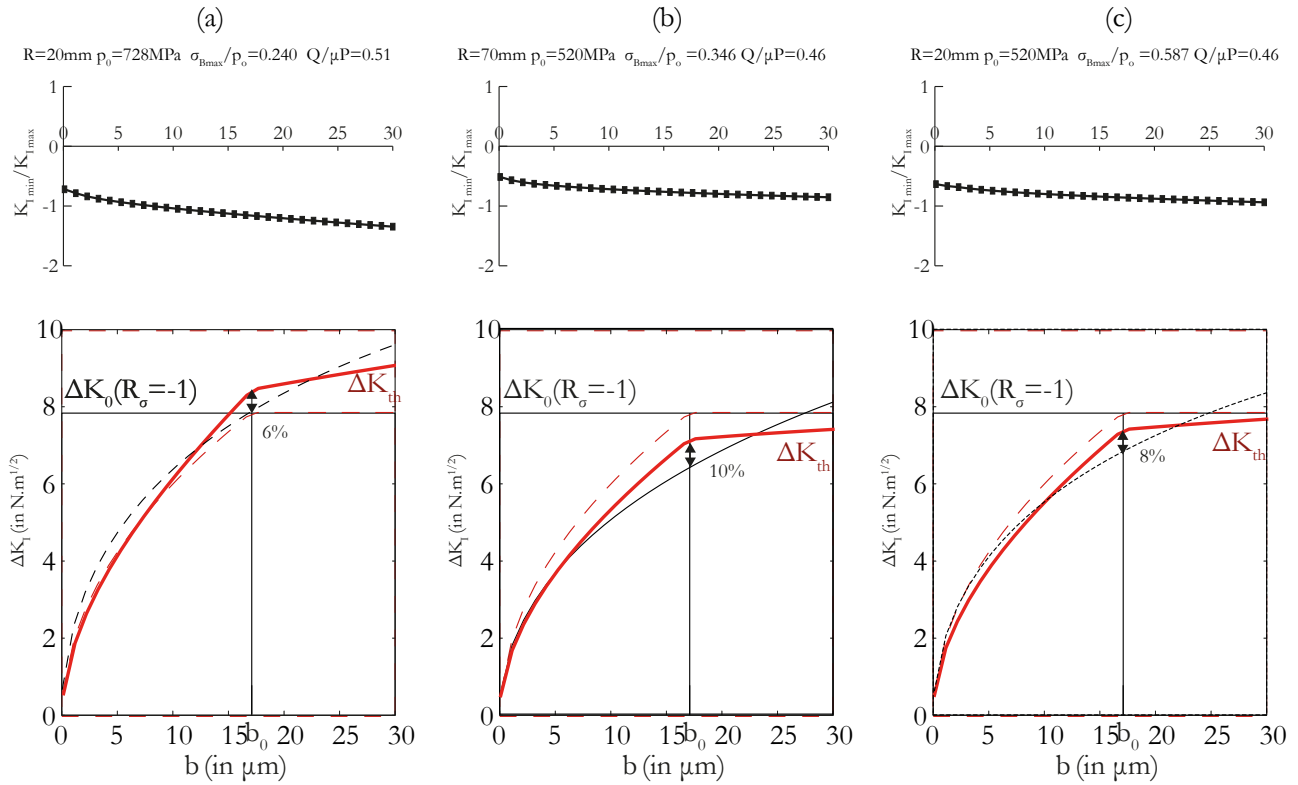


Figure 5.14: Experimental loading threshold compared with modified threshold stress intensity factor, accounting for the variation of loading ratio.

### 5.3.4 Conclusion.

This methodology assumes that a single major crack starts at the trailing edge of the contact and grows normal to the surface. Considering that short crack comparable to few grain size are examined for the life prediction, this assumption certainly affects considerably the precision of the method. Indeed, we observed that initiation occurs on an inclined plane and under a mode II dominant. But this method does not account for the mode II stress intensity factor. If both modes have to be treated, several question arise:

- How to build an equivalent stress intensity factor, and what is the weight of each mode?
- Can this equivalent SIF still be compared to the threshold in mode I?
- How to deal with the crack closure and how does it affects the mode II?
- Is the short crack regime parameter  $b_0$  still valid if the crack is inclined?
- How to decide the inclination of the initiation crack?

Moreover, we showed that the Distributed Dislocation Method cannot predict correctly the mode II in fretting fatigue (see SEC.3.3.3.ii), it is then necessary to use FEM for the calculation, which take more time than using an analytical formulation. With “only” the assumption of pure Mode I, this short crack arrest criterion proposes a simple engineering method which, after calibration of the parameters, may predict reasonably well the safe life conditions on a certain range of fretting fatigue loading.

## 5.4 A new methodology - Using the T-stress

A new method will be used in this section. This method considers a generalized von Mises yield criterion for the crack tip region. This criterion was first proposed by Thieulot-Laure et al. (2007) and later modified by De Moura Pinho et al. (2012).

### 5.4.1 Assumptions

The material is assumed to contain small cracks. The criterion is based on the assumption that fatigue cracks propagate if a cyclic plastic strain is experienced at the crack tip. The criterion is thus expressed as a threshold for plastic yield for a region of material located within a distance  $\delta$  to the crack tip and per unit of length of the crack front. This radius  $\delta$  is a length scale parameter to be identified from experiments.

The yield criterion for the crack tip region is obtained as follows. The material is assumed to obey the von Mises yield criterion at the local scale. The von Mises criterion is a critical distortional elastic energy density criterion. In order to calculate the distortional elastic energy density within the crack tip region (De Moura Pinho et al. 2012; Pommier et al. 2009; Thieulot-Laure et al. 2007), the stress, strain, and displacement fields at the crack tip from LEFM are used. In addition, since it is aimed at using this criterion for small cracks, higher-order terms (T-stresses) in the asymptotic LEFM development are also considered.

### 5.4.2 Expression of the criterion.

In plane strain condition, the asymptotic development (Williams 1957) at the crack tip of the displacement field  $\mathbf{u}$  including the  $T$ -stress is as follows.

$$\begin{aligned}
 u_x &= \frac{K_I}{2\mu} \sqrt{\frac{r}{2\pi}} \cos \frac{\theta}{2} (\kappa - \cos \theta) + \frac{T}{8\mu} (\kappa + 1) r \cos \theta \\
 &\quad + \frac{K_{II}}{2\mu} \sqrt{\frac{r}{2\pi}} \sin \frac{\theta}{2} (\kappa + 2 + \cos \theta) \\
 u_y &= \frac{K_I}{2\mu} \sqrt{\frac{r}{2\pi}} \sin \frac{\theta}{2} (\kappa - \cos \theta) - \frac{T}{8\mu} (3 - \kappa) r \sin \theta \\
 &\quad - \frac{K_{II}}{2\mu} \sqrt{\frac{r}{2\pi}} \cos \frac{\theta}{2} (\kappa + 2 + \cos \theta) \\
 u_z &= 0
 \end{aligned} \tag{5.19}$$

where  $2\mu = E/(1 + \nu)$  and  $\kappa = 3 - 4\nu$ . Using cylindrical coordinate system, the strain tensor  $\varepsilon$  is derived from the displacement field  $\mathbf{u}$ , and the stress tensor  $\sigma$  is obtained by the Hooke's law. The distortional elastic energy density  $w(r, \theta)$  at each point  $(r, \theta)$  is then obtained:

$$w(r, \theta) = \frac{1}{2} \text{Tr}(\sigma' \cdot \varepsilon') \tag{5.20}$$

where  $\sigma'$  and  $\varepsilon'$  are the deviatoric parts of the stress and strain tensors. The distortional elastic energy density is then integrated over a domain within a distance  $\delta$  to the crack tip, to get the distortional

energy per unit of length of the crack front  $U(K_I, K_{II}, T)$ :

$$U(K_I, K_{II}, T) = \int_0^\delta \int_{-\pi}^\pi w(r, \theta) r d\theta dr \quad (5.21)$$

The yield criterion is finally expressed as follows:

$$U(K_I, K_{II}, T) = U_C \quad (5.22)$$

Where  $U_C$  is a critical distortional elastic energy per unit of length of the crack front, which is determined with the additional assumption that crack growth stems from crack tip plasticity. In such a case, the threshold stress intensity factor for long cracks can be used to determine a yield threshold  $K_{IY}$  so that:

$$U_C = U(K_I = K_{IY}, K_{II} = 0, T = 0) \quad (5.23)$$

A few mathematical simplifications of Eq.5.22 allow expressing this criterion as follows:

$$f = \left( \frac{K_I}{K_{IY}} \right)^2 + \left( \frac{K_{II}}{K_{IY}} \right)^2 + \left( \frac{T}{T_Y} \right)^2 + f_1 \frac{K_I}{K_{IY}} \frac{T}{T_Y} - 1 = 0 \quad (5.24)$$

The analytic formulations of the other coefficients are reported in Table 5.1.

$K_{IY}$	$T_Y$	$f_1$
$K_{IY} \sqrt{\frac{7-16\nu+16\nu^2}{19-16\nu+16\nu^2}}$	$\frac{K_{IY}}{\sqrt{2\Pi\delta}} \frac{1}{2} \sqrt{\frac{7-16\nu+16\nu^2}{1-\nu+\nu^2}}$	$\frac{32(1-10\nu+10\nu^2)}{15\Pi\sqrt{(1-\nu+\nu^2)(7-16\nu+6\nu^2)}}$
$0.48K_{IY}$	$\frac{0.43K_{IY}}{\sqrt{\delta}}$	$-0.419$

Table 5.1: Coefficients in Eq.5.24 calculated for a Poisson's ratio  $\nu = 0.29$ .

### 5.4.3 Identification of the parameters

This yield criterion requires three material parameters,  $K_{IY}$ ,  $\nu$  and  $\delta$ . In a first time, the mode I threshold stress intensity factor for long cracks can be used to determine a yield threshold  $K_{IY}$  (Eq.5.25).

$$K_{IY} = \Delta K_{th_{R-1}}/2 \quad (5.25)$$

As the Poisson's ratio  $\nu$  is known, remain the identification of the parameter  $\delta$  in the non-propagation criterion.

Let us consider, for instance, a through thickness crack lying in the plane  $(x, z)$  and subjected to remote uniaxial loads which amplitudes are  $S_{yy}^\infty$ , the expressions of mode I SIF and  $T$ -stress are the following:

$$\begin{aligned} K_I &= S_{yy}^\infty \sqrt{\Pi a} \\ T &= -S_{yy}^\infty \end{aligned} \quad (5.26)$$

Under uniaxial loading conditions, for instance, the threshold for crack propagation can be easily calculated as a function of the crack length using Eq.5.26 and Eq.5.24. Its evolution can be plotted

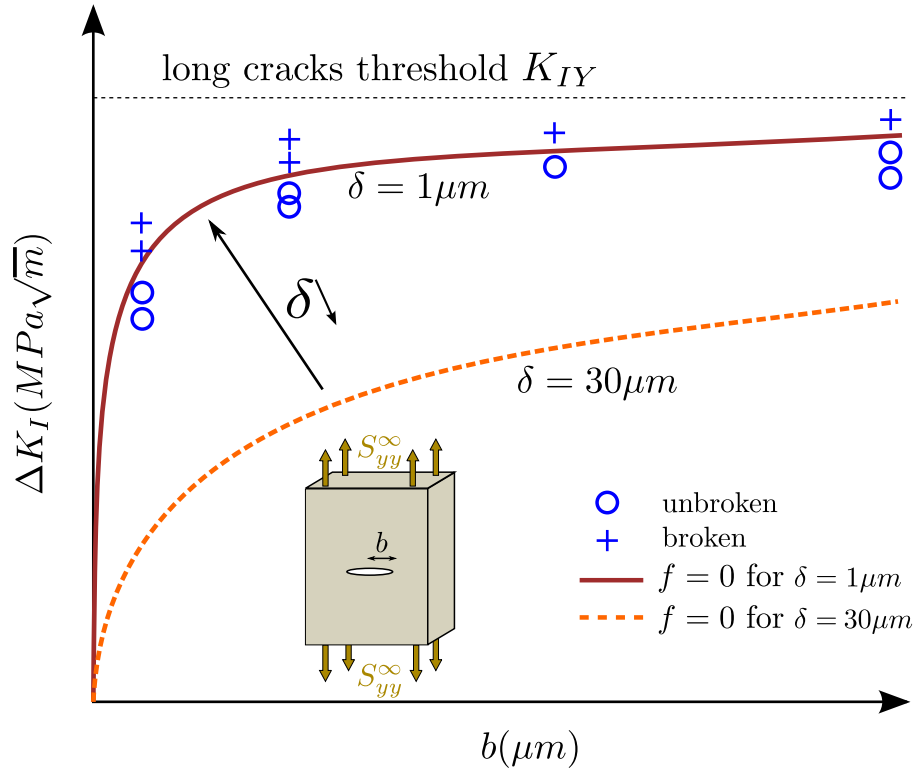


Figure 5.15: Case of a through thickness crack in an infinite media. Schematic evolution of the non propagation threshold, as calculated using the criterion, versus the crack length, for various values of  $\delta$ . Illustration of  $\delta$  identification using experimental test.

in a Kitagawa-Takahashi type diagram for various values of the dimension  $\delta$  of the integration domain. FIG.5.15 illustrates an example of growth threshold using two values of  $\delta$ .

The criterion predicts that the yield threshold is increasing with the crack length up to the saturation value  $K_{IY}$ . The saturation rate increases with the value of  $\delta$ .

Then if we have access to a Kitagawa-Takahashi type diagram from experimental test (Golden and Grandt Jr. 2004; Hutson et al. 2005; Peters et al. 2002), the dimension  $\delta$  can be identified as illustrated in FIG.5.15.

De Moura Pinho et al. (2012) used another method to identify the parameter  $\delta$ . This method required the fatigue limits in alternated tension ( $\sigma_f$ ) and in alternated torsion ( $\tau_f$ ) to identify an equivalent flaw size ( $b_0$ ) and the parameter  $\delta$ . They showed that the value of  $(\delta/b_0)$  is a function of the ratio between  $\sigma_f$  and  $\tau_f$ . The value of  $\delta = 1\mu m$  considered for the following analysis was collected from De Moura Pinho et al. (ibid.).

#### 5.4.4 Representation of the criterion.

In FIG.5.16, by way of illustration, the criterion is plotted in a  $K_I - T - K_{II}$  diagram. According to EQ.5.24, the yield criterion is an ellipsoid in this diagram. Inside the ellipse, the material within the crack tip region behaves essentially elastically and the crack is assumed to remain arrested. Loading paths corresponding to two crack lengths were plotted for a Griffith's crack (2D plane strain) subjected to a uniaxial tensile stress (i.e.  $K_I = S_{yy}^\infty \sqrt{\Pi a}$  and  $T = -S_{yy}^\infty$ ). When the loading path meets the yield

surface, crack tip plasticity and hence crack propagation is expected to occur. The frontier marked by open squares corresponds therefore to the evolution of the threshold stress intensity factor with the crack length. Various loading paths including multi-axial non-proportional cases can be considered. If the loading path remains inside the elastic domain, the crack should remain arrested.

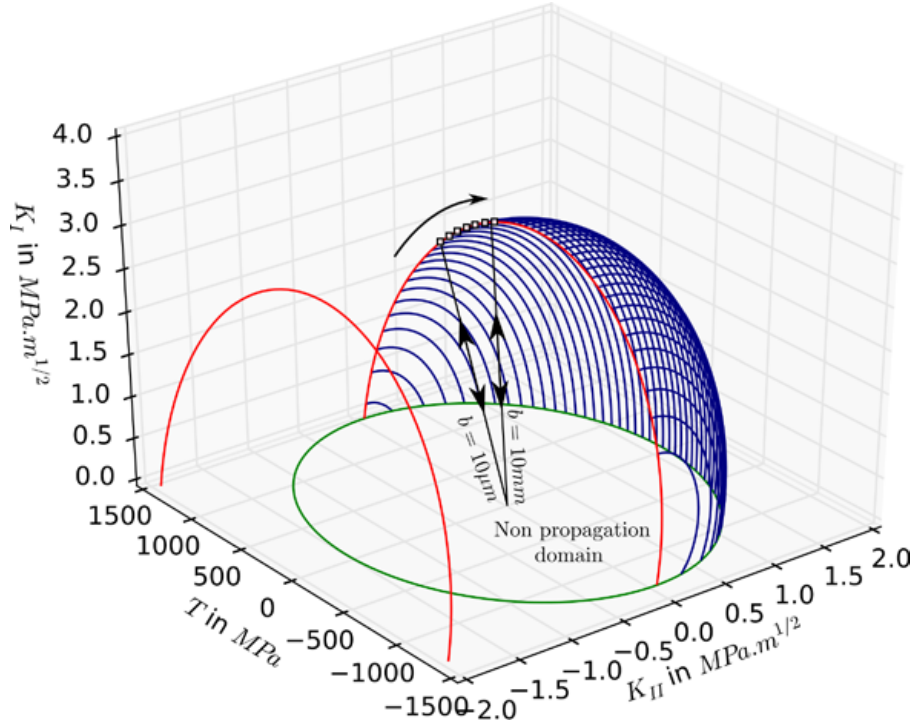


Figure 5.16: Criterion in EQ.5.24 identified for the Ti-6Al-4V titanium alloy plotted in a  $K_I - T - K_{II}$  diagram for  $\delta = 1\mu m$ , for a Griffith's crack in traction, in plane strain condition. The solid lines indicate the loading paths obtained for different crack lengths when  $S_{xx} = 0$ .

In addition, if crack growth stems from crack tip plasticity, we may assume that the crack growth rate could be roughly estimated using  $f$ . Hence, we can define an index using the function  $f$ .

$$Index = \int_{t \in T} \left( \frac{df}{dt} \right)_{>0} dt \Big|_{K_I > 0} \quad (5.27)$$

Indeed, it is assumed here that uniquely the segment of the cycle where the crack is open can generate plasticity at the tip of the crack. Then, during each fatigue cycle, different phases may appear. During a loading step,  $f$  is first negative (elasticity) then becomes positive above the yield threshold (plasticity occurs). Then, at unloading,  $f$  is positive, but  $df$  is negative.

The effective part of the loading cycle is thus the integration of  $df$  over the fatigue cycle, considering only the time steps during which plasticity is promoted i.e. the time steps during which both  $f$  and  $df$  are positive.

In the present model, it is not necessary to define a fictitious crack size to describe the anomalous short crack behavior. The variation of the threshold for  $\Delta K$  within the short crack regime can be captured by taking into account the influence of the  $T$ -stress. Moreover, the computation of the critical distortional elastic energy generates mixed mode dependence implicitly. The description of the criterion based on the concept of a two parameter ( $K$  and  $T$ ) allows the description of the stress/strain field in a region larger than the  $K$  dominated zone.

### 5.4.5 Application to fretting

In this section, the T-stress based criterion will be applied to the fretting fatigue configuration considered in the first set of tests (SEC.4.1.1). The linear elastic fracture mechanics quantities ( $K_I$ ,  $K_{II}$  and  $T$ -stress) were calculated using the finite element method (FEM) described in SEC.3.3. Two different possibilities for crack growth modeling were evaluated. In the first case, the crack path is constrained and assumed to be perpendicular to the axial fatigue load direction. Later, a more flexible modeling is experienced, where the T-stress based criterion not only evaluates the crack advance risk but also defines its path.

#### 5.4.5.i Straight crack.

As a first application of this criterion to fretting fatigue, let us consider a crack initiating at the trailing edge of the contact. This crack is assumed to grow perpendicular to the axial fatigue load direction.

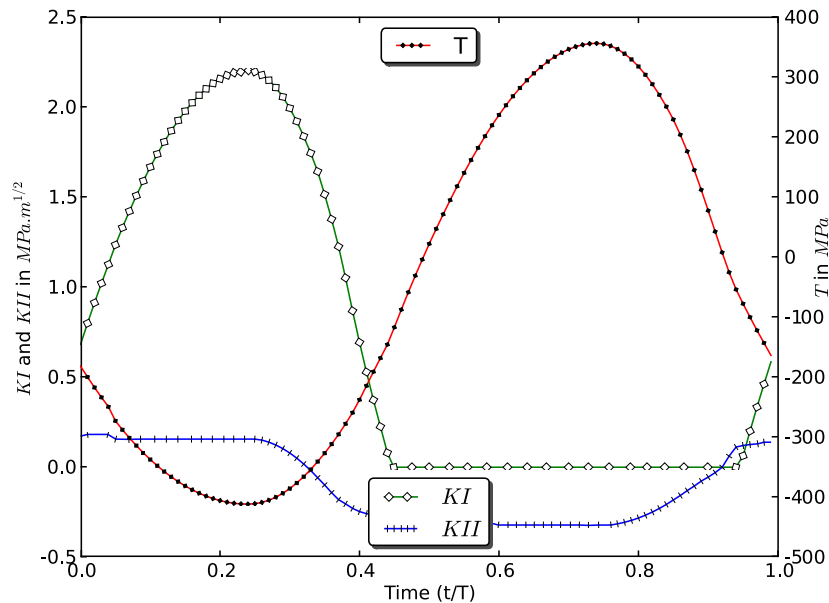


Figure 5.17: Stress intensity factor and T-stress evolutions during fretting-fatigue cycling at  $5\mu m$  below the surface.

The configuration adopted correspond to the load apply on the test 7 [SEC.4.1.1]: pad radius  $20mm$ ,  $Q/\mu P = 0.529$  and  $\sigma_{Bmax}/p_0 = 0.246$ . In this condition the stick/slip zone size ratio gives  $c/a = 0.7$ .

The time varying stress intensity factors and T-stress were computed for different crack sizes. As an example, the stabilized time history of  $K_I$ ,  $K_{II}$  and  $T$  for a crack length  $b = 5\mu\text{m}$  is reported in FIG.5.17. It can be seen that for this straight crack, the mode I is logically dominant ( $K_I \gg K_{II}$ ).

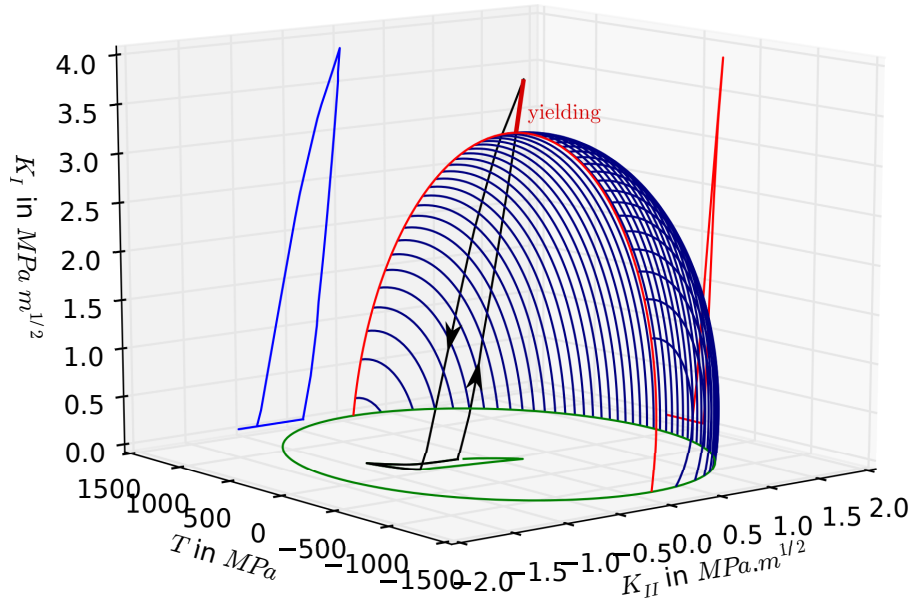


Figure 5.18: Time history of the linear elastic fracture mechanics quantities for the  $35\mu\text{m}$  crack initiating at the trailing edge of the contact.

FIG.5.18 shows the time history of the linear elastic fracture mechanics quantities for the  $35\mu\text{m}$  crack and the yielding surface defined by the function  $f$ . In this case, the curve of the history exceeds the yielding surface, crack growth is then expected.

FIG.5.19 illustrates the influence of the  $T$ -stress on the criterion. Each point in this graph represents the relative value of the terms containing the  $T$ -stress on the criterion (EQ.5.24), for a specific crack size. It seems clear from such figure that the influence of the  $T$ -stress is high for small cracks. For instance, for a  $5\mu\text{m}$  crack, the terms containing the  $T$  stress accounts for approximately 30% of the index, and of course, when the crack grows, its effect vanishes progressively.

FIG.5.20 shows the index  $\langle d\langle f \rangle \rangle$  for different vertical crack sizes  $b$  at different points under the slip zone. According to this plot, at the trailing edge of the contact ( $x/a = -1$ ), a  $10\mu\text{m}$  defect is necessary to generate plasticity at the tip of the vertical crack and hence to propagate this short defect under these loading conditions. For the other three cracks, the minimum size necessary for the crack to grow (observe a positive index) is even higher.

To sum up, when a vertical crack is assumed, the loads involved in this study would require the existence of cracks larger than  $10\mu\text{m}$  if they were to propagate. Moreover, post failure investigation of the fretting specimens has revealed inclined cracks, which vary between  $100^\circ$  and  $115^\circ$  (SEC.4.1.1). In the following, the effect of the crack orientation on the growth prediction will be examined.

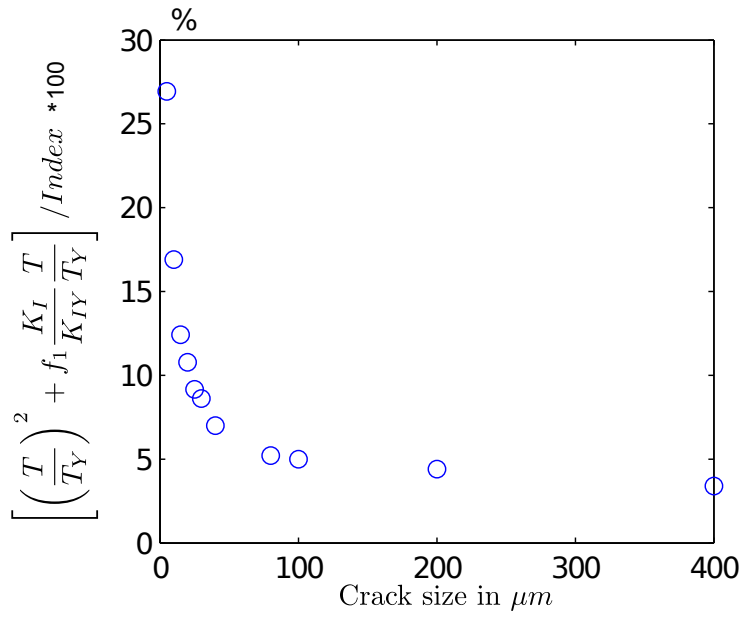


Figure 5.19: Relative influence of the  $T$ -stress in the criterion defined by the EQ.5.24, for different crack size, using the integral parameter  $\delta = 1\mu m$ .

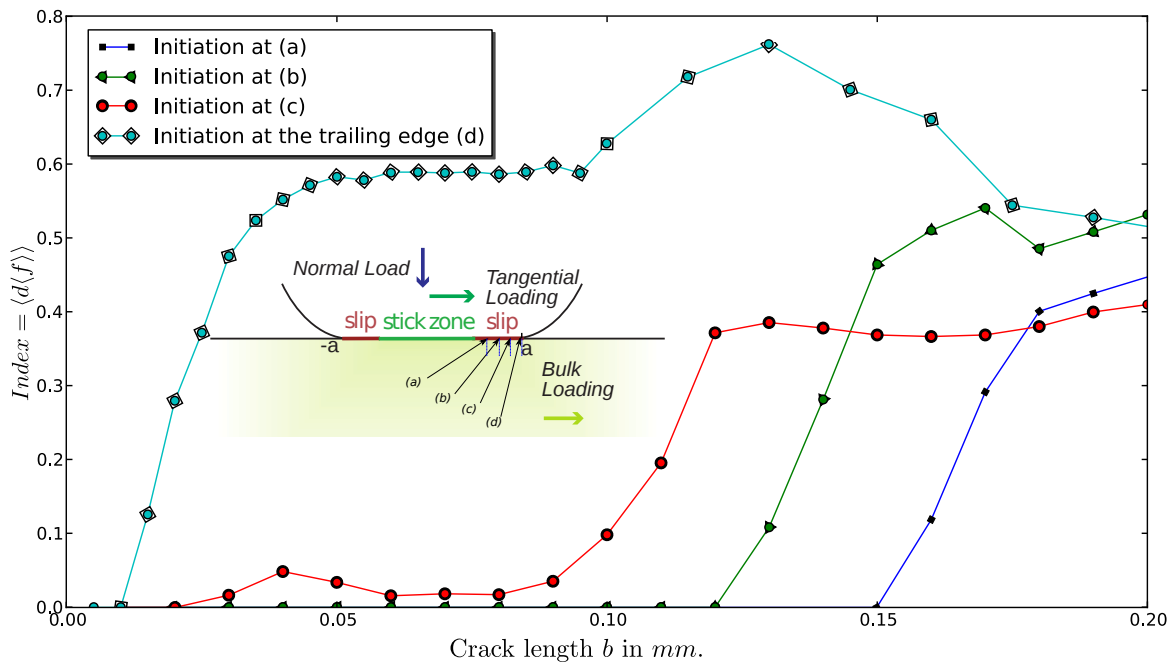


Figure 5.20: Evolution of the index with length  $b$  for vertical cracks initiating from different points under the slip zone.

### 5.4.5.ii Inclined crack.

**Path research algorithm.** The analysis has been extended with a research of the crack angle maximizing the criterion of EQ.5.27. The initiation point of the crack is however still assumed to be at the edge of the contact.

A Python script allows the automatic creation of an Abaqus model, including a crack, and a post-treatment of the results. The algorithm may be described as follows.

At the first step, a set of models is generated. Each of these models includes a short crack with the same size but with a different orientation. Using the time history of the linear elastic fracture mechanics quantities obtained from the computation, the index (EQ.5.27) is computed for each orientation. An adaptive multi-step search algorithm detailed by Norberg and Olsson (2005) and illustrated in FIG.5.21 is used to identify the orientation maximizing the index, and limit at a minimum the number of models evaluated. If the maximum found is positive, it is assumed that the crack will grow, and its direction will be the direction tested which maximized the index.

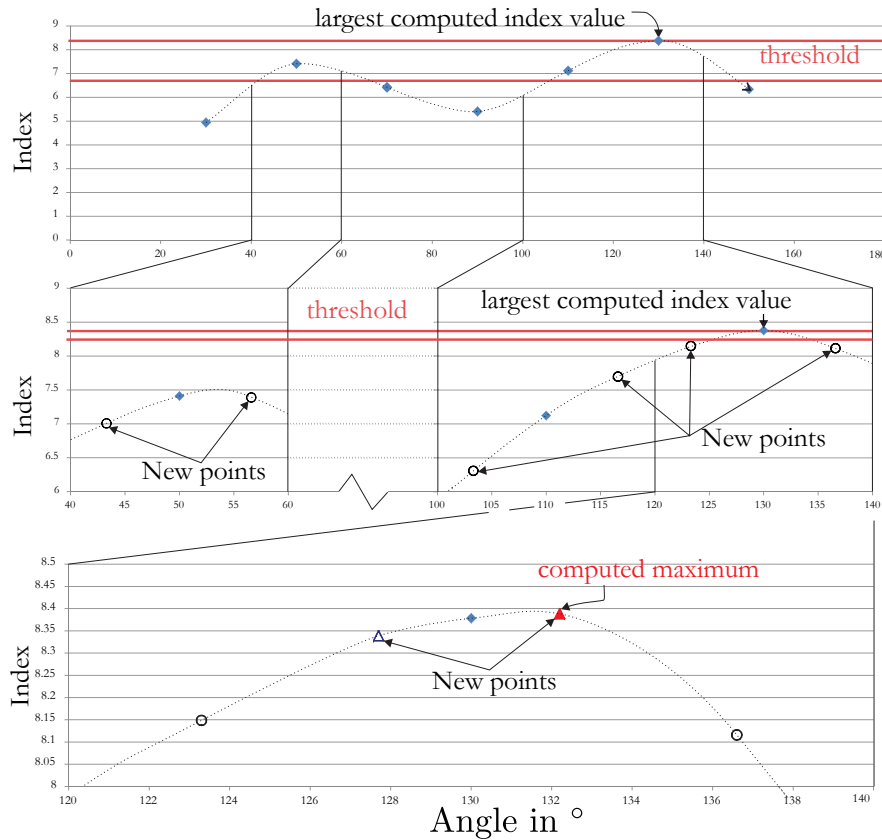


Figure 5.21: Schematic of the search algorithm used for finding the maximum value of  $f$ . Two refinement steps take place in the intervals where the extreme value may occur. (Norberg and Olsson 2005)

The process is then repeated for a given number of increments, or stopped if the index becomes negative for all acceptable orientations. The FIG.5.22 illustrates the first two steps of the procedure.

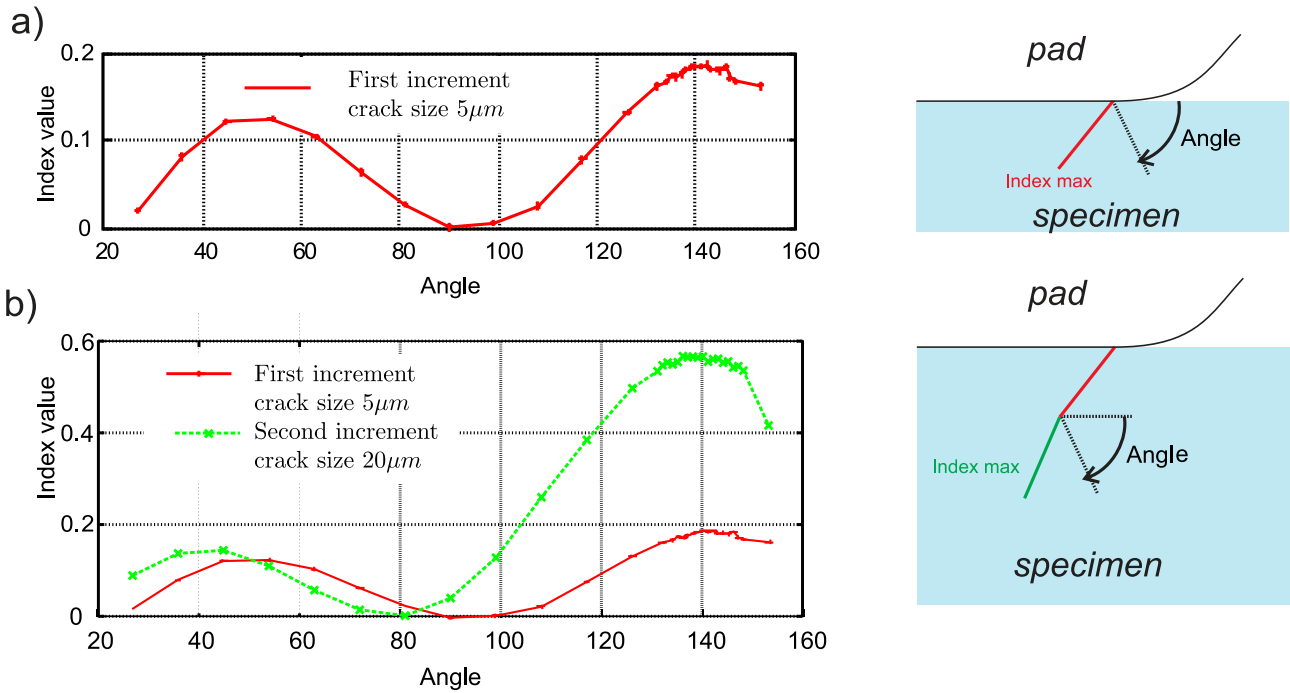


Figure 5.22: Illustration of the two first increments analyses.

**Results.** This methodology has been applied to the relevant loading configurations observed experimentally (SEC.4.1.1):

- Case 1: test 5  $Q/\mu P = 0.536$  and  $\sigma_{Bmax}/p_0 = 0.246$ : Specimen brake before  $10^6$  cycles,
- Case 2: test 4  $Q/\mu P = 0.512$  and  $\sigma_{Bmax}/p_0 = 0.240$ : Specimen survived at  $10^6$  cycles but crack arrest was observed,
- Case 3: test 1  $Q/\mu P = 0.464$  and  $\sigma_{Bmax}/p_0 = 0.219$ : Specimen survived at  $10^6$  cycles and not crack no crack initiation was observed,

Note that values of  $p_0$  and  $\sigma_{Bmax}/p_0$  were modified from TAB.4.1, to compensate the edge effect observed in SEC.3.3.2.

At the first increment, the orientation of a  $5\mu m$  crack is analyzed. Then the crack size increment is increased to  $20\mu m$ , this size increment allows a good agreement between crack path accuracy and processing time. Note that the crack is still assumed to initiate at the trailing edge of the contact. As a first observation of the results, Fig.5.22 presents the results of the angular distribution of the index at the first two increments for Case 2 loading configuration. As observed in the first part of this section, the index was null when the  $5\mu m$  crack is vertical (Angle =  $90^\circ$ ), however, two peaks with positive values of the index are observed for inclined cracks at  $45^\circ$  and  $140^\circ$ . Those two peaks present different maximums, indeed, the crack oriented towards the contact zone ( $140^\circ$ ) induces the highest index. At the second increment, the crack path direction remained roughly the same. It can be noted that the crack orientation estimation is not far from the actual crack path. The time history of the linear elastic fracture mechanics quantities are illustrated for this orientation of the  $5\mu m$  crack in FIG.5.23, the red part of the curve corresponds to the creation of plasticity at the tip of the crack.

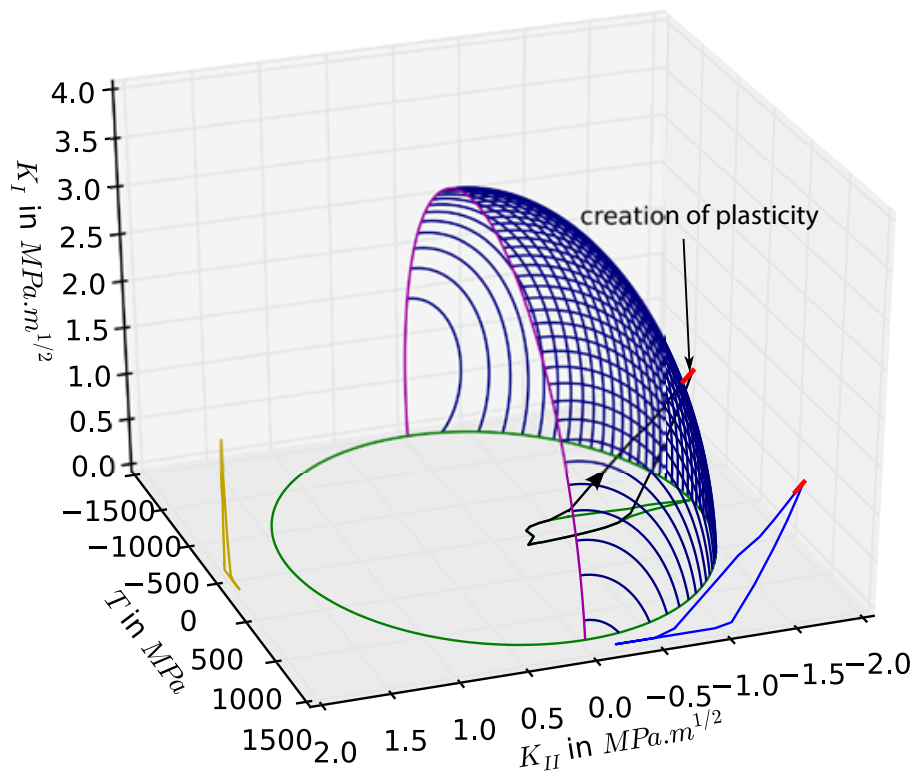


Figure 5.23: History of the linear elastic fracture mechanics quantities for a  $5\mu\text{m}$  crack, inclined at  $135^\circ$ .

FIG.5.24 presents the results of the simulation of the three loading cases. In Fig.5.25, the paths predicted for the loading cases 2 and 3 are presented. An example of crack profile observed at the middle section of the specimen is also given.

For the case 3, the index computed at the first step for all orientations was null. It means that an initial defect of  $5\mu m$  is not expected to grow with this loading. When the second loading case is considered, the model predicts a short crack grow at  $140^\circ$ . Then the crack path predicted progressively turns to mode I, which was expected. When the crack reaches a size of  $140\mu m$ , crack arrest is predicted.

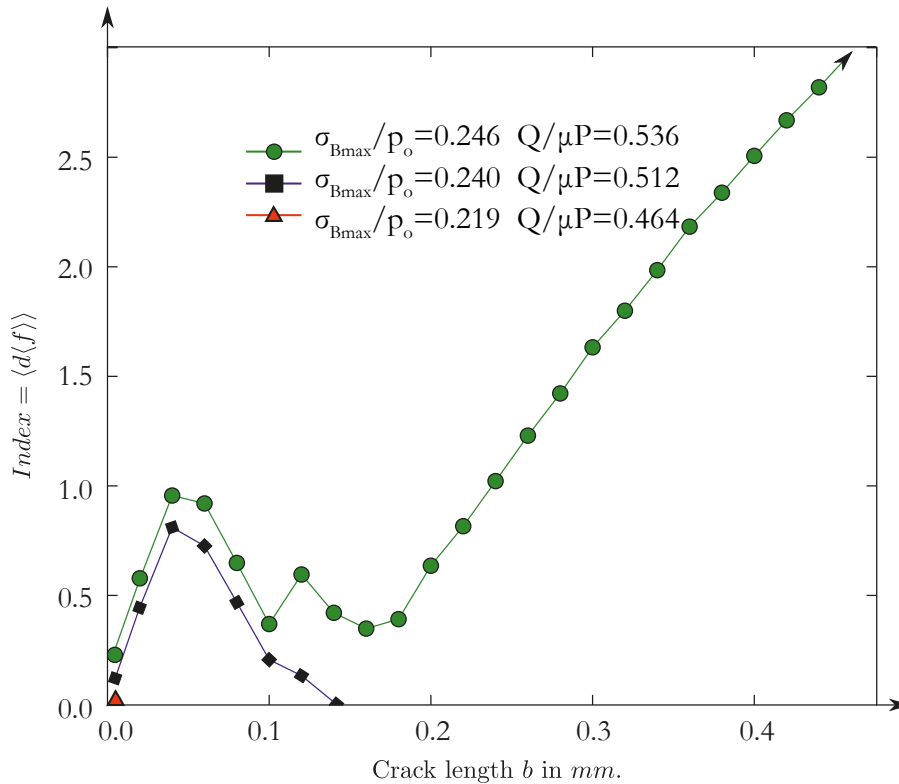


Figure 5.24: Index computed using the path search algorithm.

Indeed, the blue curve in FIG.5.24 shows a value of the index which increased until 0.8 and then decreased until 0. This profile is typical from the competition between crack length and stress gradient in fretting problem.

When the third loading case is considered, the crack profile predicted is very similar, but no crack arrest is observed. When the crack reaches a size of  $200\mu m$ , the decrease of the state of stress is not sufficient and the crack will continue its growth until failure.

After a certain distance, the crack propagation direction computed remains almost constant to the value  $45^\circ$ . This result disagrees with the experiential observations, where long cracks show a propagation in mode I governed by the bulk load. Figure 5.26 represents the history of  $K_I$ ,  $K_{II}$  and  $T$  in a 3D graph. The red surface represents the threshold of the elastic zone defined by the function  $f = 0$ . With such history, the index corresponds to the maximum value of the function  $f$  during the cycle. The iso-f surfaces in blue confirm the preference for the inclined crack.

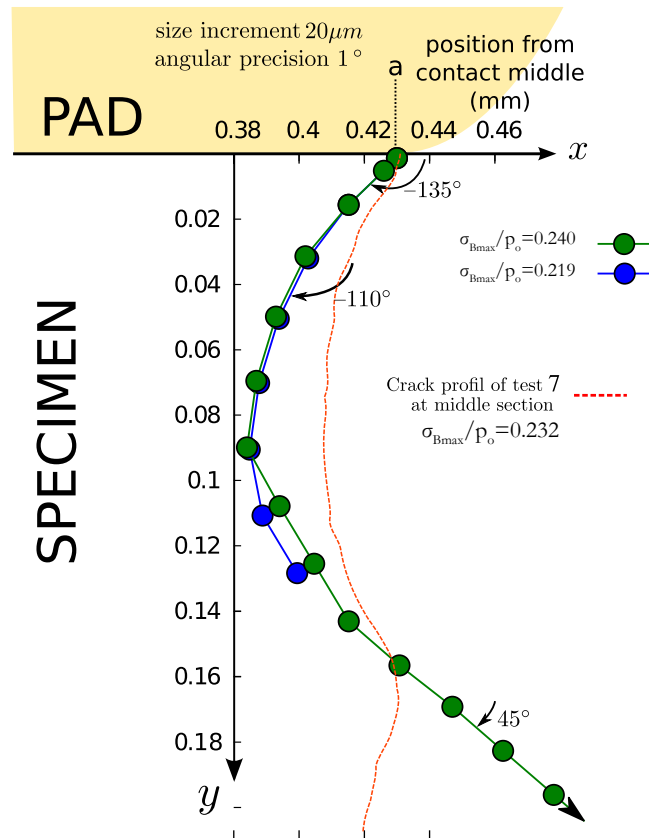


Figure 5.25: Crack path predicted for the relevant loading configurations. In red, an example of profile of the crack surface, here obtained for test 7 at the middle of the contact width.

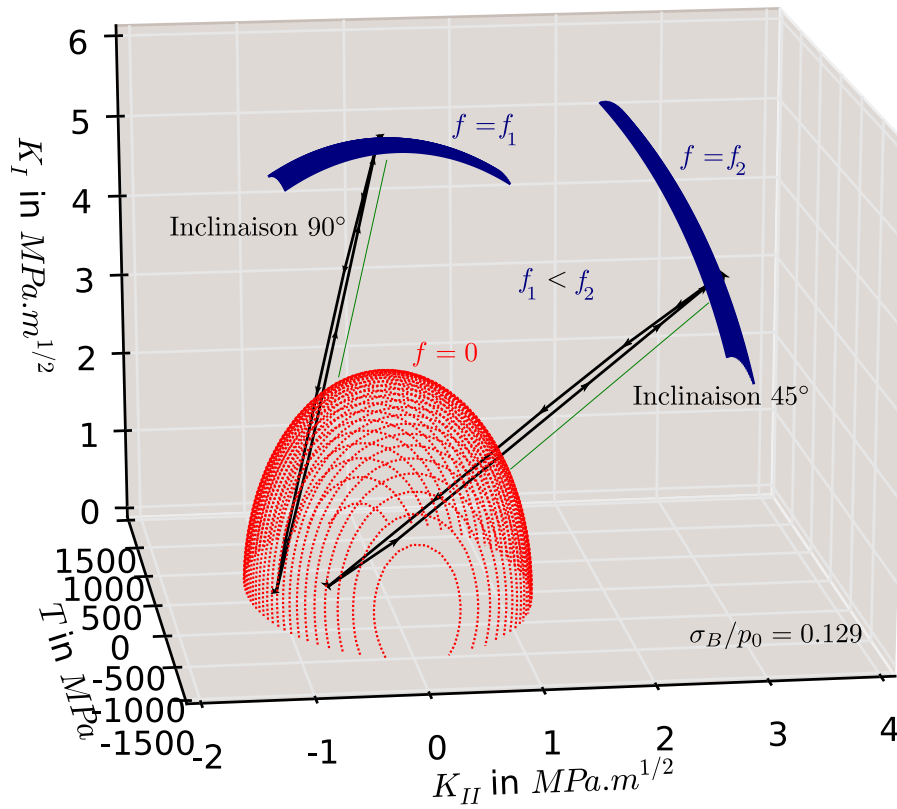


Figure 5.26: 3D representation of the orientation 45° and 90° analysed after 20 increments (crack size 400 $\mu m$ ).

The application of the proposed methodology successfully estimated the short crack arrest obtained experimentally. For larger crack sizes, an unexpected behavior was predicted. Indeed, when the crack reaches a size around  $140\mu m$ , the crack path predicted turns to a direction outside the contact zone, which is not in accordance with the actual path, where crack directions are usually observed to be perpendicular to the axial main fatigue load direction. This failure of the proposed model to estimate long crack propagation may come from the formulation of the criterion itself, or/and from assumptions used to simplify the numerical modeling. For example, the dependence of the threshold stress intensity factor on the loading ratio, discussed in the previous section, was not included in the current formulation of the criterion. This phenomenon is called displacement of the elastic domain. An enhanced version of the criterion would include the shift of the center of the elasticity domain  $\mathbf{K}^X = (K_I^X, K_{II}^X)$ , so that EQ.5.24 could be re-written as EQ.5.28.

$$f = \left( \frac{K_I - K_I^X}{K_{IY}} \right)^2 + \left( \frac{K_{II} - K_{II}^X}{K_{IIY}} \right)^2 + \left( \frac{T}{T_Y} \right)^2 + f_1 \frac{K_I - K_I^X}{K_{IY}} \frac{T}{T_Y} - 1 = 0 \quad (5.28)$$

This effect was studied by Fremy (2012), and gave good results for long cracks, however its application to the short crack regime and a correction for the T-stress terms have not been tried yet. Since the load ratio changes at the crack tip depending on the crack growth orientation, it seems reasonable to expect that an enhanced estimate of crack path can be obtained by including the displacement of the elastic domain in the proposed model.

Another likely reason of the prediction failure for long crack is the modeling of the crack closure. In the current finite elements modeling, the fracture roughness is not considered; the crack is modeled as a number of straight planes with a Coulomb interaction between them. In this case, the tangential stress between fracture faces is proportional to the pressure between the crack faces and sliding may occur. However, it is well known that crack roughness limits considerably the shear stress transmitted to the crack tip when crack closure happens. Hence, the real mode II stress intensity factor  $K_{II}$  (seen at the tip of the crack) may be considerably smaller than the one computed here. This drop of  $K_{II}$ , which is proportional to the crack length, is sometimes used to explain the transition between the different stages of the crack growth. Indeed, crack initiation is generally mode II dominant, however after a certain length of the crack, the shear resistance of crack faces is such that propagation will be directed by the mode I. In fretting fatigue, the constant pressure of the pad tends to close the crack during a non-negligible period of the cycle, even for small positive values of the bulk fatigue load. The non-consideration of the roughness induced crack closure may as well explain the unexpected propagation in mode II of long cracks in this proposition.

## Chapter 6

# Conclusions, recommendations and future work

### 6.1 Overview.

By definition, fretting fatigue is a phenomenon, in which two contact surfaces undergo a small relative oscillatory motion due to cyclic loading. Due to fretting, fatigue lifetime is significantly reduced as compared to plain fatigue. This is because of the localized high stresses that are generated at the contact surfaces of the two bodies. The gradients of the stress concentrations depend on the contact geometries and loading configuration. When the gradient is very strong, small cracks may initiate but do not necessarily lead to total failure.

The general aim of this research is to investigate the role of the stress gradient on the fretting fatigue phenomenon. In this setting, the first objective was to design and run tests with geometries which generate different stress gradients. The second was to challenge existing criteria and their ability to deal with different stress gradient and the multiaxial stresses under the contact.

### 6.2 Methodology used in this study.

#### 6.2.1 Experimental set-up

Two experimental sets up were used in this study. The first one is built around a single actuator machine and is designed for tests using two cylindrical fretting pads loaded against a flat dogbone tensile test piece. A fretting apparatus apply the normal force on the pads and, acting as a spring, also apply a tangential force proportional to the deformation of the sample. Digital Image Correlation was used to measure the deformation of the pad extremity and verify that pads remain perpendicular to the sample while the apparatus is deforming.

Three test sets were carried out with this type of set up. The first set used a pair of 20mm radius cylindrical indenters loaded with a constant normal force. The fatigue and tangential loading were increased gradually and the threshold loading for the run out was identified.

The second and third test sets were carried out with an enhanced fretting apparatus. Theses sets used 2 different pad radii (20mm and 70mm). The normal and the tangential force were kept constant

so that  $p_0$  and  $Q/\mu P$  were equal for both sets. In this setting, when the same fatigue load,  $\sigma_B$ , was applied on the sample, the stress field at the trailing edge of the contact was the same despite the difference of pad radii. The stress field far from the contact influence was also the same, and the configuration were called equivalent. The decrease of stress field intensity (i.e. the stress gradient), from the contact to the sample center depends on the pad radius. In this setting, it was possible to carry out equivalent tests but presenting a different stress gradient.

The second test set was realized using the 20mm pad radius, different fatigue loadings were tested and the maximum sustained load for run-out tests was identified. The first test with 70mm pad radius was realized with a load equivalent to the threshold identified with the 20mm pad radius. This test survived only 20% of the life obtained with the 20mm pad radius. The test was repeated with lower fatigue loading until reaching the run-out condition.

A new fretting fatigue test was also designed around a 6 actuators fatigue machine. With 4 actuators, this set up allowed to apply a complex fatigue multiaxial loading on a cruciform sample, while the two remaining actuators were used to press spherical-ended indenters on the central area of the sample.

### 6.2.2 Analytical and numerical modeling of the problem.

The 2D analytical formulation of the cylinder/plane problem was widely used in this work. This formulation is based on the classical contact analysis of (Hertz 1881; Mindlin 1949). It allows a rapid computation of the stress field at the surface and below the contact with the use of Muskhelishvili's potential (Muskhelishvili 1953).

FE modeling approach has been used to simulate fretting fatigue behavior. A 2D FEM of the cylinder plane contact was used to model the propagation of cracks. 3D FEM, more complex and time-consuming, was mainly used for the analysis of the spherical/plane problem.

### 6.2.3 Prediction of fretting fatigue lifetime

In fretting fatigue contact and bulk fatigue loads are both involved in the loading program. Therefore, the stress history in a material point within the contact interface will be invariably multiaxial and non-proportional. Moreover, initiated cracks will experience a variable load ratio,  $R_\sigma$ , as they grow away from the contact.

In this setting, the criterion previously proposed by Araújo et al. (2007) provides an interesting predictive methodology for the fretting fatigue problem. In this method, the Modified Wohler Curve Method assumes that fatigue damage depends on the shear stress amplitude,  $\tau_a$ , and on the maximum normal stress,  $\sigma_{n,max}$ , relative to a critical plane, thereby dealing with the multiaxiality and with the non proportionality of the problem. In order to account for the high-stress gradients, this model proposes to use the Theory of Critical Distances. In this model, the effect of the loading ratio is taken into account in the  $\sigma_{n,max}$  term.

Two other approaches, based on the concepts of short crack arrest were also challenged. The first method was first suggested by Nowell and Araújo (1999) and independently by Chan et al. (2001).

The method is based on the Kitagawa-Takahashi diagram (Kitagawa and Takahashi 1976) and the calculation of the stress intensity factor amplitude in mode I for a crack starting at the trailing edge of the contact and growing normal to the surface.

The second short crack arrest method considered was first proposed by Thieulot-Laure et al. (2007). This criterion is a generalized Von Mises yield criterion for the crack tip region based on the assumption that fatigue cracks propagate if a cyclic plastic strain is experienced at the crack tip. It is thus expressed as a threshold for plastic yield for a region of material around the crack tip. In this method, the distortional elastic energy density within the crack tip region is calculated using the stress, strain and displacement fields at the crack tip from LEFM. Since it is aimed at using this criterion for small cracks, non-singular terms, the T-stresses, are also considered.

## 6.3 Main conclusions

### 6.3.1 Fretting fatigue experiments

The results of fretting fatigue tests confirm the beneficial effect of stress gradient on the fatigue strength. Between two equivalent loading conditions, we observed that tests with a strong stress gradient (20mm pad radius) survived five times longer than tests with a smoother gradient (70mm pad radius).

The analyse of the fracture surface showed that initial stage of the crack propagation occurs in mixed mode condition. Moreover, cracks tend to initiate in an inclined plane which varied between  $-100^\circ$  and  $-115^\circ$  from the contact surface. After a distance comparable to the contact width, the crack propagation is mainly govern by the mode I. The observation of unbroken specimen only revealed the presence of very short crack or defect inferior to  $20\mu m$ , proving that the initiation and the first stage of the crack propagation represents the major part of the lifetime. However, we were unable to show a clear relation between the size of the arrested crack and the stress gradient.

Observation of the fretting mark of the cylinder/plane test showed small differences with the Hertz theory. The size of the contact appeared slightly larger. This phenomenon is caused by the edge effect and the redistribution of pressure. The 3D FEM confirmed that the peak pressure at the cross section of the contact was 4% higher than predicted by the Hertz theory. This phenomenon was of course absent in the spherical/plane contact.

### 6.3.2 Prediction of the fretting fatigue lifetime

**Multiaxial stress fatigue model ( MWCM with TCD):** This criterion requires a calibration of its parameter with two plain fatigue limit and the range of the stress intensity threshold. These material properties were not produced in this work. Data from the literature was then considered. Using an average of the fatigue limits found for the TI-6Al-4V, an initial set of parameters was calculated. With theses parameters, the multiaxial stress fatigue model failed to predict our experimental results. Using a reverse analysis, we showed that a different set of parameters could be used so that the criterion would correctly predict the three loading thresholds identified experimentally and then reflect the influence of the gradient.

**Short crack arrest approach based on the Kitagawa-Takahashi diagram :** The stress intensity factor range in mode I,  $\Delta K_I$ , was computed using the Distributed Dislocation Method for a crack starting at the trailing edge of the contact, and growing perpendicular to the surface. Here again, the material properties necessary for the definition of the stress intensity threshold,  $\Delta K_{th}$ , were taken from the literature. The error of prediction was very different for the three loading threshold.

Whereas the previous multiaxial criterion, this model does not account for the effect of the loading ratio variation under the contact. We proposed to modify the long crack threshold stress intensity factor  $\Delta K_0$  as a function of the load ratio  $R_\sigma$ . With this modification, the methodology still fails to predict exactly the experimental results. However, the errors obtained were almost the same for the three loading configuration. A calibration of the intrinsic crack length  $b_0 \approx 24\mu m$  would provide good agreement with the experimental results.

In those criteria, the parameters representing the critical distance,  $l_{PM}$ , or the size of the short crack domain,  $b_0$ , are in theory obtained with  $\Delta K_0$  and  $\Delta\sigma_{fl}$  which have uncertainty in measured values. The fact that these material parameters are combined and then raised to the power of two leads to significant uncertainties. Although the physical basis of those dimensions, they might be regarded as fitting parameters.

**T-stress based criterion :** An indicator of plasticity  $f$  was introduced for short cracks in mixed-mode loading conditions. The method was applied to the problem of fretting fatigue and shows that the high values of the T-stresses encountered in this problem contribute to crack tip plasticity of short crack and may promote short crack growth.

The criterion was only challenged with loading threshold identified for the first tests set. A 2D finite element model was used to compute the SIF and the T-stress.

A first approach considered straight cracks starting at different locations under the contact. The crack index was maximized for the position at the trailing edge of the contact. However, the criterion predicted that only a crack larger than  $10\mu m$  would propagate.

A path research algorithm was proposed based on the maximization of the indicator of plasticity  $f$ . This methodology successful estimated the short crack arrest obtained experimentally. However, unexpected behavior was predicted for larger crack sizes.

## 6.4 The scale effect.

This work focused on the evaluation of the gradient effect.

For that, we considered two pad radii under equivalent loading. However, as Papadopoulos and Panoskaltsis (1996) in his study of the bending of cylindrical specimens, we may have not only change the representative loaded volume (gradient effect) but also the general volume solicited (pure scale effect).

Indeed, when the 70mm pad radius configuration is considered, the stress gradient at the trailing edge of the contact is “smooth” and the representative volume of material solicited is important. But the contact is also larger than if a 20mm pad was used. This means that the area likely to present ideal sites for crack initiation is more important with the 70mm pad than with the 20mm pad.

To sum up, the effect of this superimposed “scale effect” was not separated from the effect of the gradient.

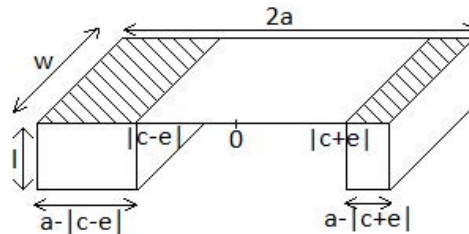


Figure 6.1: Example of volume characterizing the crack initiation risk.

This scale effect is complex to parameterized. It is unlikely that the contact size is the correct parameter to describe the general volume solicited. Other characteristic dimensions, such as the size of the slipping zone, may better characterize the initiation risk (FIG.6.1).

## 6.5 Notch analogy.

It is worth noticing that notched components and mechanical assemblies under time varying loads present quite similar characteristics. In both configurations, there are usually severe stress gradients and the state of stress becomes complex (multiaxial) as the analysis moves inside the material. It may be possible to design fretting and notch fatigue configurations, which are nominally identical in terms of damage measured by a multiaxial fatigue index.

If such experimental campaign could be generated, it would in a way isolate the role of the surface fretting wear in diminishing the material fatigue resistance of mechanical assemblies under partial slip. If both fatigue problems are equivalent in terms of fatigue loading over a material process zone, their resistance should be essentially similar. If not, the influence of the small surface damage caused by the fretting wear, and which does not exist in the notch configuration, should be considered.

Another quite important aspect that such analogy could clear out is the fact that one can use the same fatigue modeling approach to design either industrial components containing geometrical discontinuities or mechanical couplings. This would avoid the need for lengthy and costly experimental programs considering complex geometries and specific test rigs to calibrate the fatigue material constants.



# Bibliography

- Affonso, I.D. (2012). “Modelagem de ensaios envolvendo o contato entre cilindros sob condições de fadiga por fretting.” PhD thesis.
- Araújo, J.A. (2000). “On the Initiation and Arrest of the Fretting Fatigue Cracks”. PhD thesis.
- Araújo, J.A. and F.C. Castro (2012). “A comparative analysis between multiaxial stress and  $\Delta K$ -based short crack arrest models in fretting fatigue”. *Engineering Fracture Mechanics* 93, pp. 34–47.
- Araújo, J.A. and D. Nowell (1999). “Analysis of pad size effects in fretting fatigue using short crack arrest methodologies”. *International Journal of Fatigue* 21.9, pp. 947–956.
- Araújo, J.A., L. Susmel, D. Taylor, J.C.T. Ferro, and E.N. Mamiya (2007). “On the use of the Theory of Critical Distances and the Modified Wöhler Curve Method to estimate fretting fatigue strength of cylindrical contacts”. *International Journal of Fatigue* 29.1, pp. 95–107.
- Araújo, J.A., A.P. Dantas, F.C. Castro, E.N. Mamiya, and J.L.A. Ferreira (2011). “On the characterization of the critical plane with a simple and fast alternative measure of the shear stress amplitude in multiaxial fatigue”. *International Journal of Fatigue* 33.8, pp. 1092–1100.
- Arrieta, HV, P Wackers, and KD Van (2004). “Modelling Attempts to Predict Fretting-Fatigue Life on Turbine Components”.
- ASTM B861 (2014). *ASTM B861 - 14 Standard Specification for Titanium and Titanium Alloy Seamless Pipe*. Tech. rep. West Conshohocken, PA: ASTM International.
- Bantounas, I., D. Dye, and T.C. Lindley (2010). “The role of microtexture on the faceted fracture morphology in Ti-6Al-4V subjected to high-cycle fatigue”. *Acta Materialia* 58.11, pp. 3908–3918.
- Basseville, S., E. Hériprié, and G. Cailletaud (2011). “Numerical simulation of the third body in fretting problems”. *Wear* 270.11-12, pp. 876–887.
- Bathias, C. (1999). “There is no infinite fatigue life in metallic materials”. *Fatigue and Fracture of Engineering Materials and Structures* 22.7, pp. 559–565.
- Bellows, R. (1999). “Validation of the step test method for generating Haigh diagrams for Ti-6Al-4V”. *International Journal of Fatigue* 21.7, pp. 687–697.
- Bernardo, A.T., J.A. Araújo, and E.N. Mamiya (2006). “Proposition of a finite element-based approach to compute the size effect in fretting fatigue”. *Tribology International* 39.10, pp. 1123–1130.
- Blanpain, B., H. Mohrbacher, E. Liu, J.P. Celis, and J.R. Roos (1995). “Hard coatings under vibrational contact conditions”. *Surface and Coatings Technology* 74-75, pp. 953–958.
- Blau, P.J. (2013). “Amontons’ Laws of Friction”. *Encyclopedia of Tribology*. Ed. by Yip-Wah Wang, Q.Jane and Chung, pp. 71–71.
- Boddington, P.H.B., K. Chen, and C. Ruiz (1985). “The numerical analysis of dovetail joints”. *Computers & Structures* 20.4, pp. 731–735.
- Boyce, B.L. and R.O. Ritchie (2001). “Effect of load ratio and maximum stress intensity on the fatigue threshold in Ti-6Al-4V”. *Engineering Fracture Mechanics* 68, pp. 129–147.
- Bramhall, R. (1973). “Studies in fretting fatigue.” PhD thesis.

- Brown, M.W. and K.J. Miller (1973). “A theory for fatigue failure under multiaxial stress–strain conditions”. *ARCHIVE: Proceedings of the Institution of Mechanical Engineers 1847-1982 (vols 1-196)* 187.1973, pp. 745–755.
- Bueckner, H.F. (1958). “The Propagation of Cracks and the Energy of Elastic Deformation”. *Trans. A.S.M.E.* 80, p. 1225.
- Campbel, F.C. (2008). *Elements of Metallurgy and Engineering Alloys*. ASM International.
- Carpinteri, A. and A. Spagnoli (2001). “Multiaxial high-cycle fatigue criterion for hard metals”. *International Journal of Fatigue* 23.2, pp. 135–145.
- Castany, P. (2007). “Etude des Micromécanismes de Déformation d’un Alliage Ti-6Al-4V par Déformation MET in situ: Influence d’un Traitement de Surface”.
- Castro, F.C., J.A. Araújo, and N. Zouain (2009a). “On the application of multiaxial high-cycle fatigue criteria using the theory of critical distances”. *Engineering Fracture Mechanics* 76.4, pp. 512–524.
- Castro, F.C., J.A. Araújo, E.N. Mamiya, and N. Zouain (2009b). “Remarks on multiaxial fatigue limit criteria based on prismatic hulls and ellipsoids”. *International Journal of Fatigue* 31.11-12, pp. 1875–1881.
- Cattaneo, C. (1938). “Sul contatto di due corpi elastici: distribuzione locale degli sforzi. Rendiconti dell’Accademia nazionale dei Lincei”. *Rendiconti dell’Accademia nazionale dei Lincei* 27, pp. 342–348.
- CCJ, Team (2015). *Issues identified during recent borescope inspections on GE and Siemens frames*.
- Chan, K.S., Y.D. Lee, D.L. Davidson, and S. Hudak (2001). “A fracture mechanics approach to high cycle fretting fatigue based on the worst case fret concept”. *International Journal of Fracture* 112.4, pp. 331–353.
- Collins, J.A. and S.M. Marco (1964). “No Title”. *Proc.ASTM* 64, p. 547.
- Corinne, C. (2008). “Modelling microstructure evolution of weld deposited Ti-6Al-4V”. PhD thesis. Lulea University of Technology.
- Crossland, B. (1956). “Effect of large hydrostatic pressures on the torsional fatigue strength of an alloy steel”. *Proceedings of the international conference on fatigue of metals, Institution of Mechanical Engineers, London*. Ed. by IMechE. London, pp. 138–149.
- Dang Van, K. (1973). “Sur la résistance à la fatigue des métaux”. *Sciences et Techniques de l’Armement* 47.3ème fascicule, pp. 641–722.
- (1989). *On a new multiaxial fatigue limit criterion: theory and application*.
- Davoli, P., A. Bernasconi, M. Filippini, S. Foletti, and I.V. Papadopoulos (2003). “Independence of the torsional fatigue limit upon a mean shear stress”. *International Journal of Fatigue* 25.6, pp. 471–480.
- De Moura Pinho, R., S. Pommier, C. Mary, A. Longuet, and F. Vogel (2012). “A novel methodology to predict the endurance domain for a material and its evolution using a generalized fracture mechanics framework”. *International Journal of Fatigue* 42, pp. 183–193.
- Delahay, T. (2004). “Développement d’une méthode probabiliste de calcul en fatigue multiaxiale prenant en compte la répartition volumique des contraintes.” PhD thesis.
- Ding, J., I.R. McColl, S.B. Leen, and P.H. Shipway (2007). “A finite element based approach to simulating the effects of debris on fretting wear”. *Wear* 263.1-6, pp. 481–491.
- Dobromirski, J. (1992). “Variables of fretting process: are there 50 of them?” *ASTM Special Technical Publication*.
- Donachie, Matthew J. (2000). *Titanium: A Technical Guide, 2nd Edition*. ASM International, p. 381.
- Dundurs, J. and G.P. Sendeckyj (1965). “Behavior of an edge dislocation near a bimetallic interface”. *Journal of Applied Physics* 36, p. 3353.

- E2789-10, ASTM standard (2011). "Standard Guide for Fretting Fatigue Testing." *ASTM International*.
- Eden, E.M., W.N. Rose, and F.L. Cunningham (1911). "The endurance of metals: experiments on rotating beams at University College, London". *Proceedings of the Institution of Mechanical Engineers* 4, pp. 839–974.
- Edwards, P.R., R.J. Ryman, R. Cook, and G. Britain (1977). "Fracture mechanics prediction of fretting fatigue under constant amplitude loading". *Proc. Ninth ICAF Symposium, Darmstadt*.
- El Haddad, M. H., N. E. Dowling, T. H. Topper, and K. N. Smith (1980). "J integral applications for short fatigue cracks at notches". *International Journal of Fracture* 16.1, pp. 15–30.
- El Haddad, M.H., T.H. Topper, and K.N. Smith (1979). "Prediction of non propagating cracks". *Engineering Fracture Mechanics* 11.3, pp. 573–584.
- Endo, K. and H. Goto (1978). "Effects of environment on fretting fatigue". *Wear* 48.2, pp. 347–367.
- Endo, K., H. Goto, and T. Fukunaga (1969). "A Frictional force in fretting fatigue". *Bulletin of the JSME* 17.108, pp. 647–654.
- Eshelby, J.D. (1956). "The Continuum Theory of Lattice Defects". *Solid State Physics* 3, pp. 79–144.
- Farris, T.N., G. Harish, C. Tieche, T. Sakagami, and M.P. Szolwinski (2000). "Experimental Tools for Characterizing Fretting Contacts." *JSME international journal. Series A, Solid mechanics and material engineering*, 43.3, pp. 374–383.
- Fatemi, A. and D.F. Socie (1988). "Critical plane approach to multiaxial fatigue damage including out-of-phase loading". *Fatigue and Fracture of Engineering Materials and Structures* 11.3, pp. 149–165.
- Fellows, L.J., D. Nowell, and D.A. Hills (1995). "Contact stresses in a moderately thin strip (with particular reference to fretting experiments)". 185.i, pp. 235–238.
- Fenner, A.J. and J.E. Field (1958). "No Title". *Revue Métallurgie* 55, p. 1.
- Ferré, R. (2013). "Etude expérimentale et modélisation de la durabilité d'un contact aube/disque de soufflante grenailé revêtu soumis à des chargements de Fretting/Fatigue/Usure". PhD thesis. L'ECOLE CENTRALE DE LYON.
- Findley, W.N. (1959). "A theory for the effect of mean stress on fatigue of metals under combined torsion and axial load or bending." *J Eng Ind* 81, pp. 301–306.
- Fouvry, S., P. Kapsa, and L. Vincent (2003). "A global methodology to quantify fretting damages". *ASTM SPECIAL TECHNICAL ...*
- Fouvry, S., P. Duó, and Ph. Perruchaut (2004). "A quantitative approach of Ti-6Al-4V fretting damage: friction, wear and crack nucleation". *Wear* 257.9-10, pp. 916–929.
- Fouvry, S., C. Paulin, and T. Liskiewicz (2007). "Application of an energy wear approach to quantify fretting contact durability: Introduction of a wear energy capacity concept". *Tribology International* 40.10-12 SPEC. ISS. Pp. 1428–1440.
- Fremy, F. (2012). "Fissuration par fatigue en mode mixte I+II+III non proportionnel dans l'acier 316L". PhD thesis.
- Freudenthal, A.M. (1968). "Statistical approach to brittle fracture". *Fracture*.
- Frost, N.E. and D.S. Dugdale (1957). "Fatigue tests on notched mild steel plates with measurements of fatigue cracks". *Journal of the Mechanics and Physics of Solids* 5.3, 182–188, IN1–IN2, 189–192–182.
- Gerber, W (1874). "Relation Between the Superior and Inferior Stresses of a Cycle of Limiting Stress". *Zeit. Bayerischen Arch. Ing.-Vereins*.
- Giannakopoulos, A.E. and S. Suresh (1998). "A three-dimensional analysis of fretting fatigue". *Acta Materialia* 46.1, pp. 177–192.

- Golden, P.J. and A.F. Grandt Jr. (2004). "Fracture mechanics based fretting fatigue life predictions in Ti-6Al-4V". *Engineering Fracture Mechanics* 71.15, pp. 2229–2243.
- Goodman, J. (1899). *Mechanics applied to engineering*. London: Longmans, Green and Company.
- Gough, H.J. (1949). "Engineering Steels under Combined Cyclic and Static Stresses". *Proceedings of the Institution of Mechanical Engineers* 160, pp. 417–440.
- Griffith, A.A. (1921). "The Phenomena of Rupture and Flow in Solids". *Philosophical Transactions of the Royal Society A: Mathematical, Physical and Engineering Sciences* 221.582-593, pp. 163–198.
- Haigh, B.P. (1917). "Experiments on the fatigue of brasses." *Journal of the Institute of Metals* 18, pp. 55–86.
- Hénaff, G. and F. Morel (2005). *Fatigue des structures: endurance, critères de dimensionnement, propagation des fissures, rupture*, p. 275.
- Herald, The Aviation (2009). *Accident: SouthWest B733 near Dallas on Nov 17th 2007, uncontained engine failure enroute*.
- Hertz, R. (1881). "Über die Berührung fester elastischer Körper". *Journal für die reine und angewandte Mathematik* 92, pp. 156–171.
- Hills, D.A. (1994). "Mechanics of fretting fatigue". *Wear* 175.1-2, pp. 107–113.
- Hills, D.A. and D. Nowell (1992). "The Development of a Fretting Fatigue Experiment with Well Defined Characteristics". *Standardization of Fretting Fatigue Test Methods and Equipment* 1159, p. 69.
- (1993). *Mechanics of Fretting Fatigue*. Kluwer academic publishers.
- Hills, D.A., D. Nowell, and A. Sack eld (1988). "Surface fatigue considerations in fretting". *Interface Dynamics, Proceedings of the 14th Leeds-Lyon Symposium on Tribology, Elsevier, Amsterdam*, pp. 35–40.
- Hines, J. A. and G. Lutjering (1999). "Propagation of microcracks at stress amplitudes below the conventional fatigue limit in Ti-6Al-4V". *Fatigue & Fracture of Engineering Materials and Structures* 22.8, pp. 657–665.
- Hojjati Talemi, R. (2014). *Numerical Modelling Techniques for Fretting Fatigue Crack Initiation and Propagation*.
- Hutson, A., T. Nicholas, and R. John (2005). "Fretting fatigue crack analysis in Ti-6Al-4V". *International Journal of Fatigue* 27.10-12, pp. 1582–1589.
- Hyde, T.R., S.B. Leen, and I.R. McColl (2005). "A simplified fretting test methodology for complex shaft couplings". *Fatigue & Fracture of Engineering Materials and Structures* 28.11, pp. 1047–1067.
- Inglis, C.E. (1913). "Stresses in a plate due to the presence of cracks and sharp corners". *Transactions of the Institution of Naval Architects* 55, pp. 219–230.
- Irwin, G.R. (1957). "Analysis of stresses and strains near the end of a crack traversing a plate". *Journal of Applied Mechanics* 1.24, pp. 361–364.
- (1958). *Elasticity and Plasticity / Elastizität und Plastizität*. Ed. by S. Flügge. Vol. 3 / 6. Handbuch der Physik / Encyclopedia of Physics. Berlin, Heidelberg: Springer Berlin Heidelberg.
- Ivanova, S.G., F.S. Cohen, R.R. Biederman, and R.D. Sisson Jr. (1999). "Role of microstructure in the mean stress dependence of fatigue strength in Ti-6Al-4V alloy". English.
- Ivanova, S.G., R.R. Biederman, and R.D. Sisson Jr (2002). "Investigation of Fatigue Crack Initiation in Ti-6Al-4V During Tensile-Tensile Fatigue". *Journal of Materials Engineering and Performance* 11.2, pp. 226–231.
- Iyer, K. and S. Mall (2001). "Analyses of Contact Pressure and Stress Amplitude Effects on Fretting Fatigue Life". *Journal of Engineering Materials and Technology* 123.1, p. 85.

- Jayaprakash, M., Y. Mutoh, K. Asai, K. Ichikawa, and S. Sukarai (2010). “Effect of contact pad rigidity on fretting fatigue behavior of NiCrMoV turbine steel”. *International Journal of Fatigue* 32.11, pp. 1788–1794.
- Jin, O. and S. Mall (2002). “Effects of independent pad displacement on fretting fatigue behavior of Ti-6Al-4V”. *Wear* 253.5-6, pp. 585–596.
- (2004). “Shear force effects on fretting fatigue behavior of Ti-6Al-4V”. *Metallurgical and Materials Transactions A* 35.1, pp. 131–138.
- Johnson, K.L. (1985). *Contact mechanics*. Cambridge University Press.
- Kandil, F.A., M.W. Brown, and K.J. Miller (1982). “Biaxial low-cycle fatigue failure of 316 stainless steel at elevated temperatures”. . . . *steel at elevated temperatures*.
- Kim, H.S. and S. Mall (2005). “Investigation into three-dimensional effects of finite contact width on fretting fatigue”. *Finite Elements in Analysis and Design* 41.11-12, pp. 1140–1159.
- Kim, H.S., S. Mall, and A. Ghoshal (2011). “Two-Dimensional and Three-Dimensional Finite Element Analysis of Finite Contact Width on Fretting Fatigue”. *Materials Transactions* 52.2, pp. 147–154.
- Kirsch, E.G. (1898). “Die Theorie der Elastizität und die Bedürfnisse der Festigkeitslehre”. *Zeitschrift des Vereines deutscher Ingenieure* 42.
- Kitagawa, H. and S. Takahashi (1976). “Applicability of fracture mechanics to very small cracks or the cracks in the early stage”. *Proc 2nd Int. Conf. on Mech. Behavior of Materials*, pp. 627–631.
- Krenk, S. (1975). “On the Use of the Interpolation Polynomial for Solutions of Singular Integral Equations”. *Quarterly of Applied Mathematics* 32.4, pp. 479–484.
- Kubiak, K. (2006). “Quantification de la fissuration d’un contact soumis à des sollicitations complexes en fretting wear et fretting fatigue.” PhD thesis.
- Kubiak, K., S. Fouvry, and A.M. Marechal (2005). “A practical methodology to select fretting palliatives: Application to shot peening, hard chromium and WC-Co coatings”. *Wear* 259.1-6, pp. 367–376.
- Laird, C. (1967). “The influence of metallurgical structure on the mechanisms of fatigue crack propagation”. *Fatigue crack propagation, ASTM*. Ed. by ASTM. Vol. 415. Philadelphia, pp. 131–180.
- Lanning, D.B., T. Nicholas, and G.K. Haritos (2005). “On the use of critical distance theories for the prediction of the high cycle fatigue limit stress in notched Ti-6Al-4V”. *International Journal of Fatigue* 27.1, pp. 45–57.
- Larsson, S.G. and A.J. Carlsson (1973). “Influence of non-singular stress terms and specimen geometry on small-scale yielding at crack tips in elastic-plastic materials”. *Journal of the Mechanics and Physics of Solids* 21.4, pp. 263–277.
- Le Biavant, K. (2000). “Etude de l’amorçage de fissure de fatigue dans le TI-6AL-4V”. PhD thesis.
- Le Biavant, K., S. Pommier, and C. Prioul (2002). “Local texture and fatigue crack initiation in a Ti-6Al-4V titanium alloy”. *Fatigue and Fracture of Engineering Materials and Structures* 25.6, pp. 527–545.
- Lee, H. and S. Mall (2004a). “Effect of dissimilar mating materials and contact force on fretting fatigue behavior of Ti-6Al-4V”. *Tribology International* 37.1, pp. 35–44.
- (2004b). “Some Observations on Frictional Force During Fretting Fatigue”. *Tribology Letters* 17.3, pp. 491–499.
- Leonard, B.D., P. Patil, T.S. Slack, F. Sadeghi, S. Shinde, and M. Mittelbach (2011). “Fretting Wear Modeling of Coated and Uncoated Surfaces Using the Combined Finite-Discrete Element Method”. *Journal of Tribology* 133.2, p. 021601.
- Li, B., J.L.T. Santos, and M. Freitas (2007). “A Unified Numerical Approach for Multiaxial Fatigue Limit Evaluation”. en.

- Lindley, T.C. (1997). "Fretting fatigue in engineering alloys". *International Journal of Fatigue* 19.93, pp. 39–49.
- MacGregor, C.W. and N. Grossman (1952). "Effects of cyclic loading on mechanical behavior of 24S-T4 and 75S-T6 aluminum alloys and SAE 4130 Steel".
- Madge, J.J., S.B. Leen, I.R. McColl, and P.H. Shipway (2007). "Contact-evolution based prediction of fretting fatigue life: Effect of slip amplitude". *Wear* 262.9, pp. 1159–1170.
- Majzoobi, G.H., R. Hojjati Talemi, M. Nematian, E. Zalnejad, A.R. Ahmadvani, and E. Hanifepoor (2010). "A new device for fretting fatigue testing". *Transactions of the indian institute of metals* 63.2-3, pp. 493–497.
- Mamiya, E.N. and J.A. Araújo (2002). "Fatigue limit under multiaxial loadings: on the definition of the equivalent shear stress". *Mechanics Research Communications* 29.2-3, pp. 141–151.
- Mamiya, E.N., J.A. Araújo, and F.C. Castro (2009). "Prismatic hull: A new measure of shear stress amplitude in multiaxial high cycle fatigue". *International Journal of Fatigue* 31.7, pp. 1144–1153.
- Martins, L.H., L.S. Rossino, W.W. Bose Filho, and J.A. Araújo (2008). "Detailed design of fretting fatigue apparatus and tests on 7050-T7451~Al alloy". *Tribology - Materials, Surfaces and Interfaces* 2.1, pp. 39–49.
- Mary, C. (2009). "Simulation experimentale de l'usure du contact aube-disque de compresseur sous sollicitations de fretting". Theses. Ecole Centrale de Lyon.
- Mary, C. and S. Fouvry (2007). "Numerical prediction of fretting contact durability using energy wear approach: Optimisation of finite-element model". *Wear* 263.1-6, pp. 444–450.
- McColl, I.R., J. Ding, and S.B. Leen (2004). "Finite element simulation and experimental validation of fretting wear". *Wear* 256.11-12, pp. 1114–1127.
- McDowell, J.R. (1952). "Fretting Corrosion Tendencies of Several Combinations of Materials". *ASTM STP144*, pp. 24–39.
- Meggiolaro, M.A., A. Miranda, and J. Castro (2007). "Short crack threshold estimates to predict notch sensitivity factors in fatigue". *International Journal of Fatigue* 29.9-11, pp. 2022–2031.
- Meguid, S.A., P.S. Kanth, and A. Czekanski (2000). "Finite element analysis of fir-tree region in turbine discs". *Finite Elements in Analysis and Design* 35.4, pp. 305–317.
- Meriaux, J. (2010). "Etude expérimentale de modélisation de l'endommagement d'un contact aube disque de soufflante soumis à des chargements de fretting fatigue." PhD thesis.
- Milestone, W.D. and J.T. Janeczko (1971). "Friction between steel surfaces during fretting". *Wear* 18.1, pp. 29–40.
- Miller, K.J. (1987). "The behaviour of short fatigue cracks and their initiation part I—a review of two recent books". *Fatigue & Fracture of Engineering Materials & ...* 10.1, pp. 75–91.
- Mindlin, R.D. (1949). "Compliance of elastic bodies in contact". *J. Appl. Mech.* 16, pp. 259–268.
- Mohrbacher, H., J.P. Celis, and J.R. Roos (1995). "Laboratory testing of displacement and load induced fretting". *Tribology International* 28.5, pp. 269–278.
- Moshier, M.A., T. Nicholas, and B.M. Hillberry (2001). "Load history effects on fatigue crack growth threshold for Ti-6Al-4V and Ti-17 titanium alloys". *International Journal of Fatigue* 23, Supple.0, pp. 253–258.
- Murakami, Y. and M. Endo (1994). "Effects of defects, inclusions and inhomogeneities on fatigue strength". *International Journal of Fatigue* 16.3, pp. 163–182.
- Muskhelishvili (1953). *Some Basic Problems of Mathematical Theory of Elasticity*. Noordhoff, Groningen.
- Mutoh, Y. and J.Q. Xu (2003). "Fracture mechanics approach to fretting fatigue and problems to be solved". *Tribology International* 36.2, pp. 99–107.

- Nagai, K., T. Yuri, O. Umeza, T. Ogata, K. Ishikawa, and Y. Ito (1993). “High cycle fatigue properties of Ti-6Al-4V alloys at cryogenic temperatures”. *Titanium*. Ed. by Caplan IL Froes FH. Warrendale (PA), pp. 1827–34.
- Nakazawa, K., M. Sumita, and N. Maruyama (1992). “Effect of contact pressure on fretting fatigue of high strength steel and titanium alloy”. *Standardization of fretting fatigue test methods and equipment(A 93-32539 12-23)*. Philadelphia, PA, American Society for Testing and Materials.
- Nalla, R.K., B.L. Boyce, J.P. Campbell, J.O. Peters, and R.O. Ritchie (2002). “Influence of microstructure on high-cycle fatigue of Ti-6Al-4V: Bimodal vs. lamellar structures”. *Metallurgical and Materials Transactions A* 33.13, pp. 899–918.
- Nalla, R.K., I. Altenberger, U. Noster, G.Y. Liu, B. Scholtes, and R.O. Ritchie (2003). “On the influence of mechanical surface treatments—deep rolling and laser shock peening—on the fatigue behavior of Ti-6Al-4V at ambient and elevated temperatures”. *Materials Science and Engineering: A* 355.1-2, pp. 216–230.
- Nesládek, M., M. Španiel, J. Jurenka, J. Růžička, and J. Kuželka (2012). “Fretting fatigue – Experimental and numerical approaches”. *International Journal of Fatigue* 44, pp. 61–73.
- Neu, R.W., J. Pape, and D.R. Swalla (2000). “Methodologies for linking nucleation and propagation approaches for predicting life under fretting fatigue”. *Fretting Fatigue: Current Technology and Practices, ASTM STP 1367*.
- Neuber, H. (1936). “Theorie der technischen Formzahl”. *Forschung auf dem Gebiete des Ingenieurwesens* 7.6, pp. 271–274.
- (1958). “Theory of Notch Stresses”. *Kerbspannungslehre*.
- Nicholas, T. (2006). “Characterizing Fatigue Limits”. *High Cycle Fatigue*, pp. 27–69.
- Nishioka, K. and K. Hirakawa (1969a). “Fundamental Investigations of Fretting Fatigue : Part 2, Fretting Fatigue Testing Machine and Some Test Results”. *Bulletin of JSME* 12.50, pp. 180–187.
- (1969b). “Fundamental Investigations of Fretting Fatigue : Part 3, Some Phenomena and Mechanisms of Surface Cracks”. *Bulletin of JSME* 12.51, pp. 397–407.
- (1969c). “Fundamental Investigations of Fretting Fatigue : Part 4, The Effect of Mean Stress”. *Bulletin of JSME* 12.51, pp. 408–414.
- Nishioka, K., K. Hirakawa, and S. Nishimura (1968). “Fundamental Investigations of Fretting Fatigue : Part 1, On the Relative Slip Amplitude of Press-fitted Axle Assemblies”. *Bulletin of JSME* 11.45, pp. 437–445.
- Norberg, S. and M. Olsson (2005). “A fast, versatile fatigue post-processor and criteria evaluation”. *International Journal of Fatigue* 27.10-12, pp. 1335–1341.
- Nowell, D. (1988). “An analysis of fretting fatigue”. PhD thesis.
- Nowell, D. and J.A. Araújo (1999). “No Title”. *Small fatigue cracks: Mechanics, Mechanisms, and Applications*. Ed. by K S Ravichandran, R O Ritchie, and Y. Murakami. Oxford: Elsevier, pp. 361–372.
- Nowell, D., D. Dini, and D.A. Hills (2006a). “Recent developments in the understanding of fretting fatigue”. *Engineering Fracture Mechanics* 73.2, pp. 207–222.
- Nowell, D., D. Dini, and D.a. Hills (2006b). “Recent developments in the understanding of fretting fatigue”. *Engineering Fracture Mechanics* 73.2, pp. 207–222.
- Oberwinkler, B., M. Riedler, and W. Eichlseder (2010). “Importance of local microstructure for damage tolerant light weight design of Ti-6Al-4V forgings”. *International Journal of Fatigue* 32.5, pp. 808–814.
- Papadopoulos, I.V. (1997). “A comparative study of multiaxial high-cycle fatigue criteria for metals”. *International Journal of Fatigue* 19.3, pp. 219–235.

- Papadopoulos, I.V. and V.P. Panoskaltis (1996). “Invariant formulation of a gradient dependent multiaxial high-cycle fatigue criterion”. *Engineering Fracture Mechanics* 55.4, pp. 513–528.
- Papanikos, P., S.A. Meguid, and Z. Stjepanovic (1998). “Three-dimensional nonlinear finite element analysis of dovetail joints in aeroengine discs”. *Finite Elements in Analysis and Design* 29.3-4, pp. 173–186.
- Paris, P.C., M.P. Gomez, and W.E. Anderson (1961). “A rational analytic theory of fatigue”. *The trend in engineering*.
- Pelloux, R.M.N. (1969). “Mechanisms of formation of ductile fatigue striations.” *ASM Trans Quart* 62.1, pp. 281–285.
- Peters, J.O., B.L. Boyce, X. Chen, J.M. McNaney, J.W. Hutchinson, and R.O. Ritchie (2002). “On the application of the Kitagawa-Takahashi diagram to foreign-object damage and high-cycle fatigue”. *Engineering Fracture Mechanics* 69.13, pp. 1425–1446.
- Peters, M., A. Gysler, and G. Lutjering (1984). “Influence of texture on fatigue properties of Ti-6Al-4V”. *Metallurgical Transactions A* 15.8, pp. 1597–1605.
- Peterson, R.E. (1959). “Notch sensitivity”. *Metal Fatigue*, pp. 293–306.
- Pogoretskii, R.G. (1966). “Effect of test piece length on the fatigue strength of steel in air”. *Soviet materials science: a transl. of Fiziko- . . .* P. 80.
- Pommier, S. (2001). “Contribution à l’étude de la fatigue des matériaux métalliques”. PhD thesis. Ecole Centrale de Paris.
- Pommier, S., P. Lopez-Crespo, and P.Y. Decreuse (2009). “A multi-scale approach to condense the cyclic elastic-plastic behaviour of the crack tip region into an extended constitutive model”. *Fatigue and Fracture of Engineering Materials and Structures* 32.11, pp. 899–915.
- Proudhon, H., S. Fouvry, and J.Y. Buffière (2005). “A fretting crack initiation prediction taking into account the surface roughness and the crack nucleation process volume”. *International Journal of Fatigue* 27.5, pp. 569–579.
- Rao, J.S., C.B. Kishore, and V. Mahadevappa (2008). “Weight optimization of turbine blades”. *Proceedings 12th International Symposium on Transport Phenomena and Dynamics of Rotating Machinery*.
- Rice, J.R. (1968). “A Path Independent Integral and the Approximate Analysis of Strain Concentration by Notches and Cracks J”. 35, pp. 379–386.
- (1974). “Limitations to the small scale yielding approximation for crack tip plasticity”. *Journal of the Mechanics and Physics of Solids* 22.1, pp. 17–26.
- Ruiz, C., P. H. B. Boddington, and K. C. Chen (1984). “An investigation of fatigue and fretting in a dovetail joint”. *Experimental Mechanics* 24.3, pp. 208–217.
- Sabelkin, V. and S. Mall (2005). “Investigation into relative slip during fretting fatigue under partial slip contact condition”. *Fatigue & Fracture of Engineering Materials and Structures* 28.9, pp. 809–824.
- Sabsabi, M., E. Giner, and F.J. Fuenmayor (2011). “Experimental fatigue testing of a fretting complete contact and numerical life correlation using X-FEM”. *International Journal of Fatigue* 33.6, pp. 811–822.
- Salles, L. (2010). “Etude de l’usure par fretting sous chargements dynamiques dans les interfaces frottantes.” PhD thesis.
- Sato, K (1992). “Determination and control of contact pressure distribution in fretting fatigue”. *Standardization of Fretting Fatigue Test Methods and Equipments ASTM STP 1159 Attia e Waterhouse*.

- Schmidt, R.A. and P.C. Paris (1973). "Threshold for fatigue crack propagation and the effects of load ratio and frequency". *ASTM special technical publication*.
- Schütte, H. and K. Molla-Abbasi (2007). "On the full set of elastic T-stress terms of internal circular cracks under mixed-mode loading conditions". *Engineering Fracture Mechanics* 74.17, pp. 2770–2787.
- Sinclair, G. B., N. G. Cormier, J. H. Griffin, and G. Meda (2002). "Contact Stresses in Dovetail Attachments: Finite Element Modeling". *Journal of Engineering for Gas Turbines and Power* 124.1, p. 182.
- Sines, G. (1959). *Behaviour of metals under complex static and alternating stress*. MacGraw-Hi. New York, pp. 145–169.
- Snecma (Safran Group)*.
- Socie, D.F., L.A. Waill, and D.F. Dittmer (1985). "Biaxial fatigue of Inconel 718 including mean stress effects". *Multiaxial Fatigue*.
- Soderberg, C.R. and V. Sweden (1930). "Factor of safety and working stress". *ASME Transaction, AER-IS*.
- Song, W., A. Keane, J. Rees, A. Bhaskar, and S. Bagnall (2002). "Turbine blade fir-tree root design optimisation using intelligent CAD and finite element analysis". *Computers & Structures* 80.24, pp. 1853–1867.
- Stoschka, M., W. Tan, W. Eichseder, and M. Stockinger (2009). "Introduction to an approach based on the ( $\alpha+\beta$ ) microstructure of elements of alloy Ti-6Al-4V". *Procedia Engineering* 1.1, pp. 31–34.
- Stover, R. J., H. H. Mabie, and M. J. Furey (1985). "A Finite Element Investigation of a Bearing/Cartridge Interface for a Fretting Corrosion Study". *Journal of Tribology* 107.2, p. 157.
- Susmel, L. and P. Lazzarin (2001). "A bi-parametric Wöhler curve for high cycle multiaxial fatigue assessment". *Fatigue & Fracture of Engineering Materials & Structures* 25.1, pp. 63–78.
- Susmel, L. and D. Taylor (2006). "A simplified approach to apply the theory of critical distances to notched components under torsional fatigue loading". *International Journal of Fatigue* 28.4, pp. 417–430.
- Susmel, L., R. Tovo, and P. Lazzarin (2005). "The mean stress effect on the high-cycle fatigue strength from a multiaxial fatigue point of view". *International Journal of Fatigue* 27.8, pp. 928–943.
- Tada, H., P.C. Paris, and G.R. Irwin (2000). *The analysis of cracks handbook*.
- Tanaka, K. (1983). "Engineering formulae for fatigue strength reduction due to crack-like notches". *International Journal of Fracture* 22.2, R39–R46.
- Taylor, D. (1999). "Geometrical effects in fatigue: a unifying theoretical model". *International Journal of Fatigue* 21.5, pp. 413–420.
- Thevenin, J.C. (2004). "Le turboreacteur, moteur des avions a reaction". *AAF 3eme edition*.
- Thieulot-Laure, E., S. Pommier, and S. Fréchet (2007). "A multiaxial fatigue failure criterion considering the effects of the defects". *International Journal of Fatigue* 29.9-11, pp. 1996–2004.
- Tomlinson, G.A. (1927). "The Rusting of Steel Surfaces in Contact". *Proceedings of the Royal Society of London. Series A, Containing Papers of a Mathematical and Physical Character* 115.771, pp. 472–483.
- Tong, J. (2002). "T-stress and its implications for crack growth". *Engineering Fracture Mechanics* 69.12, pp. 1325–1337.
- Tsai, C.T. and S. Mall (2000). "Elasto-plastic finite element analysis of fretting stresses in pre-stressed strip in contact with cylindrical pad". *Finite Elements in Analysis and Design* 36.2, pp. 171–187.
- Vingsbo, O. and S. Söderberg (1988). "On fretting maps". *Wear* 126.2, pp. 131–147.

- Voisin, J., A. Vannes, L. Vincent, J. Daviot, and B. Giraud (1995). “Analysis of a tube-grid oscillatory contact: methodology for the selection of superficial treatments.” *Wear* 181, pp. 826–832.
- Wang, R.H., V.K. Jain, and S. Mall (2007). “A non-uniform friction distribution model for partial slip fretting contact”. *Wear* 262.5-6, pp. 607–616.
- Wang, X. and R. Bell (2004). “Elastic T-stress solutions for semi-elliptical surface cracks in finite thickness plates subject to non-uniform stress distributions”. *Engineering Fracture Mechanics* 71.9-10, pp. 1477–1496.
- Warlow-Davies, E.J. (1941). “Fretting corrosion and fatigue strength: brief results of preliminary experiments”. *Proceedings of the Institution of Mechanical Engineers* 146, pp. 32–38.
- Waterhouse, R.B. and M. Allery (1965). “The effect of non-metallic coatings on the fretting corrosion of mild steel”. *Wear* 8.2, pp. 112–120.
- Weibull, W. (1951). “A statistical distribution function of wide applicability”. *Journal of applied mechanics* 18, pp. 293–297.
- Westergaard, H.M. (1939). “Bearing Pressure and Cracks”. *Journal of Applied Mechanics*, pp. 49–53.
- Wikipedia (2015). *Delta Air Lines Flight 1288*.
- Williams, M.L. (1957). “On the stress distribution at the base of a stationary crack”. *Journal of Applied Mechanics* 24, pp. 109–114.
- Wittkowsky, B.U. and P.R. Birch (2000). “An experimental investigation of fretting fatigue with spherical contact in 7075-T6 aluminum alloy”. *ASTM SPECIAL TECHNICAL PUBLICATION 1367*, pp. 213–230.
- Wright, G.P. and J.J. O’Connor (1972). “The Influence of Fretting and Geometric Stress Concentrations on the Fatigue Strength of Clamped Joints”. *Proceedings of the Institution of Mechanical Engineers* 186.1, pp. 827–835.
- Wright, K.H.R. (1952). “An investigation of fretting corrosion”. *Proceedings of the Institute of Mechanical Engineers* 1B, pp. 556–571.
- Wu, G.Q., C.L. Shi, W. Sha, A.X. Sha, and H.R. Jiang (2013). “Effect of microstructure on the fatigue properties of Ti–6Al–4V titanium alloys”. *Materials & Design* 46, pp. 668–674.
- Zhang, T., P.E. McHugh, and S.B. Leen (2011). “Computational study on the effect of contact geometry on fretting behaviour”. *Wear* 271.9-10, pp. 1462–1480.
- Zuo, J.H., Z.G. Wang, and E.H. Han (2008a). “Effect of microstructure on ultra-high cycle fatigue behavior of Ti–6Al–4V”. *Materials Science and Engineering: A* 473.1-2, pp. 147–152.
- (2008b). “Fatigue Behaviour of Ti-6Al-4V Alloy in Vacuum and at Low Temperature”. *Advanced Materials Research*. Vol. 41-42, pp. 83–90.